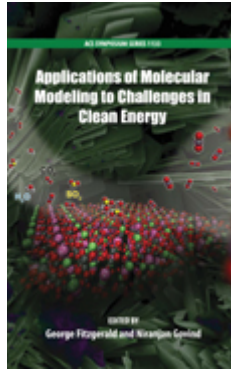
ACS SYMPOSIUM SERIES 1133
Applications of Molecular Modeling to Challenges in Clean Energy
EDITED BY
George Fitzgerald and Niranjan Govind

Applications of Molecular Modeling to Challenges in Clean Energy

In Applications of Molecular Modeling to Challenges in Clean Energy; Fitzgerald, G., et al.;
ACS Symposium Series; American Chemical Society: Washington, DC, 2013.

ACS SYMPOSIUM SERIES **1133**

Applications of Molecular Modeling to Challenges in Clean Energy

George Fitzgerald, Editor
Accelrys, Inc.
San Diego, California

Niranjan Govind, Editor
Pacific Northwest National Laboratory
Richland, Washington

Sponsored by the
ACS Division of Computers in Chemistry

American Chemical Society, Washington, DC

Distributed in print by Oxford University Press

Library of Congress Cataloging-in-Publication Data

Applications of molecular modeling to challenges in clean energy / George Fitzgerald, Niranjan Govind, editors ; sponsored by the ACS Division of Computers in Chemistry.
pages cm. -- (ACS symposium series ; 1133)
Includes bibliographical references and index.
ISBN 978-0-8412-2820-7 (alkaline paper) 1. Renewable energy sources--Research--Congresses. 2. Renewable energy sources--Molecular aspects--Congresses.
3. Renewable energy sources--Computer simulation--Congresses.
I. Fitzgerald, George Benedict. II. Govind, Niranjan. III. American Chemical Society. Division of Computers in Chemistry.
TJ808.6.A66 2013
621.04201′54122--dc23

2013016570

The paper used in this publication meets the minimum requirements of American National Standard for Information Sciences—Permanence of Paper for Printed Library Materials, ANSI Z39.48n1984.

Distributed in print by Oxford University Press

PRINTED IN THE UNITED STATES OF AMERICA

Foreword

The ACS Symposium Series was first published in 1974 to provide a mechanism for publishing symposia quickly in book form. The purpose of the series is to publish timely, comprehensive books developed from the ACS sponsored symposia based on current scientific research. Occasionally, books are developed from symposia sponsored by other organizations when the topic is of keen interest to the chemistry audience.

Before agreeing to publish a book, the proposed table of contents is reviewed for appropriate and comprehensive coverage and for interest to the audience. Some papers may be excluded to better focus the book; others may be added to provide comprehensiveness. When appropriate, overview or introductory chapters are added. Drafts of chapters are peer-reviewed prior to final acceptance or rejection, and manuscripts are prepared in camera-ready format.

As a rule, only original research papers and original review papers are included in the volumes. Verbatim reproductions of previous published papers are not accepted.

ACS Books Department

In Applications of Molecular Modeling to Challenges in Clean Energy; Fitzgerald, G., et al.;
ACS Symposium Series; American Chemical Society: Washington, DC, 2013.

Preface

As the world struggles with global climate change, rising oil costs, and increasing energy demands, it has become critical to search for alternative energy sources, more efficient chemical processes, and more environmentally benign materials. Computational methods—including molecular modeling and scientific informatics—have already made significant contributions to this area. Improved solar cells, more stable PEM fuel cells, and longer-lived batteries are just some of the outcomes.

This book is a collection of scientific papers that were presented at a COMP division symposium at the ACS National Spring Meeting in San Diego in the spring of 2012. The focus of the symposium was on "Applications of computational methods to environmentally sustainable solutions." The symposium, which was held over 3 days and 6 sessions, brought together leading researchers from academia, national laboratories, and industry within the U.S. and around the world, and covered a broad spectrum of applications of computational approaches to environmentally sustainable solutions.

The various topics that were covered included batteries, biomass conversion, catalysis, CO_2 capture and sequestration, fuel cells, H_2 generation and storage, improved chemical processes, and photovoltaic materials. With the significant advances in modeling techniques and simulation tools over the last decade, real-world materials and complex chemical processes in realistic environments can now be studied *in silico* and directly compared with experimental data. This has spawned rapid growth in the rational design of new materials and the study of complex mechanisms for energy applications.

Biofuels derived from lignocellulosic biomass are actively being pursued as an alternative to traditional fossil fuels. This widely available and biodegradable raw material when coupled with portability of liquid ethanol makes cellulosic derived ethanol a very promising transportation fuel. In Chapter 1, Muthukumar and Khare have shed light on the detailed energetics and separation mechanisms of cello-oligosaccharides from the cellulose crystal surface. This study is an important step in the detailed understanding and optimization of the enzymatic hydrolysis step.

With the role of CO_2 being clearly established as the most important greenhouse gas and a key contributor to global warming, major efforts have been initiated by nations around the world to stem the emissions of CO_2 and to focus as well on its capture and sequestration. This requires a fundamental understanding of the complex interactions of CO_2 in complex environments. Chapters 2, 3, 4, and 5 cover detailed computational studies of these interactions. Maiti (Chapter 2) has explored the ability of ionic liquids (IL) to capture carbon

In Applications of Molecular Modeling to Challenges in Clean Energy; Fitzgerald, G., et al.;
ACS Symposium Series; American Chemical Society: Washington, DC, 2013.

by studying the solubility of CO_2 in these solvents. Glezakou and McGrail (Chapter 3) have investigated chemical processes in wet supercritical CO_2 and the interaction of this fluid with solid supports, such as metals and oxides. Yoon (Chapter 4) has studied the dynamic behavior and coverage dependence of CO_2 adsorbed on the rutile TiO_2 (110) surface with surface oxygen vacancies (O_v) using dispersion-corrected density functional theory combined with *ab initio* molecular dynamics (AIMD). Chapter 5 by Liu, Cundari, and Wilson sheds light on the periodic trends in 3*d* metal mediated CO_2 activation with a focus on the reverse water–gas shift (RWGS) reaction and the hydrolysis of CO_2 using 3*d* metal β-diketiminate complexes and heterogeneous catalysis studies of the reduction of CO_2 to CO on first row transition metal surfaces like Fe, Co, Ni, and Cu, respectively.

Catalysis is a very significant area for clean energy research. Catalysts, of course, lower the energy barrier for reactions; hence, they reduce the energy required by production facilities, making them "greener." Catalysts also play a fundamental role in H_2 generation, biomass conversion, and fuel cell efficiency. Chapters 6, 7, 8, and 9 explore recent efforts in these areas. Ho and co-workers (Chapter 6) demonstrate how Ni-based bio-inspired catalysts produce H_2 at rates comparable to those of biological processes. Halasz and Liang (Chapter 7) provide three examples of using modeling to elucidate the structure and properties of "green" catalysts. In Chapter 8, Xu and Wang investigate bi-metallic nanocatalysts for dehydrogenation of methanol, which is essential to ethanol proton exchange membrane fuel cells. The section on catalysis concludes with Chapter 9 by Podkolzin, Fitzgerald, and Koel, who use a combination of modeling and experiment to determine the surface structure of two Fischer-Tropsch catalysts, which are essential for the conversion syngas into liquid fuel hydrocarbons.

Solar energy has long been argued as the ideal, sustainable energy source. Most readers will be familiar with the use of commercial photovoltaics for the direct generation of electricity from light. The authors in this volume, however, explore organic systems that mimic natural photosynthesis. The systems known as Photosystem I (PSI) and Photosystem II (PSII) both consist of an enzymatic reaction center surrounded by a light-harvesting complex. The authors take two very different approaches toward increasing our understanding of these systems. In Chapter 10, Pendley and co-authors outline a sophisticated multi-scale approach to modeling PSI; this provides a way to model the docking of the large complexes while allowing them to include the quantum mechanical effects necessary to describe the electronic processes involved. In Chapter 11, Rivalta and co-authors use a similar approach to study the oxygen-evolving complex in PSII; the results deliver fundamental insights into Mn-based water-oxidation catalysis.

Lithium (Li) ion based batteries, due to their high energy density and superior charge retention when not in operation, are among the most widely used and explored battery technologies today. The main component of a Li-ion battery is the electrochemical cell that consists of two electrodes and an electrolyte, which is used as a Li charge carrier. In Chapter 12, Ferguson and Curtiss provide a broad survey of the atomistic simulation techniques currently in use to optimize

In Applications of Molecular Modeling to Challenges in Clean Energy; Fitzgerald, G., et al.;
ACS Symposium Series; American Chemical Society: Washington, DC, 2013.

and design the cell components as well as improve cell operation. The chapter also includes an extensive literature survey which we believe will be beneficial to students and researchers entering this field of research.

We hope that this collection will benefit graduate students and researchers specializing in computational approaches for green energy solutions. We wish to thank Tim Marney and Arlene Furman of the editorial department at ACS for their assistance in preparing this volume and for keeping us on schedule.

We also wish to thank Vassiliki-Alexandra Glezakou for the cover graphic. The graphic depicts the potential of carbonate minerals for desulfurization. This scenario carries significant implications for more economic green solutions with considerable savings in retrofit costs and CO_2 clean up. The image was created by Cortland Johnson, from original figures by H. T. Schaef and V.-A. Glezakou, all of PNNL.

George Fitzgerald, Ph.D.
Accelrys, Inc.
10188 Telesis Court
San Diego, California 92121
George.Fitzgerald@accelrys.com (e-mail)

Niranjan Govind, Ph.D.
Environmental Molecular Sciences Laboratory
Pacific Northwest National Laboratory
902 Battelle Boulevard
P.O. Box 999, MSIN K8-91
Richland, Washington 99352
Niri.govind@pnnl.gov (e-mail)

In Applications of Molecular Modeling to Challenges in Clean Energy; Fitzgerald, G., et al.;
ACS Symposium Series; American Chemical Society: Washington, DC, 2013.

Chapter 1

Molecular Dynamics Simulation of Free Energy of Desorption of Cellohexaose from a Cellulose Crystal Surface

Lakshmi Muthukumar and Rajesh Khare*

Department of Chemical Engineering, Texas Tech University, Box 43121, Lubbock, Texas 79409
***Phone: +1-(806)-742-0449. Fax: +1-(806)-742-3552.**
E-mail: rajesh.khare@ttu.edu.

Cello-oligosaccharide intermediates are formed during the enzymatic hydrolysis of cellulose. Re-adsorption of these cello-oligomers on the cellulose crystal surface hinders the enzymatic hydrolysis step in the conversion of lignocellulosic biomass to biofuel. The knowledge of energetics as well as the mechanism of desorption of cello-oligosaccharides from cellulose crystal surface is thus important for optimizing the enzymatic hydrolysis process conditions. In this study, we have used molecular dynamics simulations to calculate the free energy of desorption of a short cello-oligosaccharide from the cellulose Iβ crystal surface. Specifically, we have calculated the free energy of desorption of cellohexaose from the (100) and the (110) surfaces of this cellulose crystal. In complex systems such as the one under consideration, there are several choices for defining the reaction coordinate that is required for performing these free energy simulations. We have compared the results obtained by the usage of two different reaction coordinates in our calculations. Our results show that, in general, the free energy of desorption of cellohexaose from the cellulose crystal surface exhibits a step-wise increase, corresponding to sequential peeling of the adsorbed glucose residues from the cellulose crystal surface.

In Applications of Molecular Modeling to Challenges in Clean Energy; Fitzgerald, G., et al.;
ACS Symposium Series; American Chemical Society: Washington, DC, 2013.

Keywords: Cellulose crystal surface; Cellohexaose; Molecular dynamics simulations; Free energy; Adsorption; Reaction coordinate; Desorption

Introduction

Biofuel derived from lignocellulosic biomass is an important alternative energy fuel that is being considered for replacing the traditional petroleum fuels (*1–3*). Cellulosic biomass is the most abundant renewable material available (*4–6*). This, coupled with the portability of liquid ethanol, make cellulosic ethanol a strong candidate for the large-scale production and deployment as a transportation fuel (*7*).

In the early developments, bio-ethanol was produced primarily from food crops such as corn and sugar cane (*8*); it was soon realized that any scale-up in the manufacturing capacity of fuel derived from this source will deplete the food supply. An alternative to this food based bioethanol is the lignocellulosic biomass derived fuel. The term lignocellulosic biomass includes a wide variety of sources such as agricultural waste and forest products (*4*, *7–9*). The primary source of energy in this lignocellulosic biomass is the cell wall of plants which is composed of cellulose, hemicellulose and lignin or pectin (*6*, *10*). Specifically, cellulose fibrils are embedded in a network of hemicellulose and lignin. Our main interest in lignocellulosics is limited to cellulose, a long-chain polymer of glucose.

The process of conversion of lignocellulosic biomass to biofuel consists of depolymerization of cellulose to monomeric sugars, followed by their fermentation to ethanol. Enzymatic hydrolysis plays an important role in this process. Prior to enzymatic hydrolysis of biomass, it is subjected to a pre-treatment step which loosens the lignin network thus facilitating the enzyme attack on the cellulose fibril (*5*, *10*, *11*). Of the three major steps in the conversion of lignocellulosic biomass to ethanol i.e. pre-treatment, enzymatic hydrolysis and fermentation (*2*), enzymatic hydrolysis is the slowest and hence the rate-determining step (*3*, *12*). Enzymatic hydrolysis is achieved by a group of enzymes called the "cellulases" which consists of three constituents viz., endogluconase, exoglucanase and β-glucosidase (*13*). The process of hydrolysis can be briefly summarized as follows: endoglucanase cleaves the cellulose chains at random internal locations while exoglucanase attacks the end of the cellulose chain thus producing cellobiose as the primary product. Finally, β-glucosidase acts on cellobiose to form glucose in the solution. The glucose thus obtained is fermented to yield the desired ethanol fuel product.

The enzymatic hydrolysis step described above yields small and medium molecular weight cello-oligosaccharides as reaction intermediates. These intermediates are found to re-adsorb onto the cellulose crystal surface hindering further action of the enzyme and thus reducing the rate of reaction (*14–17*). A detailed study of the energetics as well as the mechanism of separation of cello-oligosaccharides from the crystal surface will aid in optimizing these process conditions.

In Applications of Molecular Modeling to Challenges in Clean Energy; Fitzgerald, G., et al.;
ACS Symposium Series; American Chemical Society: Washington, DC, 2013.

The process of removal of cello-oligosaccharides from the cellulose crystal surface has previously been studied in molecular simulations (*18–20*). In particular, Payne *et. al*., studied the work required for decrystallizing cello-oligosaccharides of different degrees of polymerization from a cellulose crystal surface (*18*). In another study, the free energy of decrystallization of a glucan chain from the cellulose crystal surface in the presence of two different solvents was determined (*19*). In both of these studies, the glucan chain being pulled away was an intrinsic part of the cellulose crystal surface. Thus, the energetics of the process was governed by three types of interactions: inter-sheet, intra-sheet (which in this chapter are considered to consist only of the inter-chain interactions between the chains in the same sheet) and intra-chain. We are interested in the process of removal of a cello-oligosaccharide molecule that is adsorbed on the cellulose crystal surface; such a process has only two of these contributions to energy, namely, inter-sheet and intra-chain interactions. Previously, Bergenstrahle *et. al*. used steered molecular dynamics (SMD) technique to calculate the pull-off energy of cellooctaose which was placed over a cellulose crystal (*20*). In this study, we go a step further to determine the free energy of removal of a cellohexaose molecule that is adsorbed on the cellulose crystal surface. Both enthalpic and entropic contributions to the cello-oligosaccharide desorption process are incorporated in the free energy so calculated. Furthermore, we have calculated the free energy profiles for the desorption of a cellohexaose molecule from two different cellulose crystal surfaces and also compared the results obtained by the usage of different reaction coordinates. This comparison provides insight into the mechanism of desorption of cello-oligosaccharide molecules from the cellulose crystal surface.

Methods

The simulation system consists of cellulose Iβ crystal surface, cello-oligosaccharide molecule and water. The cell parameters and the unit cell coordinates of the cellulose crystal were obtained from literature (*21*). The crystal structure of cellulose Iβ is monoclinic; the cell parameters are: a = 7.784 Å, b = 8.201 Å and c = 10.380 Å (where c is the chain axis), along with the angle γ = 96.5°. The unit cell of the crystal has two parallel chains which are termed as the ‘center’ and the ‘origin’ chains. The crystal structure was generated such that an infinite slab of cellulose was obtained in the chain axis direction when periodic boundary conditions are applied. We used GLYCAM06 force field (*22*) to represent the molecular interactions for the crystal and cello-oligomer, while TIP3PF (*23*) model was used for water molecules. All of the simulations were carried out using the NAMD package (*24*). The VMD package was used for trajectory analysis and molecular visualization (*25*). The initial structure files of the system were created using the AMBERTOOLS module (*26*). A time-step of 1 fs was used for integrating the equation of motion. The non bonded interactions were cut-off at a distance of 12 Å and long-range interactions were calculated with particle mesh ewald technique (*27*). The bond lengths of the water molecules in the simulation were constrained using the SETTLE method (*28*). The initial

In Applications of Molecular Modeling to Challenges in Clean Energy; Fitzgerald, G., et al.;
ACS Symposium Series; American Chemical Society: Washington, DC, 2013.

structures were relaxed using 1000 steps of conjugate gradient method. A Langevin thermostat and a Nosé- Hoover Langevin barostat (*29–31*) were used to control temperature and pressure respectively. We have considered two different crystallographic surfaces in our study, the (100) surface which is hydrophobic, and the other (110) surface which is hydrophilic. Since cellulose crystal has specific regions, which are hydrophobic or hydrophilic in nature, in order to gain full understanding of the molecular interactions involved in the process, it is important to study both of these surfaces which expose different regions of the crystal to surrounding water. Further details of the model preparation procedure used for the systems corresponding to the two different crystal surfaces are given below.

(100) Crystal Surface

We have investigated two different scenarios for the initial adsorbed state of cellohexaose on the (100) crystal surface:

(1) adsorption in the crystallographic conformation i.e., when cellohexaose forms flat ribbon-like conformation over the cellulose crystal surface, and
(2) adsorption such that cellohexaose is not in the crystallographic conformation, henceforth termed as "adsorption with an imperfection" over the cellulose crystal surface. Figure 1a is a pictorial representation of the (100) crystal surface.

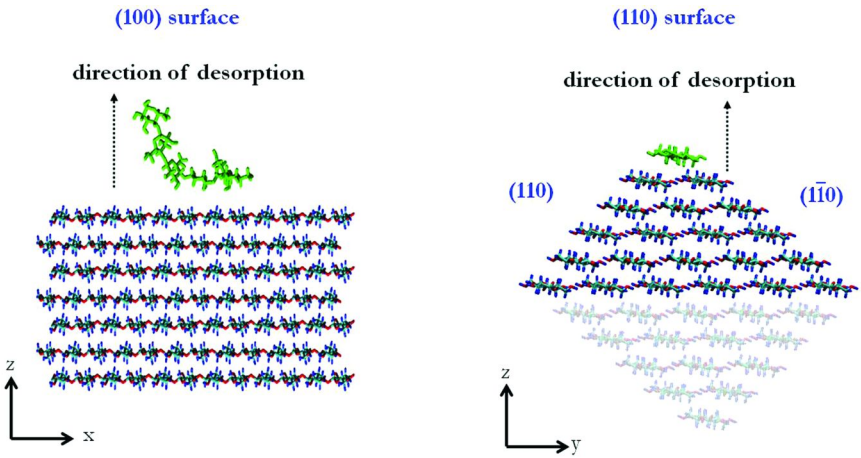

Figure 1. (a) (100) and (b) (110) surfaces of cellulose Iß crystal. The adsorbed cellohexaose molecule is shown in green color. Water molecules are not shown for the sake of clarity.

In Applications of Molecular Modeling to Challenges in Clean Energy; Fitzgerald, G., et al.;
ACS Symposium Series; American Chemical Society: Washington, DC, 2013.

Adsorption in Crystallographic Conformation (Case 1)

The (100) crystal surface used in this case had 40 glucan chains each of which consisted of 12 monomer units. These 40 chains were arranged in the surface in 5 layers. The cellohexaose molecule was placed in the "adsorbed state" on the cellulose crystal surface, in a location that conforms to a crystallographic position. In this position, the cellohexaose molecule adopted the flat-ribbon conformation with all of its native contacts with the crystal surface. A box of water was placed above the cellulose crystal surface containing the adsorbed cellohexaose molecule. It is to be noted here that, this (100) crystal surface was infinite not only in the chain axis direction, but also in the lateral intra-sheet direction. The box was equilibrated for at least 3 ns using a series of constant *NVT* (constant number of atoms, volume and temperature) and constant *NPT* (constant number of atoms, pressure and temperature) molecular dynamics (MD) simulations. During the *NPT* simulations, the box dimensions in the three directions were allowed to vary independently. These box dimensions in the x, y and z directions were: 64.207(±0.035), 65.581(±0.072) and 88.410(±0.267) Å respectively. The total number of atoms in the system was 49,803.

Adsorption with an Imperfection (Case 2)

The (100) crystal surface used in this case had 56 glucan chains each of which contained 12 monomer units. These were arranged in 7 layers with each layer containing eight chains. The cello-oligosaccharide was obtained from the 'origin' chain coordinates from the literature (*21*) and was solvated in a box of water. The box was equilibrated for at least 3 ns using a series of constant *NVT* and constant *NPT* MD simulations. During these runs, the cello-oligosaccharide molecule was allowed to adsorb freely on the cellulose crystal surface. The box dimensions in the x, y and z directions were 64.218(±0.042), 65.784(±0.048) and 88.410(±0.214) Å respectively. The total number of atoms in the system was 40,131.

(110) Crystal Surface

The (110) crystal surface studied in this work had 35 glucan chains each of which contained 12 monomer units (see Figure 1b). The cello-oligosaccharide molecule was incorporated in the system by replacing the top chain with a cellohexaose molecule (shown in green color in Figure 1b).

For the (110) crystal surface system, we have considered only the case in which the cello-oligosaccharide molecule was stationed at the crystallographic position. The crystal surface along with the cellohexaose molecule was solvated in a box of water and the system density was equilibrated using constant *NPT* MD simulation. In this case, the crystal was infinite only in the chain-axis direction. After equilibration, the bottom part of the crystal (the faded part in Figure 1b) was removed for computational efficiency. Following the strategy employed in literature (*18*), the ring carbon atoms of the bottom most layer of the crystal thus obtained were harmonically restrained to their positions with a force constant

In Applications of Molecular Modeling to Challenges in Clean Energy; Fitzgerald, G., et al.;
ACS Symposium Series; American Chemical Society: Washington, DC, 2013.

of 2 kcal/mol/Å^2 in the subsequent calculations. This system configuration was again equilibrated using constant *NPT* simulation followed by constant *NVT* simulation for a total duration longer than 3.5 ns. The box dimensions in the x, y and z directions were 64.192(±0.045), 59.045(±0.870) and 114.841(±0.214) Å respectively. The total number of atoms in the system was 44,763.

Free Energy Calculations

The free energy of desorption of cellohexaose was calculated using the umbrella sampling technique (*32*). In the highly multidimensional system studied here, there are a large number of pathways (i.e. reaction coordinates) that the system can trace in going from the initial adsorbed state to the final desorbed state in which the cellohexaose molecule loses all the interaction with the cellulose crystal surface. In this work, we have considered two different reaction coordinates: (i) the normal distance between the center of mass of the end ring of cellohexaose molecule (i.e., either the first or the last glucose residue) and the center of mass of the top layer of cellulose crystal surface (denoted as RC Ia and RC Ib, corresponding to the chains obtained by capping the reducing and non-reducing ends respectively), and (ii) the normal distance between the center of mass of the adsorbed cellohexaose molecule and the center of mass of the top cellulose crystal layer (RC II). These reaction coordinates are shown in Figure 2.

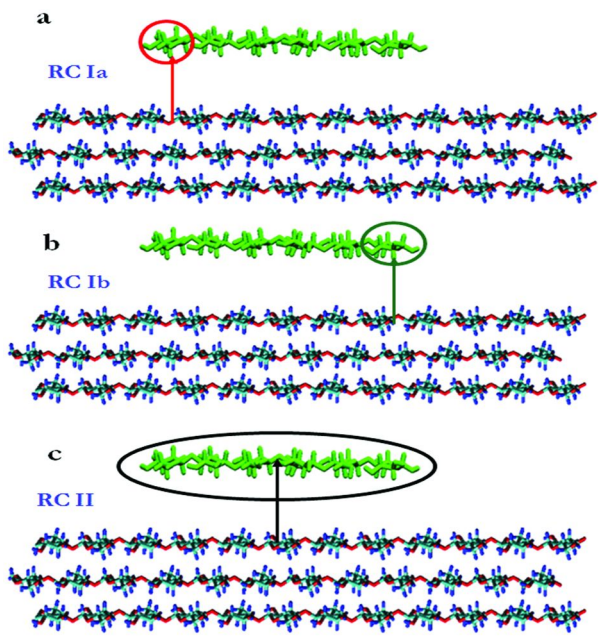

Figure 2. Illustration of the reaction coordinates on the (100) crystal surface: (a) RC Ia, (b) RC Ib, and (c) RC II.

In Applications of Molecular Modeling to Challenges in Clean Energy; Fitzgerald, G., et al.;
ACS Symposium Series; American Chemical Society: Washington, DC, 2013.

All of the free energy calculations were conducted under constant *NVT* conditions at a temperature of 300 K. The details of the umbrella sampling simulations for the different sets of calculations are given in Table 1. The probability histograms generated from these umbrella sampling simulations for each of the windows were combined using the Weighted Histogram Analysis Method (WHAM) (*33*, *34*); the WHAM code from Grossfield laboratory was used for this purpose (*35*).

Table 1. Umbrella Sampling Simulation Details

Surface studied	*Width of each window (Å)*	*Total number of windows*	*Force constant (kcal/mol/Å²)*	*Equilibration Time (ns)*	*Production Time (ns)*
(110)	0.5	73	10	0.02	1
(100) case 1	0.6	60	5	0.02	1
(100) case 2	0.5	73	10	0.20	1

Results

The potential of mean force (PMF) profiles for the desorption of cellohexaose from two different - (100) and (110) - cellulose crystal surfaces were obtained. The characteristics of these profiles are described below.

PMF for Separation of Cellohexaose from Cellulose (100) Crystal Surface

Case 1: Cellohexaose Adsorbed in Crystallographic Conformation

For case 1, when the cello-oligosaccharide was peeled from the end a (RC Ia), the PMF curve exhibited a step-wise increase (see Figure 3). The first minimum in the profile was observed at a separation distance of about 4.0 Å. The favorable van der Waal's interactions along with the hydrogen bonding interactions between the cellulose crystal and the cellohexaose molecule make this configuration highly stable. The well-depth of the first minimum is about 12 kcal/mol. As the cellohexaose molecule moves away from the first minimum, it starts losing these favorable interactions with the crystal and consequently the PMF starts increasing. Beyond this first minimum, there are two significant features in the PMF profile which occur in a repetitive fashion to yield a step-wise profile: the region of "increasing" PMF and the "plateau" region.

An inspection of the molecular structures along the PMF profile shows that the first glucose residue was completely pulled away at a reaction coordinate value of about 8-9 Å. The subsequent plateau region in PMF prevails, until the second residue gets completely pulled away. It can be generalized that for every odd numbered residue being pulled away, there is an increase in the PMF and for every even numbered residue being pulled away completely, there exists a plateau region. The origin of these steps in the PMF profile can be deduced by focusing on

In Applications of Molecular Modeling to Challenges in Clean Energy; Fitzgerald, G., et al.;
ACS Symposium Series; American Chemical Society: Washington, DC, 2013.

the hydrogen bonding interactions in cellulose. Cellulose Iβ has a characteristic network of hydrogen bonds. There are two types of hydrogen bonds in cellulose: the conventional O-H-O hydrogen bonds, and the other non-conventional C-H-O hydrogen bonds which are termed as "alternative hydrogen bonds" (*18*) or "pseudo hydrogen bonds" (*36*). The O-H-O bonds are formed either between the atoms in the same chain (intra-chain) or between two different chains in the same sheet (intra-sheet). The C-H-O bonds are formed between the chains in the adjacent sheets (inter-sheet).

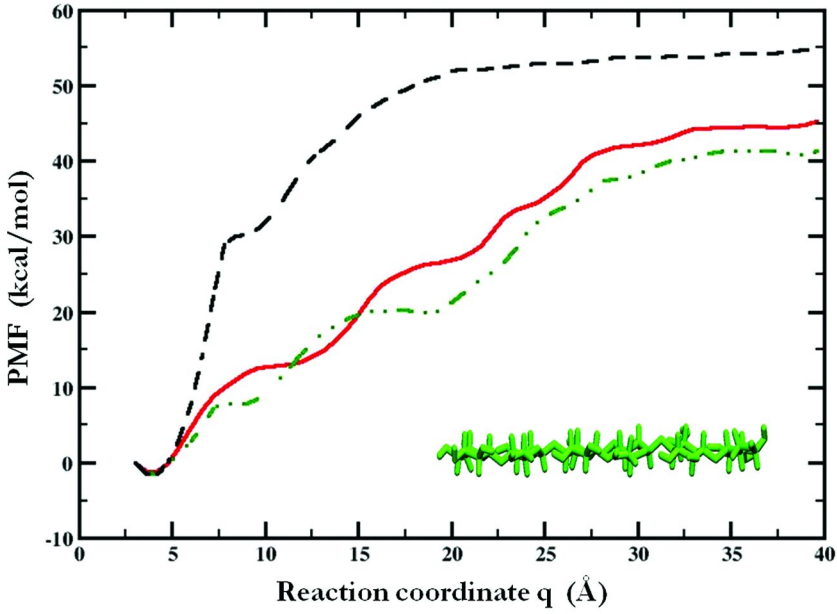

Figure 3. PMF for desorption of cellohexaose from (100) cellulose crystal surface (case 1). Results for reaction coordinates RC Ia, RC Ib and RC II are shown in red (solid line), green (dot-dash line) and black (dashed line) colors respectively. Inset: Flat ribbon configuration of cellohexaose over the (100) crystal surface.

In the process under consideration, intra-sheet interactions are absent, while the intra-chain and inter-sheet hydrogen-bonding interactions play an important role. Initially, as a glucose ring gets pulled away from the cellulose crystal during the process of desorption, the cellohexaose molecule loses its inter-sheet interactions with the crystal surface while exposing the hydrophobic moieties of the cellulose surface to water. This results in an increase in the free energy. Next, as more residues start getting pulled away, intra-chain hydrogen-bonding interactions begin to develop in the cellohexaose molecule; the favorable nature of these interactions results in a decrease in the free energy. The plateau regions in the PMF plot are obtained when these effects of loss of inter-sheet interactions and gain of intra-chain interactions compensate each other. When an odd numbered residue gets peeled away from the cellulose crystal surface, it does not have an

In Applications of Molecular Modeling to Challenges in Clean Energy; Fitzgerald, G., et al.;
ACS Symposium Series; American Chemical Society: Washington, DC, 2013.

adjacent residue in the desorbed part of the molecule to form favorable intra-chain hydrogen bonds thus resulting in an increase in the free energy. Here we note that for the first residue, no previously peeled residue is available for forming intra-chain hydrogen bonds, while for the subsequent odd numbered residues i.e. third and fifth residues, the residues that were peeled off before them have already formed hydrogen bonds and are not available for further intra-chain interactions. On the other hand, in the case of even numbered residues, the compensating intra-chain interactions with the odd numbered residue that was peeled off just before it dominate, resulting in the plateau region. Sequential occurrence of these effects leads to a step-wise increase in the free-energy. The total free energy change for cellohexaose desorption for RC Ia in this case is about 45 kcal/mol.

Another PMF plot was obtained by the use of RC Ib i.e., when the cellohexaose molecule was peeled away from the end b. The PMF profile obtained in this calculation exhibits a step-wise increase in free energy as was the case for RC Ia. The slight difference in these profiles on small sub-monomer length scales can be attributed to the chemical difference in the two ends of the molecule viz., end a and end b. We also note that on the length scales larger than a monomer, the two profiles show quantitatively similar behavior up to a distance of about 25 Å, beyond which there is an approximately constant difference of about 4 kcal/mol between them. The total free energy change for cellohexaose desorption for RC Ib is about 41 kcal/mol.

We also obtained a PMF profile by using the reaction coordinate RC II i.e., the distance between the center of mass of cellohexaose and the center of mass of the first layer of cellulose crystal surface. Usage of this type of reaction coordinate yields a PMF curve which shows a rapid and continuous increase in free energy followed by a region of approximately constant value. The process of removing the cellohexaose molecule from its center of mass i.e. using reaction coordinate RC II, is analogous to removing a "sticky strap" by pulling from its center. This is a highly unfavorable process in which both chain ends start sliding over the surface and the hydrogen bonding interactions of the entire chain are disturbed. With this reaction coordinate, the cellohexaose molecule reaches its final desorbed state without going through the process of sequential peeling of the individual glucose units starting from one end. The total free energy difference between the adsorbed and desorbed state for RC II is about 54 kcal/mol i.e., about 18 kcal/mol/cellobiose.

Case 2: Cellohexaose Adsorbed with Imperfection

Similar sets of PMF plots were obtained for case 2 as shown in Figure 4. For RC Ia and RC II, the PMF profiles resemble the corresponding profiles obtained in case 1. On the other hand, the PMF plot obtained by peeling the cello-oligosaccharide from its end b (RC Ib) in this case is considerably different from that obtained for RC Ib in case 1. Furthermore, although the two ends of the cellohexaose molecule are not chemically equivalent, one still expects the profiles obtained by peeling either end of cellohexaose (i.e. by the usage of RC Ia and RC Ib) from the same starting structure to look approximately alike on the length

In Applications of Molecular Modeling to Challenges in Clean Energy; Fitzgerald, G., et al.;
ACS Symposium Series; American Chemical Society: Washington, DC, 2013.

scales larger than the size of a glucose residue. This observation was found to hold for case 1 but not for case 2. With RC Ib for case 2, there is an initial "flat" region in the PMF plot until a distance of about 12 Å, while the corresponding region is absent in the PMF plot for RC Ia. This difference can be explained by inspection of the initial structure of the adsorbed cellohexaose molecule (see inset of Figure 4).

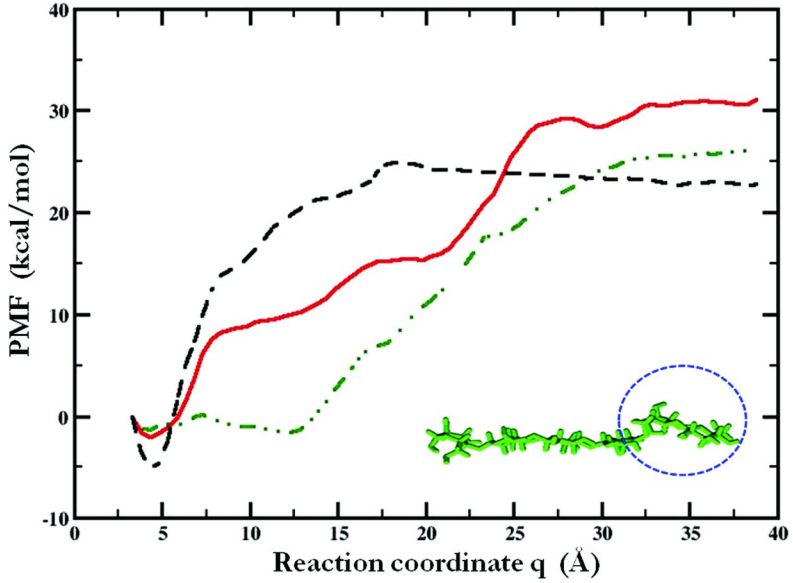

Figure 4. PMF for desorption of cellohexaose from (100) cellulose crystal surface (case 2). Results for reaction coordinates RC Ia, RC Ib and RC II are shown in red (solid line), green (dot-dash line) and black (dashed line) colors respectively. Inset: Snapshot of cellohexaose molcule in its initial state showing the bulge that was formed during free adsorption on the (100) crystal surface.

As explained in the system preparation section, the initial structure for case 2 was prepared by allowing the cellohexaose molecule to adsorb freely on the cellulose crystal surface. Therefore, in the resulting initial structure, the cellohexaose molecule did not form a flat-ribbon conformation over the surface. Specifically, there was a bulge (imperfection in the context of crystalline conformation) near the end b of the molecule which favored strong intra-chain interactions. When the cellohexaose molecule was peeled from this end, as it moved away from the surface, it continued to strengthen its favorable intra-chain interactions until the third residue was peeled away from the surface, i.e. at approximately 13 Å. After the third residue was peeled off, like case 1 PMF profiles, the PMF subsequently increased in stages where each stage of PMF increase is followed by a shoulder instead of a plateau as was the situation for the step profiles. The generalization suggestive of a step-wise PMF profile is thus not applicable in case of RC Ib since the free energy increase starts in a different

In Applications of Molecular Modeling to Challenges in Clean Energy; Fitzgerald, G., et al.;
ACS Symposium Series; American Chemical Society: Washington, DC, 2013.

fashion and the process follows a different path. The total free energy increase in this case for RC Ia is about 30 kcal/mol (i.e. 10 kcal/mol/cellobiose removed) and that for RC Ib is about 27 kcal/mol (i.e. 9 kcal/mol/cellobiose removed).

In all of the free energy simulations reported here i.e., those using the reaction coordinates RC Ia, RC Ib and RC II, for case 1 and case 2, state 1 is the one in which the cello-oligosaccharide molecule is in the completely adsorbed state on the crystal surface, whereas state 2 is the state in which the cello-oligosaccharide molecule is far away from the crystal surface such that it has lost all of its direct interactions with the cellulose crystal. Thermodynamically, since state 1 and state 2 are the same for all three pathways for a given starting structure, we expect that the total free energy differences resulting from the use of different reaction coordinates to be the same for each of the cases. Clearly, as seen from Figure 3 and Figure 4, that is not the situation. To further investigate the origin of these differences in the total PMF values for a given initial structure, we focus on the cellohexaose conformations in the final desorbed state. To this end, a plot of the time dependence of the radius of gyration (R_g) of cellohexaose molecules in case 1 and case 2 for all three reaction coordinates RC Ia, RC Ib and RC II in the last umbrella sampling window is presented in Figures 5 and 6. As can be seen, for 5 of the 6 simulations, the R_g value fluctuated around 9.4 - 9.5 Å over the entire umbrella sampling window. However, in the RC Ib calculation for case 2, the radius of gyration of cellohexaose decreased from 9.5 Å to 7.5 Å during the simulation; one snapshot of cellohexaose molecule from this window is shown in the inset of Figure 6 indicating that the molecule formed a somewhat coiled conformation in this simulation. On the other hand, the snapshots of cellohexaose molecule in the other five simulations (Figure 5 and Figure 6) clearly show that the cello-oligosaccharide molecule remained in the relatively linear conformation throughout the simulation window in these cases.

These observations suggest that the approximately linear conformation (R_g ~ 9.5 Å) is the most stable conformation of cellohexaose in water; this has also been reported in literature (*37*). However, occasionally, conformational changes in the glycosidic φ and ψ angle lead to a marked departure from this linear conformation, as has been observed here for a particular simulation window for RC Ib for case 2 and as has also been reported in the literature (*38*, *39*). The umbrella sampling simulation window needs to be long enough such that these conformational transitions are adequetely sampled. Our analysis shows that at large separation distances of the cellohexaose molecule from the cellulose crystal surface, only one of the six calculations (RC Ib for case 2) shows such a transition during the umbrella sampling window but not the other five, indicating that the run length was not long enough. We believe that these deductions on the length of the simulation run for a window apply mainly to windows at large separation distances from the surface thus explaining the differences in the PMF profiles at these distances. At smaller separations, entire molecule or a part of the cellohexaose molecule remains adsorbed on the surface. Such fully or partially adsorbed molecule does not have complete conformational freedom and hence adequete sampling of molecule conformation can be acheived in a simulation window of the 1 ns duration.

In Applications of Molecular Modeling to Challenges in Clean Energy; Fitzgerald, G., et al.;
ACS Symposium Series; American Chemical Society: Washington, DC, 2013.

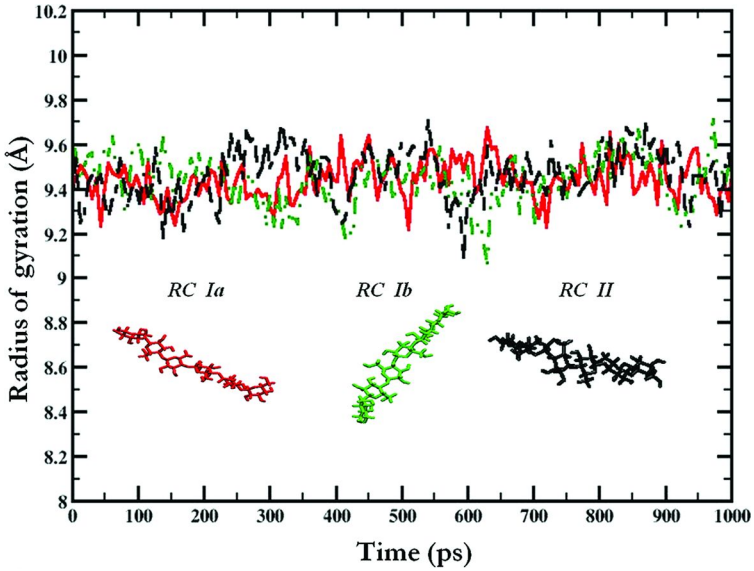

Figure 5. (100) surface, Case 1: Time dependence of radius of gyration in the 60th simulation window of the umbrella sampling calculation (line styles for the three reaction coordinates are the same as in Figure 3). Inset: Snapshots of cellohexaose molecule in the RC Ia , RC Ib and RC II calculations are shown in red, green and black colors respectively.

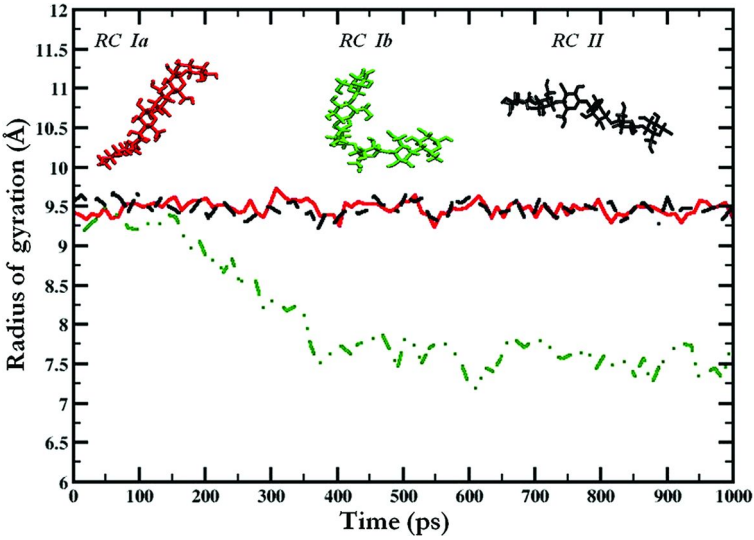

Figure 6. (100) surface, Case 2: Time dependence of radius of gyration in the 60th simulation window of the umbrella sampling calculation (line styles for the three reaction coordinates are the same as in Figure 4). Inset: Snapshots of cellohexaose molecule in the RC Ia , RC Ib and RC II calculations are shown in red, green and black colors respectively.

In Applications of Molecular Modeling to Challenges in Clean Energy; Fitzgerald, G., et al.;
ACS Symposium Series; American Chemical Society: Washington, DC, 2013.

PMF for Separation of Cellohexaose from Cellulose (110) Crystal Surface

The free energy change required for the desorption of cellohexaose molecule from the cellulose (110) crystal surface was determined using the same 3 reaction coordinates RC Ia, RC Ib and RC II as for the (100) surface. For the (110) surface, we studied only one case in which the cello-oligosaccharide molecule was initially placed at a specific crystallographic location on the surface. As seen from Figure 7, with the reaction coordinate RC Ia, the PMF value increased in steps as was the case for the (100) surface. The steps in the free energy plot are less distinct for the (110) surface than those for the (100) surface. Specifically, it appears that the plateau regions are not as distinct for the (110) crystal surface. PMF profile obtained using reaction coordinate RC Ib also shows a step-wise increase in its value. It is seen that the PMF plots resulting from RC Ia and RC Ib calculations are quantitatively similar over the length scale of a glucose residue upto a distance of about 25 Å. The last step increase exhibited by the RC Ib plot at a separation distance of about 30 Å seems to be absent in the RC Ia plot, this explains the ultimate difference in the total PMF change values (about 40 kcal/mol and 49 kcal/mol respectively for RC Ia and RC Ib) calculated from these two reaction coordinates. Similar to the case for the (100) surface, we attribute this difference to the inadequate sampling of the cellohexaose molecule conformations at these large separation distances from the cellulose crystal surface.

Lastly, as was the case for the (100) surface, the PMF profile obtained by the usage of reaction coordinate RC II here shows a sharp increase with an increase in the separation distance. The continuous breakage of hydrogen bonds between the cellulose crystal surface and the desorbing cellohexaose molecule explains this sharp increase in the PMF in the case of RC II. The total free energy increase in this calculation is about 45 kcal/mol, which is 15 kcal/mol/cellobiose removed.

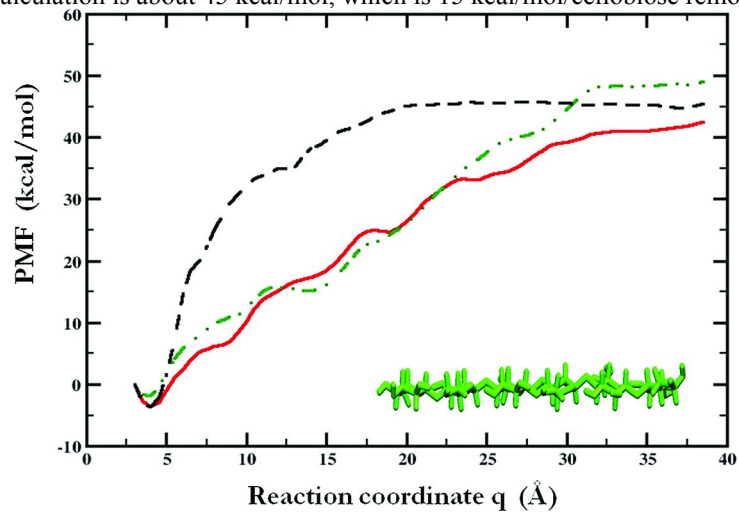

Figure 7. PMF for the desorption of cellohexaose from the (110) cellulose crystal surface. Results for reaction coordinates RC Ia, RC Ib and RC II are shown in red (solid line), green (dot-dash line) and black (dashed line) colors respectively. Inset: Flat ribbon configuration of cellohexaose over the (110) crystal surface.

In Applications of Molecular Modeling to Challenges in Clean Energy; Fitzgerald, G., et al.;
ACS Symposium Series; American Chemical Society: Washington, DC, 2013.

Summary and Discussion

The energetics involved in the desorption of cellohexaose for three different cases - one for the (110) surface and two for the (100) surface - of cellulose Iβ crystal were studied. Different reaction coordinates were chosen to study the desorption process on these surfaces. All PMF profiles showed distinct first minima at short separations, where cellohexaose has maximum favorable interactions with the crystal surface. Beyond the first minimum, in general, the PMF increased in a step-wise manner when the reaction coordinate consisted of peeling the cellohexaose molecule from one end. This behavior is a result of the interplay of intra-chain interactions of the cellohexaose molecule and the inter-sheet interactions between the cellulose crystal surface and the cellohexaose molecule. On the other hand, the PMF profiles that are obtained by considering the reaction coordinate based on the center of mass distance of the cellohexaose molecule from the crystal surface show a continuous increase in value followed by a plateau region. In practice, such a pathway which leads to a large continuous increase in free energy is unlikely. Rather, the process is likely to occur by the other type of path – the one corresponding to the stepwise increase in energy with individual steps being of the order of 15 kcal/mol.

The total free energy change for the desorption of cellohexaose from the (110) cellulose crystal surface is about 45 kcal/mol. The total free energy change for the desorption of the cellohexaose from the (100) crystal surface when it was adsorbed in the crystallographic conformation (case 1) is about 43 kcal/mol, while the value is about 30 kcal/mol when the adsorbed cellohexaose was in one of the conformations that is not the crystallographic conformation (case 2). This difference in the free energy change values in these cases can be explained as follows: in case 1, the cellohexaose molecule acted as an extension of the crystal structure thus retaining all of its native inter-sheet as well as intra-chain hydrogen bonding interactions. On the other hand, in case 2, where the cellohexaose molecule was allowed to freely adsorb on the crystal surface, it got adsorbed in an "imperfect" conformation, and thus was not able to regain the full intersheet interactions similar to those in a native crystal. Moreover, due to the resulting bulge in the chain conformation at one end, the cello-oligosaccharide in case 2 also had stronger intra-chain interactions, compared to those in the native crystal. The combined effect of the loss of inter-sheet interactions and the presence of additional intra-chain interactions made it easier to remove the cellohexaose molecule from the crystal surface in case 2, thus resulting in a smaller total free energy difference between the two end states. This observation can also be extended to suggest that the hydrolytic enzymes will preferentially attack those regions in the crystal which exhibit imperfect conformation and hence are more susceptible to enzyme attack.

The steps in the free-energy profiles obtained here are similar to those previously reported in the literature for the de-crystallization of a chitin chain from the α-chitin crystal surface (*40*). The free energy changes calculated in our simulations are much higher than those found in literature from decrystallization simulations of cellulose (*18*, *19*). Specifically, Payne *et. al.* (*18*) reported that the free energy required for removing a cellohexaose segment which is a part of the

In Applications of Molecular Modeling to Challenges in Clean Energy; Fitzgerald, G., et al.;
ACS Symposium Series; American Chemical Society: Washington, DC, 2013.

(110) crystal surface to be 11-12 kcal/mol (i.e. about 4 kcal/mol per cellobiose removed). In another study, the free-energy required for removing a 11-residue glucan chain from the (110) crystal surface in the presence of water as the solvent was determined to be about 18-20 kcal/mol (i.e. about 3.5 kcal/mol per cellobiose removed) (*19*). These values are lower than the free energy change value that we obtained here for the (110) surface (i.e. about 15 kcal/mol per cellobiose removed). This difference in the values can be attributed to the following factors: difference in the force-field used in the simulations [GLYCAM (*22*) in our case and CHARMM (*41*, *42*) in the case of these literature studies], the difference in the construction of the system (cellohexaose molecule was adsorbed on top of the crystal surface in our case while it was part of the crystal surface in these literature studies), and the difference in the reaction coordinate (center of mass distance based reaction coordinate in our case and native contacts based reaction coordinate in the case of these literature studies).

For both (100) and (110) crystal surfaces, the PMF profiles obtained by removing the adsorbed molecule from either end are approximately the same up to a separation distance of about 25 Å from the crystal surface, while they exhibit a difference beyond this distance. This result coupled with an inspection of chain size at large separations from the crystal, suggests that while the simulation run length may be long enough for the umbrella sampling windows in which part of the chain is still adsorbed on the crystal surface, for the fully desorbed state, the full range of chain conformations is not sampled over the MD simulation run for each umbrella sampling window. This aspect will be further investigated in future work. Furthermore, as described above, the choice of force field seems to be an important factor that results in a quantitative difference in the free energy value in the one case where a comparison could be made with the previous literature results (*18*, *19*). A detailed comparison of the free energy profiles obtained by the usage of the same reaction coordinate but different force fields will also be carried out in future.

Acknowledgments

The authors gratefully acknowledge the financial support of this work by the National Science Foundation (Grant Number: NSF CBET 0854463). We also thank the Texas Advanced Computing Center (TACC) at The University of Texas at Austin for providing computational resources that have contributed to the research results reported in this paper. Part of the simulations were also done on the computational cluster supported by CRIF MU instrumentation grant (Grant Number: NSF CHE 0840493) from the National Science Foundation.

References

1. Lynd, L. R. *Appl. Biochem. Biotechnol.* **1990**, *24−25*, 695–719.
2. Sun, Y.; Cheng, J. *Bioresour. Technol.* **2002**, *83*, 1–11.
3. Lynd, L. R. *Annu. Rev. Energy Environ.* **1996**, *21*, 403–465.
4. Lin, Y.; Tanaka, S. *Appl. Microbiol. Biotechnol.* **2006**, *69*, 627–642.

5. Zhang, Y. H. P.; Ding, S. Y.; Mielenz, J. R.; Cui, J. B.; Elander, R. T.; Laser, M.; Himmel, M. E.; McMillan, J. R.; Lynd, L. R. *Biotechnol. Bioeng.* **2007**, *97*, 214–223.
6. Pauly, M.; Keegstra, K. *Plant J.* **2008**, *54*, 559–568.
7. Demirbas, A. *Energy Sources* **2005**, *27*, 327–337.
8. Limayem, A.; Ricke, S. C. *Prog. Energy Combust. Sci.* **2012**, *38*, 449–467.
9. Wyman, C. E. *Bioresour. Technol.* **1994**, *50*, 3–16.
10. Gibson, L. J. *J. R. Soc., Interface* **2012**, *9*, 2749–2766.
11. Mosier, N.; Wyman, C.; Dale, B.; Elander, R.; Lee, Y. Y.; Holtzapple, M.; Ladisch, M. *Bioresour. Technol.* **2005**, *96*, 673–686.
12. Zhang, Y. H. P.; Lynd, L. R. *Biotechnol. Bioeng.* **2004**, *88*, 797–824.
13. Zhang, Y. H. P.; Himmel, M. E.; Mielenz, J. R. *Biotechnol. Adv.* **2006**, *24*, 452–481.
14. Laureano-Perez, L.; Teymouri, F.; Alizadeh, H.; Dale, B. *Appl. Biochem. Biotechnol.* **2005**, *121*, 1081–1099.
15. Himmel, M. E.; Ding, S.-Y.; Johnson, D. K.; Adney, W. S.; Nimlos, M. R.; Brady, J. W.; Foust, T. D. *Science* **2007**, *315*, 804–807.
16. Klemanleyer, K.; Agosin, E.; Conner, A. H.; Kirk, T. K. *Appl. Environ. Microbiol.* **1992**, *58*, 1266–1270.
17. Klemanleyer, K. M.; Gilkes, N. R.; Miller, R. C.; Kirk, T. K. *Biochem. J.* **1994**, *302*, 463–469.
18. Payne, C. M.; Himmel, M. E.; Crowley, M. F.; Beckham, G. T. *J. Phys. Chem. Lett.* **2011**, *2*, 1546–1550.
19. Cho, H. M.; Gross, A. S.; Chu, J.-W. *J. Am. Chem. Soc.* **2011**, *133*, 14033–14041.
20. Bergenstrahle, M.; Thormann, E.; Nordgren, N.; Berglund, L. A. *Langmuir* **2009**, *25*, 4635–4642.
21. Nishiyama, Y.; Langan, P.; Chanzy, H. *J. Am. Chem. Soc.* **2002**, *124*, 9074–9082.
22. Kirschner, K. N.; Yongye, A. B.; Tschampel, S. M.; González-Outeiriño, J.; Daniels, C. R.; Foley, B. L.; Woods, R. J. *J. Comput. Chem.* **2008**, *29*, 622–655.
23. Price, D. J.; Brooks, C. L., III *J. Chem. Phys.* **2004**, *121*, 10096–10103.
24. Phillips, J. C.; Braun, R.; Wang, W.; Gumbart, J.; Tajkhorshid, E.; Villa, E.; Chipot, C.; Skeel, R. D.; Kalé, L.; Schulten, K. *J. Comput. Chem.* **2005**, *26*, 1781–1802.
25. Humphrey, W.; Dalke, A.; Schulten, K. *J. Mol. Graphics* **1996**, *14*, 33–38.
26. Case, D.; Darden, T. A.; Cheatham, T. E.; Simmerling, C.; Wang, J.; Duke, R.; Luo, R.; Crowley, M.; Walker, R.; Zhang, W.; Merz, K. M.; Wang, B.; Hayik, S.; Roitberg, A.; Seabra, G.; Kolossváry, I.; Wong, K. F.; Paesani, F.; Vanicek, J.; Wu, X.; Brozell, S.; Steinbrecher, T.; Gohlke, H.; Yang, L.; Tan, C.; Mongan, J.; Hornak, V.; Cui, G.; Mathews, D. H.; Seetin, M. G.; Sagui, C.; Babin, V.; Kollman, P. *Amber 11* **2010**.
27. Darden, T.; York, D.; Pedersen, L. *J. Chem. Phys.* **1993**, *98*, 10089–10092.
28. Miyamoto, S.; Kollman, P. A. *J. Comput. Chem.* **1992**, *13*, 952–962.
29. Hoover, W. G. *Phys. Rev. A* **1985**, *31*, 1695–1697.

30. Feller, S. E.; Zhang, Y.; Pastor, R. W.; Brooks, B. R. *J. Chem. Phys.* **1995**, *103*, 4613–4621.
31. Martyna, G. J.; Tobias, D. J.; Klein, M. L. *J. Chem. Phys.* **1994**, *101*, 4177–4189.
32. Torrie, G. M.; Valleau, J. P. *J. Comput. Phys.* **1977**, *23*, 187–199.
33. Kumar, S.; Rosenberg, J. M.; Bouzida, D.; Swendsen, R. H.; Kollman, P. A. *J. Comput. Chem.* **1992**, *13*, 1011–1021.
34. Roux, B. *Comput. Phys. Commun.* **1995**, *91*, 275–282.
35. Grossfield, A. *WHAM: The Weighted Histogram Analysis Method*, version 2.0.4. http://membrane.urmc.rochester.edu/content/wham
36. Gross, A. S.; Chu, J.-W. *J. Phys. Chem. B* **2010**, *114*, 13333–13341.
37. Umemura, M.; Yuguchi, Y.; Hirotsu, T. *J. Mol. Struct.: THEOCHEM* **2005**, *730*, 1–8.
38. Peri, S.; Muthukumar, L.; Karim, M. N.; Khare, R. *Cellulose* **2012**, *19*, 1791–1806.
39. French, A. D.; Johnson, G. P.; Cramer, C. J.; Csonka, G. b. I. *Carbohydr. Res.* **2012**, *350*, 68–76.
40. Beckham, G. T.; Crowley, M. F. *J. Phys. Chem. B* **2011**, *115*, 4516–4522.
41. Guvench, O.; Greene, S. N.; Kamath, G.; Brady, J. W.; Venable, R. M.; Pastor, R. W.; Mackerell, A. D. *J. Comput. Chem.* **2008**, *29*, 2543–2564.
42. Guvench, O.; Hatcher, E.; Venable, R. M.; Pastor, R. W.; MacKerell, A. D. *J. Chem. Theory Comput.* **2009**, *5*, 2353–2370.

Chapter 2

Ionic Liquids for Carbon Capture: Solubility Computation Using an Implicit Solvent Model

Amitesh Maiti*

Lawrence Livermore National Laboratory,
Livermore, California 94550, U.S.A.
***E-mail: amaiti@llnl.gov**

Through a large number of solubility measurements over the last decade and a half, Ionic Liquids (ILs) have been demonstrated as a great medium for the physical dissolution of CO_2. However, there are numerous possible variations on the component ions of an IL, only a small fraction of which has actually been synthesized so far. In order to screen for the best solvents it is necessary to adopt a theoretical approach that can quickly compute the CO_2 solubility with reasonable quantitative accuracy. Here we report a theoretical prescription that involves computing the chemical potential of CO_2 in the solvent phase with a density-functional-theory-based implicit solvation code (COSMO-RS) and computing the gas fugacity with a cubic equation of state. The approach yields excellent agreement with a large volume of experimental data on CO_2 solubility in diverse classes of ILs over a wide range of temperatures and pressures. The resulting quantitative trends can be used to discover solvents with much higher CO_2 uptake per kg of solvent than has been experimentally achieved so far.

In Applications of Molecular Modeling to Challenges in Clean Energy; Fitzgerald, G., et al.;
ACS Symposium Series; American Chemical Society: Washington, DC, 2013.

Introduction

With the status of CO_2 as a prominent greenhouse gas and a major contributor to the global climate change now established, major efforts are being put forth by governments and private agencies in order to cut down CO_2 emission into the atmosphere. Research efforts are focusing on developing technologies in the areas of CO_2 capture, storage, monitoring, mitigation, and verification (*1*). The very first step, i.e., capture, is the separation of CO_2 from emissions sources, *e.g.*, flue gas in a coal-fired power plant, and the recovery of a concentrated stream of CO_2 that is amenable to sequestration or conversion. Given that CO_2 in the flue gas is present only in dilute quantities, ~ 10-14% by volume, the common strategy of carbon capture has so far involved chemical absorption in amine-based solvents (*2*). Much of the effort has so far involved aqueous solutions of monoethanolamine (MEA). Pilot plants have implemented MEA-based capture systems, although at a scale that is an order-of-magnitude smaller than that required for commercial power plants. Unfortunately, MEA has some shortcomings including, somewhat nonselective against other pollutants, prone to degradation and equipment corrosion, unstable at high concentrations, and finite vapor pressure that results in solvent loss and environmental pollution. Besides, a chemical absorption based strategy is typically associated with a large energy cost in solvent regeneration.

With the above deficiencies in mind, there has been a significant effort in exploring and designing solvents that adsorb CO_2 molecules, *i.e.*, physically bind them without involving any chemical reactions. Ionic Liquids (ILs) (*3–6*) constitute such an alternative solvent system that offer distinct advantages over traditional solvents like MEA, some of which include: (1) high chemical stability; (2) low corrosion; (3) almost zero vapor pressure; (4) supportable on membranes (*7*); and (5) a huge library of anion and cation choices, which can be potentially optimized for CO_2 solubility and selectivity.

Over the last few years several ILs have been experimentally demonstrated (*8–15*) to be efficient solvents for CO_2. A collection of this data does provide useful trends that can be used to optimize the choice of ILs for CO_2 capture. However, each new experiment costs time and money, and is often hindered by the fact that a specific IL may not be readily available. To this end, it is highly desirable to have a computational/theoretical tool that can quickly and accurately compute CO_2 solubility in any solvent (as a function of pressure and temperature). Atomic level simulations, molecular dynamics, Monte Carlo, or binding-energy calculations can provide useful insights into the interactions of CO_2 with the cation and the anion (*16–18*). However, predicting solubility involves determining the difference in chemical potential between the solute in the solvent phase and the solute in its source phase. There are theoretical procedures to compute such chemical potential differences from first-principles, e.g., through simulations using advanced sampling techniques, e.g., umbrella sampling (*19*), free energy perturbation (*20*), thermodynamic integration (*21*), or constrained molecular dynamics (*22*). However, a successful use of such techniques in complex molecular systems like ILs has its challenges, including large ion sizes, high viscosity, low mobility, and often the lack of interaction parameters.

In Applications of Molecular Modeling to Challenges in Clean Energy; Fitzgerald, G., et al.;
ACS Symposium Series; American Chemical Society: Washington, DC, 2013.

Computational Strategy

For fast computation of solubility in a wide variety of solvents it is thus desirable to adopt a quantum-chemistry-based strategy with a large coverage of the periodic table. At the same time, it should be able to yield quantities averaged over orientational and configurational degrees of freedom of the solvent molecules. A widely used method in this regard is the implicit solvent method called COSMO-RS (COnductor-like Screening MOdel for Real Solvents) (*23*, *24*), in which one represents both the solute and the solvent molecules by the histogram of their surface screening charges called the σ-profile. All interactions, including coulombic, van der Waals, and hydrogen bond interactions are then defined in terms of these σ-profiles. One can use this formalism to compute the partition function, the Gibbs free energy, and many other important thermodynamic quantities, including the pseudo-chemical potential (μ*) (i.e., the Gibb's free energy per molecule without the mixing entropy contribution). If the pseudo-chemical potential of a solute molecule in a solution containing x mole-fraction of the solute is $\mu_{\text{solution}}^*(x,T)$, and that in the solute's own liquid environment is $\mu_{self}^*(T)$, then under dilute conditions, the solubility (in mole-fraction) is given by the expression (*24*):

$$x = \exp[\{\mu_{self}^*(T) - \mu_{solution}^*(x,T)\}/k_B T] \quad (1)$$

where T is the absolute temperature and k_B the Boltzmann constant, respectively.

The COSMO-RS program was originally developed with the aim of modeling condensed phases, primarily liquid, with solubility and liquid-liquid phase equilibrium (LLE) being one of its primary application domains. For a solid dissolving into a liquid solvent one needs to include an additional contribution due to the heat of fusion. From extensive tests on the aqueous solubility of a large dataset of drug molecules and organic solutes it appears that COSMO-RS incurs an average error of the order of 0.3-0.5 log units (*25*). Based on this, an accuracy of the computed solubility to within a factor of 2–3 can be considered reasonable. At the same time the COSMO-RS errors are not random, but are rather systematic within classes of solvents. Therefore, one can still expect to obtain useful trends from such calculations. There have been several recent reports on COSMO-RS computation of CO_2 solubility in different ILs (*26–30*) with the aim of uncovering trends that can serve as a guide to solvent optimization.

One challenge for the present application is that the solute species (CO_2) is dissolving not from the solid or liquid, but from the gas phase. Although, there is a standard prescription of computing gas solubility with COSMO-RS that involves the experimental vapor pressure, this can lead to a severe overestimation of CO_2 solubility at a given pressure and temperature as compared to experimental results (*31*). As an alternative strategy, we have recently shown that the following equation works better with consistent accuracy (*32*):

$$P = \frac{P^0}{\phi(P,T)} x \exp[\{\mu_{solution}^*(x,T) - \mu_{ig}^*(T)\}/k_B T] \quad (2)$$

In Applications of Molecular Modeling to Challenges in Clean Energy; Fitzgerald, G., et al.;
ACS Symposium Series; American Chemical Society: Washington, DC, 2013.

where x is the mole-fraction gas-solubility at pressure P and temperature T, $\varphi(P, T)$ is the fugacity coefficient of the dissolving gas, and μ_{ig}* the dilute-limit pseudo-chemical potential of the ideal dissolving gas defined at a low reference pressure of $P^0 = 1$ bar. To use eq. (2) successfully we adopt the following strategy:

- The chemical potentials $\mu_{solution}^*(x,T)$ are computed by COSMO-RS using the commercial code COSMOtherm version C2.1, Release 01.10 (*33*). For this, the **σ**-profiles are first obtained by self-consistently computing the electronic charge density of each molecule, both the solute (CO_2) and the solvent (a series of IL's). Our calculations employ the Density-Functional-Theory (DFT) code Turbomole (*34*, *35*), the BP exchange-correlation functional (*36*, *37*), and an all-electron representation in the triple-zeta valence basis set with polarization (TZVP) (*38*, *39*). For each IL a separate σ-profile is constructed for the cation and the anion, and the solvent represented as a 50:50 molar mixture of the two fragments (*24*).
- The fugacity coefficient φ is computed by the standard formula:

$$\ln(\phi) = (k_B T)^{-1} \int_0^P (V - k_B T / P) dP$$

  To evaluate the above integral we use the Soave-Redlich-Kwong (SRK) (*40*, *41*) equation of state (EOS) for CO_2. Figure 1 displays results for the fugacity coefficient of CO_2 as a function of P for three different temperatures of our interest, where we have used CO_2 SRK parameters. As expected, φ monotonically decreases as a function of increasing P and decreasing T. At T around T_c, the SRK EOS is known to become less accurate for P greater than P_c (*40*). Thus, our analysis was confined to P not much higher than P_c= 73.7 bar (for CO_2).
- Finally, a proper computation of $\mu_{ig}^*(T)$ within the COSMO-RS framework would involve a complete analysis of the differences between partition function of a free molecule and a molecule in the condensed phase, including rotational, translational, vibrational, and zero-point contributions. Fortunately, in practice, a simple empirical free-energy correction term appears sufficient for the subcritical region $T < 0.7\ T_c$ (*24*). However, for the near-critical and supercritical region of our interest, corrections to the COSMOtherm-computed μ_{ig}* became necessary. From extensive numerical experiments, we found that the following simple 2-parameter formula works well in the 20-100 °C temperature range:

$$\mu_{ig}^*(T) = \mu_{ig}^*(T_c) + \alpha(T - T_c) \qquad (3)$$

In Applications of Molecular Modeling to Challenges in Clean Energy; Fitzgerald, G., et al.;
ACS Symposium Series; American Chemical Society: Washington, DC, 2013.

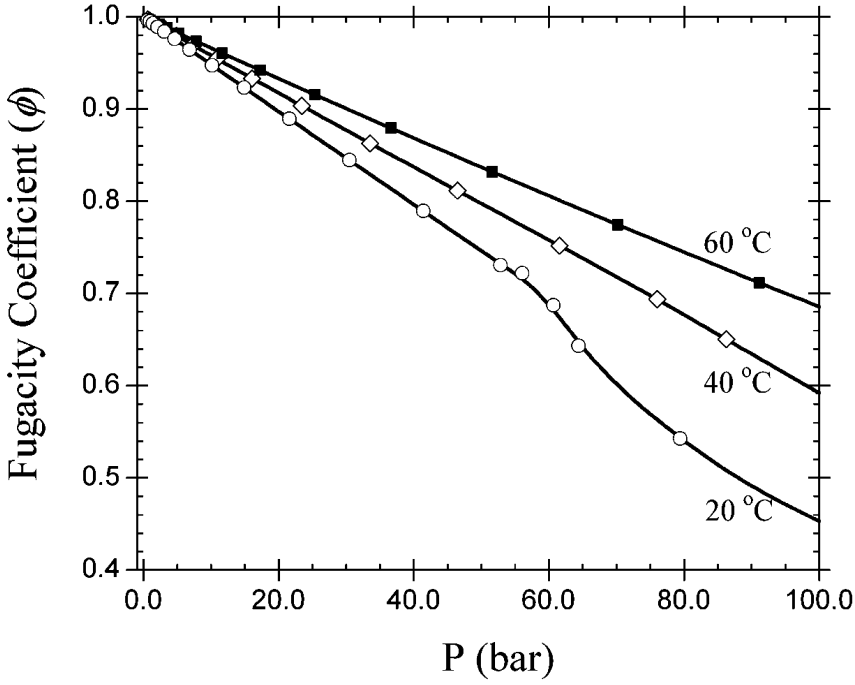

Figure 1. Fugacity coefficient (φ) of CO_2 at three different temperatures computed using the SRK equation of state.

Results

In our previous work (*32*) we tested the above formalism on a limited dataset and recommended values of $\mu_{ig}^*(T_c)$ = -4.43 kcal/mol and α = -0.02 kcal/mol/K. The emphasis in that work was placed on establishing the validity of the above computational scheme and looking for consistency in solubility trends rather than the optimization of the accuracy of the predicted solubility. When a larger dataset of CO_2 solubility measurements is included, the computed solubility using the above parameter values displays a significant deviation from the 45° line (see Figure 2 (left)), although there is still a strong linear correlation. In other words, the original parameter values of $\mu_{ig}^*(T_c)$ and α introduces a bias, as recently pointed out by ref. (*42*). As a remedy, these authors introduce an additional pressure-dependent parameter.

In this work we show that it is unnecessary to introduce any additional parameters, either involving pressure-dependence or non-linear dependence on temperature. Rather, a simple optimization of the parameter values to $\mu_{ig}^*(T_c)$ = -4.10 kcal/mol and α = -0.019 kcal/mol/K solves the problem, as shown in Figure 2 (right). Note that the experimental data points correspond to several temperatures varying between 20 °C and 100 °C, and the accuracy of the results do not deteriorate at elevated temperatures. The mean deviation in predicted fugacity as compared to the experimental values (for a given solubility level of

In Applications of Molecular Modeling to Challenges in Clean Energy; Fitzgerald, G., et al.;
ACS Symposium Series; American Chemical Society: Washington, DC, 2013.

CO_2) is ~ 5.5 bar. Above pressures of 15 bar the average accuracy of prediction is within 20%. At low pressures (a few bars or less) the predicted solubility displays Henry's behavior. However, from a few limited calculations we found that the predicted Henry's constant could show significant deviation from experimental values, up to 50% or larger.

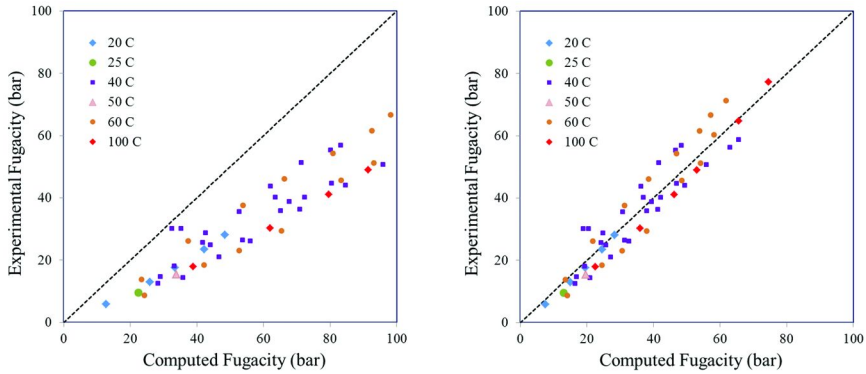

Figure 2. Computed CO_2 fugacity vs. experimental fugacity for different CO_2-IL solutions with varying levels of dissolved CO_2 at different temperatures (color coded). The experimental CO_2 pressure data obtained from references (8–15) were converted to experimental fugacity using the SRK equation of state (see Figure 1). The computed fugacity was obtained using the two-parameter model for $\mu_{ig}^*(T)$ (see eqs. (2) and (3) of text): (left graph) using previous parameters from ref. (32), (right graph) using presently optimized parameters with values $\mu_{ig}^*(T_c)$ = -4.10 kcal/mol and α = -0.019 kcal/mol/K. The data points represent many different ILs including the imidazolium cations of Table 1, and most of the anions of Table 2.

Using the new optimized parameters we screened for the IL solvents with the best solubility of CO_2 in the range of pressures 30-50 bar and at T = 40 °C. Figure 3 displays the computed results at P = 50 bar as a function of twelve different cations for a fixed anion [Tf_2N], one of the most commonly studied anions with a high mole-fraction solubility for CO_2. Figure 3 plots the CO_2 solubility both in mole-fraction (x) and in a more practical molality scale, defined by the number of moles of CO_2 dissolved per kg of the solvent:

$$molality\ (\text{mol/kg}) = \frac{x}{(1-x)M_w}$$

where M_w is the molecular weight of a solvent ion-pair in kg/mol. The molality scale emphasizes the amount (i.e. mass) of solvent required to dissolve a given amount of CO_2.

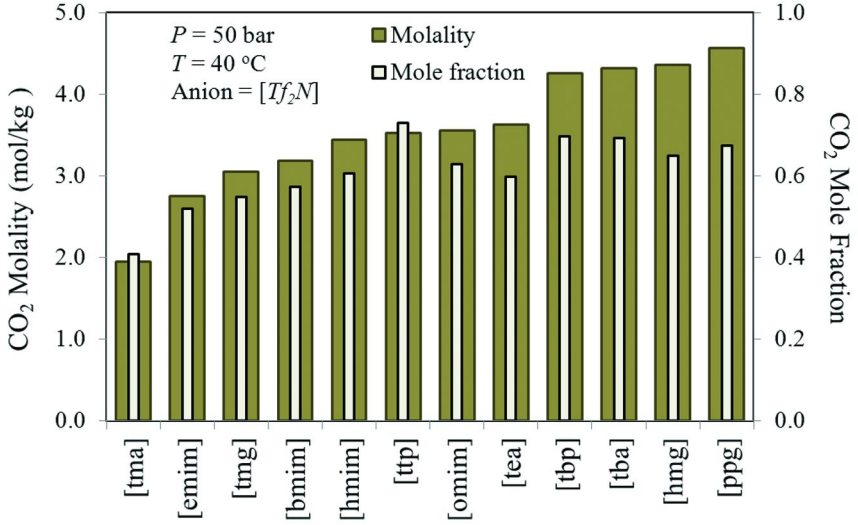

Figure 3. Computed CO_2 solubility in various ILs as a function of cations for a fixed anion [Tf_2N] at T = 40 °C and P = 50 bar. The solubility is computed in two different scales: molality scale (mol CO_2/ kg solvent) and mole-fraction. Fully functionalized ammonium, phosphonium, and guanidinium cations appear to possess higher CO_2 solubility as compared to imidazolium, the most commonly studied class of cations in the experimental literature. In this group, the IL [ppg][Tf_2N] possesses the highest molal solubility, while the IL [ttp][Tf_2N] possesses the highest mole-fraction solubility of CO_2. The IL acronyms are explained Tables 1 and 2.

The results in Figure 3 are arranged from left to right in the increasing order of the molality values. The most notable results can be summarized as: (1) the mole-fraction solubility increases as a function of the size of the functional group on the cations, as evident from the orderings: [emim] < [bmim] < [hmim] < [omim]; [tbp] < [ttp]; [tma] < [tea] < [tba]; and [hmg] < [ppg]; (2) for the ions chosen in this group, the molal solubility follows the same order as the mole-fraction solubility in spite of the increasing molecular weight of the larger functional groups. The only exception is [ttp] < [tbp], and is clearly a result of [ttp] possessing a much higher molecular weight than [tbp] (see Table 1). The case of [ttp] having lower molal solubility of CO_2 than [tbp] implies that the molal solubility within a cationic class attains a maximum value for ions of masses somewhere in the range 200-400 g/mol depending on the class; (3) by comparing different classes with similar functional groups we can draw the conclusion that the molal solubility increases in the order imidazolium < phosphonium ~ ammonium < guanidinium.

In Applications of Molecular Modeling to Challenges in Clean Energy; Fitzgerald, G., et al.;
ACS Symposium Series; American Chemical Society: Washington, DC, 2013.

Table 1. Chemical Names, Molecular Weight, and Class Categories of the Cations in Figure 3

Acronym	*Chemical Name*	*Molecular Weight (g/mol)*	*Class*
[emim]	1-ethyl-3-methyl-imidazolium	111.2	imidazolium
[bmim]	1-butyl-3-methyl-imidazolium	139.2	imidazolium
[hmim]	1-hexyl-3-methyl-imidazolium	167.3	imidazolium
[omim]	1-octyl-3-methyl-imidazolium	195.3	imidazolium
[tma]	tetra-methyl-ammonium	74.1	ammonium
[tea]	tetra-ethyl-ammonium	130.3	ammonium
[tba]	tetra-n-butyl-ammonium	242.5	ammonium
[tbp]	tetra-butyl-phosphonium	259.4	phosphonium
[ttp]	trihexyl-tetradecyl-phosphonium	483.9	phosphonium
[tmg]	tetra-methyl-guanidinium	116.2	guanidinium
[hmg]	hexa-methyl-guanidinium	144.2	guanidinium
[ppg]	n, n, n, n, n-pentamethyl-n-propyl-guanidinium	172.3	guanidinium

Table 2. Chemical names, Molecular Weight, and Class Categories of the Anions in Figure 4

Acronym	*Chemical Name*	*Molecular Weight (g/mol)*
[BF_4]	tetrafluoroborate	86.8
[PF_6]	hexaflurophosphate	145.0
[Tf_2N]	bis(trifluoromethylsulfonyl)imide	280.1
[NO_3]	nitrate	62.0
[TfO]	trifluoromethanesulfonate	149.1
[FEP]	tris(pentafluoroethyl)trifluorophosphate	445.0

To test the last point, and to see which cation-anion combination (within our limited set) could lead to an IL with the maximum molal solubility of CO_2, we computed the CO_2 solubility in six different anions ([BF_4], [PF_6], [Tf_2N], [NO_3], [TfO], and [FEP]) and three different cations ([omim], [tba], and [ppg]). The three cations chosen are the most efficient (within our data set) solvent representatives of the three classes imidazolium, ammonium, and guanidinium respectively (the results for phosphonium are very similar to ammonium and are

In Applications of Molecular Modeling to Challenges in Clean Energy; Fitzgerald, G., et al.;
ACS Symposium Series; American Chemical Society: Washington, DC, 2013.

not reported separately). Figure 4 displays the results at T = 40 °C and P = 30 bar. The most notable results are: (1) for the imidazolium class [FEP] leads to the highest mole-fraction solubility, in agreement with a previous publication (*43*) while Tf_2N is a close second. However, within the ammonium and the guanidinium classes, [FEP] is not as efficient. [Tf_2N] appears to possess the highest or near-highest mole-fraction across all cationic classes, which perhaps justifies the reason for it being one of the most studied IL anions; (2) for both ammonium and guanidinium classes the molal solubility increases in the order [FEP] < [Tf_2N] < [PF_6] < [TfO] < [BF_4] < [NO_3]. This order nearly holds for the Imidazolium class as well, with the molal solubility of the middle four groups being close to each other. In particular, note that [FEP] is the least efficient and [NO_3] the most efficient for all cations in terms of molal solubility; (3) overall, the efficiency order in terms of molal solubility appears to be imidazolium < ammonium < guanidinium, as also seen in Figure 3. In particular, [PPG][NO_3] possess the highest molal solubility of CO_2, roughly 2.6 times (i.e. 160 % higher) as compared to [omim][NO_3], the highest value for the most commonly studied imidazolium class. Interestingly, for the imidazolium class the [NO_3] group does not stand out in its mole-fraction solubility of CO_2. That could be the reason why much attention was not paid to it in our previous study (*32*), and [PPG][BF_4] was assigned the most efficient solvent within the data set. One should note that the molal solubility in [omim][NO_3] is high within the imidazolium class simply because of the small size of the [NO_3] anion. However, for the ammonium and guanidinium groups even the mole-fraction solubility is the highest or near-highest in presence of the [NO_3] anion. This, in combination with the small size of [NO_3] makes the molal solubility of CO_2 in [NO_3] much higher than other anions. This is especially true for [PPG], where the mass of the cation is also smaller compared to [omim] or [TBA].

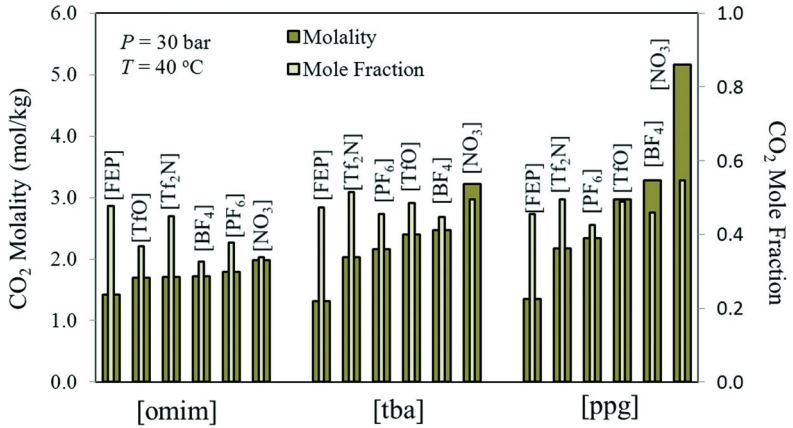

Figure 4. Computed CO_2 solubility in various ILs as a function of six different anions and three different cations belonging to the imidazolium ([omim]), ammonium ([tba]), and guanidinium ([ppg]) classes; T = 40 °C and P = 30 bar. The solubility is computed in two different scales: molality scale (mol CO_2/ kg solvent) and mole-fraction.

In Applications of Molecular Modeling to Challenges in Clean Energy; Fitzgerald, G., et al.;
ACS Symposium Series; American Chemical Society: Washington, DC, 2013.

Conclusions

In summary, we show that the two-parameter model previously introduced (*32*) is adequate for accurate prediction of CO_2 solubility in diverse ionic liquids over a range of temperatures and pressures. The previous parameters were not properly optimized and led to a bias that has been corrected in the present work. With these new parameters, the average accuracy of prediction is within 20% in pressures > 15 bar. The Henry's constant prediction (low pressures) is more in error, with an average error of ~ 50%, which is still in line with factors of 2-3 inaccuracy inherent in COSMO-RS when tested against the aqueous solubility of drug molecules (*25*). With these new parameters we show that the $[NO_3]$ anion is particularly efficient in dissolving CO_2, and in combination with ammonium or guanidinium cations should lead to much higher molal solubility as compared to the highest experimentally observed value within the imidazolium class. Although the method presented here is simple, one needs to exert caution in applying to a new IL system because of inherent inaccuracies of COSMO-RS in dealing with certain functional groups (*24*).

Finally, we should point out that the method and analysis shown here is only one part of the puzzle that needs to be solved in order to make ILs a commercial success in carbon capture. There are several other considerations that need to be kept in mind, including: (1) the thermophysical properties of the IL, e.g., melting point, viscosity, and specific heat; (2) selectivity of CO_2 against other gases (e.g., N_2, O_2, S-containing pollutants, etc.); and (3) cost of IL synthesis. Also, physical dissolution is probably practical only when the CO_2 concentration in the feed stream is high. For post-combustion capture one may need task-specific ILs functionalized with amines (*44–46*), so that a dilute amount of CO_2 can be captured through chemisorption.

Acknowledgments

This work was performed under the auspices of the U.S. Department of Energy by Lawrence Livermore National Laboratory under Contract DE-AC52-07NA27344.

References

1. *Carbon Capture and Storage*. Wikipedia. http://en.wikipedia.org/wiki/Carbon_capture_and_storage.
2. Rochelle, G. T. *Science* **2009**, *325*, 1652.
3. Welton, T. *Chem. Rev.* **1999**, *99*, 2071.
4. Holbrey, J. D.; Seddon, K. R. *Clean Prod. Processes* **1999**, *1*, 223.
5. Dupont, J.; de Souza, R. F.; Suarez, P. A. *Chem. Rev.* **2002**, *102*, 3667.
6. *Green Industrial Applications of Ionic Liquids*; R. D. Rogers, K. R. Seddon, S. Volkov, Eds.; NATO Science Series; Kluwer: Dordrecht, 2002.
7. Ilconich, J.; Myers, C.; Pennline, H.; Luebke, D. *J. Membrane Sci.* **2007**, *298*, 41.

8. (a) Blanchard, L. A.; Hancu, D.; Beckman, E. J.; Brennecke, J. F. *Nature* **1999**, *399*, 28. (b) Blanchard, L. A.; Brennecke, J. F. *Ind. Eng. Chem. Res.* **2001**, *40*, 2550.
9. Blanchard, L. A.; Gu, Z. Y.; Brennecke, J. F. *J. Phys. Chem. B* **2001**, *105*, 2437.
10. Aki, S. N. V. K.; Mellein, B. R.; Saurer, E. M.; Brennecke, J. F. *J. Phys. Chem. B* **2004**, *108*, 20355.
11. Zhang, S. J.; Yuan, X. L.; Chen, Y. H.; Zhang, X. P. *J. Chem. Eng. Data* **2005**, *50*, 230.
12. Muldoon, M. J.; Aki, S. N. V. K.; Anderson, J. L.; Dixon, J. K.; Brennecke, J. F. *J. Phys. Chem. B* **2007**, *111*, 9001.
13. Schilderman, M.; Raeissi, S.; Peters, C. J. *Fluid Phase Equilib.* **2007**, *260*, 19.
14. Kumełan, J.; Kamps, A. P-S.; Tuma, D.; Maurer, G. *J. Chem. Eng. Data* **2006**, *51*, 1802.
15. Kumełan, J.; Kamps, A. P-S.; Tuma, D.; Maurer, G. *J. Chem. Thermodyn.* **2006**, *38*, 1396.
16. Cadena, C.; Anthony, J. L.; Shah, J. K.; Morrow, T. I.; Brennecke, J. F.; Maginn, E. J. *J. Am. Chem. Soc.* **2004**, *126*, 5300.
17. Deschamps, J.; Gomes, M. F. C.; Padua, A. A. H. *ChemPhysChem* **2004**, *5*, 1049.
18. Bhargava, B. L.; Balasubramanian, S. *Chem. Phys. Lett.* **2007**, *444*, 242.
19. Torrie, G. M.; Valleau, J. P. *J. Comput. Phys.* **1977**, *23*, 187.
20. Jorgensen, W. L.; Buckner, J. K.; Boudon, S.; Tirado-Reeves, J. *J. Chem. Phys.* **1988**, *89*, 3742.
21. Mezei, M.; Beveridge, D. L. *Ann. N.Y. Acad. Sci.* **1986**, *482*, 1.
22. Ciccotti, G.; Ferrario, M.; Hynes, J. T.; Kapral, R. *Chem. Phys.* **1989**, *129*, 241.
23. Klamt, A.; Schüürmann, G. *J. Chem. Soc., Perkin Trans.* **1993**, *2*, 799.
24. Klamt, A. *COSMO-RS: From Quantum Chemistry to Fluid Phase Thermodynamics and Drug Design*; Elsevier: Amsterdam, 2005.
25. Klamt, A.; Eckert, F.; Hornig, M.; Beck, M. E.; Burger, T. *J. Comput. Chem.* **2001**, *23*, 275.
26. Sumon, K. Z.; Henni, A. *Fluid Phase Equilibr.* **2011**, *310*, 39.
27. Sistla, Y. S.; Khanna, A. *J. Chem. Eng. Data* **2011**, *56*, 4045.
28. Gonzalez-Miquel, M.; Palomar, J.; Omar, S.; Rodriguez, F. *Ind. Eng. Chem. Res.* **2011**, *50*, 5739.
29. Palomar, J.; Gonzalez-Miquel, M.; Polo, A.; Rodriguez, F. *Ind. Eng. Chem. Res.* **2011**, *50*, 3452.
30. Lei, Z.; Chen, B.; Li, C. *Chem. Eng. Sci.* **2007**, *62*, 3940.
31. Kolář, P.; Nakata, H.; Shen, J. W.; Tsuboi, A.; Suzuki, H.; Ue, M. *Fluid Phase Equilib.* **2005**, *228*, 59.
32. Maiti, A. *ChemSusChem* **2009**, *2*, 628.
33. Cosmologic Inc. http://www.cosmologic.de.
34. Ahlrichs, R.; Bär, M.; Häser, M.; Horn, H.; Kölmel, C. *Chem. Phys. Lett.* **1989**, *162*, 165.

35. Schäfer, A.; Klamt, A.; Sattel, D.; Lohrenz, J. C. W.; Eckert, F. *Phys. Chem. Chem. Phys.* **2000**, *2*, 2187.
36. Becke, A. D. *Phys. Rev. A* **1988**, *38*, 3098.
37. (a) Perdew, J. P. *Phys. Rev. B* **1986**, *33*, 8822. (b) Perdew, J. P. *Phys. Rev. B* **1986**, *34*, 7406.
38. Eichkorn, K.; Weigend, F.; Treutler, O.; Ahlrichs, R. *Theor. Chim. Acta* **1997**, *97*, 119.
39. Schäfer, A.; Huber, C.; Ahlrichs, R. *J. Chem. Phys.* **1994**, *100*, 5829.
40. Soave, G. *Chem. Eng. Sci.* **1972**, *27*, 1197.
41. Tassios, D. P. *Applied Chemical Engineering Thermodynamics*; Springer-Verlag: Berlin, 1993.
42. Mortazavi-Manesh, S.; Satyro, M.; Marriott, R. A. *Can. J. Chem. Eng.* **2012**, DOI10.1002/cjce.21687.
43. Zhang, X.; Liu, Z.; Wang, W. *AIChE J.* **2008**, *54*, 2717.
44. Bates, E. D.; Mayton, R. D.; Ntai, I.; Davis, J. H. *J. Am. Chem. Soc.* **2002**, *124*, 926.
45. Gurkan, B. E.; de la Fuente, J. C.; Mindrup, E. M.; Ficke, L. E.; Goodrich, B. F.; Price, E. A.; Schneider, W. F.; Brennecke, J. F. *J. Am. Chem. Soc.* **2010**, *132*, 2116.
46. Gurkan, B. E.; Goodrich, B. F.; Mindrup, E. M.; Ficke, L. E.; Masel, M.; Seo, S.; Senftle, T. P.; Wu, H.; Glaser, M. F.; Shah, J. K.; Maginn, E.; Brennecke, J.; Schneider, W. F. *J. Phys. Chem. Lett.* **2010**, *1*, 3494.

Chapter 3

Density Functional Simulations as a Tool To Probe Molecular Interactions in Wet Supercritical CO_2

Vassiliki-Alexandra Gleazkou*,[1] and B. Peter McGrail[2]

[1]Chemical Physics and Analysis, FCSD Pacific Northwest National Laboratory, 902 Battelle Boulevard, P.O. Box 999, Richland, Washington 99352
[2]Energy Processes and Materials, EED Pacific Northwest National Laboratory, 902 Battelle Boulevard, P.O. Box 999, Richland, Washington 99352
***E-mail: Vanda.Glezakou@pnnl.gov**

Recent advances in mixed Gaussian and plane wave algorithms have made possible the effective use of density functional theory (DFT) in *ab initio* molecular dynamics (AIMD) simulations for large and chemically complex models of condensed phase materials. In this chapter, we are reviewing recent progress on the modeling and characterization of co-sequestration processes and reactivity in wet supercritical CO_2 (sc-CO_2). We examine the molecular transformations of mineral and metal components of a sequestration system in contact with water-bearing scCO_2 media and aim to establish a reliable correspondence between experimental observations and theory models with predictive ability and transferability of results in large-scale geomechanical simulators.

Introduction

Carbon Capture and Sequestration (CCS) technologies have gained considerable momentum in a globally organized effort to limit and mitigate anthropogenic emissions and concomitant climate change (*1*). Co-sequestration of carbon dioxide with its common minor contaminants (SO_x, NO_x, Hg, etc.) in subsurface formations, offers the potential to make carbon management more

In Applications of Molecular Modeling to Challenges in Clean Energy; Fitzgerald, G., et al.;
ACS Symposium Series; American Chemical Society: Washington, DC, 2013.

economically acceptable to industry relative to sequestration of pure CO_2. This may be achieved through significant savings in plant (and retrofit) capital costs, operating costs, and energy savings also by eliminating the need for one or more individual pollutant capture systems (such as SO_2 scrubbers) (*2*). The latter point is important because co-sequestration may result in a net positive impact to the environment through avoided loss of power generation capacity from parasitic loads and reduced fuel needs.

Understanding the physical processes involving a sequestration system is extremely important in advancing technologies for CO_2 capture and permanent storage and connect with other mitigation strategies, such as facile *in situ* stripping of CO_2 contaminants (*3*), catalytic conversion of CO_2, its use as a green solvent, or use of ionic liquids for its capture. Every step of all these strategies involves interactions of CO_2 in condensed form (supercritical state $scCO_2$) with metal surfaces, cements, mineral surfaces and geologic formations. Liquid/supercritical CO_2 even if it is initially dry, it quickly absorbs water to become water-bearing supercritical fluid, (WBSF) (*4*, *5*). It often contains other S- or N-containing contaminants (SO_x, NO_x) that require prior removal, usually associated with significant costs. Therefore, co-sequestration offers the potential of substantial savings coupled to carbon management.

However, unlike the well-defined concepts of reactivity in aqueous environments, the same cannot be said for reactivity in $scCO_2$. As we will see, carbonation reactions in otherwise neutral $scCO_2$ environments depend on the water content and do not necessarily proceed through formation of carbonic acid and its ions:

$$CO_2 + H_2O \rightleftharpoons H_2CO_3 \rightleftharpoons HCO_3^- + H^+ \rightleftharpoons CO_3^{2-} + H^+$$

which is the mechanism commonly written to describe the CO_2 dissolution in water.

Use of theoretical models can help us bridge the gap between molecular level and macroscopic observations and enhance the predictive ability of our large-scale simulation models for geomechanical and geochemical changes.

Saharay and Balasubramanian first used Carr-Parrinello molecular dynamics simulations to study the structure and dynamics of $scCO_2$ (*6*, *7*). They showed that the CO_2 molecules fluctuate about a distorted T-shaped orientation. This interaction can be identified as a shoulder at ~3.4 Å in the pair distribution function of all O-C pair interactions. Recently, we used DFT-based dynamics to understand isotopic effects in the spectral signatures of $scCO_2$ (*8*) and how the low solubility of water in $scCO_2$ manifests itself in the intermolecular interactions in water-bearing supercritical CO_2 (*9*). The latter study showed that low water contents in $scCO_2$ do not interfere with the CO_2-CO_2 interactions, and that the H_2O-CO_2 interactions are strongest when water is in monomeric form. Interestingly, the relative distances between any neighboring CO_2 and H_2O molecules are in fact larger in the condensed system compared to the gas phase H_2O-CO_2 dimer or H_2O-$(CO_2)_2$ trimer. Under supercritical conditions and low degrees of hydration, we saw no evidence of carbonic acid formation. Based on the mechanistic details of $scCO_2$ interactions with metal (*5*) or mineral surfaces (*10*) we have concluded

In Applications of Molecular Modeling to Challenges in Clean Energy; Fitzgerald, G., et al.;
ACS Symposium Series; American Chemical Society: Washington, DC, 2013.

that carbonation mechanisms in $scCO_2$ environments can be dramatically different than those formulated for aqueous media. Our simulations imply that monomeric water in the supercritical CO_2 medium may even play a catalytic role.

In the following section, we will provide a brief overview of our efforts in modeling chemical processes in $scCO_2$ and the interaction of this fluid with solid supports such as metals and oxides (*11*) which are relevant to technological bottlenecks related to CO_2 sequestration. Particular emphasis will be placed upon connecting these results to concurrent experimental results obtained within our laboratory.

Theoretical Considerations and Models

The problems presented in this chapter have very stringent requirements for theoretical simulations. The systems of interest are not only chemically complex but they also undergo chemical reactions. As a result, the proper atomistic models involve a large number of atoms (ca in the hundreds of atoms) that must be described by electronic structure methods of reasonable chemical accuracy in order to predict reaction energies. In addition, many of these chemical reactions are not known a priori, and this requires that we have available tools to help us determine these reaction paths. The final, most stringent requirement is that the medium for these reactions is liquid/supercritical CO_2, which partakes in the reactions being described. The answer to the latter constraint relies on a statistical mechanical approach to chemical reactivity, and as such, requires adaptable sampling techniques able to describe reactivity on a free energy surface. Given these constraints we have embarked upon employing *ab initio* molecular dynamics approaches with the inherent capability to couple both electronic structure theory and statistical mechanics.

In this section, we will briefly review the successful implementation of *ab initio* molecular dynamics and the framework of the Gausian basis-planewave-pseudopotential density functional theory (*12*) in the CP2K code (*13*), the program of our choice for the molecular dynamics simulations. Taking advantage of parallel computer architectures and advanced algorithms, the resulting codes encompass a range of advanced techniques from the molecular dynamics domain, such as constant temperature or constant pressure simulations, and electronic structure capabilities. These novel techniques allow us to circumvent the problem of the determination the interatomic interactions potential terms normally required for any type of molecular dynamics approaches based on a classical force field. Although classical MD techniques are indispensable, their dependence on a fixed potential, which often is system-specific, and their difficulty to describe basic chemical transformations, such as bond-breaking or bond formation, is one of the biggest drawbacks (*14*, *15*).

More recent algorithms have given rise to mixed Gaussian-plane wave implementations (GPW) (*15–19*) that can treat gas and condensed phase molecular simulations on equal footing. The computational cost is usually linear and allows for efficient treatment of systems with hundreds or even thousands of electrons and a large number of the accompanying Gaussian basis functions.

In Applications of Molecular Modeling to Challenges in Clean Energy; Fitzgerald, G., et al.;
ACS Symposium Series; American Chemical Society: Washington, DC, 2013.

Density functional methods (DFT) can describe the electronic state of matter in terms of a 3D formulation of the system's electronic density, circumventing the more costly wavefuction theories (WFT) (*20*). These approaches are based on a functional form of the many-electron spin density, ρ:

$$E[\rho] = V_{ne}[\rho] + T[\rho] + V_{ee}[\rho]$$

where T[ρ] is the kinetic energy, $V_{ne}[\rho]$the electron-nuclear attraction and $V_{ee}[\rho]$ is the electron-electron interaction containing the Coulomb interaction. The computation of this term and the non-linear process of orthogonalization of the wavefunction are responsible for the major computational costs especially for larger systems.

Modern implementations and novel functional forms have made possible the treatment of open shell systems and electron correlation, two of the main challenges of the density functional methods. These, along with the favorable cost, have made DFT competitive with WFT, even for demanding systems such as metals. A more informed overview of the advances in density functional theory can be found in the literature, see for example references (*20*, *21*). The accuracy/success of DFT methods relies on the judicious choice of the functional form, and, in this respect, they are of semi-empirical nature. However, they have been heavily tested and benchmarked against very accurate WFT and nowadays they are routinely used for reliable predictions in the fields of chemistry, materials or biochemistry.

A hybrid Gaussian and plane-wave method formulated by Lippert et al. (*22*) circumvents this computational bottleneck associated with the use of basis functions, while maintaining the accuracy of the method. This method has been implemented in QUICKSTEP (*18*) as a part of the freely available CP2K code (*13*) to perform atomistic and molecular simulations. The method uses Gaussian-type basis sets to describe the wave function just like any other electronic structure code, but introduces a grid-defined auxiliary plane-wave basis to describe the density. This discretized, plane-wave expression of the density referred to as Gaussian-Plane Wave (GPW) method, can take advantage of Fast Fourier Transform (FFT) methods, a well-established tool in GPW implementation, to obtain the Coulomb energy in a fashion that scales linearly with size (*23*) and benefits from similar numerous applications of plane-wave codes (*12*). One advantage of Gaussian-type basis sets is that they can be systematically improved, while maintaining a compact form (*24*). Taking advantage of efficient wavefunction solvers, the current implementation allows for linear scaling which improves with the system size. Normally, this implementation also calls for the use of psedopotentials for the description of the nuclei. Usually, the highly accurate Goedecker-Teter-Hutter pseudopotentials are used (*25*, *26*), but an extension of the code, Gaussian and augmented-plane-wave (GAPW) method, can also work with all-electron basis sets (*16*, *22*).

Finally, we should point out that periodic boundary conditions (PBC) naturally integrate with FFT methods, making them suitable for the representation of condensed systems (liquids, solids) (*27*).

In Applications of Molecular Modeling to Challenges in Clean Energy; Fitzgerald, G., et al.;
ACS Symposium Series; American Chemical Society: Washington, DC, 2013.

A detailed account of the method, implementation and program structure, discussion on the basis set and psedopotential construction and accuracy can be found in the relevant publications by the developers (*17–19*). In the following sections we will discuss how these algorithms helped us in the study of a variety of problem relevant to co-sequestration. We should point out that a number of other codes are also available for the study of extended systems from first principles. CASTEP (*28*), CPMD (*29*), QUANTUM ESPRESSO (*30*) and VASP (*31*) are only some of the most commonly used plane-wave codes, with quadratic scaling with respect to system size. More information about these codes can be found at their respective websites listed above. Our choice of software was influenced by the ease of use, availability, portability and ability to handle metallic and non-metallic systems equally efficiently. Based on the criteria listed above, CP2K was found to be the best choice.

For the problems presented below, we use density functional methods based on the generalized gradient approximation (GGA). Core electrons are represented by pseudo-potentials and valence electrons by well-conditioned basis sets within the periodic boundary conditions (PBC) to suitably describe extended, condensed systems. Since our models include explicit treatment of electrons, we can study reactivity and processes involving bond dissociation/formation. *Ab initio* molecular dynamics (AIMD) simulations allow us to observe the evolution of our systems with time, while they naturally include the temperature effects and anharmonic contributions. Since only rarely can we directly determine measurable quantities by molecular simulations, we normally obtain the relevant information through post-processing analysis using various types of auto-correlations of the positions and velocities of the atoms as a function of time (*32*). Dispersion interactions are not naturally part of the GGA approximation, and often, the commonly used functionals cannot describe the long-range interactions properly. In these cases, these interactions can be estimated through the implementation of an empirical correction as suggested by Grimme (*33–35*). In the studies reported here, we used the Grimme correction to account for dispersion interactions in our systems.

In the following sections, we will present a short account of some of the problems we studied using the techniques we outlined in the previous sections:

(i) Effect of isotopic substitution on the Raman spectrum of $scCO_2$.
(ii) Intermolecular structure of wet $scCO_2/(H_2O)_n$, n=0-4 and the possibility of carbonic acid (H_2CO_3) formation in neutral $scCO_2$ systems.
(iii) Mechanistic steps of steel corrosion in wet-$scCO_2$, the role of monomeric (molecular) H_2O in the propagation of carbonation reactions.
(iv) Mechanism of sulfation reaction and *in situ* removal of SO_2 from CO_2 streams using carbonate reservoirs.
(v) Calcium ion solvation in wet $scCO_2$.

All studies reported here were done with CP2K (*13*), while NWCHEM (*36*) was used for some benchmark calculations on certain small models.

In Applications of Molecular Modeling to Challenges in Clean Energy; Fitzgerald, G., et al.;
ACS Symposium Series; American Chemical Society: Washington, DC, 2013.

Results and Discussion

Isotopic Effects in the Ferm Dyad of $scCO_2$

The vibrational signature of CO_2 in gas, liquid or supercritical states, includes a characteristic doublet the Fermi dyad (FD) arising from a resonance of the fundamental symmetric stretch and the first overtone of the bending mode (*37*, *38*). The dyad is observed approximately at 1285 (ν-, lower) and 1388 (ν+, upper) cm^{-1} with relative intensity ratio I+/I- >1. The peak assignment may vary with the isotopic substitution of C and/or O (*39–42*) or the density (*41*, *43*). For liquid or supercritical CO_2, it was concluded that $\nu_1 > 2\nu_2$, for densities > 1g/ml (*43*). However, none of these earlier studies discusses how isotopic substitution or density may affect the mixing of the fundamental modes.

Our interest in this phenomenon originates in the kinetics studies of carbonation reactions of minerals relevant to co-sequestration under supercritical environments. To our knowledge, the spectra reported in Figure 1 are the first Raman spectra of $scC^{18}O_2$, and, at first glance, they show almost a complete inversion between the two isotopic variants in the Fermi dyad region (*8*). The peak frequencies and intensities are consistent with the literature, $\Delta\nu$=104 cm^{-1} (^{16}O) and 116 cm^{-1} (^{18}O). The intensity ratios are I+/I- =0.56 and 2.2 respectively.

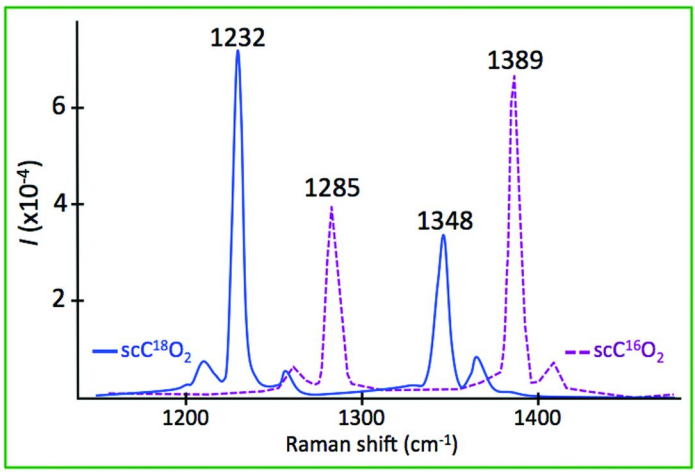

Figure 1. Raman spectrum of $scCO_2$ (with ^{16}O and ^{18}O) in the Fermi region at T=313K and P~8.7MPa. (see color insert)

In order to understand the isotopic effect on the FD, we performed from *ab initio* molecular dynamics simulations on $scCO_2$ (different simulations with $^{16}O$and ^{18}O) at T~315 K and d~0.5 g/ml, conditions very similar to the experimental ones. From those, we obtained the power spectrum of the vibrational frequencies of the two variants of $scCO_2$, through the Fourier transform of the autocorrelation of the velocities of the molecules. The FD region of the spectra is shown in Figure 2. In addition, we were able to project out the two normal modes, ν_1 and ν_2 overtone, and observe how the individual modes contribute to

In Applications of Molecular Modeling to Challenges in Clean Energy; Fitzgerald, G., et al.;
ACS Symposium Series; American Chemical Society: Washington, DC, 2013.

the FD peaks. These contributions to the modes are shown with the green (ν_1) and orange lines (ν_1) under the total peak. Details on the simulation and analysis can be found in the paper by Windisch et al. (*8*). It is worth noting that the theory underestimates the peak positions by ~ 50 cm^{-1}, however, the relative positions of the peaks within the FD are only ~10 cm^{-1} smaller than the experimental values. The relative intensities I+/I- are 0.5 and 2.5 respectively, in excellent agreement with our experimental measurements.

Given the importance of Raman spectroscopy as a diagnostic tool in reactivity studies, we are very confident that this type of theoretical approach can help us interpret complicated spectra. Our results indicate that the relative shifts in spectra due to isotopic substitution are beyond interpretation based on simple criteria such as density.

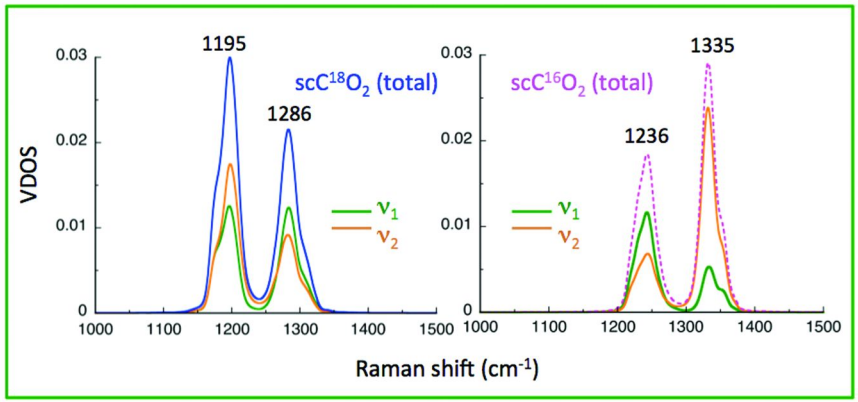

Figure 2. MD simulated vibrational spectra of the Fermi dyad for $scCO_2$, with ^{16}O and ^{18}O. The spectra show the contributions of the two vibrational components v_1 and 2 v_2 and the relevant shifts due to the isotopic substitution. Simulations were performed at T~315 K and d~0.5 g/ml. (see color insert)

Intermolecular Structure of $scCO_2/(H_2O)_n$, n=0-4

In the introduction, we discussed how originally dry $scCO_2$ could easily adsorb water to become WBSF. In spite of the well-known fact that water has very low solubility in supercritical CO_2, it comes somewhat as a surprise that reactivity in these environments was not given more attention yet. Our group is engaged in wide range of experimental studies, employing different spectroscopic (Raman, IR) or surface science techniques (XRD), in our effort to understand molecular transformations as a result of carbon sequestration efforts. Atomistic simulations can also be used as another characterization technique to shed light in these molecular changes. From these studies, it was obvious that a more detailed understanding of the WBSF, here modeled as $scCO_2$ with a finite number of waters, was imperative. In this section, we will briefly summarize what is known about the $scCO_2$ phase and its structure, and the effect of finite amounts of water.

In Applications of Molecular Modeling to Challenges in Clean Energy; Fitzgerald, G., et al.;
ACS Symposium Series; American Chemical Society: Washington, DC, 2013.

Neutron diffraction experiments and early theoretical studies on $scCO_2$ (*6*, *44–46*) report on a quasi T-shape orientation of nearest CO_2 neighbors (1st shell structure), Figure 3(a), at approximately 3.4 Å.

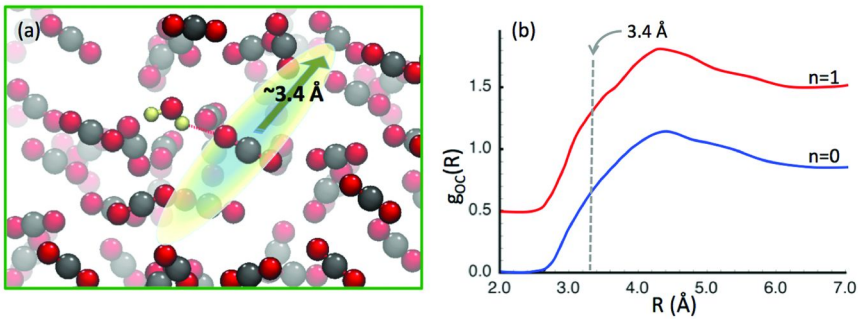

Figure 3. (a) Snapshot from AIMD simulation of $scCO_2/(H_2O)_n$, n=1. (b) Pair distribution function of C-O intra-molecular interactions showing the characteristic shoulder at 3.4 Å due to the distorted T-shaped orientation of the CO_2 molecules. (see color insert)

The intermolecular interactions between 1st shell carbon-oxygen neighbors appear as a shoulder in the pair distribution function, Figure 3(b). Such a feature was observed in all of our simulations, so it would be reasonable to conclude that the water does not perturb this structural characteristic of the $scCO_2$ matrix.

Theoretical estimates of the barrier of formation of carbonic acid from CO_2 and H_2O range from ~48 kcal/mol (gas-phase estimate, CO_2+H_2O), to about 25 kcal/mol (gas-phase CO_2+3H_2O) to about 22 kcal/mol from continuum solvent models (*47*). In all cases, close proximity of the two molecules is required, with C-O_w within ~2.8 Å, or closer. Such an association would require any water molecules to penetrate this 1st CO_2 shell, in order to start forming the H_2O-CO_2 pre-complex and finally H_2CO_3.

Figure 4(a) shows the pair distribution functions between O_w-C (average distances between any C and any water oxygen) and the corresponding pair distribution for al H-O_C interaction, Figure 4(b). The g_{OwC} pair distribution shows a double peak at the lowest hydration level (n=1) at ~3.0 and 4.0 Å. As the number of waters increases, the first peak (closest interaction) goes away. Similarly, the closest H/O_c interactions show as a shoulder of the main peak, which becomes less pronounced as the number of waters increases. For higher degrees of hydration, the waters start forming clusters making it even more difficult to approach CO_2.

Finally, we should point out that compared to the gas-phase parameters in the $H_2O(CO_2)_2$ trimer, the corresponding distances in the condensed phase are significantly larger, ~3 and ~4 Å vs 2.5 and 3.7 Å for the O_w-C distances, and ~3 and 4 Å vs 2.7 and 3.6 Å for the H-O_c distances. Interestingly, the closest H-O_c interaction happens between the water whose oxygen center is more likely to be the farthest from the C center of the CO_2.

In Applications of Molecular Modeling to Challenges in Clean Energy; Fitzgerald, G., et al.;
ACS Symposium Series; American Chemical Society: Washington, DC, 2013.

This last observation further confirms our conclusion that direct formation of H_2CO_3 in $scCO_2$ under low hydration is unlikely.

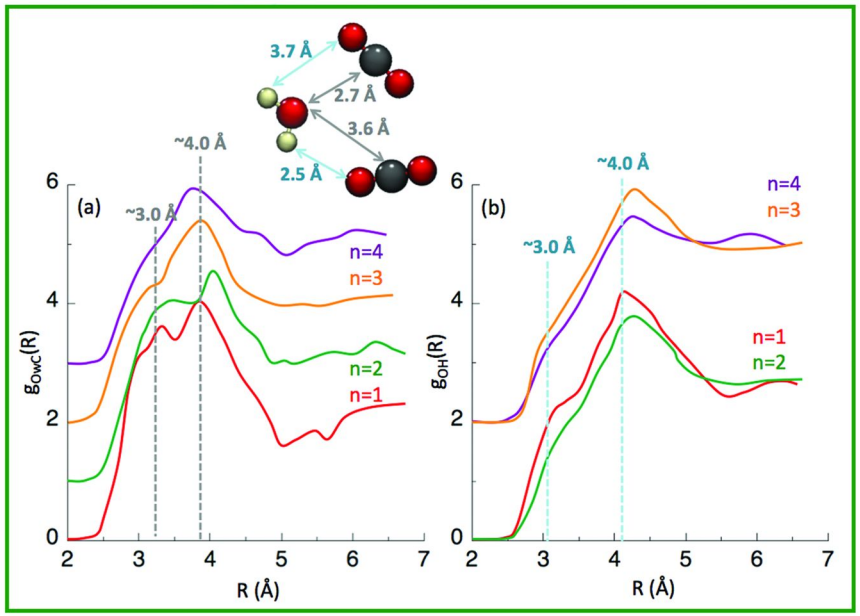

Figure 4. (a) Pair distibution function between Ow and C in $scCO_2/(H_2O)_n$, n=1-4 systems. (b) Pair distribution function between water H and O_c. Insert compares the gas phase parameters in the $H_2O(CO_2)_2$ trimer. (see color insert)

Steel Corrosion in Wet $scCO_2$

Exposure of tool steels, similar to those used for pipelines and casings, to water-saturated liquid CO_2 showed very fast corrosion (24-48 h) (*5*). The main product identified was siderite, $FeCO_3$, covering the steel surface in contact with the CO_2 phase. Atomistic simulations of CO_2 adsorption on Fe(100) surface (*48*) show spontaneous activation and strong binding of CO_2 (~17 kcal/mol) as CO_2^-. The adsorbed CO_2 can easily dissociate to O+CO adsorbed on the surface, with a low barrier of about 6 kcal/mol. In the gas phase, the barrier to H_2CO_3 formation by its components CO_2 and water involves a high barrier associated with initial charge transfer from O_w to C, about 48 kcal/mol (*47*). Since in our case the adsorbed CO_2 has a strong radical character, it is reasonable to assume that the carbonic acid formation from the co-adsorbed species might be more favorable. The energy requirements for this transformation computed via a Nudged elastic Band (NEB) (*49*, *50*) are shown in Figure 5.

We see that co-adsorption significantly reduces the barrier to ~35 kcal/mol, however, this still remains a fairly expensive molecular transformation.

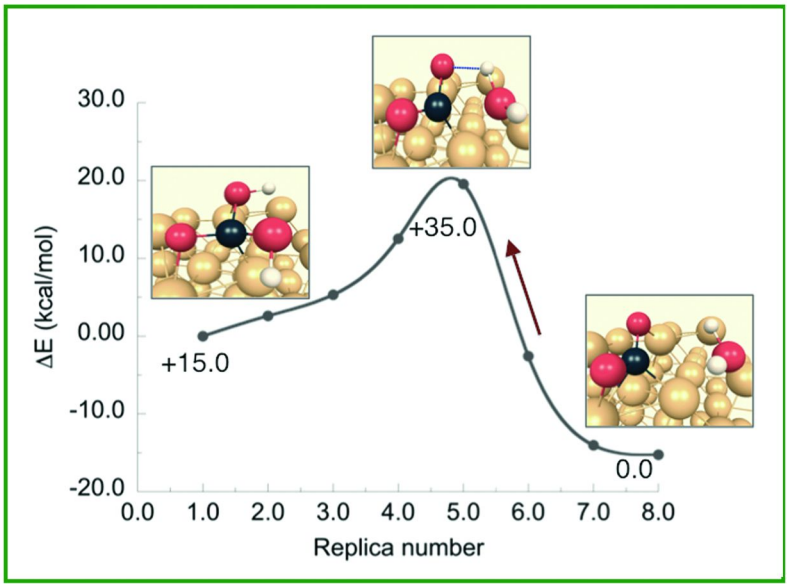

Figure 5. NEB profile for the estimation of the barrier to H_2CO_3 formation on Fe(100) surface from co-adsorbed CO_2 and H_2O. (see color insert)

Another set of calculations however uncovered an alternative route. Short trajectories from molecular dynamics simulations reveal that once the CO_2 adsorbs it easily dissociates to O+CO. Adsorbed oxygen atoms increase the adsorption energy of water, which eventually dissociates to form adsorbed hydroxyl groups. CO_2 insertion on the adsorbed OH proceeds with a barrier of ~ 8 kcal/mol, compared to CO_2 addition on adsorbed oxygen atoms (with a barrier ~ 15 kcal/mol):

$$O_{ads} + H_2O_{ads} \rightarrow 2OH_{ads}$$

$$CO_2 + OH_{ads} \xrightarrow{+8Kcal/mol} O_2COH_{ads} \rightarrow CO_{3_{ads}} + H_2O_{ads}$$

The above reactive scheme is shown in Figure 6.

This mechanism implies catalytic activity of monomeric water as was indicated by the simulations of $scCO_2$ under low hydration. It also explains the propagation of corrosion within the CO_2 phase only, in excellent agreement with the experimental characterization.

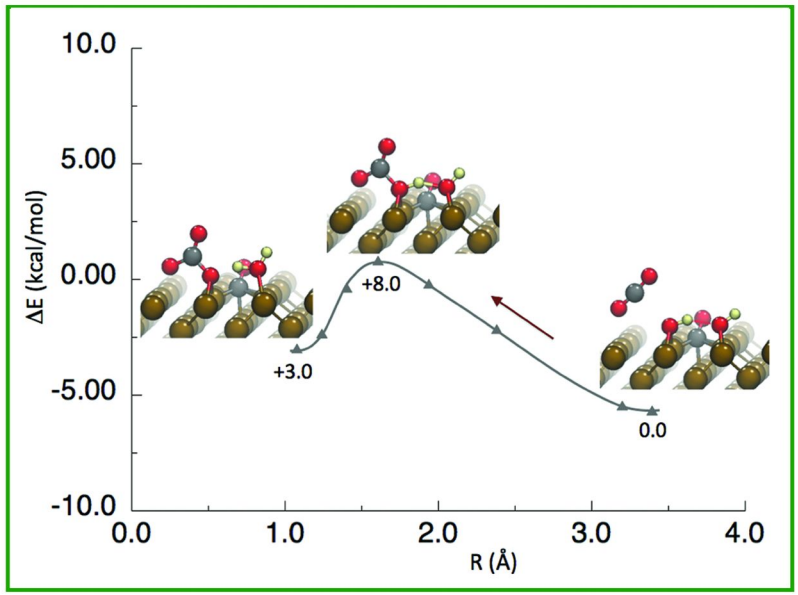

Figure 6. NEB for the CO_2 insertion onto adsorbed OH on Fe(100). (see color insert)

Co-Sequestration Studies with Carbonate Minerals

High-pressure testing with carbonate minerals under co-sequestration conditions showed formation of sulfites (hannebachite) for Ca-containing minerals (calcite, dolomite), contrary to magnesite where no sulphites were detected (*10*). Experiments were done under excess water or simply water-saturated $scCO_2$ and in both cases calcium sulfite minerals were the only products.

We used AIMD to understand the initial reactive steps that strip the SO_2 from the $scCO_2$ phase, by means of periodic boundary conditions on calcite [$10\bar{1}4$] and dolomite [$10\bar{1}4$] and [$10\bar{1}0$]. Details on the computations can be found in reference by Glezakou et al. (*10*). Molecular dynamics simulations of carbonate minerals slabs with a water layer showed shorter Mg-O_w distances compared to Ca-O_w. The binding energies of water over Mg sites are about 30% bigger than the corresponding Ca-water ones. Water-assisted sulfite formation on perfect dolomite surfaces results in stable product ($CaSO_3{\cdot}1/2H_2O$), but proceeds with a steep barrier, ~2.5 eV. CO_2 vacancies however on the surface completely change the picture, Figure 7(a). At defects, water spontaneously dissociates to form surface hydroxyls, readily reacting with SO_2 to form $CaSO_3$ lowering the barrier to about 0.5 eV. The local $CaSO_3H\ldots O_wH$ structure is very similar to crystallographic data for hannebachite. Estimated reaction rates computed using the estimated barrier and a simple Arrhenius formula are on the order 10-10^4 sec^{-1}.

Our studies of carbonate mineral reactivity under co-sequestration conditions suggest the potential of carbonate reservoirs for in situ SO_2 removal from CO_2 streams, see schematic Figure 7(b). Combustion gases from burning coal,

In Applications of Molecular Modeling to Challenges in Clean Energy; Fitzgerald, G., et al.;
ACS Symposium Series; American Chemical Society: Washington, DC, 2013.

natural gas and biomass contain SO_2 anywhere from 100 to 6000 ppm (wt.). Plant retrofitting imposed by regulatory restrictions is a major cost and could be mitigated by *in situ* scrubbing of pipeline grade CO_2 at nearby carbonate reservoirs. The clean CO_2 steams could subsequently be permanently sequestered on site or extracted for further use.

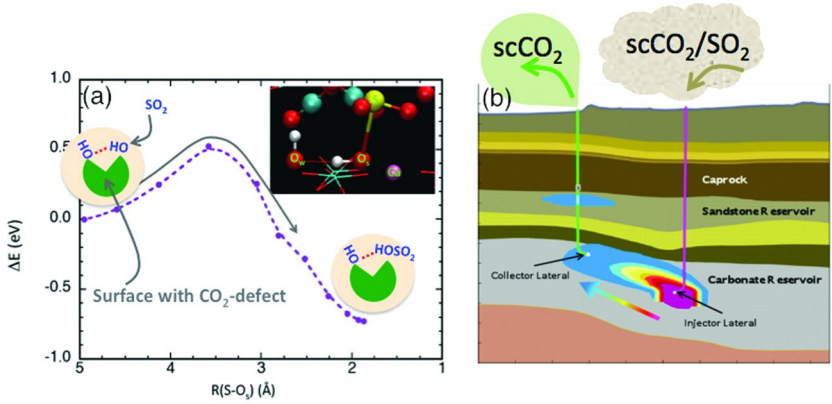

Figure 7. (a) Reaction profile for $CaSO_3H$ formation at a CO_2 defect of a cabonate mineral. (b) Schematic representation for in situ removal of SO_2 using carbonate reservoirs. (see color insert)

Ca^{2+} Interactions in Wet $scCO_2$ Informed by Density Functional Theory

CO_2 sequestration in subsurface geologic formation rich in phyllosilicates is of particular interest due to their low permeability (*51*, *52*). These minerals intercalate ions, molecules and water, expanding their interlayer space and possibly lowering their permeability, at least at their high-volume state. Their capability to expand, however, is much less studied at low-hydration states. Recent experimental in situ studies with Ca-montmorillonites (*53*, *54*) show that there is a complex correlation between the water content and expansion upon exposure to $scCO_2$. More specifically, Ca-montomorillonite with one layer of hydration (~1W) will undergo d001 expansion of about 0.8 Å when exposed to dry $scCO_2$ at T~328 K and P=90-180 bar. For hydration levels 2W and higher, exposure to $scCO_2$ produces no expansion, implying that CO_2 probably will not migrate in the interlayer.

There have been a small number of theoretical studies, using mainly force fields, reporting on the interactions of clays with water or CO_2 (*55–58*). Cygan et al. (*57*) have constructed a flexible force field which was used to study the H_2O-CO_2 interaction, vibrational spectra and water interactions with a pyrophyllite surface (*58*), concluding that water will cluster on the surface due to the stronger water-water compared to the water-surface interactions.

Density functional theory and DFT-based dynamics give us the flexibility to also study reactive events involving the interacting components. We used two

In Applications of Molecular Modeling to Challenges in Clean Energy; Fitzgerald, G., et al.;
ACS Symposium Series; American Chemical Society: Washington, DC, 2013.

types of models with periodic boundary conditions with the PBE functional (*59*) including Grimme's dispersion corrections (*34*, *35*). One simulation consists of hydrated Ca^{2+} in $scCO_2$, and the other consists of Ca-montorrillonite (001) surface with intercalated Ca^{2+} ions/water or Ca^{2+}/water/$scCO_2$. The temperature and pressure of the simulations was adjusted to be within the experimental conditions described by Schaef *et al*. (*54*), T~ 328 K and P~90 bar.

Figures 8(a) and (d) show snapshots from the $Ca^{2+}(H_2O)_6/scCO_2$ and $Ca^{2+}(H_2O)_{12}/scCO_2$, corresponding to ~1W and ~2W degrees of hydration. Panels (b) and (e) show the pair distribution functions of the Ca^{2+}/O_w water interactions (blue line) and an average coordination number (grey dotted line). For ~1W state, a narrow distribution corresponding to the 1st hydration shell of the Ca^{2+} ion with a maximum at ~2.3 signifies the strong ion/water interacions. At the higher hydration state (~2W) we see a multiple shell structure developing, with the 2nd shell including about five waters with the remaining water being a spectator in a more distant shell. Panels (c) and (f) show the corresponding pair distributions for the Ca^{2+}/C interactions, at longer distances from the ion center. Regardless of the hydration level, these register at distances > 5 Å.

At the lower hydration state, the first CO_2 coordination shell includes only ~3 CO_2 molecules lying outside the first H_2O shell. In this case, on average and within 6 Å, the Ca^{2+} cations are surrounded by two distinct shells of 6 H_2O and ~3 CO_2 molecules separated by about 2 Å.

At the higher hydration state, the Ca^{2+}/C interactions also start at ~5Å, and they include about 2 CO_2 molecules. In this case, there is a clear overlap between H_2O and CO_2 solvation shells with about 40% more solvent molecules within the 6 Å radius from the Ca center.

Figure 9 shows snapshots from AIMD simulations with periodic slab models of Ca-montmorillonite.

The unit cell includes only 2 Ca ions and 11 H_2O representing the ~1W state, Figure 9(a). Neat $scCO_2$ was added to the previous model and the last snapshot from this simulations is shown in Figure 9(b). Analysis of the positions trajectory showed that on average, the interlayer spacing increased from 10.6 Å to 11.4 Å after the $scCO_2$ intercalation. STX measurements of $scCO_2$ uptake by the 1W Ca-montmorillonite at T~330 K and P~90 bar registered an interlayer expansion from 11.38 A to ~11.9 A (*54*). At the same time, the clay layer also expanded slightly, by about 0.4 Å. The pair distribution functions for the Ca^{2+}/O_w interactions shows a sharp peak at about 2.5 A, shifting slightly to smaller distances as $scCO_2$ is introduced.

This is consistent with the picture emerging from the simulations of $Ca^{2+}(H_2O)_6/scCO_2$: at the ~1W hydration state, the minimally solvated Ca^{2+} ions will segregate from CO_2, contributing to the expansion of the interlayer space. Despite the strong Ca^{2+}/CO_2 interactions (Ca^{2+}/CO_2 binding energy -38.0 kcal/mol compared to -57.0 kcal/mol for Ca^{2+}/H_2O) it is not likely for CO_2 to replace some of the 1st shell water, once the Ca^{2+} ions are already solvated by water. In fact, experimentally in the case of Ca-montorillonite, it is not possible to reduce the water content below the 1W state. For higher hydration states, spectator CO_2 can freely exchange with H_2O in the outer shells, and at this point no expansion is necessary, or observed.

In Applications of Molecular Modeling to Challenges in Clean Energy; Fitzgerald, G., et al.;
ACS Symposium Series; American Chemical Society: Washington, DC, 2013.

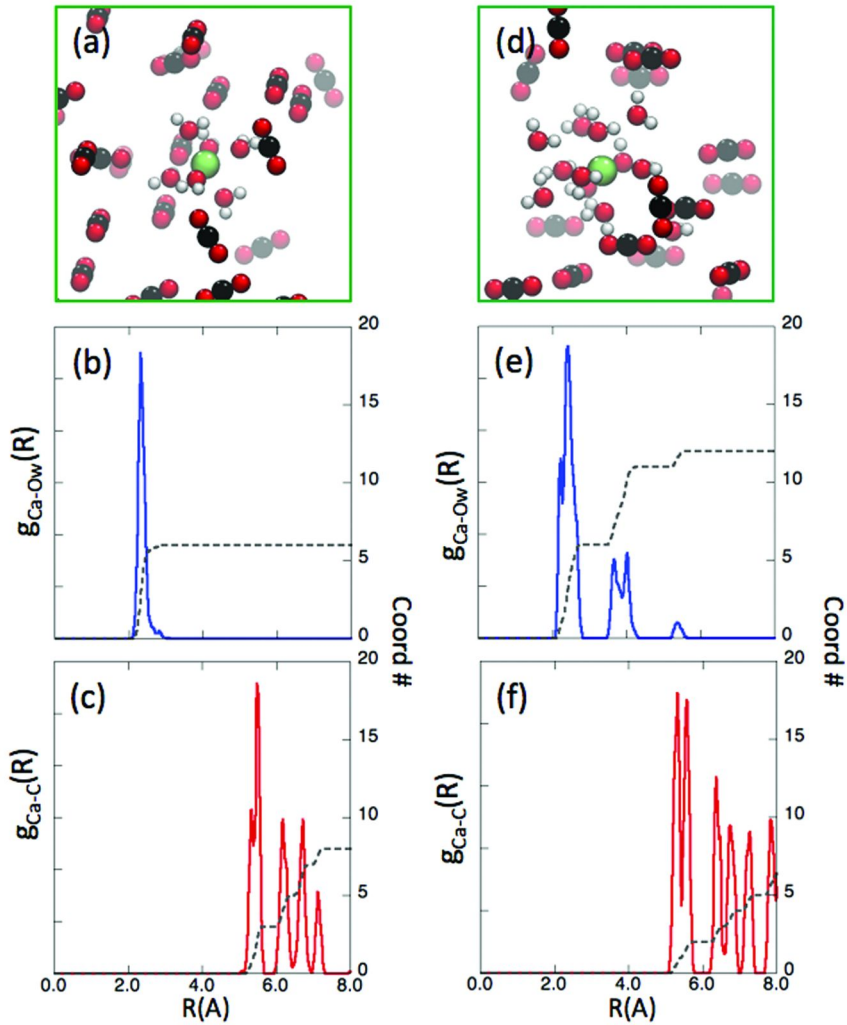

Figure 8. Snapshots of AIMD simulations of $Ca^{2+}(H_2O)_6$ (a) and $Ca^{2+}(H_2O)_{12}$ (b) in $scCO_2$. Pair distribution functions of Ca^{2+}/O_w interactions (b) and (e), and Ca^{2+}/C (c) and (f) respectively. (see color insert)

In Applications of Molecular Modeling to Challenges in Clean Energy; Fitzgerald, G., et al.;
ACS Symposium Series; American Chemical Society: Washington, DC, 2013.

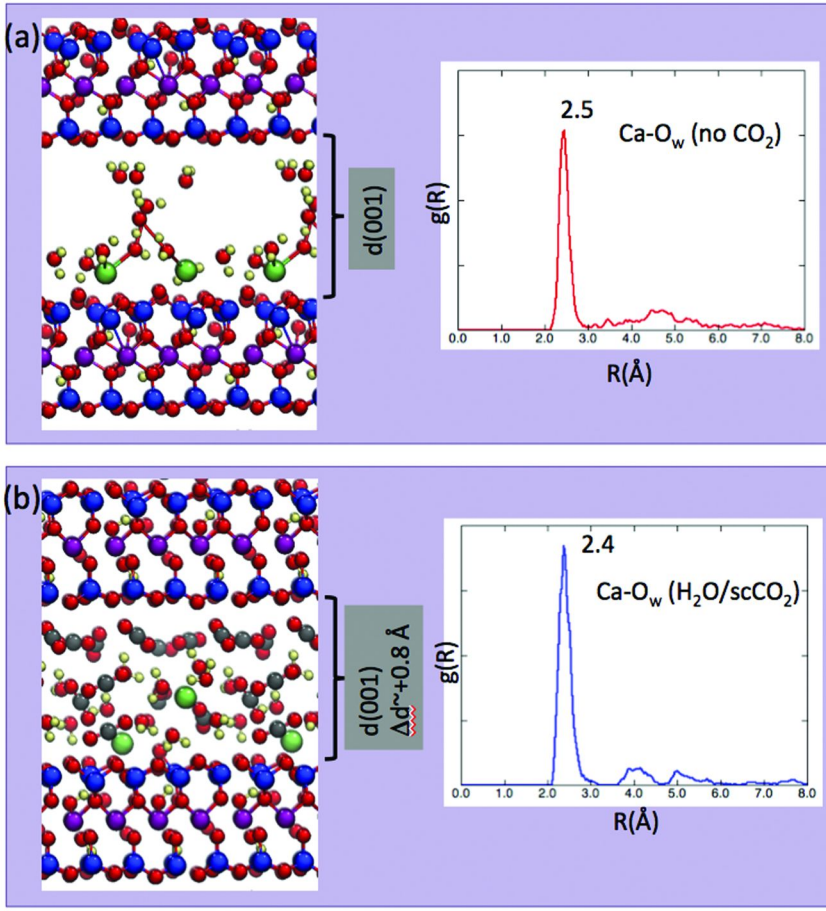

Figure 9. (a) Periodic models of Ca-montmorillonite at ~1W. (b) Simulation with intercalated $scCO_2$ causes interlayer expansion of ~0.8 Å. The corresponding pair distributions Ca^{2+}/O_w functions are also shown in the inserts. (see color insert)

Conclusions

In this chapter, we presented theoretical studies, taken in the context of complementing novel experimental studies examining interactions of sequestration components under supercritical conditions. The complexity of the chemical systems and the extreme nature of the conditions under which these materials exist and react necessitate relatively complex and large atomistic models that are on the forefront of what can be addressed by electronic structure methods. Nonetheless, we have taken steps in this direction by way of AIMD methods in the context of linear scaling DFT calculations.

In Applications of Molecular Modeling to Challenges in Clean Energy; Fitzgerald, G., et al.;
ACS Symposium Series; American Chemical Society: Washington, DC, 2013.

Implementation of a combined Gaussian basis and planewave representation for the description of the density, supplemented with balanced basis sets and tailored ECPs, allows for efficient treatment of the two-electrons terms in DFT theory. The result is a linear-scale algorithm that can take advantage of effective screening techniques and sparse matrix methods, and in fact become more efficient with increasing system size. Such an approach has been implemented in QUICKSTEP, the density functional part of CP2K. Furthermore, the synchronous development of localized basis sets with the effective core potentials afford a compact representation of systems and problems ranging from gas to condensed phase. The resulting code is fairly straightforwardly parallelized and portable to a large number of computer architectures. One of the initial drawbacks of lack of correlation in DFT has been remedied in the recent years by inclusion of the Grimme corrections for dispersion and their availability for a variety of functional forms.

Using these tools, we were able to show that reactivity in $scCO_2$ environments can be dramatically different than what is believed to be in aqueous environments. Small amount of waters in $scCO_2$ may very well be responsible for 'catalytic' activity, without direct solvation of CO_2 and prior formation of carbonic acid and its companion carbonate anions. Recent experiments supported by theoretical modeling, show potential of carbonate sub-surface reservoirs for chemical scrubbing and SO_2-removal and potential saving from plant retrofit costs.

Simulations involving interactions of clay minerals with $scCO_2$ help us understand the structural changes of the minerals, an effect that ultimately has roots in the very nature of the supercritical fluid.

Detailed knowledge of elementary reaction steps, reaction energetics, barriers and kinetic rates are expected to significantly enrich parameter datasets used for CCS simulation models and help create more robust models for a variety of field conditions.

Acknowledgments

This work is funded by the Department of Energy, Office of Fossil Energy. A portion of the research was performed using EMSL, a national scientific user facility sponsored by the Department of Energy's Office of Biological and Environmental Research located at Pacific Northwest National Laboratory. The Pacific Northwest National Laboratory (PNNL) is operated by Battelle for DOE under contract DE-AC06-76RL01830. The authors have benefited by useful discussions with Drs. R. Rousseau and H. T. Schaef.

References

1. Bachu, S.; Adams, J. J. *Energy Convers. Manage.* **2003**, *44*, 3151.
2. Zhang, W.; Xu, T.; Li, Y. *J. Geophys. Res.* **2011**, *116*, 7652.
3. Bandosz, T. J. Carboneceous Materials as Desulfurization Media. In *Combined and Hybrid Adsorbents: Fundamentals and Applications*; Loureiro, J. M., Kartel, M. T., Eds.; Springer: New York, 2006; pp 145−164.

4. Spycher, N.; Pruess, K.; Ennis-King, J. *Geochim. Cosmochim. Acta* **2003**, *67*, 3015.
5. McGrail, B. P.; Schaef, H. T.; Glezakou, V.-A.; Dang, L. X.; Owen, A. T. *Energy Procedia* **2009**, *1*, 3415.
6. Saharay, M.; Balasubramanian, S. *J. Chem. Phys.* **2004**, *120*, 9664.
7. Saharay, M.; Balasubramanian, S. *J. Phys. Chem. B* **2007**, *111*, 387.
8. Windisch, C. F.; Glezakou, V. A.; Martin, J. M. L.; McGrail, B. P.; Schaef, H. T. *Phys. Chem. Chem. Phys.* **2012**, *14*, 2560.
9. Glezakou, V. A.; Rousseau, R.; Dang, L. X.; McGrail, B. P. *Phys. Chem. Chem. Phys.* **2010**, *12*, 8759.
10. Glezakou, V.-A.; McGrail, B. P.; Schaef, H. T. *Geochim. Cosmochim. Acta* **2012**, *92*, 265.
11. Lin, X.; Yoon, Y.; Petrik, N. G.; Li, Z.; Wang, Z.-T.; Glezakou, V.-A.; Kay, B. D.; Lyubinetsky, I.; Kimmel, G. A.; Rousseau, R.; Dohnálek, Z. *J. Phys. Chem. C* **2012**, *116*, 26322.
12. Marx, D., Hutter, J. *Modern Methods and Algortihms of Quantum Chemistry*; NIC Series, John von Neumann Institute for Computing: Forschungszentrum, Jülich, 2000; Vol. 1.
13. CP2K: CP2K is a freely available (GPL) program, written in Fortran 95, to perform atomistic and molecular simulations of solid state, liquid, molecular and biological systems. It provides a general framework for different methods such as, e.g., density functional theory (DFT) using a mixed Gaussian and plane waves approach (GPW), and classical pair and many-body potentials. http://www.cp2k.org/, v2.3 (accessed September 3, 2012).
14. Payne, M. C.; Teter, M. P.; Allan, D. C.; Arias, T. A.; Joannopoulos, J. D. *Rev. Mod. Phys.* **1993**, *64*, 1045.
15. Remler, D. K.; Madden, P. A. *Mol. Phys.* **1990**, *70*, 921.
16. Krack, M.; Parrinello, M. *Phys. Chem. Chem. Phys.* **2000**, *2*, 2105.
17. VandeVondele, J.; Hutter, J. *J. Chem. Phys.* **2007**, *127*, 114105.
18. VandeVondele, J.; Krack, M.; Fawzi, M.; Parrinello, M.; Chassaing, T.; Hutter, J. *Comput. Phys. Comm.* **2005**, *167*, 103.
19. VandeVondele, J.; Mohamed, F.; Krack, M.; Hutter, J.; Sprik, M.; Parrinello, M. *J. Chem. Phys.* **2005**, *122*, 14515.
20. Cramer, J. C. *Essentials of Computational Chemistry. Theories and Models*; Wiley and Sons, Ltd., West Sussex, England, 2004.
21. Cramer, J. C.; Truhlar, D. G. *Phys. Chem. Chem. Phys.* **2009**, *11*, 10757.
22. Lippert, G.; Hutter, J.; Parrinello, M. *Mol. Phys.* **1997**, *92*, 477.
23. Beck, L. T. *Rev. Mod. Phys.* **2000**, *72*, 1041.
24. Dunning, T. H. *J. Chem. Phys.* **1989**, *90*, 1007.
25. Goedecker, S.; Teter, M.; Hutter, J. *Phys. Rev. B* **1996**, *54*, 1703.
26. Hartwigsen, s.; Goedecker, S.; Hutter, J. *Phys. Rev. B* **1998**, *58*, 3641.
27. Laino, T.; Mohamed, F.; Laio, A.; Parrinello, M. *J. Chem. Theory Comput.* **2006**, *2*, 1370.
28. CASTEP: CASTEP is a leading code for calculating the properties of materials from first principles,using density functional theory. It can simulate a wide range of properties of materials proprieties including energetics,

structure at the atomic level, vibrational properties, electronic response properties etc. In particular it has a wide range of spectroscopic features that link directly to experiment, such as infra-red and Raman spectroscopies, NMR, and core level spectra. Outside UK, it is available through Accelrys. http://www.castep.org/, 6.0 (accessed 2012).
29. CPMD: The CPMD code is a parallelized plane wave/pseudopotential implementation of Density Functional Theory, particularly designed for ab-initio molecular dynamics. http://www.cpmd.org/, 3.15 (accessed 2013).
30. Quantum Espresso: Quantum ESPRESSO is a software suite for ab initio electronic-structure calculations and materials modeling distributed for free under the GNU General Public License. It is based on Density Functional Theory, plane wave basis sets, and pseudopotentials (both norm-conserving and ultrasoft). ESPRESSO is an acronym for opEn-Source Package for Research in Electronic Structure, Simulation, and Optimization. http://www.quantum-espresso.org/ (accessed 2009).
31. VASP: The Vienna Ab initio Simulation Package (VASP) is a computer program for atomic scale materials modelling, e.g. electronic structure calculations and quantum-mechanical molecular dynamics, from first principles. http://www.vasp.at/, VASP.5.3.3. (accessed December 18, 2012).
32. Allen, M. P., Tildesley, D. J. *Computer Simulations of Liquids*; Oxford University Press: Oxford, U.K., 1987.
33. Grimme, S. *J. Comput. Chem.* **2006**, *27*, 1787.
34. Grimme, S. *WIRE's Comput. Mol. Sci.* **2011**, *1*, 211.
35. Grimme, S.; Anthony, J.; Ehrlich, S.; Krieg, H. *J. Chem. Phys.* **2010**, *132*, 154104.
36. Valiev, M.; Bylaska, E. J.; Govind, N.; Kowalski, K.; Straatsma, T. P.; van Dam, H. J. J.; Wang, D.; Nieplocha, J.; Apra, E.; Windus, T. L.; de Jong, W. A. *Comput. Phys. Commun.* **2010**, *181*, 1477.
37. Dennison, D. M. *Phys. Rev.* **1932**, *41*, 304.
38. Fermi, E. *Z. Phys.* **1931**, *71*, 250.
39. Amat, G.; Pimbert, M. *J. Mol. Spec.* **1965**, *16*.
40. Cihla, Z.; Chedin, A. *J. Mol. Spec.* **1971**, *40*, 337.
41. Garrabos, Y.; Chandrasekharan, V.; Echargui, M. A.; Marsaultherail, F. *Chem. Phys. Lett.* **1989**, *160*.
42. Wieder, I.; McCurdy, G. B. *Phys. Rev. Lett.* **1966**, *16*, 565.
43. Garrabos, Y.; Echargui, M. A.; Marsaultherail, F. *J. Chem. Phys.* **1989**, *91*.
44. Savage, P. E.; Gopalan, S.; Mizan, T. I.; Martino, C. J.; Brock, E. E. *AlChE J.* **1995**, *206*, 107.
45. Wu, B. C.; Klein, M. L.; Sandler, S. I. *Ind. Eng. Chem. Res.* **1991**, *30*, 822.
46. Saharay, M.; Balasubramanian, S. *J. Phys. Chem. B* **2007**, *111*, 387.
47. Nguyen, M. T.; Matus, M. H.; Jackson, V. E.; Ngan, V. T.; Rustad, J. R.; Dixon, D. A. *J. Phys. Chem. A* **2008**, *112*, 10398.
48. Glezakou, V.-A.; Dang, L. X.; McGrail, B. P. *J. Phys. Chem. C* **2009**, *113*, 3691.
49. Henkelman, G.; Jónsson, H. *J. Chem. Phys.* **2000**, *113*, 9978.
50. Henkelman, G.; Uberuaga, B.; Jonsson, H. *J. Chem. Phys.* **2000**, *113*, 9978.
51. Gaus, I. *Int. J. Greenhouse Gas Control* **2010**, *4*, 73.

52. Li, Z.; Dong, M.; Li, S.; Huang, S. *Energy Convers. Manage.* **2006**, *47*, 1372.
53. Loring, J. S.; Schaef, H. T.; Turcu, R. V. F.; Thompson, C. J.; Miller, Q. R. S.; Martin, P. F.; Hu, J. Z.; Hoyt, D. W.; Qafoku, O.; Ilton, E. S.; Felmy, A. R.; Rosso, K. M. *Langmuir* **2012**, *28*, 125.
54. Schaef, H. T.; Ilton, E. S.; Q., Q.; Martin, P. F.; Felmy, A. R.; Rosso, K. M. *Int. J. Greenhouse Gas Control* **2012**, *6*, 220.
55. Botan, A.; Rotenberg, B.; Marry, V.; Turq, P.; Noetinger, B. *J. Phys. Chem. C* **2010**, *114*, 14962.
56. Criscenti, L. J.; Cygan, R. T. *Environ. Sci. Technol.* **2013**, *47*, 87.
57. Cygan, R. T.; Romanov, V. N.; Myshakin, E. M. *J. Phys. Chem. C* **2012**, *116*, 13079.
58. Zhang, G.; Al-Saidi, W. A.; Myshakin, E. M.; Jordan, K. D. *J. Phys. Chem. C* **2012**, *116*, 17134.
59. Perdew, J. P.; Burke, K.; Erzenhof, M. *Phys. Rev. Lett.* **1996**, *77*, 3865.

Chapter 4

Characterization of CO_2 Behavior on Rutile TiO_2 (110) Surface

Yeohoon Yoon*

Fundamental and Computational Science Directorate, Pacific Northwest National Laboratory, Richland, Washington 99352
***E-mail: yeohoon.yoon@pnnl.gov**

The dynamic behavior of carbon dioxide (CO_2) adsorbed on the rutile TiO_2 (110) surface is studied by dispersion corrected density functional theory (DFT) and combined *ab initio* molecular dynamics (AIMD) simulation. Understanding the behavior of CO_2 is important regarding possible applications for treating CO_2 in current environmental problems along with the consideration as a renewable energy source. Concerning the ability as a reducible support of TiO_2 surface, a fundamental understanding of the interaction between CO_2 and TiO_2 surface will help extending the possible applications. In the current study, CO_2 interaction and dynamic behavior on the TiO_2 surface is characterized including the effect of the oxygen vacancy (O_V) defect. Also the coverage dependence of CO_2 behavior is investigated since more contribution of the intermolecular interaction among CO_2 molecules can be expected as the coverage increasing.

Introduction

The increasing energy demand requires the development of new energy sources and it is expected to be environmentally sustainable at the same time (*1*). Hydrocarbon fuel is currently a primary source of energy since it is provided by nature with its ease of transportation and storage. Unfortunately, the amount of this resource is limited and the combustion of these fuels carries the significant

In Applications of Molecular Modeling to Challenges in Clean Energy; Fitzgerald, G., et al.;
ACS Symposium Series; American Chemical Society: Washington, DC, 2013.

environmental pollution including carbon dioxide (CO_2). Concerning a particular impact of CO_2 to the global warming through the greenhouse effect, there is an increasing interest in technological solution to alleviate CO_2 emission (*2*, *3*). Some of such strategies concern the possibility of capture, storage and sequestration. Additionally, a possibility of converting CO_2 into a valuable fuel should be an important application among CO_2 treatments. For facilitating such solutions, a fundamental understanding of CO_2 activation is required while this activation should overcome the extremely strong chemical bonds accompanied by the carbon atom. Considering a possible role of surface including oxide surface as a (photo-) catalyst and a support of reducibility, only little is known about the interaction of CO_2 with the surface (*4*).

Accomplishing such understanding of fundamental interaction requires the ability of design and modeling at the level of atoms. This kind of detailed knowledge can be provided by the theory and computation so that such molecular modeling can be applied to challenges in clean energy problems (*5*). While the collective observables are obtained commonly in the laboratory, the computational modeling allows us to examine in more detailed manner at the atomic level. In regards to the physical origin of CO_2 activation and related interactions, the contributions by electronic and thermal environment are necessary to be investigated. Contemporary quantum mechanical approach based on the density functional theory (DFT) is able to address such points and combining molecular dynamics technique can provide macroscopic ensemble nature which can be compared directly to the observation in the laboratory (*6*, *7*).

For the applications by taking advantage of oxide surfaces, a specific interest can be focused on TiO_2 surface with the motivation initially arisen from the capability of its photo reduction of CO_2 to hydrocarbons or methanol (*3*, *8*, *9*). Besides, CO_2 has been utilized for characterizing different sites on TiO_2 surface (*10*) as well. To date, rutile TiO_2 (110) surface is the most studied single crystal surface due to its stability (*11*), and the characterization of CO_2 on rutile TiO_2 (110) surface has been studied extensively so far (*10*–*16*). Concerning the adsorption site on the surface, CO_2 initially adsorbs weakly on oxygen vacancies (O_V) and subsequently populates on five-coordinated Ti (Ti_{5C}) sites (*11*). The CO_2 molecule adsorbed on O_V can be reduced to CO by applying energy above ~1.8 V which can be observed, for example, in the scanning tunneling microscopy (STM) experiment with the injected electrons from tip (*13*, *14*, *16*). Alternatively, it can also diffuse from O_V with barrier energy of 0.14 eV (*12*). Furthermore, the CO_2 on Ti_{5C} site is shown to be mobile with relatively low diffusion barriers (*12*).

In this chapter, the basic understanding of CO_2 adsorption is addressed quantitatively by means of DFT and combined AIMD simulation. Then a detailed character of the coverage dependent binding configurations of CO_2 and their dynamic behaviors are investigated. The organization of this chapter is as follows: The theoretical method and the model system are explained in Method section along with the verification for their suitability. In the Results and Discussion section, the single CO_2 adsorption and diffusion on TiO_2 surface is addressed firstly, and then the effect of O_V is discussed followed by the characterization of CO_2 according to the different coverages. In the Conclusions section, all results are summarized and overall collective perspective is discussed.

In Applications of Molecular Modeling to Challenges in Clean Energy; Fitzgerald, G., et al.;
ACS Symposium Series; American Chemical Society: Washington, DC, 2013.

Methods

Model System

The TiO_2 surface is flexible to its electronic environment so that it becomes acidic if there are excess electrons, and that happens commonly when studying materials as a reducible support concerned in the energy related research (*2*, *17*). When modeling such system, cares should be taken to describe proper electronic environment at the surface. The current model system is constructed in order to avoid large dipole moment in the slab and provide reasonable work function within the adopted theoretical method. Such requirement can be achieved by using larger number of layers and six TiO_2 tri-layers are applied in the current study. In addition, the bottom Ti layer is fixed to their bulk lattice positions while other layers are allowed to relax. The validity is confirmed with consistent electrostatic (Hartree) potential along the direction of surface normal. Also a 10 Å thick vacuum layer is applied above the surface to minimize electrostatic interaction between periodic images in the same direction. For the surface area included in the model, (3×4) rutile TiO_2(110) slab model is considered as a surface of wide enough and this model has been focused on with its stability. The large area of the model surface makes it possible to avoid the intermolecular interaction between single isolated CO_2 molecule and its periodic image, while many CO_2 molecules in high coverage can be described regardless of this factor by nature of periodic boundary condition. For the modeling of various coverages, four different coverages are considered by placing 4, 6, 8, 12 CO_2 molecules on the slab which represent 1/3, 1/2, 2/3, 1 monolayer (ML), respectively. Particularly when a possible oxygen vacancy (O_v) defect is considered, one O_v is considered within the size of the current model, in which the concentration of O_V corresponds to 0.083 ML, and it is reasonable to be compared with the experimental observation (*18*, *19*).

Computational Details

For the electronic structure calculation, density functional theory (DFT) is adopted as implemented in the CP2K package (*20–22*) with gradient corrected (PBE) functional for exchange and correlation (*23*). Norm-conserving pseudopotentials are used to describe core electrons (*24*). The wave functions are constructed for the calculation of electrostatic energy by expanding a double-ζ Gaussian basis set in which basis superposition errors are minimized (*25*) combined by an additional auxiliary plane wave basis with 400 Ry energy cutoff. Brillouin zone sampling is performed by using Γ-point. In order to describe more precisely for the long range interaction among adsorbed molecules and the surface, the dispersion forces are modeled by the DFT-D3 method (*26*). By doing this, an attractive dispersion coefficient and the corresponding cutoff function are added to the DFT potential using the standard parameter set by Grimme (*26*) with a cutoff of 10 Å. The effect of dispersion correction is observed as up to 0.05 eV increase of the binding energy difference among various CO_2 configurations and this approach is believed to represent adequate potential energy surfaces for hydrocarbons on oxides (*27*, *28*) as well as the structural and spectroscopic properties of liquid supercritical CO_2 based on the previous studies

In Applications of Molecular Modeling to Challenges in Clean Energy; Fitzgerald, G., et al.;
ACS Symposium Series; American Chemical Society: Washington, DC, 2013.

(*29*, *30*). When considering kinetic coordinates, the climbing image nudged elastic band method (CI-NEB) (*31*) is adopted employing 13-17 replica. For a finite temperature sampling, *ab initio* molecular dynamics (AIMD) simulations are performed within a canonical (NVT) ensemble using Nosé-Hoover thermostat (*32*, *33*) with a time step of 0.5 fs during more than 20 ps of equilibrated trajectory at the temperature of 130 K. Note that this temperature is near the desorption temperature so as to increase the ability of sampling relevant configurational space within relatively short time (20 ps) duration of trajectory due to the limitation of AIMD. By doing so, we are able to observe CO_2 rotation and diffusion events from the sampled trajectories, yet not the desorption events. When thermally equilibrated configurations are quenched, the simulated annealing technique is adopted by rescaling the velocity with a factor of 0.99 at each time step. For the calculation of the electrostatic potential at each time step, DFT calculation is performed as explained above. For the model of a reduced TiO_2 surface, an accurate description is required for the excess electrons produced by O_V. For this case, DFT+U method (*34*) is used with an effective U parameter (U_{eff}) applied to the Ti 3d electrons within a local spin density approximation for the spin polarized formalism. While focusing on the correct description of the work function and relative band gap position, test calculations have been performed as shown in Figure 1. When large value is chosen as effective U parameter, the location of defect state is fairly well separated from the conduction band so that excess electrons are easily localized at that state. On the other hand, the work function is increasing by increasing effective U parameter, which results in rather unreal nature of the role of excess electrons. Therefore an optimal condition is required to be defined first, and in the current study, the effective U parameter of 4.1 eV is adopted since an adequate work function (4.9 eV) (*35*) was able to be reproduced while the location of defect states is still reasonably described based on the expected position at 0.9 eV below conduction band (*36*, *37*).

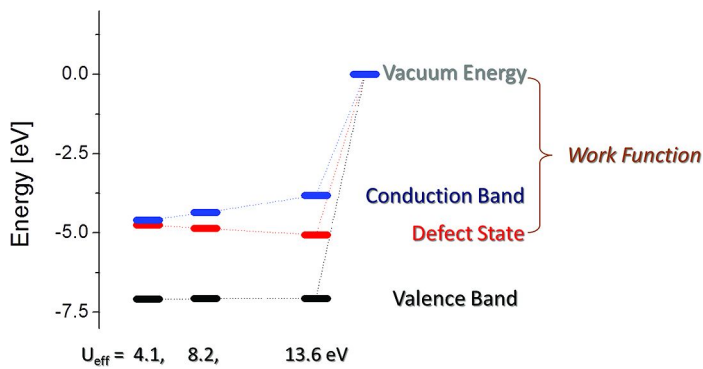

Figure 1. Electronic structures depending on the different U_{eff} values within DFT+U method. The energies are relative to the energy at vacuum state and the work functions are obtained by the difference between the vacuum and defect state energy. These electronic structures are obtained from the (3×4) TiO_2 (110) slab model with six tri-layers and one O_V defect on the surface.

In Applications of Molecular Modeling to Challenges in Clean Energy; Fitzgerald, G., et al.;
ACS Symposium Series; American Chemical Society: Washington, DC, 2013.

Results and Discussion

Single CO_2

When a single CO_2 molecule is adsorbed on the TiO_2 (110) surface, it prefers to bind on O_V site and heals this vacancy defect first. Then additional CO_2 molecules begin to populate on the five-coordinated Ti sites (Ti_{5C}) as the coverage increased (*13–16*). Therefore, when considering single CO_2 adsorption on the surface in the present study, O_V sites are assumed to be healed so that CO_2 molecule on the Ti_{5C} row on the clean surface is able to be considered. As a first assessment of the behavior of CO_2, numbers of single CO_2 binding configurations to the TiO_2 surface are investigated. Figure 2 shows several noteworthy configurations including the energetically most stable configuration as shown in Figure 2(a). In this configuration, CO_2 binds with one O atom to top of a Ti_{5C} site while the O=C=O molecular axis is tilted by a polar angle, $\psi \simeq 45°$ with respect to the surface normal direction and by an azimuthal angle, $\varphi = 90°$ along the $[1\bar{1}0]$ direction toward neighboring bridge bond oxygen (O_b) at the same time. The binding energy can be calculated by subtracting the energy of gas phase CO_2 and bare TiO_2 slab from the energy of whole CO_2 adsorbed TiO_2 slab model, and the resulting binding energy of the most stable configuration is obtained as 0.45 eV. It is in good agreement with previous DFT calculation in which it was 0.44 eV or 0.39 eV depending on the different methods of dispersion correction (*17*).

The other configurations in Figure 2 are considerable in the sense of possible diffusion path of adsorbed CO_2 molecule. First of all, the rotation of CO_2 is regarded as one of the possible dynamic motion. In this case, dangling O atom out of the surface (denoted O_d) rotates while keeping the other bound O atom to top of a Ti_{5C} site as an anchor (denoted O_a). In Figure 2(b), CO_2 molecule has rotated azimuthally by $\varphi \approx 45°$ with respect to the $[1\bar{1}0]$ direction and the energy difference to the most stable one is just 0.02 eV which can be overcome easily in thermal condition. In other words, the initiation of the rotation of adsorbed CO_2 about Ti_{5C}-O_a axis is thermally facile. Note that the O_d atom tries to come close to the neighboring Ti lattice during rotation, and as a result, the length of O=C=O projected to the surface normal, i.e. molecular height should change as well. During the rotation, CO_2 molecule is supposed to be able to pass through the configuration parallel to the surface with $\psi = 90°$, $\varphi = 0°$ in which each O atom binds at the distance of 2.33 Å to two neighboring Ti_{5C} sites (Figure 2(c)). In this configuration, the molecular height should be close to 0 Å. In order to reach this configuration from the most stable one, it is required the energy increasing by 0.03 eV. When CO_2 molecule happens to have this configuration during the thermal motion, one can expect the possibility of its tumbling to the neighboring Ti_{5C} site by exchanging the role of O atom as an anchor. Besides, when CO_2 molecule is adsorbed to O_b site as shown in Figure 2(d), the binding energy is 0.24 eV smaller than that of the most stable configuration. Thus O_b site can be excluded from the concerns of the most probable single CO_2 adsorption site.

In Applications of Molecular Modeling to Challenges in Clean Energy; Fitzgerald, G., et al.;
ACS Symposium Series; American Chemical Society: Washington, DC, 2013.

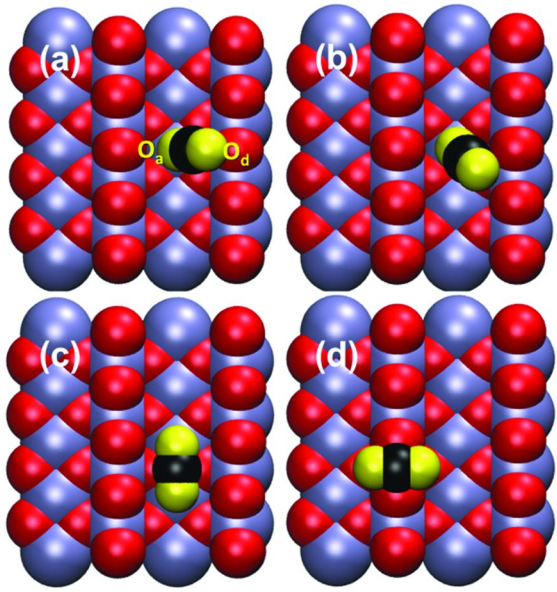

Figure 2. Single CO_2 molecule adsorption configurations on TiO_2(110) surface. Four representative configurations are shown and their binding energies are (a) 0.45 eV, (b) 0.42 eV, (c) 0.33 eV and (d) 0.21 eV. (For interpretation by color, see the web version of this article.)

Regarding the facile thermal rotation and the probable tumbling motion along the Ti_{5C} row as a hypothetical diffusion mechanism, the kinetic barrier energies of such kind of motions are examined by CI-NEB as shown in Figure 3. When CO_2 starts rotating from the most stable configuration, it can reach to the intermediate configuration corresponds to Figure 2(c). From this configuration, the molecule can reverse the process or rotate further to end up back to the most stable configuration. This rotation motion requires 0.05 eV activation energy between two symmetrically equivalent stable configurations which is represented by a rotation about the Ti_{5C}-O_a axis by $\Delta\varphi$=180°. Alternatively, it may be able to tumble to the neighboring Ti_{5C} site through this intermediate configuration. In this case, the molecule switches its anchoring O_a atom to O_d atom while O_d atom becomes anchor O_a bound to top of the neighboring Ti_{5C} site, then it keeps rotating about new generated Ti_{5C}-O_a axis. This process exhibit an energy barrier of 0.06 eV and this implies extremely fast diffusion even at low temperatures. In fact, this diffusion along the Ti_{5C} row is competitive with the rotation mechanism described earlier in terms of the activation energy. The remaining possible diffusion path on the surface should be related to the path involving O_b sites. The diffusion path across the O_b row shows the barrier energy of 0.21 eV and it is much higher than others considered previously. Thus it can be disregarded from the probable dominant diffusion process on the surface while the diffusion can be conclusively characterized by the combined rotation and tumbling motion along the Ti_{5C} row.

In Applications of Molecular Modeling to Challenges in Clean Energy; Fitzgerald, G., et al.;
ACS Symposium Series; American Chemical Society: Washington, DC, 2013.

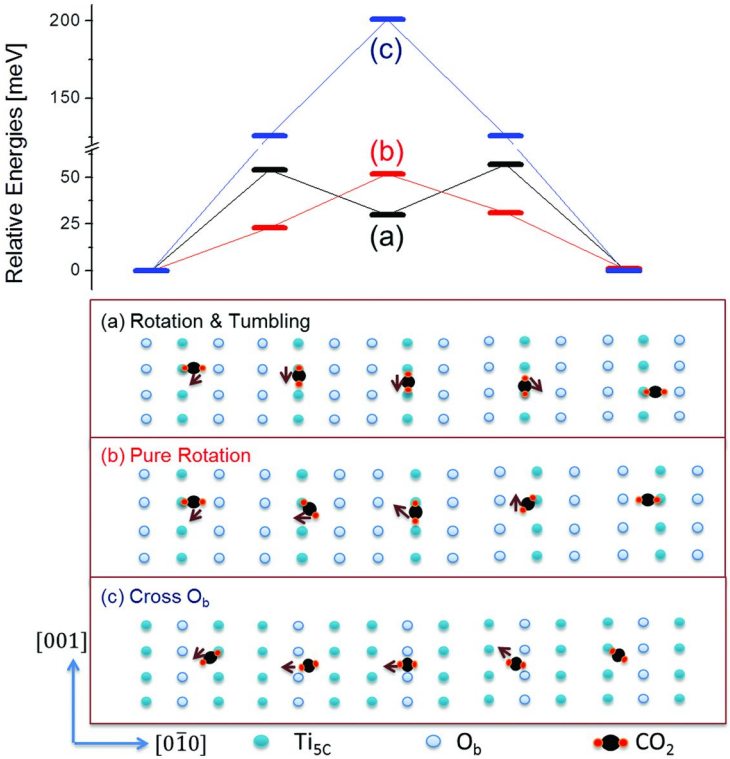

Figure 3. Diffusion energy barriers corresponding to three different diffusion pathways and their schematic cartoon with (a) rotation and tumbling, (b) pure rotation and (c) crossing O_b row. (For interpretation by color, see the web version of this article.)

Effect of O_V Defect on Single CO_2 Binding

In the previous section, a single CO_2 binding to the TiO_2 surface is considered assuming all possible O_V defects are already healed while a CO_2 molecule is fairly far away from such O_V. However, there could be some differences if a CO_2 molecule happens to adsorb on the O_V defect site or reside near that site in the presence of the CO_2 molecule already adsorbed on it. When considering the defected surface, there are two excess electrons generated by O_V defect. In order to account for proper charge distribution by those electrons (*38*), DFT+U method (*34*) is applied to determine the configuration and the binding energy. As a first result, the binding energy of CO_2 on O_V site is found to be 0.60 eV and this shows that the binding is 0.17 eV stronger than the strongest binding to regular Ti_{5C} site. It supports the assumption that a CO_2 is preferentially adsorbed on O_V defect site first.

Then the CO_2 molecule adsorbed next to another CO_2 already bound to an O_V site is considered as shown in Figure 4. If they are placed two Ti lattice distance (2×2.96 Å) away as a model of fairly isolated molecule (Figure 4(a)), the binding

energy is 0.43 eV which is similar to the binding energy of single CO_2 on a regular Ti_{5C} site. Note that this binding energy is 0.02 eV lower than on clean surface though, as a result of the DFT+U description of TiO_2 slab which is opposed to the normal DFT description. However, the binding energy increases to be 0.48 and 0.49 eV as CO_2 coming close to another CO_2 on O_V site respectively to the different configurations (Figure 4(b) and (c)). Thus it is confirmed that there is stronger binding of CO_2 next to O_V adsorbed CO_2 about 0.05 and 0.06 eV comparing to the binding on the regular Ti_{5C} site. When considering the reason of such stronger binding, it can be interpreted that the intermolecular interaction between CO_2 molecules is dominant while the electrostatic energy from the excess electron is almost disappeared on the surface region by healing O_V. The resulting two most stable binding configurations also support this when compared to two typical liquid CO_2-CO_2 interactions through T-shaped and slipped parallel configurations (*29*, *39*). In summary, one can see stronger binding of CO_2 on the Ti_{5C} site near another CO_2 adsorbed on O_V but the binding energy is still enough for it to make a thermal diffusion such as the one described in the previous section.

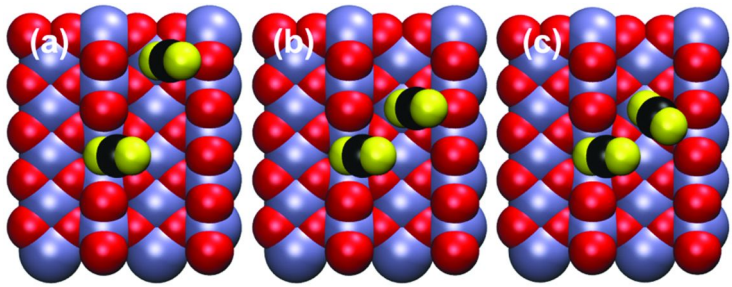

Figure 4. Single CO_2 adsorption configurations on TiO_2 surface in the presence of neighboring CO_2 adsorbed on O_V and their binding energies are (a) 0.43 eV, (b) 0.48 eV and (c) 0.49 eV. (For interpretation by color, see the web version of this article.)

Coverage Dependence of CO_2 Binding Configurations

Although the single CO_2 interaction with TiO_2 surface and its dynamic behavior are intensively investigated, things shall be changed if there are more CO_2 molecules on the surface which can interact to one another. In order to understand such an adlayer configurations at higher coverages, model systems with four different coverages (1/3, 1/2, 2/3, and 1 ML) are constructed and the ensembles of those configurations are sampled by AIMD simulations at the finite temperature of 130 K.

In general, the Ti_{5C} bound CO_2 are free of motion including on-site rotation and diffusion at low coverage while their configurations become more restricted at high coverages. Even though the diffusion rate is hardly quantified due to the limit of statistics from AIMD simulations, several CO_2 hopping events are observed from one Ti_{5C} site to the next during 20 ps sampling. In the lowest coverage, i.e. 1/3 ML case, 0.125 counts/ps hopping events are observed per CO_2 molecule

which is almost 10 times more than the one from 1 ML trajectory. Assuming Arrhenius formula is applicable with the preexponential factor of 1×10^{-13} s^{-1}, the hopping energy barrier of 1/3 ML coverage is 0.055 eV which is very close to the value of 0.050 eV obtained by CI-NEB calculation as shown in Figure 2. This energy barrier is enough to activate the diffusion motion from the energetically most stable configuration (Figure 2(a)) in thermal condition around at 130 K.

When looking into overall features of sampled ensemble configurations at all coverages, basically no well-ordered ones are observed from AIMD, indicating the structures are characterized by a component of dynamic disorder. A representative set of configurations observed at different coverages are considered in order to investigate the relation between such disordered and ordered configurations. For the ordered configuration, CO_2 molecules are placed to be hypothetically well ordered based on the single CO_2 adsorption configuration. And then this is thermalized at the temperature of 50 K followed by a slow simulated annealing to the temperature of 0 K. By doing so, well-ordered thermal configuration can be quenched while avoiding major rotation and translational motion. On the other hand, one random configuration from the AIMD trajectory is extracted and quenched to temperature of 0 K as a representative set of disordered configuration. During this simulated annealing, one can expect the maximal structure optimization while suppressing possible energy interconversions seen at higher temperature and the resulting configurations are shown in Figure 5. And then the energy differences of ordered and disordered configurations are assessed according to the different coverages. When comparing the binding energy per molecule based on the configurations obtained as above, ordered configurations are generally less stable by 0.06 to 0.09 eV/CO_2 than the disordered dynamic configurations from the equilibrated ensemble. In principle, such energy difference is small within the kinetic energy distribution at this temperature so that both of configurations are energetically feasible. However, disordered configurations become more populated concerning free energy nature accompanying entropic effect. As a result, only partially ordered configurations are observed during the simulation. If one look into more in detail of the configurations from Figure 5, the popular configuration is the CO_2 bound to Ti_{5C} site while being toward O_b direction with tilting in the possible range of azimuthal rotation angle. Even though the majority of configurations are tilted CO_2, note that there is a non-negligible fraction of CO_2 lying in between two neighboring Ti_{5C} sites ($\varphi\approx0°$) and this configuration is able to stabilize the neighboring CO_2 next to it.

We have discussed observed CO_2 configurations so far, as a single molecule separately. Now the averaged feature from the ensemble of configurations will be considered, which are observed practically in most cases of experiments. As a meaningful quantity describing ensemble configurations, the distributions of CO_2 orientation is considered as shown in Figure 6. This distribution can be obtained through the 3-dimensional maps of projected O_d positions relative to Ti_{5C} bound O_a position onto the TiO_2(110) surface plane. The CO_2 molecules which have no O atom within 2.5 Å from any Ti_{5C} site are excluded from the distribution. The distance criteria of 2.5 Å is obtained from the first nearest neighbor distance of radial distribution of Ti_{5C}-O_a distance.

In Applications of Molecular Modeling to Challenges in Clean Energy; Fitzgerald, G., et al.;
ACS Symposium Series; American Chemical Society: Washington, DC, 2013.

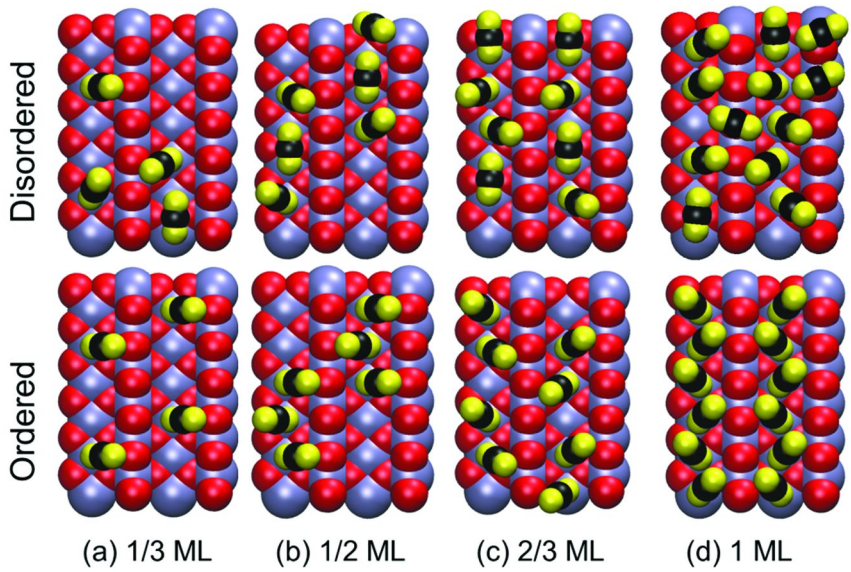

Figure 5. The representative snapshots of "disordered" configurations extracted from the 130 K AIMD trajectories followed by being quenched to 0 K. The "ordered" configurations constructed based on the most stable single CO_2 at the temperature of 50 K at four different coverages. (For interpretation by color, see the web version of this article.)

In general, there are two mainly populated orientations at φ=0° and in the range of φ=45~90° with maximum near φ≈65° for all coverages. The former configuration can be interpreted as the one laying down flat, i.e. ψ=0°, on the surface. This type of configuration can be easily found during the AIMD simulation as shown in the snapshot from Figure 5. The coverage dependence of the population of this flat lying configuration is decreasing from about ~25% at 1/2, 2/3 ML to ~10% at 1 ML which indicates the contribution of CO_2-CO_2 interaction is decreasing as the coverage is increasing. The distance of this configuration from the surface is approximately the same as the height of C atom of tilted standing CO_2 in φ=45~90° range so that it can generate T-shaped dimer which is a common feature in both liquid and solid CO_2 structures (*29*, *40*). The second most populated configuration is distributed in rather wider space range while it represents to be oriented φ=45~90° with polar tilting ψ≈45° with respect to surface normal. This configuration is similar to most stable single CO_2 configuration (Figure 1(a)). The rotation between two configurations is feasible with a barrier energy (ΔE) of 0.06 to 0.07 eV at all coverages based on the population ratio by $\Delta E = -\ln\left(P_{\varphi=45\sim90^{\circ}} / P_{\varphi=0^{\circ}}\right)$, where P_i is the population of configuration i. Note that this barrier energy is similar but a little higher than that of single CO_2 rotation possibly due to the contribution of the intermolecular CO_2-CO_2 interaction.

In Applications of Molecular Modeling to Challenges in Clean Energy; Fitzgerald, G., et al.;
ACS Symposium Series; American Chemical Society: Washington, DC, 2013.

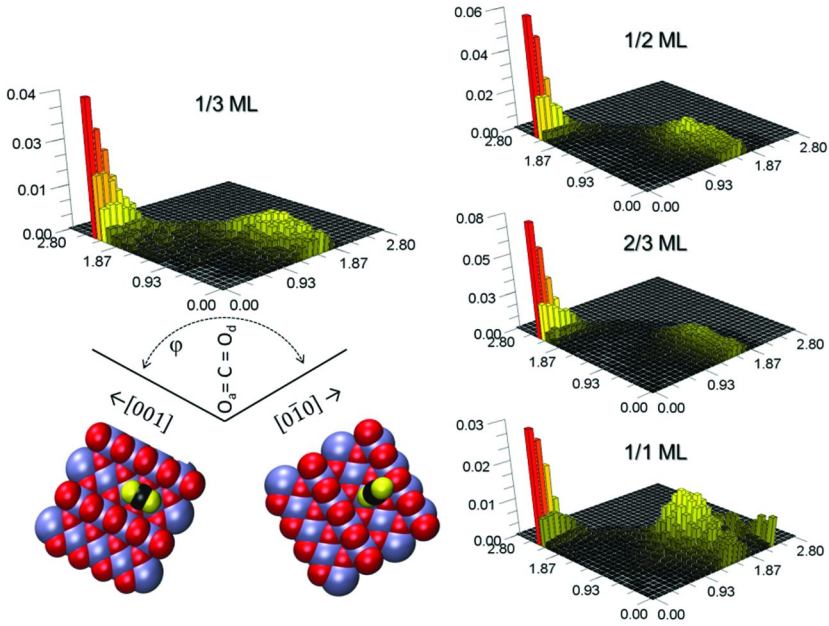

Figure 6. The distributions of projected position of O_d relative to O_a onto the TiO_2(110) surface plane for CO_2 molecules that are bound to Ti_{5C} sampled from AIMD simulations at 130 K. The x- and y-axis represent the surface plane with [0$\bar{1}$0] and [0$\bar{1}$0] directions and z-axis represents the population of O_d at that position. The resulting arc shape distributions correspond to the distribution by the azimuthal angle φ. (For interpretation by color, see the web version of this article.)

There is one more noteworthy feature from Figure 6 particularly at 1 ML coverage exhibiting an additional narrow band in the range of φ=60~90° at longer O_a-O_d distance around 2.3 Å while the population coming from this configuration is non-negligible with around 9%. This type of configuration can be assigned as CO_2 molecules on the O_b row in parallel to the surface plane as it can also be found from the snapshot from Figure 5(d). If this configuration is taken out as a single molecule, the binding energy in the temperature of 0 K can be calculated to be 0.23 eV higher than that of the most stable single molecule configuration as shown in Figure 1(a) and (d). However, when the binding energy per molecule at 1 ML is considered after being quenched to the temperature of 0 K, it becomes larger to be 0.45~0.49 eV as comparable to the strongest binding energy of single CO_2 on regular Ti_{5C} site (Figure 1(a)). Therefore, two bound configurations either at O_b or Ti_{5C} can be in thermal equilibration and this implies that the interaction between CO_2 molecules participates in stabilizing the configuration on O_b at 1 ML.

In order to examine relative positions of neighboring CO_2 molecules beyond overall ensemble configuration, their relative spacing is examined as well by pair distribution functions ($g(r)$) while all $g(r)$ are normalized with respect to the

In Applications of Molecular Modeling to Challenges in Clean Energy; Fitzgerald, G., et al.;
ACS Symposium Series; American Chemical Society: Washington, DC, 2013.

volume of a hemisphere. When O atoms are within the first nearest neighbor distance of Ti_{5C}-O_a distance distribution (2.5 Å), they are considered as anchor O_a whereas the others should be dangling O_d. Then the pair distribution function of O_a-O_a distance is considered first among all CO_2 molecules on the surface (Figure 7(a)), and this quantity shows the average spacing among CO_2 molecules. For the O_d distribution, the population along the O_d-O_d distance is counted within the first nearest neighboring O_d-O_d pair distribution peak (Figure 7(b)) and this represents the distribution of relative tilting direction of one another. In the case of low coverages such as 1/3 and 1/2 ML, O_a-O_a distribution shows that two neighboring CO_2 molecules reside on next to each other approximately 63 and 75 % of the time, respectively. This implies that CO_2 intermolecular interactions are considerably large even when they are spatially well distributed initially with the binding to surface Ti_{5C} site. Even though there is a free space for CO_2 can visit, they prefer to gather to have a dimer-like configuration due to the CO_2-CO_2 interaction. Regarding O_d-O_d population distribution, a broad feature is shown between one to two Ti_{5C} lattice spacing which corresponds to 2.96~5.92 Å with maximal population near 5 Å. This implies that two neighboring CO_2 molecules prefer to tilt away from each other. At the high coverage, O_a-O_a distribution becomes rigid with one Ti_{5C} lattice distance as expected and O_d-O_d distribution shows sharper peak near 4.5~5.0 Å which is almost the same as the one in lower coverages. The sharper peak indicates the geometric structure is more rigid and in other words, the structure of overall CO_2 molecules becomes crystal-like with each CO_2 azimuthally tilted.

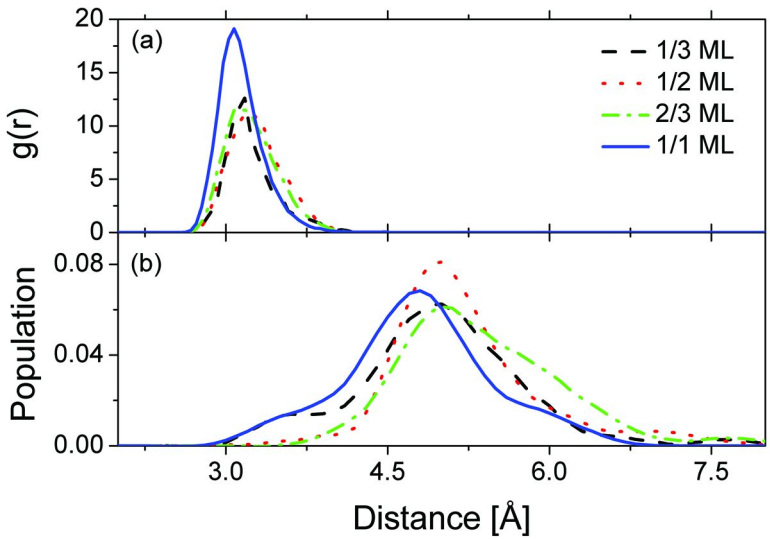

Figure 7. (a) g(r) of O_a in the range corresponding to first nearest neighbor distances. The relative populations by integration are 1:1.27:1.28:1.59 for the coverages of 1/3, 1/2, 2/3 and 1 ML, respectively. (b) The population of the O_d-O_d distance from their corresponding O_a within the range of the first peak from (a).

In Applications of Molecular Modeling to Challenges in Clean Energy; Fitzgerald, G., et al.;
ACS Symposium Series; American Chemical Society: Washington, DC, 2013.

We have investigated so far the dynamic nature of adlayer configurations due to non-negligible interaction among CO_2 molecules comparable to that between CO_2 and TiO_2 surface. Indeed, the quantification of such interactions will provide the physical origin of the interactions. For that reason, the energetics of those two interactions are considered by pair distribution functions ($g(r)$) again for the relevant pairs of interactions. For the interactions among CO_2 molecules, a pair of C of CO_2 and O of another CO_2 (O_C) is taken into account, while another pair of C of CO_2 and bridge bond O from TiO_2 surface (O_b) is considered for the interaction between CO_2 and TiO_2 surface. When considering the first nearest neighbor peak, both types of contact shows at the similar location around 3.0 Å regardless of the coverage and it implies that those two interactions are competitive on the TiO_2 surface. As shown in Figure 8, these pair distribution functions can be converted to potential of mean force (PMF) by $A(r) = -k_BT \ln(g(r))$ which allows us to quantify the magnitude of the interactions between these species. Here k_B is the Boltzmann constant and T is the temperature (*41*). Particularly, 1 ML configuration is focused on since it is expected to be the most ordered and possible maximum interactions should be contained at this coverage. As a result, the binding free energies of CO_2-CO_2 and CO_2-TiO_2 surface are 0.05 eV and 0.06 eV, respectively. Although the strength of those interactions are smaller than typical Ti_{5C}-O_a interaction (ca 0.40 eV) inferred from binding energies, they still should be considered as non-negligible magnitude particularly when they contribute collectively. Comparison of these interactions to the ones in gas phase will provide the physical character of interactions while gas phase interactions are well classified (*30*). There are two typical interactions in gas phase; one is T-shaped quadrupole-quadrupole interaction and the other is slipped parallel dipole-dipole interaction. Those interactions are able to be quantified with binding free energies of 0.06 eV and 0.07 eV respectively, and they are quite similar to currently obtained CO_2-CO_2 and CO_2-TiO_2 surface interactions in both of the magnitude of binding free energy and the interacting configuration.

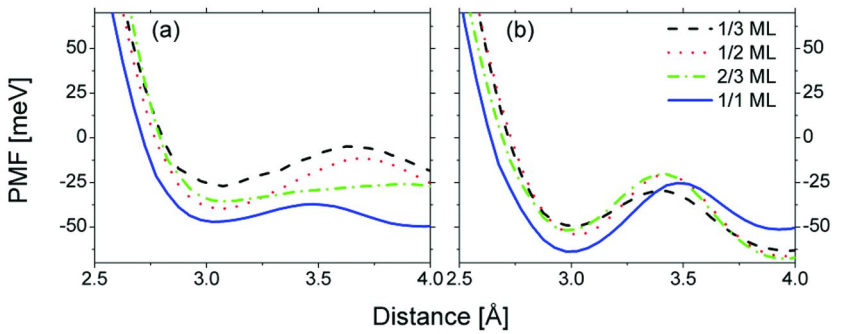

Figure 8. The potential of mean force (PMF) in the range of the first peak from g(r) of (a) C-O_C and (b) C-O_b for the coverages of 1/3, 1/2, 2/3 and 1 ML, respectively.

In Applications of Molecular Modeling to Challenges in Clean Energy; Fitzgerald, G., et al.;
ACS Symposium Series; American Chemical Society: Washington, DC, 2013.

Conclusions

The overall behavior of CO_2 molecules on TiO_2 surface can be summarized as follows. At first, O_V defect sites are the most favorable adsorption sites for CO_2 with the binding energy of 0.60 eV. Additional CO_2 can be stabilized stronger next to O_V bound CO_2 on neighboring Ti_{5C} site and then additional CO_2 molecules start populating on regular Ti_{5C} sites. When CO_2 molecules are adsorbed with low coverage, the isolated CO_2 molecule binds to one of the O atom on Ti_{5C} site while it is tilted toward nearest neighboring O_b row with a binding energy of 0.45 eV. This adsorbed molecule can rotate with a low barrier of 0.05 eV via flat-lying configuration in between two neighboring Ti_{5C} sites. At the same time, this intermediate configuration is able to participate in tumbling of CO_2 to the next Ti_{5C} site with a low barrier of 0.06 eV and further diffusion is possible in the same manner along the Ti_{5C} row.

As the coverage increases, CO_2 molecule tends to be paired with another CO_2 molecule while their configurations are tilted away from each other. At 1 ML coverage, the configuration of each CO_2 molecule is governed by competition between attractive quadrupole-quadrupole interaction and steric repulsion. Note that the CO_2 resided on O_b site is also available with being stabilized by neighboring CO_2 molecules. As a result, the potential energy surface on TiO_2 surface is corrugated in the presence of weak interactions characterized by CO_2 interactions with another CO_2 and TiO_2 surface. In addition, relatively low barriers for CO_2 rotation and diffusion can lead to a partial ordering of molecules at any instance. Extending each configuration to whole ensemble at the same time, the averaged features can show the regular pattern at the high coverage.

In conclusion, the behavior of CO_2 molecule on the TiO_2 surface can be characterized by highly dynamic nature, and the fine structures are generated by the competition of interactions of CO_2 with neighboring CO_2 as well as with TiO_2 surface. The present molecular modeling approach can provide useful information particularly when it is applied to various experimental observations to be collectively interpreted (*7*).

Acknowledgments

The author would like to thank Dr. Roger Rousseau for the helpful discussions and advices on the present study and the preparation of this manuscript. This work is supported by the US Department of Energy (DOE), Office of Basic Science, Division of Chemical Sciences, Geosciences and Biosciences. Pacific Northwest National Laboratory (PNNL) is multiprogram national laboratory operated for DOE by Battelle. A portion of the research was performed using EMSL, a national scientific user facility sponsored by the Department of Energy's Office of Biological and Environmental Research and located at Pacific Northwest National Laboratory.

References

1. Chu, S.; Majumdar, A *Nature* **2012**, *488*, 294–303.

2. Indrakanti, V. P.; Kubicki, J. D.; Schobert, H. H. *Energy Environ. Sci.* **2009**, *2*, 745–758.
3. Roy, S. C.; Varghese, O. K.; Paulose, M.; Grimes, C. A. *ACS Nano* **2010**, *4*, 1259–1278.
4. Freund, H. J.; Roberts, M. W. *Surf. Sci. Rep.* **1996**, *25*, 225–273.
5. *Basic Research Needs: Catalysis for Energy*. http://www.pnl.gov/main/publications/external/technical_reports/PNNL-17214.pdf.
6. Marx, D.; Hutter, J.; Ab Initio Molecular Dynamics: Theory and Implementation. In *Modern Methods and Algorithms of Quantum Chemistry*; Grotendorst, J., Ed.; John von Neumann Institute for Computing Series: Jülich, 2000; Vol. 3, pp 329−477.
7. Lin, X.; Yoon, Y.; Petrik, N. G.; Li, Z.; Wang, Z. T.; Glezakou, V. A.; Kay, B. D.; Lyubinetsky, I.; Kimmel, G. A.; Rousseau, R.; Dohnálek, Z. *J. Phys. Chem. C* **2012**, DOI: 10.1021/jp308061j.
8. Inoue, T.; Fujishima, A.; Konishi, S.; Honda, K. *Nature* **1979**, *277*, 637–638.
9. Pang, C. L.; Lindsay, R.; Thornton, G. *Chem. Soc. Rev.* **2008**, *37*, 2328–2353.
10. Thompson, T. L.; Diwald, O.; Yates, J. T. *J. Phys. Chem. B* **2003**, *107*, 11700–11704.
11. Henderson, M. A. *Surf. Sci.* **1998**, *400*, 203–219.
12. Lee, J.; Sorescu, D. C.; Deng, X.; Jordan, K. D. *J. Phys. Chem. Lett.* **2011**, *2*, 3114–3117.
13. Lee, J.; Sorescu, D. C.; Deng, X. Y. *J. Am. Chem. Soc.* **2011**, *133*, 10066–10069.
14. Tan, S. J.; Zhao, Y.; Zhao, J.; Wang, Z.; Ma, C. X.; Zhao, A. D.; Wang, B.; Luo, Y.; Yang, J. L.; Hou, J. G. *Phys. Rev. B* **2011**, *84*, 155418.
15. Sorescu, D. C.; Lee, J.; Al-Saidi, W. A.; Jordan, K. D. *J. Chem. Phys.* **2011**, *134*, 104707.
16. Acharya, D. P.; Camillone, N.; Sutter, P. *J. Phys. Chem. C* **2011**, *115*, 12095–12105.
17. Dohnálek, Z.; Lyubinetsky, I.; Rousseau, R. *Prog. Surf. Sci.* **2010**, *85*, 161–205.
18. Henderson, M. A. *Surf. Sci. Rep.* **2002**, *46*, 5–308.
19. Diebold, U. *Surf. Sci. Rep.* **2003**, *48*, 53–229.
20. *The CP2K Developers Group*, 2009. http://cp2k.org/.
21. VandeVondele, J.; Krack, M.; Mohamed, F.; Parrinello, M.; Chassaing, T.; Hutter, J. *Comput. Phys. Commun.* **2005**, *167*, 103–128.
22. Lippert, G.; Hutter, J.; Parrinello, M. *Mol. Phys.* **1997**, *92*, 477–487.
23. Perdew, J. P.; Burke, K.; Ernzerhof, M. *Phys. Rev. Lett.* **1996**, *77*, 3865–3868.
24. Goedecker, S.; Teter, M.; Hutter, J. *Phys. Rev. B* **1996**, *54*, 1703–1710.
25. VandeVondele, J.; Hutter, J. *J. Chem. Phys.* **2007**, *127*, 114105.
26. Grimme, S. *J. Comp. Chem.* **2006**, *27*, 1787–1799.
27. Zhang, Z. R.; Rousseau, R.; Gong, J. L.; Kay, B. D.; Dohnálek, Z. *J. Am. Chem. Soc.* **2009**, *131*, 17926–17932.
28. Kwak, J. H.; Rousseau, R.; Mei, D. H.; Peden, C. H. F.; Szanyi, J. *ChemCatChem* **2011**, *3*, 1557–1561.

In Applications of Molecular Modeling to Challenges in Clean Energy; Fitzgerald, G., et al.;
ACS Symposium Series; American Chemical Society: Washington, DC, 2013.

29. Glezakou, V. A.; Rousseau, R.; Dang, L. X.; McGrail, B. P. *Phys. Chem. Chem. Phys.* **2010**, *12*, 8759–8771.
30. Windisch, C. F.; Glezakou, V. A.; Martin, P. F.; McGrail, B. P.; Schaef, H. T. *Phys. Chem. Chem. Phys.* **2012**, *14*, 2560–2566.
31. Henkelman, G; Uberuaga, B. P.; Jonsson, H. *J. Chem. Phys.* **2000**, *113*, 9901–9904.
32. Nosé, S. *J. Chem. Phys.* **1984**, *81*, 511–519.
33. Hoover, W. G. *Phys. Rev. A* **1985**, *31*, 1695–1697.
34. Dudarev, S. L.; Botton, G. A.; Savrasov, S. Y.; Humphreys, C. J.; Sutton, A. P. *Phys. Rev. B* **1998**, *57*, 1505–1509.
35. Borodin, A.; Reichling, M. *Phys. Chem. Chem. Phys.* **2011**, *13*, 15442–15447.
36. Yim, C. M.; Pang, C. L.; Thornton, G. *Phys. Rev. Lett.* **2010**, *104*, 036806.
37. Di Valentin, C.; Pacchioni, G.; Selloni, A. *Phys. Rev. Lett.* **2006**, *97*, 166803.
38. Deskins, A.; Rousseau, R.; Dupuis, M. *J. Phys. Chem. C* **2011**, *115*, 7562–7572.
39. Saharay, M; Balasubramanian, S. *J. Chem. Phys.* **2004**, *120*, 9694–9702.
40. Santoro, M.; Gorelli, F. A. *Chem. Soc. Rev.* **2006**, *35*, 918–931.
41. McQuarrie, D. A. *Statistical Mechanics*; University Science Books: Sausalito, CA, 2000; pp 261−264.

Chapter 5

Periodic Trends in 3*d* Metal Mediated CO_2 Activation

Cong Liu, Thomas R. Cundari, and Angela K. Wilson*

Department of Chemistry and Center for Advanced Scientific Computing and Modeling (CASCaM), University of North Texas, 1155 Union Circle, #305070, Denton, Texas 76203-5017
***E-mail: akwilson@unt.edu**

This chapter reviews our computational studies on 3*d* transition metal catalysts mediated CO_2 activation in consideration of both homogeneous and heterogeneous catalysis. Our homogeneous catalysis studies focused on the catalysis of the reverse water-gas shift (RWGS) reaction and the hydrolysis of CO_2 using 3*d* metal β-diketiminate complexes while the heterogeneous catalysis study considered the reduction of CO_2 to CO on Fe, Co, Ni and Cu surfaces. These systematic studies on 3*d* transition metals showed periodic energetic trends in the catalytic pathways as a function of metal. The correlations and differences between the homogeneous and the heterogeneous catalysis are overviewed and additional chemical insight that has been gained in this effort about the CO_2 binding, charge transfer, and energetics of the hydrolysis of CO_2 is discussed.

Carbon dioxide activation and conversion continue to gain much attention as a result of the alarming reports that link global warming and its potentially devastating effects with the rapidly increasing atmospheric levels of CO_2. An effective solution is to use CO_2 as a renewable resource, *i.e.*, recycle existing CO_2 as a source of carbon for producing useful chemicals, such as CO, which can be used in synthesis gas to produce long chain hydrocarbons in industry via the Fischer-Tropsch reaction (*1*). However, because CO_2 is a highly oxidized, thermodynamically stable compound, its conversion often requires high energy

In Applications of Molecular Modeling to Challenges in Clean Energy; Fitzgerald, G., et al.;
ACS Symposium Series; American Chemical Society: Washington, DC, 2013.

substances or reductive processes. Thus, activation of CO_2 is a challenge to carry out selective reactions on this molecule under mild conditions.

Transition Metals Interacting with CO_2

The interactions between transition metals (TM) and CO_2 have been of great interest in the field of catalytic CO_2 activation, since coordination to TMs is one of the most powerful and universal ways of activating inert molecules. It is important to understand the fundamental information of bonding nature, stereochemistry, and electronic structure of CO_2 with metal centers.

The ground state CO_2 is a $D_{\infty h}$ molecule. Its C-O distance (1.16 Å) is shorter than a sp^2 C-O double bond but longer than a sp C-O triple bond. This is due to the pair of orthogonal π molecular orbitals (π_u bonding orbitals and π_g non-bonding orbitals). The oxygen atoms hold partially negative charges because of the stronger electronegativity, while the carbon atoms have a positive partial charge. With these features, CO_2 exhibits several distinct interactions with potential coordinating centers that have specific electronic structures (*2–5*). Figure 1 shows the most common linkage isomers of CO_2-metal complexes described with molecular orbital (MO) theory.

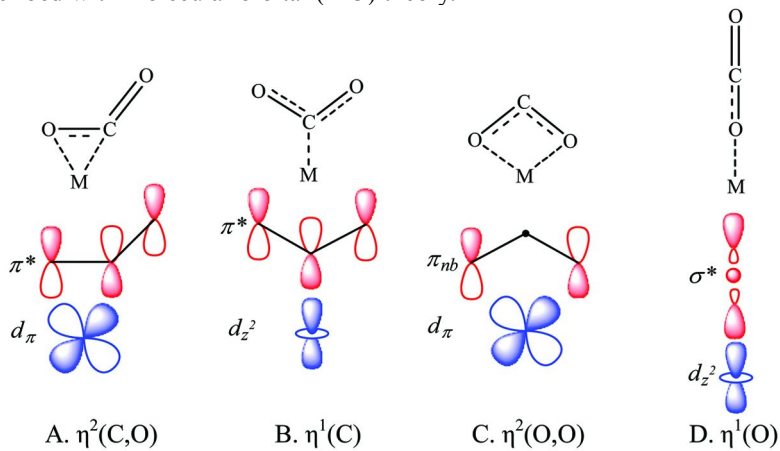

Figure 1. Common linkage isomers of CO_2 interacting with a metal center.

In A (η^2(C,O)), the d_π orbital of the metal center has a π interaction with the anti-bonding π^* orbital of CO_2, while in B (η^1(C)) it is the doubly occupied d_{z^2} orbital of the metal that forms an σ interaction with the π^* orbital of CO_2. The π^* orbital is the LUMO of a ground state CO_2. Coordination of CO_2 results in a net transfer of electron density from the metal center to the LUMO of CO_2 when the coordination occurs via the double bond or the slightly electrophilic carbon atom. Gaining the extra charge from the metal center makes CO_2 molecule a bent structure that is similar to the anion CO_2^- (*2*). X-ray crystal structures of A (η^2(C,O)) and B (η^1(C)) have been reported for metal CO_2 complexes (*6–10*). Linkage isomer C (η^2(O,O)) affords the d_π orbital of the metal center bonding to the non-bonding π orbitals of CO_2, which represent the lone pairs on the two

In Applications of Molecular Modeling to Challenges in Clean Energy; Fitzgerald, G., et al.;
ACS Symposium Series; American Chemical Society: Washington, DC, 2013.

oxygen atoms. This usually requires metal centers that are electrophilic. Finally, in the D (η^1(O)) structure, the d_{z^2} orbital of the metal interacts with the σ* orbital of CO_2, which has higher energy than the π* orbital. In this sense, D (η^1(O)) shows a weaker interaction between the metal center and CO_2 compared to the other linkage isomers.

Catalysis of CO_2 Activation

Studies of transition metal mediated CO_2 activation and conversion have been focused on both homogeneous and heterogeneous catalysis (*11–27*). Homogeneous catalysis usually involves TM complexes, a number of which have been shown to have favorable catalytic properties to activate the C=O bond of CO_2. Some have been chosen by nature: CO_2 reduction to CO can be mediated by enzymes such as nitrogenase (*e.g.*, MoFeP and FeP), and carbon monoxide dehydrogenase (*17*). Other studies have shown that middle to late 3*d* metal complexes have remarkable properties to interact with CO_2. For instance, Isaacs *et al.* (*14*) studied the reduction of CO_2 mediated by Co, Ni and Cu aza-macrocyclic complexes. The electronic spectra showed that CO_2 reduction is mainly due to the presence of a formal 1+ metal, despite the importance of the ligand. In addition, Lu *et al.* (*18*) studied Fe(I)-mediated reductive cleavage and coupling of CO_2; the *tris*(phosphino)borate complex [$PhBP^{CH2Cy3}$] of Fe interacts rapidly with CO_2 at ambient temperature to generate a Fe(μ-CO)(μ-O)Fe complex, and a Fe(μ-η^2:η^2-oxalato)Fe complex. Molecular modeling has helped better understand the reaction mechanism of CO_2-metal complex chemistry. Recently, Ariafard *et al.* (*16*) reported a density functional theory (DFT) study (B3LYP) (*19–22*) of the reductive cleavage of CO_2 using β-diketiminate complex $L^{Me}FeNNFeL^{Me}$; CO_2 inserts into two Fe atoms and then N_2 is released, followed by the cleavage of CO_2 and the formation of a L^{Me}Fe-O-Fe(CO) L^{Me} complex.

In addition to homogeneous catalysis, heterogeneous catalysis of CO_2 activation has received much attention because of its practical applications in industry. Since the 1940s researchers have known that CO_2 in gaseous or aqueous phase is able to interact with TM solid state materials spontaneously. This results in one of the major problems in the oil and gas industry, the CO_2 corrosion of steel (*23*). This might have inspired the chemistry of CO_2 recycling; the adsorption and activation of CO_2 on clean metal surfaces is a topic of considerable interest to solve fundamental issues in the heterogeneous catalysis of CO_2. A number of studies have been focused on 3*d* transition metals, among which iron (*24*), cobalt (*25*), nickel (*26*) and copper (*27*) were found to adsorb/activate CO_2. Computational studies have helped understand the structures and energetics of metal surface/CO_2 chemistry. For instance, Glezakou *et al.* (*28*) reported the mechanism of CO_2 absorption and corrosion on an Fe bcc (100) surface using generalized gradient approximation (GGA) with Perdew-Burke-Ernzerhof (PBE) (*29*) functional, showing that CO_2 is spontaneously activated on a clean Fe(100) surface. In addition, Ding *et al.* (*30*) investigated the adsorption of CO_2 on a Ni(110) surface, via both experimental (temperature-programmed desorption (TPD)) and computational (local spin density approximation (LSDA) and GGA)

In Applications of Molecular Modeling to Challenges in Clean Energy; Fitzgerald, G., et al.;
ACS Symposium Series; American Chemical Society: Washington, DC, 2013.

methods. The calculations suggested that CO_2 weakly binds to Ni(110), and different chemisorbed structures with similar adsorption energies are possible. A recent focus of interest has been comparing catalytic properties on different faces of a metal surface. For example, de la Peña O'Shea *et al.* (*25*) studied CO_2 adsorption on Co(100), (110), and (111) fcc surfaces using GGA methods with the exchange and correlation functional of Perdew and Wang (PW91) (*31*, *32*). According to the calculated reaction energetics, the interaction with CO_2 is surface sensitive; the (110) surface showed the strongest interaction with CO_2 and involves charge transfer from the metal surface to the substrate.

For both homogeneous and heterogeneous catalysis, the studies have shown that in addition to properties like the structures of clusters (*e.g.*, surfaces and frameworks) and ligand effects (*e.g.*, for complexes) that affect the properties of catalysts, the internal chemical properties of the TM elements seem to play a primary role in CO_2 activation. A number of fundamental questions then arise from the rational design of CO_2 catalysts: What is the role of the metal in TM mediated CO_2 activation? Which metal should be chosen? Is there any correlation between heterogeneous and homogeneous CO_2 catalysts? Although several researchers (*18*, *24–27*) have studied CO_2 interaction with either TM surfaces or TM complexes, a paucity of research has focused on the comparison (a) of homogeneous/heterogeneous systems among different metals, or (b) between heterogeneous and homogeneous catalysts. Studies on homogeneous catalysis would help better understand the chemical and mechanistic insights of the reactions, while heterogeneous catalysis supports the majority of industrial processes often lacks these insights due to the innate complexity of the catalytic material. Better understanding the similarities and differences between homogeneous and heterogeneous catalysis using computational techniques can have great contribution to rational design of catalysts, which can ultimately lead to novel industrial processes.

In this chapter, we overview our systematic computational studies of CO_2 activation and reduction using 3*d* TM catalysts, in consideration of both homogeneous and heterogeneous catalysis, based on our earlier work on CO_2 catalysis (*33–35*). Moreover, new calculations have been carried out for this chapter to provide further explanations about CO_2 binding and charge transfer, as well as new chemical insights to the catalysis of the hydrolysis of CO_2. For the homogeneous catalysis, previous studies were focused on the thermodynamics of the component reactions of the reverse water gas shift (RWGS) reaction ($CO_2 + H_2 \rightarrow CO + H_2O$) using β-diketiminate complexes L′M of all 3*d* metals (L′ = β-diketiminate; M = Sc, Ti, V, Cr, Mn, Fe, Co, Ni, Cu and Zn) (*33*, *34*). The hydrolysis of CO_2 is a remaining problem in the previous studies. The homogeneous catalysis leads to a product/intermediate that is a potential catalyst for CO_2 hydrolysis. Thus, a thermodynamic study was carried out for CO_2 hydrolysis using L′Mn, L′Fe, and L′Co complexes. On the other hand, heterogeneous catalysis was focused on CO_2 adsorption and decomposition on Fe, Co, Ni, and Cu(100) surfaces (*35*). In order to explicitly investigate the intrinsic catalytic properties of the 3*d* elements, the energetics were compared among the four different metals, while all the other variables remain the same, *i.e.*, the (100) surface of a face centered cubic (fcc) structure is used for all solid-state

In Applications of Molecular Modeling to Challenges in Clean Energy; Fitzgerald, G., et al.;
ACS Symposium Series; American Chemical Society: Washington, DC, 2013.

simulations. Fe (bcc) and of Co (hcp) were also investigated for the sake of completeness as well as calibration versus literature data.

Computational Details

For the previously reported homogeneous studies (*33*, *34*), the Gaussian 03 (*36*) and 09 (*37*) program packages were used for the homogeneous models. Geometry optimizations and frequency calculations were carried out using the B3LYP functional with aug-cc-pVTZ basis set. Frequency calculations were performed to identify all of the stationary points as minima or transition states and to provide Gibbs free energies at STP in gas phase. The metals in the L′M all have a 1+ formal charge to best coincide with complexes reported by Holland and coworkers (*38–41*). According to our previous studies, continuum solvents effects do not have a remarkable contribution to reaction energies (changes of ~ 0.001 – 0.005 kcal/mol in the reaction energies) (*34*).

For the additional calculations on molecular orbitals and charge transfer of L′M(CO_2) and hydrolysis of CO_2, B3LYP/aug-cc-pVTZ was used for geometry optimization and frequency calculations in Gaussian 09, and all the calculations are at STP in gas phase. Partial charges of L′M(CO_2) were calculated with natural bond orbital (NBO) analysis implemented in Gaussian 09.

For our earlier work on heterogeneous catalysis (*35*), the structures and total energies were determined using plane-wave density functional theory (PW-DFT) calculations within the Vienna *ab initio* Simulation Package (VASP) (*42*, *43*). Spin polarization and dipole corrections were taken into account. The total energy was calculated using the PBE functional (*29*) with a plane wave basis set, whereas the effect of the inner core was considered via the projected augmented wave (PAW) method (*44*). A 550 eV cutoff energy was chosen, and a 5×5×1 *k*-points grid within the Monkhorst-Pack scheme (*45*) was used to sample the Brillouin zone of the surface unit cell. All calculations were done at 0 K. The climbing image nudged elastic band (CI-NEB) (*46–48*) method was used for transition states (TS) and reaction coordinates calculations. TSs were further confirmed through frequency calculations. Bader analysis was carried out to access the charge transfer between the surface and the substrate, using the code developed by Henkelman and coworkers (*49–51*).

Homogeneous Catalysis of Reverse Water-Gas Shift (RWGS) Reaction Using 3*d* TM β-Diketiminate Complexes

Previously, the reaction mechanism (*33*) of RWGS reaction was initially proposed to be five-step catalysis (Figure 2). The first step includes the coordination of a CO_2 molecule (Step **1**). The second step involves breaking the C-O bond of L′M(CO_2) to form L′M(CO) and L′M(O) (Step **2**); this is followed by the hydrogenation of L′M(O) (Step **3**) to generate L′M(H_2O); the last two steps are the release of H_2O and CO products (Step **4** and **5**, respectively) (*33*).

In Applications of Molecular Modeling to Challenges in Clean Energy; Fitzgerald, G., et al.;
ACS Symposium Series; American Chemical Society: Washington, DC, 2013.

Descriptions of Selected Compounds

In the previous study, all four linkage isomers in Figure 1 were taken into account to identify the preferred CO_2 bonding mode. In this chapter, the molecular orbitals were calculated for L′M(CO_2) complexes to provide further explanations for the interaction of CO_2 with the metal center. Linkage A (η^2(C,O) in Figure 1 is predominant in Sc, Ti, V, Cr, Mn, Fe, Co, and Ni complexes. It is notable that in Sc, Ti, and V complexes, the C-O bond of CO_2 moiety has been cleaved due to the strong interaction with the metal center and formed, in effect, an oxo-carbonyl complex (Figure 3, (*33*)). The molecular orbitals of V complex (Figure 4 (a) and (b)), for instance, showed that the interactions of the coordinate O and the carbonyl ligand with the metal center are relatively independent. The 2*p* orbital of the coordinate O overlapped with the d_{z^2} orbital of V and formed an σ interaction (Figure 4 (a)); the carbonyl ligand formed a π interaction with V through its π^* orbital overlapping a d_π of V (Figure 4 (b)). For the Cr, Mn, Fe, Co, and Ni complexes, on the other hand, the metal center and the coordinated C and O kept a triangle shape, as expected (Figure 3, (*33*)). The molecular orbitals of the Co complex (Figure 4 (c)) showed a typical π bonding interaction in most cases: the overlap between the π^* orbital of CO_2 and a d_π orbital of the metal center. This agrees with the bonding orbitals of linkage η^2(C,O) introduced earlier. However, L′Cu(CO_2) and L′Zn(CO_2) prefer conformation C (η^1(O)) (Figure 1); the metal centers ligated to a single oxygen atom of CO_2, which is slightly bent in both complexes (Figure 3, (*33*)). The molecular orbitals of the Zn complex showed that the interaction mainly involves the overlap of the σ^* orbital of CO_2 and the d_{z^2} orbital of the metal center, which is also consistent with the previously introduced η^1(O) linkage (Figure 1).

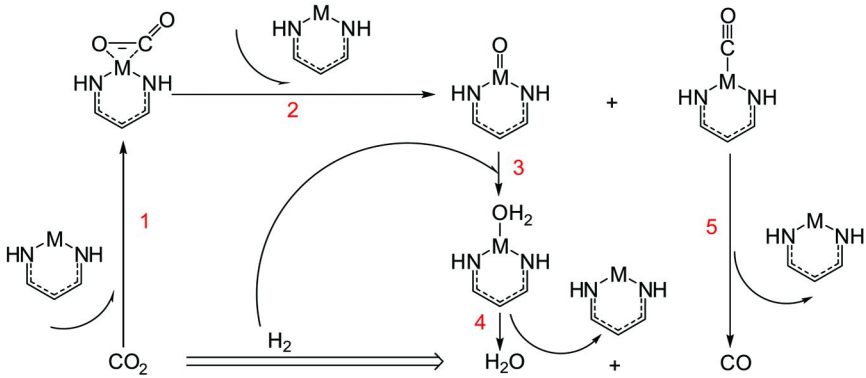

Figure 2. Proposed catalytic cycle of RWGS. (Reproduced with permission from Ref. (33). Copyright 2010 ACS).

In Applications of Molecular Modeling to Challenges in Clean Energy; Fitzgerald, G., et al.;
ACS Symposium Series; American Chemical Society: Washington, DC, 2013.

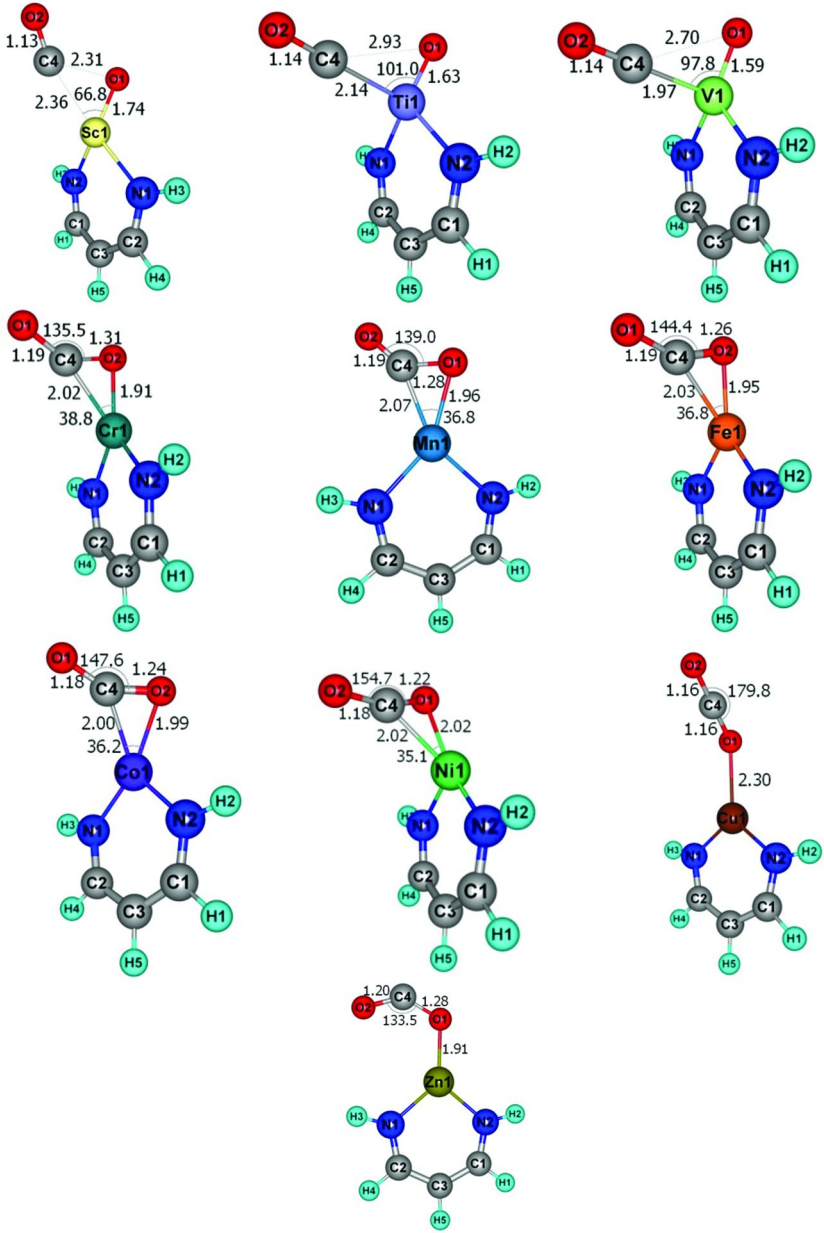

Figure 3. Optimized structures of L'M(CO_2) (Å) (deg). (Adapted with permission from Ref. (33). Copyright 2010 ACS).

In Applications of Molecular Modeling to Challenges in Clean Energy; Fitzgerald, G., et al.;
ACS Symposium Series; American Chemical Society: Washington, DC, 2013.

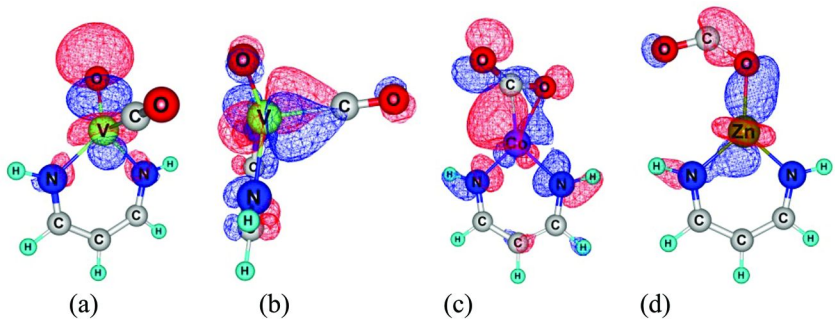

Figure 4. Important bonding orbitals of selected CO_2 complexes. (a) σ bonding between a 2p orbital of the coordinate O and the d_z^2 orbital of V (b) π interaction between the π orbital of CO and a d_π orbital of V (c) π bonding between the π* orbital of CO_2 and a d_π orbital of Co (d) σ bonding between the σ* orbital of CO_2 and the d_z^2 orbital of Zn.*

Thermodynamic Analysis

Previously, the reaction energetics were reported with enthalpies (ΔH), (*33*). In this chapter, the reaction free energies (ΔG) were reported for the convenience of comparisons with later reports (*34*) and new calculations (Figure 5 and Table I). Generally speaking, ΔG of step **1**, coordination of CO_2, becomes more endergonic from Sc to Zn; hence, CO_2 coordination is thermodynamically more favorable for earlier 3*d* series than later metals (Figure 5) (*33*). Step **2**, reduction of CO_2, follows a similar trend as a function of metal; it is exergonic for Sc, Ti, V, Mn, and Fe, while the rest are endergonic (*33*). Thus, CO_2 binding and reduction become increasingly thermodynamically favorable as one traverses from right to left in the 3*d* series (*33*). Nevertheless, in step **3**, the hydrogenation of the oxo complex follows a different energetic trend; the reactions of earlier metal systems tend to be more endergonic than those of later metals (Figure 5) (*33*). For steps **4** and **5**, all the reactions are endergonic as expected for ligand dissociation and the reaction energies do not reveal a remarkable trend as a function of metal (Table I) (*33*). In summary, the thermodynamics suggested that CO_2 binding and reduction are the key discriminating steps for the modeled catalytic cycle for the RWGS reaction (*33*). Earlier 3*d* metals show a thermodynamic preference in these steps; however, later metals are more favorable for the hydrogenation of the oxo complex. In reality, an effective catalytic cycle favors the reaction pathways with smaller energetic fluctuation; any highly endergonic or exergonic step would either create a high barrier or generate a thermodynamic sink, and thus, is not favorable. In this case, Mn, Fe and Co complexes show more favorable thermodynamic profiles than the others by providing smaller fluctuations on the energetic pathways. In other words, the catalytic pathways of Mn, Fe and Co systems are neither highly endergonic nor highly exergonic, which meet the thermodynamic requirement of effective catalysts (Figure 5) (*33*).

In Applications of Molecular Modeling to Challenges in Clean Energy; Fitzgerald, G., et al.;
ACS Symposium Series; American Chemical Society: Washington, DC, 2013.

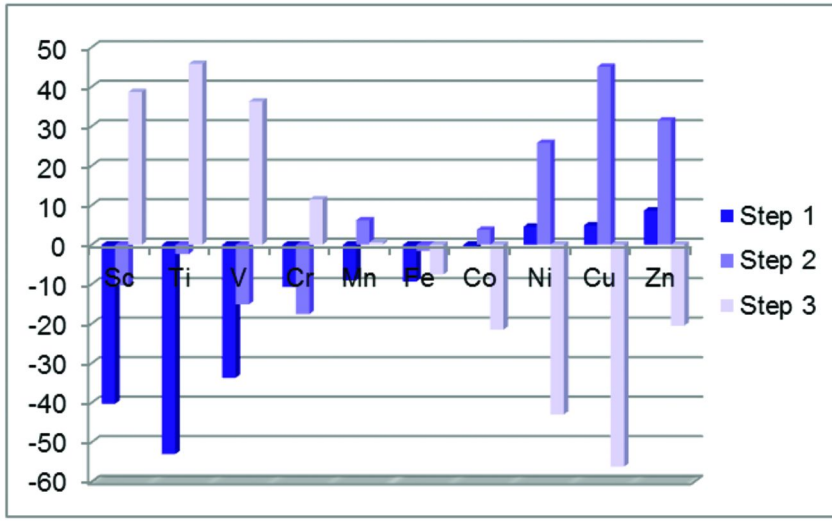

Figure 5. Reaction free energies of steps 1, 2 and 3 for each metal system. (33)

Table I. Calculated ΔG (kcal/mol) of Steps 4 and 5 (298.15K) (*33*)

	Sc	***Ti***	***V***	***Cr***	***Mn***	***Fe***	***Co***	***Ni***	***Cu***	***Cu***
Step 4	9.7	5.2	3.9	5.0	-3.5	3.1	2.6	1.8	-0.7	-6.6
Step 5	13.7	16.0	20.1	23.3	17.2	27.0	27.6	22.2	18.4	-1.6

Reaction Mechanism of the RWGS Reaction Using Middle 3*d* Transition Metal Catalysts L′M (M: Mn, Fe, Co)

Based on the initial investigations (*33*), more detailed studies were reported for the β-diketiminate complexes of Mn, Fe and Co (*34*). Our previous study proposed a reaction pathway including both mono- and bimetallic systems (Figure 6 (*34*)), which was inspired by recent experimental reports from the Peters (*18*) and Holland (*38–41*) groups. Step **A**, coordination of CO_2, forms the L′M(CO_2) complex, which then goes through a transition state (TS) for C-O bond activation to form L′M(CO)(O) (Steps **B** and **C**). Subsequently, L′M(CO)(O) would either release CO to form L′M(O) (Step **D**) or interact with another L′M to generate a bimetallic intermediate complex L′M(CO)OML′ (Step **I**). In Step **D**, the oxo complex L′M(O) may then react with another L′M to form a bimetallic oxide complex (L′M)$_2$O (Step **L**), or react with H_2 and form a L′M(OH) and H radical (Steps **E** and **F**). The species of L′M(OH) and H mixture results in an aqua complex L′M(OH_2) (Step **G**). L′M(OH_2) will release H_2O and yield back the

In Applications of Molecular Modeling to Challenges in Clean Energy; Fitzgerald, G., et al.;
ACS Symposium Series; American Chemical Society: Washington, DC, 2013.

model catalyst (Step **H**). On the other hand, L′M(CO)OML′ may decompose to L′M(CO) and L′M(O) (Step **J**), or just release CO to form $(L'M)_2O$ (Step **K**) that could bind CO_2 and generate a bridging carbonate complex $L'M(CO_3)ML'$ (Step **M**). Combining this with the research from last section, we are able to describe reaction mechanisms and compare the favorability of the various pathways for Fe, Mn and Co catalyst models (*34*).

The previously calculated geometries and spin states (*34*) of $(L'Fe)_2O$ and $L'Fe(CO_3)FeL'$ are in good agreement with the corresponding bulkier β-diketiminate derivatives experimentally characterized by the Holland group (*18*, *38–41*). For instance, $(L'Fe)_2O$ shows similar structure with $(L^{tBu}Fe)_2O$ that was synthesized from $(L^{tBu}FeH)_2$ or $(L^{tBu}FeN)_2$ (*38–41*). It has been reported that $(L^{tBu}Fe)_2O$ reacts with CO_2 rapidly at room temperature and forms a carbonate-diiron complex $L^{tBu}Fe(CO_3)FeL^{tBu}$, which illustrates Step **M** in Figure 6. The structure of $L'Fe(CO_3)FeL'$ in this work is in good agreement with the crystal structure of $L^{tBu}Fe(CO_3)FeL^{tBu}$ (*15*).

Thermodynamic Analysis

From the perspective of monometallic reactions, the kinetics of the whole catalytic process significantly depends on the effective reaction barrier, $\Delta G^{\ddagger}_{eff}$, the Gibbs free energy difference between the highest energy TS (TS-2) and the lowest energy point ($L'M(CO_2)$) that precedes it (Figure 7). In the mono-metallic pathway, L′Mn shows the lowest $\Delta G^{\ddagger}_{eff}$ (38.6 kcal/mol), implying the highest reaction rate. L′Fe has a higher $\Delta G^{\ddagger}_{eff}$ (46.5 kcal/mol) than L′Mn, followed by a much higher $\Delta G^{\ddagger}_{eff}$ for L′Co complexes (50.6 kcal/mol) (*34*). Considering the local reaction barriers, for the C-O bond cleavage (Step **B**, Figure 7), Fe shows the lowest barrier (23.9 kcal/mol), while Mn (38.1 kcal/mol) and Co (35.1 kcal/mol) have much higher barriers. For the hydrogenation of L′M(O) (Step **E**, Figure 7), Mn has a slightly lower barrier (19.0 kcal/mol) than the other two metals (Fe 24.8 kcal/mol; Co 21.0 kcal/mol) (*34*). and Co (13.9 kcal/mol).

One important aspect of the thermodynamics reported previously is to compare the relative energies between mono-metallic and bimetallic systems (*34*). For the Fe system (Table II), for example, all the diiron complexes tend to have much lower energies than the mono-iron systems: the formation of L′Fe(CO)OFeL′ is highly exergonic (Step **I**, ΔG_r = -58.9 kcal/mol) while the cleavage of L′Fe(CO)OFeL′ to L′Fe(O) and L′Fe(CO) is highly endergonic (Step **J**, ΔG_r = 36.5 kcal/mol). At the same time, the formation of $(L'Fe)_2O$ from L′Fe(O) and L′Fe is also highly exergonic reaction (ΔG_r = -71.9 kcal/mol, Step **L**). The relative energies of L′Fe(CO)OFeL′, $(L'Fe)_2O$, and $L'Fe(CO_3)FeL'$ agree quite well with the computational studies by Ariafard *et al.* (*16*). Similar relative energetic trend between the mono-metallic and bimetallic systems were observed for Mn and Co complexes (Table II, (*34*)). In general the bimetallic complexes engender thermodynamic sinks in the reaction pathway and would terminate RWGS catalytic cycle. Thus, one important challenge for realistic homogeneous CO_2 is to avoid dimerization reactions.

In Applications of Molecular Modeling to Challenges in Clean Energy; Fitzgerald, G., et al.;
ACS Symposium Series; American Chemical Society: Washington, DC, 2013.

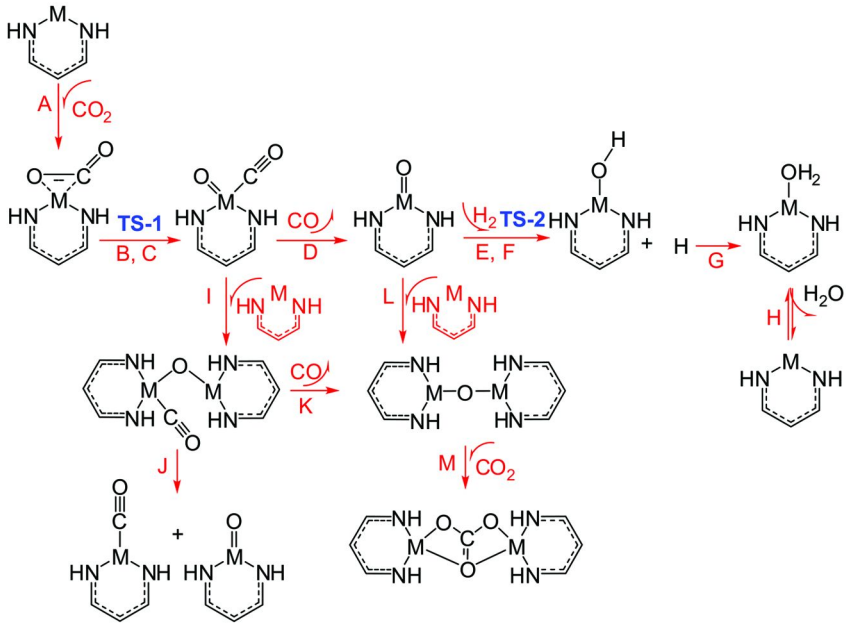

Figure 6. Proposed reaction pathways for RWGS reaction for Mn, Fe and Co systems. (Adapted with permission from Ref. (34). Copyright 2011 ACS)

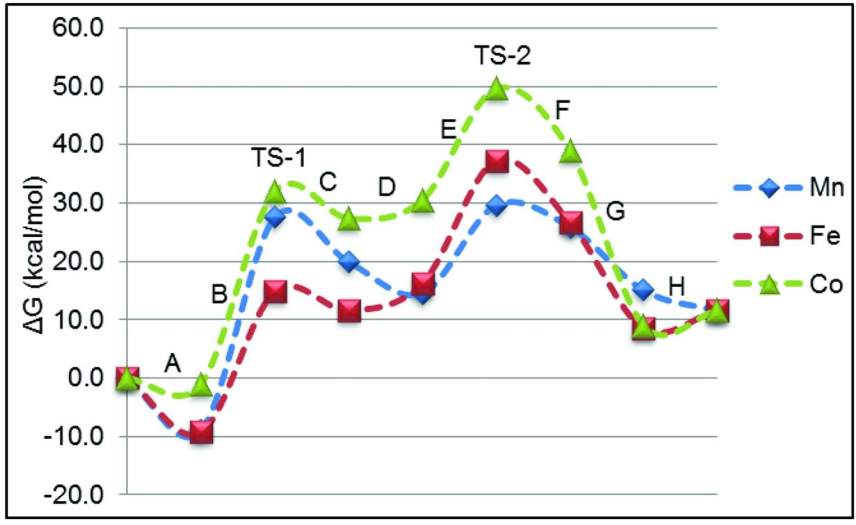

Figure 7. Reaction coordinate of the monometallic RWGS catalysis (34).

Table II. Reaction Free Energies of Bimetallic Reactions (ΔG_r, kcal/mol) (*34*)

	I	*J*	*K*	*L*	*M*
Mn	-69.2	46.6	-6.2	-70.0	-17.0
Fe	-58.9	36.5	-8.4	-71.9	-7.4
Co	-57.5	32.9	-0.4	-61.0	-17.0

One reasonable solution proposed earlier was to modify the β-diketiminate ligand by introducing bulky functional groups, *e.g.*, substituting hydrogens on the nitrogen and carbon atoms of the backbone with bulky groups would prevent the metal centers from interacting with each other (*34*). Another possible solution was to explore heterogeneous reactions. Since metal centers play a significant role in the catalysis, metal surface mediated scission of CO_2 is a possible strategy to avoid dimerization and oligomerization pathways to catalyst inactivation (*34*). We will return to this point later.

Hydrolysis of CO_2 ($CO_2 + H_2O = H_2CO_3$) Mediated by β-Diketiminate Complexes

A remaining question from ref. (*34*) is how CO_2 interacts with the hydroxo hydride complex L′M(OH)(H) transformed from the aqua complex L′M(H_2O). Previous calculations showed that L′M(H_2O) can overcome a barrier of less than 20 kcal/mol to rearrange to L′M(OH)(H) (Figure 8 and Figure 9, Steps **H-1** and **H-2**) (*34*). This hydroxo hydride complex has a great potential to interact with another CO_2 molecule, which leads to a new direction of CO_2 activation, the hydrolysis of CO_2. Transition metal hydroxo complexes interacting with CO_2 has been discovered in biological systems (*52–54*). The carbonic anhydrases are Zn metalloenzymes that catalyze the hydration of CO_2 (*52–56*). The most commonly accepted mechanism is as follows (*52–54*): (1) LZn(H_2O) deprotonation, (2) CO_2 binding to LZn(OH^-), (3) formation of LZn(HCO_3^-), and (4) release of HCO_3^-. Inspired by this mechanism, the catalytic pathway of the hydrolysis of CO_2 using L′M complexes (L′= β-diketiminate, M = Mn, Fe, Co) was proposed in this chapter (Figure 8): Binding of H_2O to L′M (Step $\mathbf{H_{-1}}$) is considered as a reversible reaction because of the small values of reaction energies for the three metal systems (Step **H**, Figure 8). The L′M(OH)(H) rearranged from L′M(H_2O) (Steps **H-1** and **H-2**) first binds to CO_2 through the O on the hydroxo group and forms an adduct (**H-3**). The adduct then transforms to L′M(HCO_3)(H)-1 (Lindkog mechanism, (*55*)) (**H-4**), which then goes through a proton transfer and forms a more stable structure L′M(HCO_3)(H)-2 (Lipscomb mechanism, (*56*)) (**H-5**). The hydrogen on the metal center then transfers to one of coordinate oxygens and forms L′M(H_2CO_3) (**H-6** and **H-7**), which will release H_2CO_3 (**H-8**).

The calculated reaction energies for all three metal systems are shown in Figure 9. Considering local barriers for the two transition states (TS-3 and TS-4), for both of which Fe tends to have the smallest barriers among the three

In Applications of Molecular Modeling to Challenges in Clean Energy; Fitzgerald, G., et al.;
ACS Symposium Series; American Chemical Society: Washington, DC, 2013.

metals. However, Mn and Fe systems showed higher effective barriers (33.5 and 24.5 kcal/mol, respectively) due to the highly stable L′M(OH)(H) leading the reaction coordinate to a thermodynamic sink (**H-2**), while Co showed a relatively small effective barrier (the energy difference between TS-4 and L′M(H_2O), 19.8 kcal/mol). The greater stability of L′Mn(OH)(H) is probably due to the stronger electron donation from the metal center to the coordinate H. In general, Co complex showed the most favorable energetic pathway for the hydrolysis of CO_2. It is interesting that this catalytic trend is opposite to the RWGS reaction, in which Mn showed the lowest effective barrier, followed by Fe and Co. On the other hand, in all cases the Lindkog intermediate (L′M(HCO_3)-1) shows higher energy than the Lipscomb intermediate (L′M(HCO_3)-2). This agrees with previous investigations (*54*, *56*). In summary, based on the calculated thermodynamics, Co and Fe complexes catalyze the CO_2 hydrolysis efficiently; later metals tend to perform better than earlier metals.

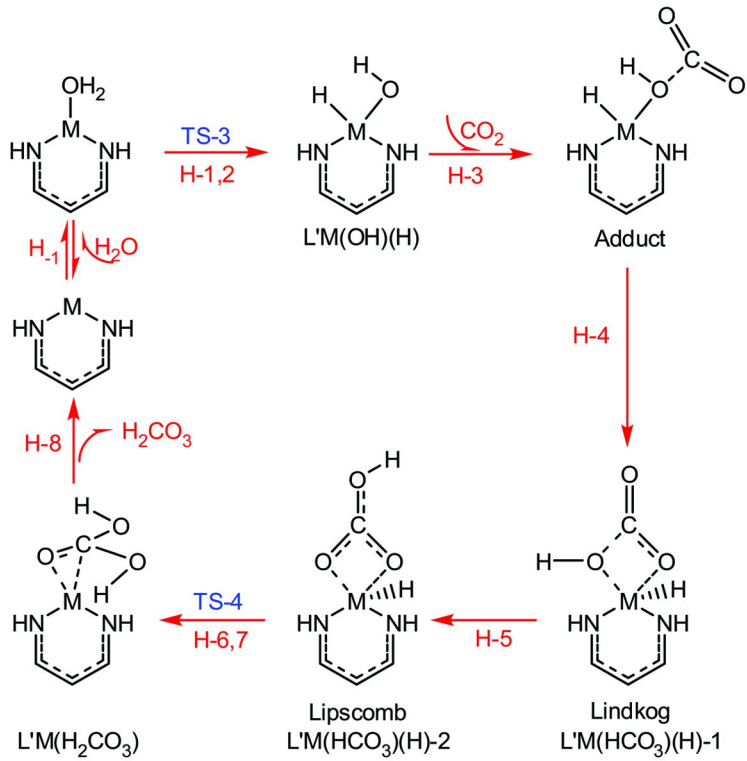

Figure 8. Reaction pathway for the catalysis of CO_2 hydrolysis.

Heterogeneous Catalysis of CO_2 Reduction on TM Surfaces

Transition metal clean surfaces are good candidates to investigate heterogeneous catalysis of CO_2. In this section, previous studies of the catalysis of CO_2 reduction to CO on Fe, Co, Ni and Cu surfaces are summarized (*35*).

In Applications of Molecular Modeling to Challenges in Clean Energy; Fitzgerald, G., et al.;
ACS Symposium Series; American Chemical Society: Washington, DC, 2013.

Surface Models

Our previous study utilized fcc (100) surfaces for Fe, Co, Ni and Cu to investigate the intrinsic catalytic properties of the metal (*35*). However, surfaces derived from the ground state of Fe (bcc), and of Co (hcp) were also studied (*35*). The calculated lattice parameters were in good agreement with the experimental values; the differences are within 0.03 Å (*35*, *57*). A five-layer periodic slab was built with a ~ 10 Å vacuum above the surface. The top three layers of the slab were allowed to relax, while the bottom two layers were fixed. A 3×3 super cell was built, containing nine metal atoms per layer and a total of 45 metal atoms (*35*) in the surface unit cell.

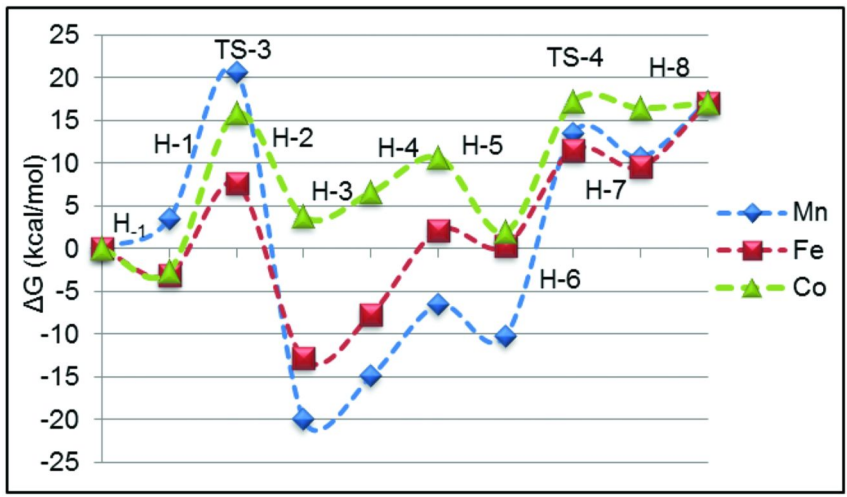

Figure 9. Reaction coordinate for the catalysis of $CO_2 + H_2O = H_2CO_3$ using L'Mn, L'Fe, and L'Co.

CO_2 Adsorption: $M + CO_2 = CO_2/M$

Eight different starting conformations were considered in the previous studies (*35*), and the most stable structures for each metal and selected geometrical parameters are shown in Figure 10. The O-C-O angle is reduced to 120.5 ~ 127.7 degrees, as expected, suggesting a reduction of the CO_2 moiety. In all cases the CO_2 moiety is stabilized on the surface by multiple bonds to surface metal atoms (*35*). On Fe and Co surfaces, O_2 also shows a weaker interaction with the surface besides the carbon and O1, showing a stronger binding of the molecule to the surface, compared to Ni and Cu systems. It is possible that additional energy is necessary to "pull" O2 from the Fe and Co fcc (100) surfaces, and this might increase the kinetic barrier to C-O bond cleavage (*35*). We will return to this point later.

The binding energy changes from a highly negative value (-33.4 kcal/mol) to a positive value (17.3 kcal/mol), as going from Fe to Cu (Table III); a similar energetic trend was obtained for CO_2 binding the surface as for the homogeneous

In Applications of Molecular Modeling to Challenges in Clean Energy; Fitzgerald, G., et al.;
ACS Symposium Series; American Chemical Society: Washington, DC, 2013.

system in the previous section. A positive binding energy for Cu surface suggests that CO_2 could not be stabilized on the Cu fcc (100) surface spontaneously (*35*). CO_2 chemisorbed upon surface generally results in a reduced CO_2. Hence, the valence charge density calculations showed that CO_2 binding on the surface involves a charge transfer from the metal surface toward the CO_2 moiety, which is transformed effectively to a CO_2^- (*35*). In addition, CO_2 adsorption on Fe bcc (100) and Co hcp (1010) surfaces were also investigated previously and the calculated binding energies showed that the structure of a surface has great impact on CO_2 adsorption (*35*).

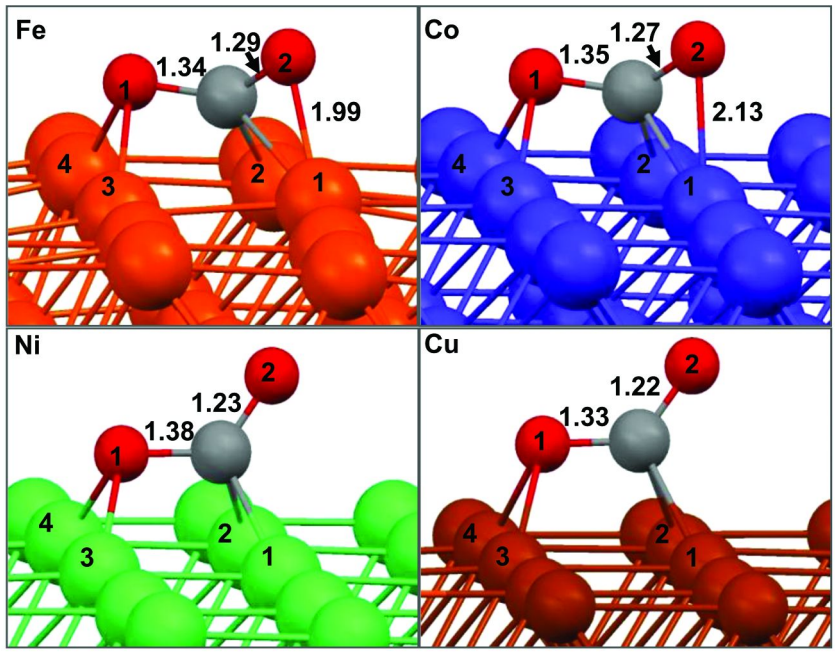

Figure 10. The most favorable calculated binding conformations of CO_2 on fcc (100) surfaces. (Adapted with permission from Ref. (35). Copyright 2012 ACS).

Table III. Calculated Adsorption Energies of CO_2 Species on fcc (100) Surfaces (*35*)

Reaction	*Fe*	*Co*	*Ni*	*Cu*
E_{ads} (kcal/mol)	-33.4	-9.6	-1.1	17.3
ΔE_{dec} (kcal/mol)	-24.1	-22.3	-20.4	-0.6

Decomposition of CO_2: CO_2/M = (CO+O)/M

Binding of CO_2 is followed by breaking the coordinated C-O1 bond, which gives a surface-bound oxygen and a surface-bound CO (*35*). In the (CO+O)/Fe system, the oxygen atom binds to four Fe atoms (four-fold site), whereas the carbon of the CO moiety binds to one Fe atom (*35*). On Co, Ni and Cu surfaces, the oxygen also has a fourfold binding, but the carbon of CO binds to two metal atoms (short-bridge) on Fe surface. As shown in Table III, the Fe (100) system gives the lowest reaction energy (-24.1 kcal/mol), followed by Co (-22.3 kcal/mol), Ni (-20.4 kcal/mol), and Cu (-0.6 kcal/mol) . It is notable that for Fe, Co and Ni (100) surfaces, the reaction energies are very close to each other, although in the first step (CO_2 chemisorption) Fe has a much more negative binding energy than Co, which in turn has a much more negative CO_2 binding energy than Ni (*35*). In other words, Fe does not show remarkable thermodynamic favorability in CO_2 decomposition, possibly due to the stronger interaction of O_2 and the surface in the first step (*35*). Therefore, even though the reaction energies of CO_2 decomposition still follows the similar trend with the binding energies, this may not translate into a lower reaction barrier, *i.e.*, additional energy may need to be consumed for O2 to "escape" from the surface (*35*).

The total reaction barrier (relative to the initial state gas phase energy) for CO_2 reduction on the Fe surface is -6.3 kcal/mol. For Co, Ni and Cu (100) surfaces, the total barriers were calculated to be 3.0, 11.1 and 39.5 kcal/mol, respectively (*35*). In general, the total reaction barriers still keep the same trend with the reaction energies: Fe < Co < Ni < Cu. Moreover, the total barriers ($\Delta E^{\ddagger}$) and the reaction energies ($\Delta E = E_{ads} + \Delta E_{dec}$) follow a linear relationship for the C-O bond scission of CO_2, and the Brønsted-Evans-Polanyi (BEP) relationship was developed: $\Delta E^{\ddagger} = 0.63\Delta E + 26.7$ (kcal/mol) (*35*). This linear relationship could be useful to estimate reaction barriers on other metal surfaces for the C-O bond scission of CO_2. It is also notable that regardless of the lowest total barrier for Fe system, its system falls into a thermodynamics sink, due to the "over-binding" of CO_2, which requires 27.1 kcal/mol energy for CO_2/Fe to climb over the TS; that is much higher than that for Co (12.6 kcal/mol) and Ni (12.2 kcal/mol) (*35*). Therefore, the "over-binding" of O2 of CO_2 greatly impacts the reaction coordinate on the Fe surface as we expected earlier, but not as dramatically for the Co surface. Thus, Co and Ni are more favorable in terms of a smaller fluctuation on reaction energies/barriers of the elementary catalytic steps (*35*).

Desorption of CO: (CO+O)/M = O/M + CO

CO dissociation from Fe, Co and Ni surfaces were reported to be highly endergonic (*35*), which would be a challenge to carry out the catalysis in practice. Future investigations shall be focused on discovering effective approaches such as mixing metal elements (*i.e.*, metal alloy) and applying additional catalysts to reduce the dissociation energy.

Comparison between Homogeneous and Heterogeneous Catalysis

In the previous sections, we discussed the CO_2 activation and reduction mediated by first-row TM homogeneous complexes L′M (L′ = β-diketiminate, M = TM) and solid state surfaces. The mechanism of homogeneous catalysts is quite similar to that on the metal surfaces in terms of CO_2 binding and C-O bond activation (Figure 11) (*35*). Natural bond orbital (NBO) analysis and Bader analysis were carried out for the homogeneous and the heterogeneous systems, respectively (Table IV), for the CO_2 bonded systems (L′M(CO_2) and CO_2/M). In both cases, CO_2 moiety gains more electron density within the earlier metal systems than the later metal systems. Moreover, most of the electron density was transferred towards the carbon atom (except for L′Cu(CO_2), in which the electron density of the carbon atom was reduced). Earlier metal systems tend to have more electrons transferred to the CO_2 moiety than the later metal systems. This trend is consistent with the binding energies.

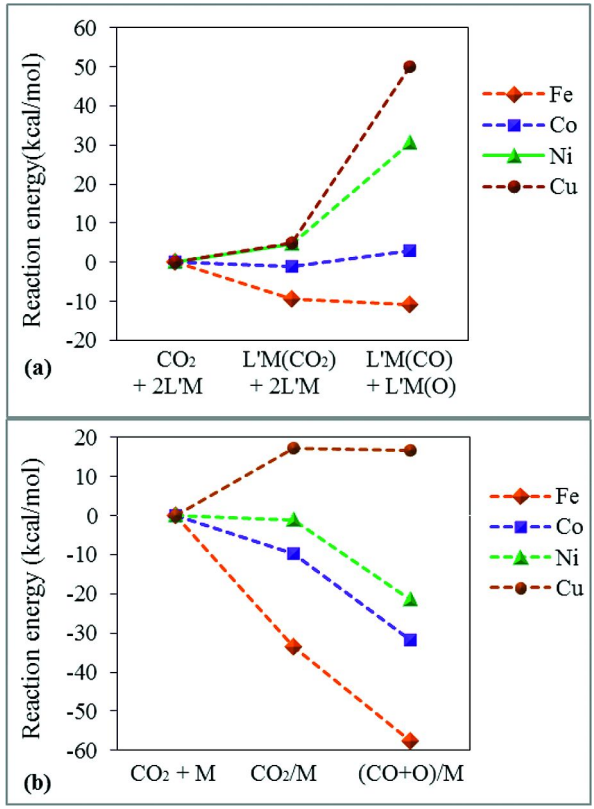

Figure 11. (a) Reaction energies of CO_2 activation by L'M (L = β-diketiminate, M = Fe, Co, Ni and Cu). (b) Reaction energies of CO_2 activation on Fe, Co, Ni and Cu fcc (100) catalysis, indicating that reactions for earlier metals are more exergonic. (Reproduced with permission from Ref. (35). Copyright 2012 ACS).

In Applications of Molecular Modeling to Challenges in Clean Energy; Fitzgerald, G., et al.;
ACS Symposium Series; American Chemical Society: Washington, DC, 2013.

Previously, we have discovered a important correlation between the homogeneous and the heterogeneous catalyst models: an interesting energetic trend was obtained for both, as a function of metal (Figure 11); from the earlier metal Fe to the later metal Cu, reactions tend to be more endergonic (*35*). In other words, earlier 3*d* metals are thermodynamically more favorable in terms of CO_2 binding and C-O bond cleavage than later metals (*35*). This energetic trend could be used to help design new metal catalysts for CO_2 activation in the future.

Table IV. Partial Charges for CO_2 Bonded Systems (NBO Analysis Was Carried Out for the Homogeneous Systems (This Chapter) and Bader Snalysis for the Heterogeneous Systems (*35*))

	O1	*C*	*O2*	*CO_2 moiety*
CO_2	-1.061	2.122	-1.061	0
CO_2/Fe	-1.119	1.018	-1.054	-1.155
CO_2/Co	-1.037	1.086	-1.035	-0.986
CO_2/Ni	-1.020	1.188	-0.971	-0.802
CO_2/Cu	-1.095	1.470	-1.004	-0.629
CO_2	-0.494	0.988	-0.494	0
L′Fe(CO_2)	-0.607	0.727	-0.511	-0.391
L′Co(CO_2)	-0.572	0.756	-0.511	-0.327
L′Ni(CO_2)	-0.545	0.842	-0.484	-0.187
L′Cu(CO_2)	-0.505	1.013	-0.467	0.041

Summary

This chapter reviewed our previous studies (*33–35*) on homogeneous and heterogeneous catalysis of CO_2 activation and conversion using 3*d* metal catalysts in a greater and more profound perspective. For the β-diketiminate 3*d* metal complexes mediated reverse water-gas shift reaction, the CO_2 binding and C-O bond cleavage are thermodynamically more favorable for earlier metals than later metals (*33*). The hydrogenation of L′M(O) by H_2, however, displays a different trend as a function of metal; reactions of the later metal complexes are more exergonic than earlier metal complexes (*33*). The dissociation of H_2O and CO from the coordinated products are all endergonic, and yield no large differences among the metals studied. In general, the middle 3*d* series – Mn, Fe and Co catalysts – show more favorable thermodynamic paths than the other metals, due to the smallest fluctuations on the energetic pathway (*33*). According to the more detailed thermodynamic and kinetic studied were reported for Mn, Fe and Co systems; L′Mn yields the lowest calculated effective reaction barrier, and Fe also shows the lowest local barrier for the C-O bond cleavage (24.1 kcal/mol) (*34*).

In Applications of Molecular Modeling to Challenges in Clean Energy; Fitzgerald, G., et al.;
ACS Symposium Series; American Chemical Society: Washington, DC, 2013.

In addition, catalysis of the hydrolysis of CO_2 by L′Mn, L′Fe and L′Co was investigated (L′ = β-diketiminate). Fe and Co complexes gave feasible thermodynamics. The reaction coordinate showed an opposite energetic trend as a function of metal, compared to C-O activation of CO_2: Co complex gave the lowest $\Delta G^{\ddagger}_{eff}$ (19.8 kcal/mol), followed by Fe (24.5 kcal/mol) and Mn (33.5 kcal/mol). Mn system forms a much more stable L′M(OH)(H) intermediate, leading to an unfavorable thermodynamic sink.

The formation of bimetallic intermediates (*e.g.*, from reaction of L′M(CO)(O), and L′M(O) with the catalyst L′M) during the RWGS catalysis generate thermodynamic sinks that would terminate the catalysis (*34*). Heterogeneous reactions could help reduce the possibility of dimerization reactions. Thus the CO_2 reduction on Fe, Co, Ni, and Cu fcc (100) surfaces were studied (*35*). Calculations showed spontaneous chemisorption of CO_2 and favorable thermodynamic properties for Fe, Co, and Ni surfaces, whereas the Cu surface has only a very weak interaction with CO_2. Reaction energies and total barriers showed an interesting trend as a function of metal: reactions of earlier metals are more exergonic and have lower total barriers than those of later metals (*35*). However, the "over-binding" of CO_2 on Fe surface creates a thermodynamic sink on the reaction pathway. Thus Co and Ni surface systems are considered to have favorable reaction energies and lower barriers (*35*).

Comparison between the homogeneous and the heterogeneous catalysis of CO_2 activation and reduction suggests that a thermodynamic trend applies to both sub-disciplines of catalysis: earlier metal reactions tend to be more exergonic than those of later metals; the metal plays an important role in CO_2 catalysis. This important conclusion provides advice for the rational design of metal catalysts on C-O bond activation of CO_2. In addition, the homogeneous avoids the "over-binding" of CO_2 that happened on the surfaces, while the heterogeneous catalysis is free of dimerization reactions that could happen in the homogeneous catalysis (*35*).

In the massive experimental and computational studies on transition metal mediated small molecule activation and conversion, tremendously little research has been focused on the comparison between homogeneous and heterogeneous catalysis. Discovering the correlations and the differences between homogeneous and heterogeneous catalysis provides significant chemical insights to the intrinsic catalytic properties of transition metals, and helps guide the rational design of promising catalysts.

Acknowledgments

The authors acknowledge the support of the United States Department of Energy (BER-08ER64603) and NSF-CRIF (CHE-0741936) for equipment support. Additionally, the authors acknowledge the UNT Computing and Information Technology Center (CITC) for computing resources.

References

1. Chen, C.; Cheng, W.; Lin, S. *Catal. Lett.* **2000**, *68*, 45.
2. Sakaki, S.; Dedieu, A. *Inorg. Chem.* **1987**, *26*, 3278.
3. Leitner, W. *Coord. Chem. Rev.* **1996**, *153*, 257.
4. Gibson, D. H. *Coord. Chem. Rev.* **1999**, *185-186*, 335.
5. Alcock, N. W. *Bonding and Structure*; Ellis Horwood: London, 1990.
6. Sakamoto, M.; Shimizu, I.; Yamamoto, A. *Organometallics* **1994**, *13*, 407.
7. Ishida, T.; Hayashi, T.; Mizobe, Y.; Hidai, M. *Inorg. Chem.* **1992**, *31*, 4481.
8. Carmona, E.; Munoz, M. A.; Perez, P. J.; Poveda, M. L. *Organometallics* **1990**, *9*, 1337.
9. Carmona, E.; Hughes, A. K.; Munoz, M. Z.; O'Hare, D. M.; Perez, P. J.; Poveda, M. L. *J. Am. Chem. Soc.* **1991**, *113*, 9210.
10. Komiya, S.; Akita, M.; Kasuga, N.; Hirano, M.; Fukuoka, A. *J. Chem. Soc., Chem. Commun.* **1994**, 1115.
11. Isaacs, M.; Canales, J. C.; Aguirre, M. J.; Estiu, G.; Caruso, F.; Ferraudi, G.; Costamagna, J. *Inorg. Chim. Acta* **2002**, *339*, 224.
12. Li, J.; Jia, G.; Lin, Z. *Organometallics* **2008**, *27*, 3892.
13. Lu, C. C.; Saouma, C. T.; Day, M. W.; Peters, J. C. *J. Am. Chem. Soc.* **2006**, *129*, 4.
14. Allen, O. R.; Dalgarno, S. J.; Field, L. D.; Jensen, P.; Turnbull, A. J.; Willis, A. C. *Organometallics* **2008**, *27*, 2092.
15. Sadique, A. R.; Brennessel, W. W.; Holland, P. L. *Inorg. Chem.* **2008**, *47*, 784.
16. Ariafard, A.; Brookes, N. J.; Stranger, R.; Boyd, P. D. W.; Yates, B. F. *Inorg. Chem.* **2010**, *49*, 7773.
17. Walther, D.; Rubens, M.; Rau, S. *Coord. Chem. Rev.* **1999**, *182*, 67.
18. Lu, C. C.; Saouma, C. T.; Day, M. W.; Peters, J. C. *J. Am. Chem. Soc.* **2006**, *129*, 4.
19. Becke, A. D. *J. Chem. Phys.* **1993**, *98*, 5648.
20. Lee, C.; Yang, W.; Parr, R. G. *Phys. Rev. B* **1988**, *37*, 785.
21. Vosko, S. H.; Wilk, L.; Nusair, M. *Can. J. Phys.* **1980**, *58*, 1200.
22. Stephens, P. J.; Devlin, F. J.; Chabalowski, C. F.; Frisch, M. J. *J. Phys. Chem.* **1994**, *98*, 11623.
23. Obuka, N. S. P.; Okoli, N. C.; Ikwu, G. R. O.; Chukwumuanya, E. O. *Int. J. Sci. Technol. Res.* **2012**, *1*, 156.
24. Freund, H.-J. *Surf. Sci.* **1987**, *180*, 550.
25. de la Peña O'Shea, V. A.; González, S.; Illas, F.; Fierro, J. L. G. *Chem. Phys. Lett.* **2008**, *454*, 262.
26. Ding, X.; De Rogatis, L.; Vesselli, E.; Baraldi, A.; Comelli, G.; Rosei, R.; Savio, L.; Vattuone, L.; Rocca, M.; Fornasiero, P.; Ancilotto, F.; Baldereschi, A.; Peressi, M. *Phys. Rev. B* **2007**, *76*, 195425.
27. Wang, G.-C.; Nakamura, J. *J. Phys. Chem. Lett.* **2010**, *1*, 3053.
28. Glezakou, V.; Dang, L. X. *J. Phys. Chem. C* **2009**, *113*, 3691.
29. Perdew, J. R.; Burke, K.; Ernzenhof, M. *Phys. Rev. Lett.* **1996**, *77*, 3865.
30. Ding, X.; Pagan, V.; Peressi, M.; Ancilotto, F. *Mater. Sci. Eng. C* **2007**, *27*, 1355.

In Applications of Molecular Modeling to Challenges in Clean Energy; Fitzgerald, G., et al.;
ACS Symposium Series; American Chemical Society: Washington, DC, 2013.

31. Perdew, J. P.; Chevary, J. A.; Vosko, S. H.; Jackson, K. A.; Pederson, M. R.; Singh, D. J.; Fiolhais, C. *Phys. Rev. B* **1992**, *46*, 6671.
32. Perdew, J. P.; Wang, Y. *Phys. Rev. B* **1992**, *45*, 13244.
33. Liu, C.; Munjanja, L.; Cundari, T. R.; Wilson, A. K. *J. Phys. Chem. A* **2010**, *114*, 6207.
34. Liu, C.; Cundari, T. R.; Wilson, A. K. *Inorg. Chem.* **2011**, *50*, 8782.
35. Liu, C.; Cundari, T. R.; Wilson, A. K. *J. Phys. Chem. C* **2012**, *116*, 5681.
36. Frisch, M. J.; Trucks, G. W.; Schlegel, H. B.; Scuseria, G. E.; Robb, M. A.; Cheeseman, J. R.; Montgomery, J. A., Jr.; Vreven, T.; Kudin, K. N.; Burant, J. C.; Millam, J. M.; Iyengar, S. S.; Tomasi, J.; Barone, V.; Mennucci, B.; Cossi, M.; Scalmani, G.; Rega, N.; Petersson, G. A.; Nakatsuji, H.; Hada, M.; Ehara, M.; Toyota, K.; Fukuda, R.; Hasegawa, J.; Ishida, M.; Nakajima, T.; Honda, Y.; Kitao, O.; Nakai, H.; Klene, M.; Li, X.; Knox, J. E.; Hratchian, H. P.; Cross, J. B.; Bakken, V.; Adamo, C.; Jaramillo, J.; Gomperts, R.; Stratmann, R. E.; Yazyev, O.; Austin, A. J.; Cammi, R.; Pomelli, C.; Ochterski, J. W.; Ayala, P. Y.; Morokuma, K.; Voth, G. A.; Salvador, P.; Dannenberg, J. J.; Zakrzewski, V. G.; Dapprich, S.; Daniels, A. D.; Strain, M. C.; Farkas, O.; Malick, D. K.; Rabuck, A. D.; Raghavachari, K.; Foresman, J. B.; Ortiz, J. V.; Cui, Q.; Baboul, A. G.; Clifford, S.; Cioslowski, J.; Stefanov, B. B.; Liu, G.; Liashenko, A.; Piskorz, P.; Komaromi, I.; Martin, R. L.; Fox, D. J.; Keith, T.; Al-Laham, M. A.; Peng, C. Y.; Nanayakkara, A.; Challacombe, M.; Gill, P. M. W.; Johnson, B.; Chen, W.; Wong, M. W.; Gonzalez, C.; and Pople, J. A.*Gaussian 03*, Revision D.02; Gaussian, Inc.: Wallingford, CT, 2004.
37. Frisch, M. J.; Trucks, G. W.; Schlegel, H. B.; Scuseria, G. E.; Robb, M. A.; Cheeseman, J. R.; Scalmani, G.; Barone, V.; Mennucci, B.; Petersson, G. A.; Nakatsuji, H.; Caricato, M.; Li, X.; Hratchian, H. P.; Izmaylov, A. F.; Bloino, J.; Zheng, G.; Sonnenberg, J. L.; Hada, M.; Ehara, M.; Toyota, K.; Fukuda, R.; Hasegawa, J.; Ishida, M.; Nakajima, T.; Honda, Y.; Kitao, O.; Nakai, H.; Vreven, T.; Montgomery, Jr., J. A.; Peralta, J. E.; Ogliaro, F.; Bearpark, M.; Heyd, J. J.; Brothers, E.; Kudin, K. N.; Staroverov, V. N.; Kobayashi, R.; Normand, J.; Raghavachari, K.; Rendell, A.; Burant, J. C.; Iyengar, S. S.; Tomasi, J.; Cossi, M.; Rega, N.; Millam, J. M.; Klene, M.; Knox, J. E.; Cross, J. B.; Bakken, V.; Adamo, C.; Jaramillo, J.; Gomperts, R.; Stratmann, R. E.; Yazyev, O.; Austin, A. J.; Cammi, R.; Pomelli, C.; Ochterski, J. W.; Martin, R. L.; Morokuma, K.; Zakrzewski, V. G.; Voth, G. A.; Salvador, P.; Dannenberg, J. J.; Dapprich, S.; Daniels, A. D.; Farkas, Ö.; Foresman, J. B.; Ortiz, J. V.; Cioslowski, J.; Fox, D. J. *Gaussian 09*, Revision A.02; Gaussian, Inc.: Wallingford, CT, 2009.
38. Smith, J. M.; Sadique, A. R.; Cundari, T. R.; Rodgers, K. R.; Lukat-Rodgers, G.; Lachicotte, R. J.; Flaschenriem, C. J.; Vela, J.; Holland, P. L. *J. Am. Chem. Soc.* **2006**, *128*, 756.
39. Smith, J. M.; Lachicotte, R. J.; Pittard, K. A.; Cundari, T. R.; Lukat-Rodgers, G.; Rodgers, K. R.; Holland, P. L. *J. Am. Chem. Soc.* **2001**, *123*, 9222.

40. Ding, K.; Pierpont, A. W.; Brennessel, W. W.; Lukat-Rodgers, G.; Rodgers, K. R.; Cundari, T. R.; Bill, E.; Holland, P. L. *J. Am.Chem. Soc.* **2009**, *131*, 9471.
41. Holland, P. L. *Can. J. Chem.* **2005**, *83*, 296.
42. Kresse, G.; Furthmüller, J. *Phys. Rev. B* **1996**, *54*, 11169.
43. Kresse, G.; Hafner, J. *Phys. Rev. B* **1993**, *47*, 558.
44. Blöchl, P. E. *Phys. Rev. B* **1994**, *50*, 17953.
45. Monkhorst, H. J.; Pack, J. D. *Phys. Rev. B* **1976**, *13*, 5188.
46. Ulitsky, A.; Elber, R. *J. Chem. Phys.* **1990**, *92*, 1510.
47. Mills, G.; Jónsson, H.; Schenter, G. K. *Surf. Sci.* **1995**, *324*, 325.
48. Henkelman, G.; Uberuaga, B. P.; Jónsson, H. *J. Chem. Phys.* **2000**, *113*, 9901.
49. Henkelman, G.; Arnaldsson, A.; Jónsson, H. *Comput. Mater. Sci.* **2006**, *36*, 254.
50. Sanville, E.; Kenny, S. D.; Smith, R.; Henkelman, G. *J. Comput. Chem.* **2007**, *28*, 899.
51. Tang, W.; Sanville, E.; Henkelman, G. *J. Phys.: Condens. Matter* **2009**, *21* (084204).
52. Bertini, I.; Luchinat, C.; Maret, W.; Zeppezauer, M., Eds.; *Zinc Enzymes*; Birkhäuser: Boston, 1986.
53. Muguruma, C. *J. Mol. Struct. Theochem* **1999**, *461-462*, 439.
54. Bräuer, M.; Pérez-Lustres, J. L.; Weston, J.; Anders, E. *Inorg. Chem.* **2002**, *41*, 1454.
55. Silverman, D. N.; Lindskog, S. *Acc. Chem. Res.* **1988**, *21*, 30.
56. Liang, J.-Y.; Lipscomb, W. N. *Int. J. Quantum Chem.* **1989**, *36*, 299.
57. Downs, R. T.; Hall-Wallace, M. *Am. Mineral.* **2003**, *88*, 247.

Chapter 6

Bio-Inspired Molecular Catalysts for Hydrogen Oxidation and Hydrogen Production

Ming-Hsun Ho, Shentan Chen, Roger Rousseau, Michel Dupuis, R. Morris Bullock, and Simone Raugei*

Center for Molecular Electrocatalysis, Pacific Northwest National Laboratory, P.O. Box 999, K1-83 Richland, Washington 99352
***E-mail: simone.raugei@pnl.gov**

Recent advances in Ni-based bio-inspired catalysts obtained in the Center for Molecular Electrocatalysis, an Energy Frontier Research Center (EFRC) led by the Pacific Northwest National Laboratory, demonstrated the possibility of cleaving H_2 or generating H_2 heterolytically with turnover frequencies comparable or superior to those of hydrogenase enzymes. In these catalysts the transformation between H_2 and protons proceeds via an interplay between proton, hydride and electron transfer steps, and involves the interaction of a dihydrogen molecule with both a Ni(II) center and pendent amine bases incorporated in six-membered rings, which function as proton relays. These catalytic platforms are well designed in that when protons are correctly positioned (endo) toward the metal center, catalysis proceeds at very high rates. We show here that the proton removal from the molecular catalysts (for H_2 oxidation) and proton delivery to the molecular catalysts (for H_2 production) are often the rate-determining steps. Furthermore, the presence of multiple protonation sites gives rise to reaction intermediates with protons incorrectly positioned (exo relative to the metal center). These isomers are kinetically easily accessible and are detrimental to catalysis because the isomerization processes necessary to convert them to the catalytically competent endo isomers are slow. In this chapter we give an overview of the major findings of our computational investigation of proton relays for H_2 chemistry

In Applications of Molecular Modeling to Challenges in Clean Energy; Fitzgerald, G., et al.;
ACS Symposium Series; American Chemical Society: Washington, DC, 2013.

and provide guidelines for the design of catalysts with enhanced activity.

Introduction

The increased use of energy from intermittent renewable sources such as solar and wind power requires the ability to store the excess energy produced and retrieve it on demand. In this context, electrocatalysts for rapid and efficient interconversion between electrical energy and chemical energy (bonds) will be of critical importance. H_2 production and oxidation are the simplest reactions that can be used for energy storage. Platinum and the hydrogenase enzymes represent excellent catalysts for both reactions. Their use for large-scale applications is, however, problematic. Platinum is a precious metal with high cost and low abundance. Hydrogenase enzymes are remarkably efficient natural catalysts but unreasonably expensive to be obtained in large amounts, and difficult to adapt to large scale commercial applications. These considerations have prompted significant efforts to design molecular catalysts, which employ more abundant metals (*1–3*), such as nickel (*4–14*), cobalt (*15–18*) and iron (*19–23*) as electrocatalysts for the production and oxidation of H_2.

Although impractical for widespread application, hydrogenases continue to provide important insights on H_2 activation by a mono-atomic metal center as well as proton delivery to it. A significant advance in understanding proton movement in hydrogenases was made when the crystal structure of the Fe-Fe hydrogenase revealed a azadithiolate bridge featuring an amine base positioned toward the distal Fe of the catalytic [FeFe] cluster (the so-called H-cluster, Figure 1, left) (*24–26*). In other words, the base is properly positioned to transfer protons to and from the catalytic center. These considerations and others led our laboratory to develop $[Ni(P^R_2N^{R'}_2)_2]^{2+}$ electrocatalysts containing 1,5-diaza-3,7-diphosphacyclooctane ($P^R_2N^{R'}_2$, often referred to as P_2N_2 in this review) ligands that include similarly positioned pendent amines in the second coordination sphere to facilitate proton movement (Figure 1, right) (*27–36*). The pendent amines have been shown to be necessary for the fast rates observed for hydrogen production (turnover frequency, TOF, up to 1850 s^{-1} at 22 °C) (*37*), exceeding those of the Ni-Fe hydrogenase (700 s^{-1} at 30 °C) (*38*). Indeed, pendent amines incorporated into such six-membered ring facilitates heterolytic cleavage or formation of the H-H bond while serving as proton relays for proton transfers in the catalytic oxidation and production of H_2. Catalytic activity for complexes containing so positioned pendent amines occurs at much higher rates and/or lower overpotentials compared to catalysts that have no pendent amines, indicating the critical role of proton relays in lowering barriers for these catalytic reactions (*34*, *35*, *39*). More recently, variants of these catalysts for hydrogen production with formula $[Ni(7P^R_2N^{R'}_2)_2]^{2+}_2$, where $7P^R_2N^{R'}$ stands for the 1-R′-3,6-R derivative of 1-aza-3,6-diphosphacycloheptane, have been shown to overcome some of the limitations of the P_2N_2 ligand platform. $[Ni(7P^{Ph}_2N^{Ph})_2]^{2+}_2$ (Ph = phenyl) catalysts have a TOF of about 100,000 s^{-1} for H_2 production. Catalysts for H_2 oxidation have a significant lower TOF (at most 50 s^{-1} at 22 °C), but still they represent the fastest molecular catalysts available

In Applications of Molecular Modeling to Challenges in Clean Energy; Fitzgerald, G., et al.;
ACS Symposium Series; American Chemical Society: Washington, DC, 2013.

today. Although these mononuclear complexes catalysts feature high TOFs, they suffer from high overpotentials (300 – 600 mV) when compared to hydrogenases. Research efforts are currently aimed at reducing this penalty.

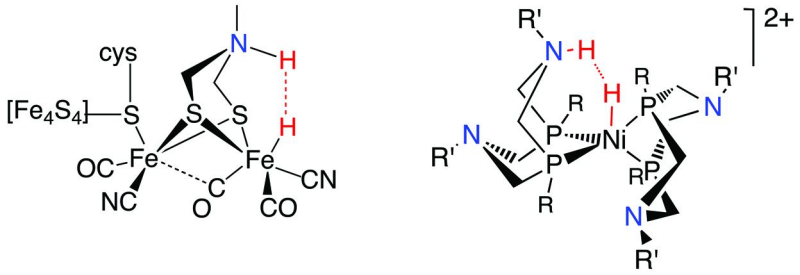

Figure 1. Schematic representation of the proposed transition state structure for the heterolytic H-H bond formation in the active site of the enzyme [FeFe]-hydrogenase (left) and of the [Ni($P^R{}_2N^{R'}{}_2$)$_2$]$^{2+}$ electrocatalyst (right).

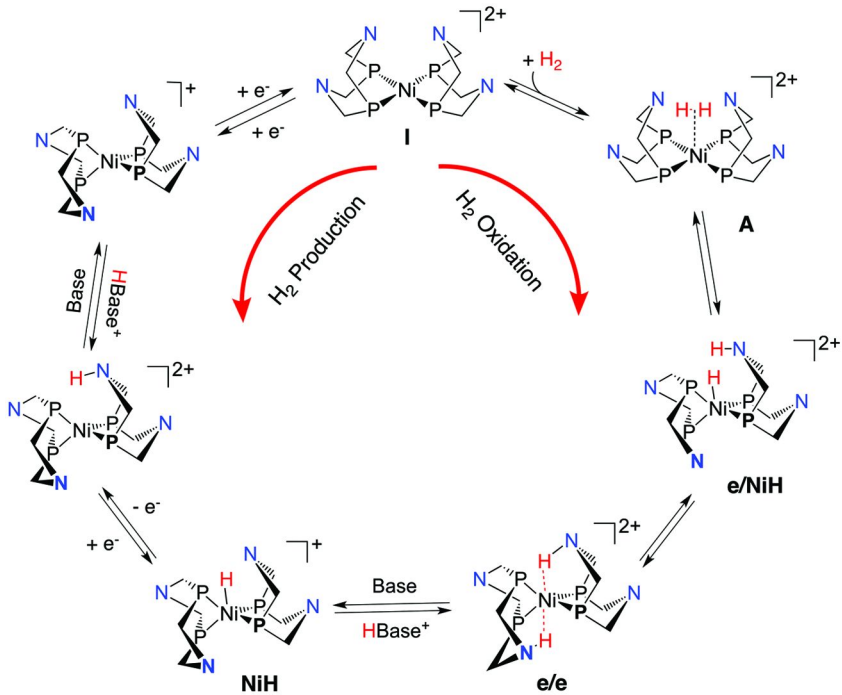

Figure 2. Proposed catalytic mechanism for H_2 oxidation (clockwise) and H_2 production (counter clockwise) by [Ni($P^R{}_2N^{R'}{}_2$)$_2$]$^{2+}$ catalyst family. For clarity the substituents on the P and N atoms are not shown the chemical structures.

In Applications of Molecular Modeling to Challenges in Clean Energy; Fitzgerald, G., et al.;
ACS Symposium Series; American Chemical Society: Washington, DC, 2013.

The catalytic cycle for H_2 oxidation and production by $[Ni(P^R_2N^{R'}_2)_2]^{2+}$ complexes, as the result of an extensive experimental and theoretical investigation, is reported in Figure 2. The computational studies of the catalytic activity of the $[Ni(P^R_2N^{R'}_2)_2]^{2+}$ activity discussed in this chapter show that H_2 oxidation proceeds with the formation of a transient, loosely bound H_2 adduct (**A**), which promptly undergoes heterolytic H_2 splitting with the formation of a N-protonated nickel hydride species (proton/hydride species, **e/NiH**). The latter easily evolves toward a doubly-protonated Ni(0) species (**e/e**). Two proton and electron transfers (or proton-coupled electron transfers) complete the catalytic cycle. H_2 evolution follows the cycle counterclockwise, with the two initial reduction/protonation steps. Probably, in this case, the **e/e** intermediate is not involved but rather catalysis proceeds via the **e/NiH** species only. It will be shown that, during H_2 evolution, the existence of multiple protonation sites gives rise to species with protons not properly positioned, which are detrimental to catalysis.

In this chapter we will review the most important findings of our computational studies of the catalytic activity of the $[Ni(P^R_2N^{R'}_2)_2]_2^{2+}$ platforms (*40–53*) and provide guidance for the design of new platforms with improved performance. We will start discussing the computational philosophy we followed to obtain quantitative information on the activity of these catalysts in solution. Next we will describe the early stages of hydrogen oxidation, which are also the final stages of H_2 production. Then we will focus on protonation/deprotonation events, which, as we will show, represent the most critical steps along the catalytic cycles.

General Computational Philosophy

The computational study of hydrogen oxidation and production requires the modeling of H_2 binding/dissociation, H-H bond breaking and forming, intramolecular proton transfers, (intermolecular) protonation and deprotonation steps and conformational changes. Intramolecular proton transfers and chair/boat conformational changes can be easily described using standard quantum chemistry methodologies based on density functional theory (DFT) and on stationary point searches on the potential energy surface. We have shown that if the catalytic pathways are known, these calculations, complemented by harmonic thermal and entropic corrections to free energy along with a continuum description of the solvent, are adequately accurate, and are therefore employed to describe the energetics of intramolecular processes (*44*, *48*, *49*). In contrast, the modeling of the acid/base reactions required for the intermolecular protonation/deprotonation steps cannot be easily modeled within the standard quantum chemistry computational framework. The major problems encountered regard the calculation of (1) the entropic contribution to the reaction free energy and (2) the activation free energy barrier. Indeed, the complex solvation/desolvation processes underlying the intermolecular protonation and deprotonation steps cannot be easily captured by a stationary point search on the potential energy surface of the reacting system (acid/base and the Ni complex) with a polarizable continuum (PCM) description of the solvent. This is

In Applications of Molecular Modeling to Challenges in Clean Energy; Fitzgerald, G., et al.;
ACS Symposium Series; American Chemical Society: Washington, DC, 2013.

particularly true for large molecular systems, such as those in our research, with strong specific interactions with the solvent, which might be very problematic to be accurately described within PCM theories. Indeed, the inclusion of a few explicit molecules of the solvent is still problematic, as the number (and location) of molecules needed to correctly describe these processes is not known *a priori*. In contrast, molecular dynamics (MD) simulations represent a powerful tool to explore the complex interplay between solvent, acid/base and Ni complex at finite temperature. Therefore, protonation/deprotonation steps were explored via hybrid quantum mechanics/molecular mechanics (QM/MM) simulations (*54*) along with enhanced sampling techniques for free energy calculations (*55*). Ab initio MD was also employed to explore the possible pathways for H_2 binding and splitting and for the intramolecular proton reorganization. Such simulations are computationally demanding and cannot be applied to the study of all of the possible situations these catalysts can display (*e.g.*, different catalyst conformations and the alternative pathways they lead to). Rather, they were performed on selected conformers and reactions and the results extended to the other processes.

The details of the computational procedure employed in our studies are provided at the end of this chapter along with some comments on the accuracy of the DFT calculations performed.

Heterolytic Splitting and Formation of Molecular Hydrogen

H_2 addition to $[Ni(P^R_2N^{R'}_2)]_2^{2+}$ hydrogen oxidation catalysts result in the formation of doubly protonated Ni(0) species. These species are key in the catalysis, and their reactivity will be discussed in detail in the next section. Here we focus on the mechanism of formation of these intermediates during H_2 oxidation and, conversely, their implications to H_2 evolution (*40*, *43*, *49*). In particular we will focus on the following key issues: (1) the number of positioned pendent amines that are needed for optimal catalysis and (2) their role in the thermal H_2 splitting and formation steps.

$[Ni(P^R_2N^{R'}_2)]_2^{2+}$ molecular systems are characterized by a rich conformational space. Each of the four six-membered rings can adopt either a boat or a chair conformation, which yields a total of seven possible conformers. Depending on the type of substituents on the P and N atoms, two or three isomers are nearly iso-energetic and equally probable under ambient conditions. Pendent amines in a ring with a boat conformation are closer to the metal center than pendent amines in a ring with a chair conformation (N to Ni distance of 3.3 Å and 3.8 Å, respectively). Interconversion among isomers is relatively fast, with the barrier for ring inversion being in the range of 7-12 kcal/mol, depending on the substituents. This conformational complexity offers several binding possibilities for the H_2 molecule.

Theoretical modeling was carried out on the $[Ni(P^{Cy}_2N^{Me}_2)_2]^{2+}$ catalyst (Cy = cyclohexyl and Me = methyl) to study the reaction mechanism of the oxidative addition of H_2 for three representative configurations. QM/MM simulations were employed to explore all the possible H_2 binding and splitting pathways at finite

In Applications of Molecular Modeling to Challenges in Clean Energy; Fitzgerald, G., et al.;
ACS Symposium Series; American Chemical Society: Washington, DC, 2013.

temperature. This study revealed that only binding on a side featuring at least one ring in a boat conformation leads to a facile H_2 splitting. This finding confirms the critical role of the pendent amine in the H-H bond breaking. The free energy landscape for the binding and subsequent splitting of H_2 on a side with both pendent amines in a boat conformation is reported in Figure 3. Upon crossing a (mostly entropic) free energy barrier of about 9 kcal/mol (not shown in Figure 3), H_2 binds, forming a (η^2) dihydrogen adduct **A**, which promptly splits according to two pathways. The lowest-energy path (Figure 3, solid line) corresponds to heterolytic splitting of the H-H bonds, which yields a proton-hydride (**e/NiH1**) species where one of the pendent amines is protonated and interacting with the Ni-hydride moiety. The same intermediate can be obtained also via a higher-energy homolytic cleavage (Figure 3, dashed line), which leads to a transient cis-dihydride intermediate (**cH**). The **e/NiH1** intermediate can easily evolve toward a second, slightly higher in energy proton-hydride species, **e/NiH2**, where the Ni-H moiety is oriented toward the other pendent amine nitrogen. The reaction continues toward a lower-energy doubly protonated Ni(0) species (**e/e**), where the two N-H bonds are oriented endo with respect to the metal center. The latter is the experimentally observed product for H_2 addition to $[Ni(P^{Cy}_2N^{Me}_2)_2]^{2+}$.

The reaction pathway when only one pendent amine is in a boat conformation is very similar. H_2 binds to Ni(II), forming a transient dihydrogen adduct, which dissociates following either heterolytic (low-energy) route or a homolytic (high-energy) route. In both cases, a proton-hydride species is obtained. After a very facile rotation of the hydride around the metal center, a doubly protonated Ni(0) complex is finally formed.

In stark contrast, when the H_2 binding occurs to side of the square planar complex with both pendent amines in a chair conformation, H_2 splitting can occur only via a homolytic process, which leads to the formation of a high-energy cis-dihydride ($\Delta G > 20$ kcal/mol). This species, upon migration of the hydrides around the metal center yields, also in this case, to a doubly protonated Ni(0) intermediate.

Refinement of the stationary points with more accurate DFT schemes (see comments in the Appendix) indicates that the overall barrier for H_2 oxidation with the formation of the doubly protonated **e/e** isomer is about 14 kcal/mol, a value that does not depend appreciably on the conformation of the catalyst as long as at least one pendent amine is properly positioned (*i.e.*, in a six-membered ring in a boat conformation).

The same species were found to be involved in H_2 evolution from the doubly protonated intermediate **e/e** of the hydrogen production electrocatalyst $[Ni(P^{Ph}_2N^{Ph}_2)_2]^{2+}$. However, for this complex, the free energy of the proton-hydride **e/NiH** intermediate is systematically lower by about 4 kcal/mol than that of the doubly protonated **e/e** species. The same holds for the mono-protonated species Ni(0), which are systematically higher in energy than the corresponding mono-hydride species. This is likely due to the low pK_a value of the N-H bond compared to that of the Ni-H bond, which favors proton migration from the nitrogen to the metal. This implies that during the catalytic cycle of H_2 production, upon protonation of Ni(0) species or Ni(I) species, the pendent amine accepts a proton from the acid and then relays it to the metal. The calculated barrier for the intramolecular proton transfer is small (7 kcal/mol).

In Applications of Molecular Modeling to Challenges in Clean Energy; Fitzgerald, G., et al.;
ACS Symposium Series; American Chemical Society: Washington, DC, 2013.

The protonation of a second pendent amine leads to the **e/NiH** species, which can easily evolve H_2. These concepts will be further elaborated later on in this chapter.

The analysis of the molecular orbital rearrangement upon Ni complex/H_2 interaction indicates that the pendent amine acts as electron donor interacting with the antibonding σ* orbital of H_2, whereas the metal center accepts the electrons from the σ bond of the H_2. In other words, the metal center and the pendent amine can be viewed as a "frustrated" Lewis acid/base pair (*56–58*).

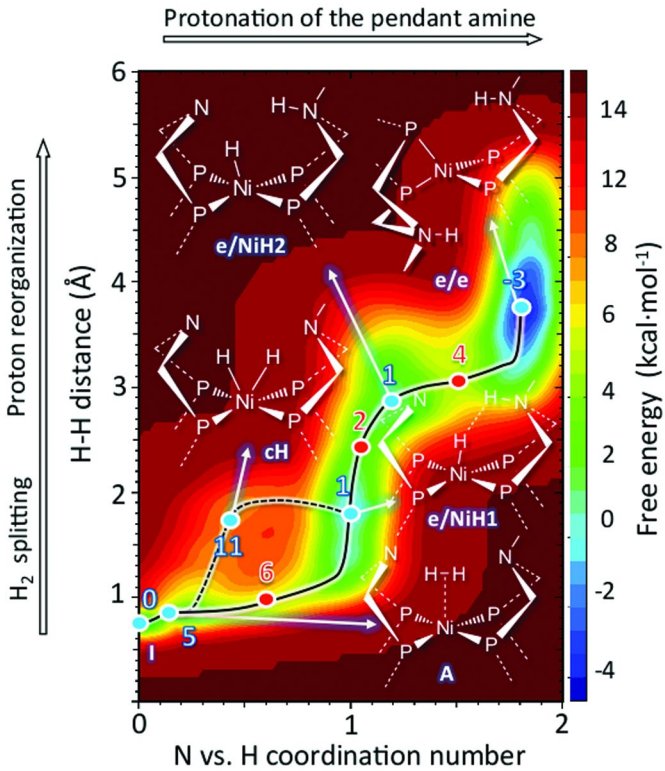

Figure 3. Bi-dimensional projection of the free-energy surface (FES) for the H_2 oxidation by $[Ni(P_2{}^{Cy}N_2{}^{Me})_2]^{2+}$ in acetonitrile as obtained from QM/MM Born-Oppenheimer meta-dynamics molecular dynamics simulations. The reaction coordinate is described in terms of three collective variables: Ni-H_2 distance, HH distance, N/H coordination number (see appendix). Blue dots indicate local minima on the FES, whereas the red dots indicate transition states between them. The corresponding free energy is reported near the symbols. For clarity the 2+ charge on the complexes is not shown in the chemical structures.

In Applications of Molecular Modeling to Challenges in Clean Energy; Fitzgerald, G., et al.;
ACS Symposium Series; American Chemical Society: Washington, DC, 2013.

Thermodynamic Driving Force for H_2 Addition and H_2 Release

In the previous section it was mentioned that the formation of the doubly protonated **e/e** intermediate is exothermic for H_2 oxidation catalysts and endothermic for H_2 production catalysts. There are two key thermodynamics quantities that determine the free energy (ΔG_{H2}) for H_2 addition: the hydride donor ability $\Delta G°_{H}$-, and the pK_a of the protonated pendent amine of the doubly protonated reaction intermediate. Simple thermodynamic considerations (Scheme 1) suggest the $\Delta G°_{H2}$ is the result of a fine balance between $\Delta G°_{H}$- and pK_a (*46*):

$$\Delta G^{o}_{H2} = -\Delta G°_{H}- - 1.364\mathrm{p}K_a + 76.0 \text{ kcal/mol}$$

where 76.0 kcal/mol is the standard free energy for the heterolytic splitting of H_2 in acetonitrile. The higher the hydride donor ability and the lower the basicity of the pendent amine, the larger the $\Delta G°_{H2}$. $\Delta G°_{H}$- is mostly dictated by the twisting angle at the metal center (dihedral angle between the planes identified by the P atoms of each ligand and the Ni atom). Generally the bulkier the substituent on P atom, the more twisted the catalyst is and the smaller $\Delta G°_{H}$- (*34*, *35*, *46*). For instance $\Delta G°_{H}$- decreases along the following series of substituents: R = Ph < Cy < *t*-Bu (*t*-Bu = tert-butyl). In contrast, the pK_a is mostly influenced by the acid/base properties of the parent amine R´-NH_2. The electron withdrawing capabilities of the substituent of the P atoms, R, also contribute to $\Delta G°_{H}$- and pK_a. Changing R and R´ makes it possible to perform fine-tuning of $\Delta G°_{H2}$ and smoothly progress from hydrogen oxidation catalysts to hydrogen production catalysts (Table 1).

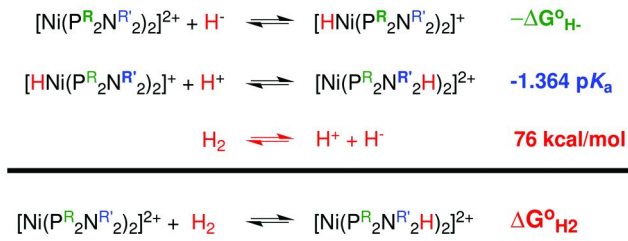

Scheme 1. Thermodynamics cycle for the calculation of the free energy (ΔG_{H2}) for H_2 addition to $[Ni(P^R{}_2N'_2)_2]^{2+}$ complexes.

In Applications of Molecular Modeling to Challenges in Clean Energy; Fitzgerald, G., et al.;
ACS Symposium Series; American Chemical Society: Washington, DC, 2013.

Table 1. Standard Free Energy ($\Delta G°_{H2}$ in kcal/mol) for H_2 Addition to Various $[Ni(P^R{}_2N^{R'}{}_2)_2]^{2+}$ Complexes

R	*R′*	$\Delta G°_{H2}$
Cy	*t*-Bu	-6.0
Cy	Bn	-3.1
Ph	Me	-0.7
Ph	OMe	0.4
Ph	Bn	2.7
Ph	Ph	9.0

Proton Movement and Pendent Amines

Addition of H_2 to a hydrogen oxidation catalyst leads to a Ni^0 complex with two endo (with respect to the metal center) protonated amines, **e/e** (*32*). The computational studies discussed above are able to provide a vivid description of the reaction mechanism. Detailed ^1H, ^{31}P and ^{15}N NMR studies on $[Ni(P^{Cy}{}_2N^{Bn}{}_2H)_2]^{2+}$ (Bn = benzyl) revealed that this doubly protonated **e/e** intermediate isomerizes to other two species, the endo/exo, **e/x**, and exo/exo, **x/x**, isomers (Figure 4) (*8*). The three isomers differ in the orientation of the N-H bonds. Isomer **e/e** has both N-H bonds endo to the nickel, while isomer **x/x** has both N-H bonds exo to the nickel, in a "pinched" (N-H-N) configuration. Isomer **e/x** has a mixed endo-exo geometry.

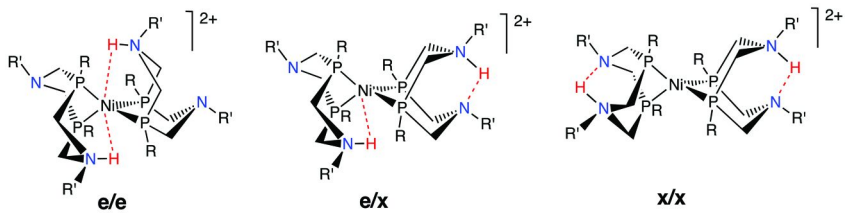

Figure 4. Products of the H_2 addition to $[Ni(P^R{}_2N^{R'}{}_2)_2]^{2+}$ catalysts for H_2 oxidation. Hydrogen bonds are indicated as red dashed lines.

Equilibration was recently monitored using $^{31}P\{^1H\}$ and ^1H EXSY NMR spectroscopy starting from the **e/e** isomer (*42*). At room temperature in deuterated acetonitrile, the **e/e** to **e/x** equilibration is nearly complete after 10 hours, at which time the **x/x** isomer begins to appear. The formation of the **x/x** isomer is much slower, taking over 60 hours to reach equilibrium. The distribution of the three isomers at equilibrium for $[Ni(P^{Cy}{}_2N^{Bn}{}_2H)_2]^{2+}$ is 30% **e/e**, 57% **e/x**, and 13% **x/x**. These findings suggest a stepwise formation of isomers, from **e/e** to **e/x**, then to **x/x**, where protons are sequentially transferred from the interior (endo position) to the exterior (exo position) of the complex. ^1H EXSY experiments unambiguously indicate that isomerization is the result of intermolecular proton transfer. The time to reach equilibrium decreases with the addition of bases. The

In Applications of Molecular Modeling to Challenges in Clean Energy; Fitzgerald, G., et al.;
ACS Symposium Series; American Chemical Society: Washington, DC, 2013.

isomerization rate increases with the strength of the base used: 2,6-dichloroaniline < dimethylformamide (DMF) < aniline (pK_a of the conjugate acids being 5.1 (*59*), 6.1 (*60*), and 10.6 (*59*) respectively). The formation of the **x/x** isomer was ~28 times faster in the presence of 10 equivalents of aniline compared to the rate in CD_3CN alone with no added base. It is important to note that while the isomerization rate increased, the isomer distribution was unaffected by the presence of the bases.

Variable-temperature one-dimensional NMR techniques and two-dimensional EXSY experiments indicate fast intramolecular proton exchange processes for two (*i.e.* **e/e** and **e/x**) of the three experimentally observable isomers of the doubly protonated Ni(0) intermediate (rate constants between 10^4 to 10^5 s^{-1} at 25 °C) (*44*). Theoretical calculations highlighted that endo protons rapidly move from a pendent amine to another, and that this movement is mediated by the metal center. The mechanism of this fast intramolecular proton transfer and of the slower intramolecular proton transfer, which leads to the interconversion between isomers **e/e**, **e/x**, and **x/x** is key to understanding the catalytic activity of these complexes, and offers precious insights on how to improve them. The two processes, and their implication to catalysis, are analyzed below.

Intramolecular Proton Transfer

Theoretical modeling (*44*) showed that endo protonated pendent amines readily transfer a proton to the metal center, forming a N-protonated nickel hydride with one proton on a pendent amine (**NiH**). The hydride can easily rotate around the face of the metal center and move to another pendent amine. Chair/boat interconversions of the six-membered ring containing the pendent amines are necessary to make the overall process happen. Depending of the sequence of proton transfers and chair/boat conformational changes, several different pathways are possible for the intramolecular proton transfer (*i.e.*, isomerization). Up to 10 species can be involved in the intramolecular transfer of a proton from N_a to N_b (Figure 5). Independent of which pathway is chosen, the chair-to-boat interconversion is the rate-limiting step in all cases, a result that was not obvious or anticipated.

The rate constants for the intramolecular proton exchange range from 10^4 to 10^5 s^{-1} at 25 °C, depending on isomer and solvent and, therefore, the process does not represent a bottleneck for catalysis. Computations reproduce these rates in remarkable accord with experiments. The calculated overall activation free energy for the intramolecular proton exchange is 10.7 kcal/mol and 10.2 kcal/mol for the **e/e** and the **e/x** isomer of $[Ni(P^{Cy}_2N^{Me}_2H)_2]^{2+}$, respectively. These values are to be compared to 11.9 kcal/mol and 11.4 kcal/mol provided by NMR measurements on $[Ni(P^{Cy}_2N^{Bn}_2H)_2]^{2+}$.

There is an important message emerging from these studies: when the pendent amine is properly positioned, the proton can be efficiently moved from the Ni to the nitrogen (or vice versa). Due to the rapid intramolecular proton exchange, this family of catalysts for oxidation and production of H_2 may be considered as a metal center "immersed" in a cloud of protons, allowing multiple pathways for subsequent catalytic steps. More generally, the facile transfer of protons between

In Applications of Molecular Modeling to Challenges in Clean Energy; Fitzgerald, G., et al.;
ACS Symposium Series; American Chemical Society: Washington, DC, 2013.

the metal center and positioned bases/acids in the second coordination sphere of these $[Ni(P^{R}_2N^{R'}_2)_2]^{2+}$ complexes provides strong support for similar mechanisms proposed, but not directly observed, in enzymes.

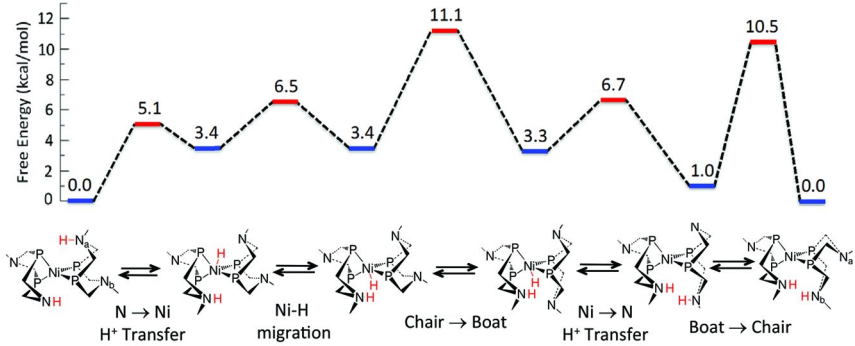

*Figure 5. Intramolecular proton exchange between N_a to N_b in the **e/e** isomer of $[Ni(P^{Cy}_2N^{Me}_2H)_2]^{2+}$. Different nearly equienergetic pathways are possible depending of the sequence of events that take place. For clarity the 2+ charge on the complexes is not shown in the chemical structures.*

Intermolecular Proton Exchange: Proton Delivery and Removal

Moving the proton into solution for catalyst regeneration in the case of H_2 oxidation or from a proton source in solution to the catalysts in the case of H_2 production turns out to be one of the most important catalytic steps. In the $[Ni(P^{R}_2N^{R'}_2)_2]_2^{2+}$ systems, protons can be positioned either endo or exo. Only pendent amines having endo geometry are properly positioned to function efficiently as proton relays during catalysis. The isomers with exo positioned protons are not catalytically active (catalytic trap) and therefore the interconversion to the endo position is necessary for catalytic turnover to occur. Our theoretical work showed that the precise delivery of protons and the rate of protonation/deprotonation are regulated in a nontrivial way by the combination of three factors: steric effects, hydrogen bonding, and electrostatic interactions (*42*).

Experimental evidence strongly suggests that protonation at the exo position is kinetically favored over protonation at the endo position. Consistent with NMR results and electrochemistry measurements, computations indicate that steric hindrance is the major discriminator promoting protonation at the exo site rather than at the endo site. Based on the observation that exo protonation is kinetically favored, isomerization to the catalytically active **e/e** isomer may be an essential process for the majority of the catalyst. Extensive ab initio MD simulations allowed us to unravel the mechanism for the isomerization (Figure 6). In the presence of a base such as aniline, isomerization involves several steps. The detailed mechanism for isomerization is discussed in great detail elsewhere (*42*). Briefly, isomerization requires the initial formation of a hydrogen-bonded complex between a given isomer and the base. This association is then followed by a sequence of steps, whose order depends on the starting isomer (**e/e**, **e/x**, or

In Applications of Molecular Modeling to Challenges in Clean Energy; Fitzgerald, G., et al.;
ACS Symposium Series; American Chemical Society: Washington, DC, 2013.

x/x) and deprotonation site (endo or exo). These steps include the conformational change of one of the six-membered rings of the ligand, such as boat-chair conversions, *inter*molecular proton transfers and *intra*molecular proton transfers mediated by the metal center. The reaction pathway connecting the two isomers is uphill to generate the **NiH** intermediate for the **e/e** ⇆ **e/x** isomerization or to generate the exo mono proton species **x** for the **e/x** ⇆ **x/x** isomerization (Figure 6). Each step contributes to the overall free energy barrier. The most important steps for the **e/e** ⇆ **e/x** isomerization are shown in Figure 7. As can be seen, for both endo and exo deprotonation (protonation), the dissociation of the protonated base (*i.e.*, anilinium) and its re-association during the re-protonation stage, constitute the largest barriers to the overall process (Figure 7, second reaction of each panel). These barriers are primarily due to strong hydrogen bonding interactions for the dissociation and electrostatic repulsion between anilinium and the monocationic species **NiH** or **x** for the re-protonation reaction. In addition, the association of both aniline and anilinium to the endo position is further disfavored with respect to the more accessible exo position (Figure 7, first reaction). The origin of this steric penalty for binding to the endo position is in the larger structural distortion required to form the association complex at the endo site compared to the exo site. As a result, the interconversion of the **e/x** isomer and the **NiH** intermediate is faster in both directions than the interconversion of the **e/e** isomer and the **NiH** intermediate. The difference in steric accessibility of the endo and exo sites is the principal cause of the different reactivity.

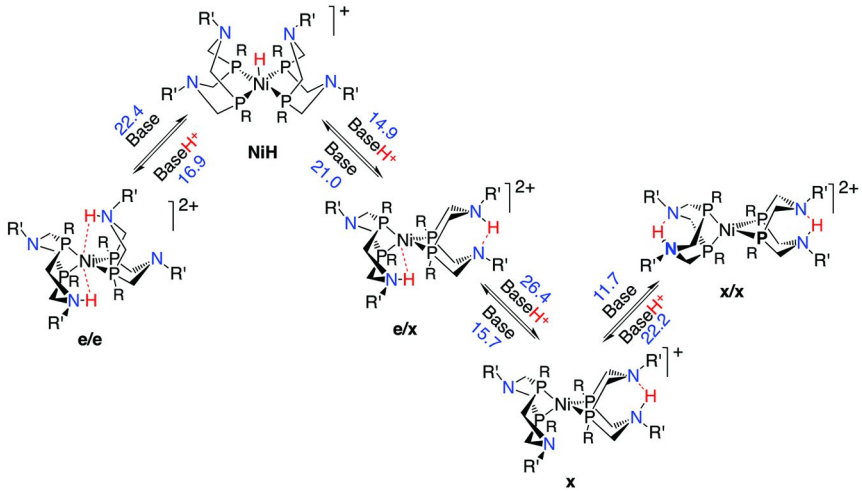

Figure 6. Schematic representation of the isomerization ***e/e*** ⇆ ***e/x*** ⇆ ***x/x*** *in the presence of base. The numbers on the arrows indicated the overall activation free energy (in kcal/mol) in the direction of the arrow for* $[Ni(P^{Cy}{}_2N^{Me}{}_2)_2]_2^{2+}$ *in acetonitrile with aniline as a base. Only the major species involved in the isomerization are reported in the scheme: the actual* ***e/e*** ⇆ ***e/x*** *isomerization involves 7 elementary steps, whereas the* ***e/x*** ⇆ ***x/x*** *isomerization involves 5 elementary steps for a total of 12 steps.*

In Applications of Molecular Modeling to Challenges in Clean Energy; Fitzgerald, G., et al.;
ACS Symposium Series; American Chemical Society: Washington, DC, 2013.

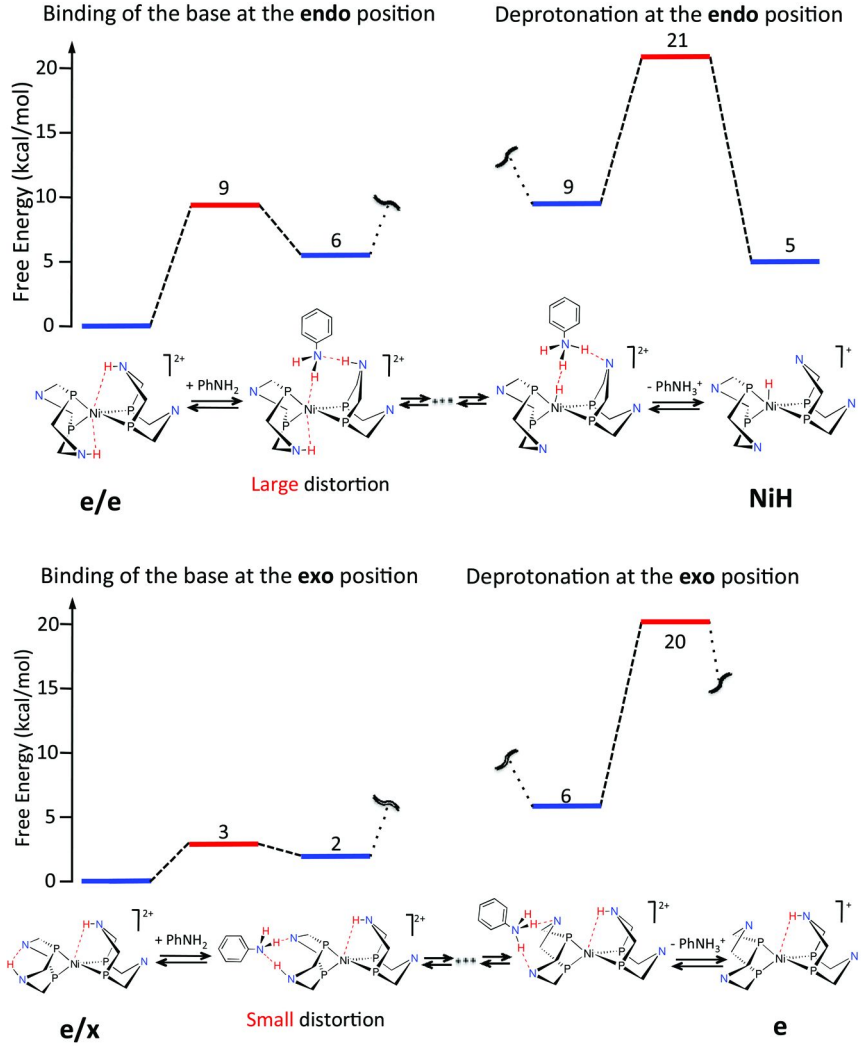

Figure 7. Energetics of the key steps for the ***e/e*** *⇆* ***e/x*** *isomerization of [Ni(P*$_2^{Cy}$*N*$_2^{Me}$*H)*$_2$*]*$^{2+}$ *by aniline in acetonitrile. Top panel: deprotonation at the endo side; bottom panel: deprotonation at the exo side. For clarity the substituents on the P and N atoms are not shown in the chemical structures.*

Proton Delivery and Catalysis

Based on the analysis reported above, we can elaborate the catalytic mechanism reported in Figure 2 by considering the possibility of both endo and exo protonation. The extended mechanism illustrated in Figure 8 can be proposed. Here we assume that hydrogen production (counterclockwise direction) starts by the reduction of Ni(II) to Ni(I), followed by either endo or exo protonation of the Ni(I) complex, as it is the case for the most of H_2 oxidation catalysts developed

in our group. A similar mechanism holds if Ni(II) is pre-protonated first. In the present section, using this extended catalytic cycle, we discuss the implications of the above mechanistic results to catalysis.

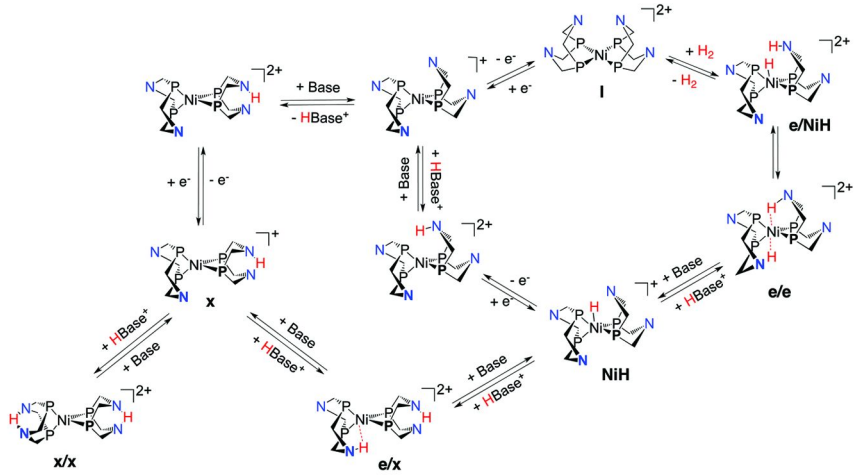

*Figure 8. Mechanism of hydrogen oxidation (clockwise direction starting from **I**) and production (counter-clockwise direction starting from **I**). Protonation of exo positions results in branching to less productive pathways. The two possible exo protonated isomers (i.e. **e/x** and **x/x**) have to undergo deprotonation/protonation step in order to rejoin the main catalytic cycle via the mono hydride species (**NiH**). For clarity the substituents on the P and N atoms are not shown in the chemical structures.*

Hydrogen Production

Protonation at the exo position is kinetically favored over protonation at the endo site, as predicted by our theoretical modeling. This finding suggests that the product of the two protonation steps plus and the two electron transfer steps is the **x/x** isomer. Experimentally it is not possible to isolate the protonation products of the H_2 evolution catalysts, as they quickly evolve toward the release of molecular hydrogen (*12*). To mimic the hydrogen production conditions, protonation studies of the reduced form $[Ni(P^{Cy}_2N^{Bn}_2)_2]^0$ of a catalyst for H_2 oxidation were carried out. These experiments showed that the **x/x** isomer is indeed the only protonation product (*42*). The build-up of the **x/x** isomer has been observed in the protonation of the hydrogen production catalyst, $[Ni^0(P^{Ph}_2N^{Bn}_2)_2]$, at low temperature (*61*). As a whole, these results suggest that a large fraction of the catalyst has to undergo isomerization before H_2 production can occur. Therefore, during catalysis for H_2 production, a large fraction of the catalyst exists as **x/x** isomer, which requires isomerization to the **e/e** isomer prior to H_2 elimination. We have shown that isomerization from the **x/x** isomer to the **e/x** isomer and then to the **e/e** isomer is slow. Therefore this required isomerization process must considerably reduce the catalytic efficiency.

In Applications of Molecular Modeling to Challenges in Clean Energy; Fitzgerald, G., et al.;
ACS Symposium Series; American Chemical Society: Washington, DC, 2013.

It is important to point out that for hydrogen evolution catalysts that endo monoprotonated Ni(0) species rapidly isomerize to form Ni(II) hydride species, **NiH** (*40*, *44*, *51*, *52*). The calculation results suggest that the **NiH** species is more stable than the corresponding N-mono protonated species by at least 6-7 kcal/mol. Of course, no such intramolecular isomerization for the **x** species is available. Protonation of the **NiH** yields directly endo protonated hydride, **e/NiH**, and the corresponding exo protonated Nickel hydride instead of the corresponding (far less stable) doubly protonated **e/e** and **e/x** species.

Finally, our simulations also indicate that protonation in general can be rate-determining in hydrogen evolution. This is supported by the experimental observation that the rate of H_2 production strongly depends on type of acid employed (*12*, *13*, *48*).

Hydrogen Oxidation

The **e/e** isomer is the kinetic product of H_2 addition for $[Ni(P^{Cy}_2N^{Bn}_2)_2]^{2+}$ and other $[Ni(P^{Cy}_2N^{R}_2)_2]_{2+}$ complexes (*8*, *48*), and, as was discussed in the previous section, the deprotonation from the endo position is a high energy process. Using aniline as a base, the calculated barrier to deprotonation at the endo site of $[Ni(P^{Cy}_2N^{Me}_2H)_2]^{2+}$ is 21.4 kcal/mol, and 17.2 kcal/mol for $[Ni(P^{Cy}_2N^{Bn}_2H)_2]^{2+}$ based on NMR spectroscopy. These barriers are similar to the overall barrier (around 15 - 16 kcal/mol) for H_2 oxidation as determined from the measured TOFs for $[Ni(P^{Cy}_2N^{tBu}_2)_2]^{2+}$, $[Ni(P^{Cy}_2N^{Bn}_2)_2]^{2+}$, and $[Ni(P^{Cy}_2N^{Me}_2)_2]^{2+}$ using significantly stronger bases (*10*, *44*, *48*). Similar to H_2 production catalysis, different maximum TOFs are observed depending on the base used, where rates obtained with *n*-butylamine are faster than those with *t*-butylamine (*62*). This supports the idea that steric accessibility of the endo site may also limit the rate of deprotonation, which, in turn, may limit catalytic rates for H_2 oxidation.

Conclusions

In this chapter we have reviewed some of the most important results of our studies on the role of pendent amines incorporated in the second coordination shell of Ni/diphosphine electrocatalysts for H_2 oxidation and production. The simplicity of these catalysts with their similarity to the active site [FeFe]-hydrogenase enzyme provides also an opportunity to investigate proton movement to and from the metal at a molecular level, with implications for both enzymatic systems and organometallic catalysts involved in multi-proton and multi-electron reactions.

Our investigation revealed that the H_2 binding and splitting are a relatively facile processes when H_2 binding takes place on a side of the distorted square planar Ni(II) complex featuring positioned pendent amines, *i.e.*, located in a boat conformation of a six-membered ring. The calculated barrier for the oxidative addition of H_2 to $[Ni(P^{Cy}_2N^{Me}_2)_2]^{2+}$ is about 14 kcal/mol, and it does not depend appreciably on the particular conformation of the catalysts. Only one positioned pendent amine is required for the process, as there is no apparent energetic benefit derived from the presence of a second positioned amine group. The lowest free

In Applications of Molecular Modeling to Challenges in Clean Energy; Fitzgerald, G., et al.;
ACS Symposium Series; American Chemical Society: Washington, DC, 2013.

energy splitting pathway involves a transient dihydrogen adduct, proton-hydride intermediates, **e/NiH**, and doubly protonated Ni(0) species, **e/e**. A higher energy pathway via a dihydride intermediate is also possible. The latter is only accessible when both rings on the binding side are in a chair conformation.

The production of H_2 by $[Ni(P^R_2N^{R'}_2)_2]^{2+}$ involves the same species discussed above for the H_2 oxidation, but is exothermic from **e/e** to the dihydrogen complex **A** (Figure 2). Most likely the species **e/e** is never involved, rather catalysis proceeds trough the intermediate **e/NiH** only. The H_2 formation step is characterized by the association of the acidic proton at the pendent amine and the hydridic hydrogen at the metal center. The pendent amines are able to efficiently shuttle protons toward and from the metal center.

Proton delivery to the catalysts from a proton source in solution in the case of H_2 production and proton removal from the catalysts by a base have been shown to be high barrier processes. In particular the barrier (> 10 kcal/mol) for protonation is considerably higher than the barrier for H_2 formation from **e/NiH** (about 7 kcal/mol). Therefore proton delivery is likely rate determining for H_2 evolution. In the case of H_2 oxidation, proton removal and H_2 binding and splitting have similar barriers and, depending on the catalysts and the conditions, one can prevail over the other.

The positioning of the protons is crucial for catalysis. In particular only *endo* protonation of the pendent amines leads to H_2 evolution. We have shown that protonation at the *exo* position is sterically favored over the *endo* position (*63*). This leads to the formation of pinched doubly protonated intermediates, which are detrimental to catalysis because these species are unable to facilitate proton removal or delivery to the metal center (*64*). It therefore becomes crucial to properly direct the protons into the *endo* position. On the basis of these findings, new catalytic platforms have been proposed where only one pendent amine per phosphine ligand is present (*65*). These catalysts do not lead to exo pinched protonated intermediates and feature remarkably high turnover frequencies (> 100,000 s^{-1}), although they suffer from very high overpotentials (> 500 V) (*65*). How to reduce the overpotential is the focus of current work.

Acknowledgments

This research was carried out in the Center for Molecular Electrocatalysis, an Energy Frontier Research Center funded by the U.S. Department of Energy, Office of Science. Pacific Northwest National Laboratory is operated for the U.S. Department of Energy by Battelle. Computational resources were provided at W. R. Wiley Environmental Molecular Science Laboratory (EMSL), a national scientific user facility sponsored by the Department of Energy's Office of Biological and Environmental Research located at Pacific Northwest National Laboratory, the National Energy Research Scientific Computing Center (NERSC) at Lawrence Berkeley National Laboratory, and the Jaguar supercomputer at Oak Ridge National Laboratory (INCITE 2008-2011 award supported by the Office of Science of the U.S. DOE under Contract No. DE-AC0500OR22725).

Appendix: Computational Details

In this appendix we provide a brief description of the computational methodology employed to study the activity of the $[Ni(P^R_2N^{R'}_2)_2]^{2+}$ catalytic platforms. A more detailed discussion of the various computational protocols is provided elsewhere (*40*, *43*, *44*, *49*). In the last section of the appendix, we will discuss some issues related to the accuracy of the quantum chemical calculations performed.

QM/MM Simulations

Possible reaction channels for H_2 binding and dissociation as well as binding and dissociation of a base and the conjugate acid to the Ni-catalyst were calculated via ab initio QM/MM Born-Oppenheimer metadynamics molecular dynamics simulations (*54*, *66*, *67*). The Ni catalyst, H_2, the base or its conjugate acid were treated at the QM level, whereas the solvent was described using an empirical potential (*68*). Simulations were performed in the density functional theory (DFT) framework with a PBE functional level (*69*, *70*), augmented with Grimme's correction for the dispersion energy (PBE+D2) (*71*). The van der Waals interaction between the QM atoms and the solvent was calculated using Lennard-Jones potentials.

The metadynamics technique (*66*, *67*) was employed to obtain the free-energy profile for the binding and dissociation of aniline and anilinium as well the intermolecular proton transfer steps. Metadynamics is an adaptive biasing potential technique, which disfavors configurations that have been already explored, and consequently favors situations that would have been poorly explored thermally. The bias can be applied to any quantity (generally indicated as a collective variable) describing the process being studied. Various collective variables were employed. Depending on the process studied, we used distances (*e.g.*, H-H bond distance, base/catalyst distance), coordination numbers (*e.g.*, number of protons on the pendent amine or the external base), or more complex variables to describe conformational changes of the complex during catalysis. To increase the sampling efficiency, a variant of metadynamics called multiple-walker metadynamics (*66*) has been employed (*72*), where 20 replicas of the system ("walkers") are propagated in time, all contributing to the exploration of the free energy surface defined by a given set of collective variables.

All of these simulations were performed with using the CP2K package (*73*).

Molecular Electronic Structure Calculations

Structures of all of the possible conformers for the various species found with QM/MM simulations were refined using molecular DFT calculations using the B3P86 hybrid functional (*74*, *75*) along with the Stuttgart-Dresden relativistic effective core potential and associated basis set (SDD) for Ni (*76*), and 6-31G* for all non-metal atoms with additional *p* polarization function on H_2 molecule (*77*). As discussed in the next section, this level of theory has been shown to describe the Ni-based H_2 chemistry with semi-quantitative accuracy compared to

In Applications of Molecular Modeling to Challenges in Clean Energy; Fitzgerald, G., et al.;
ACS Symposium Series; American Chemical Society: Washington, DC, 2013.

coupled cluster CCSD(T) calculations, within 5 kcal/mol for relative energetics of intermediates and transition states (*78*). Harmonic vibrational frequencies were calculated at the optimized structures using the same level of theory to estimate the zero-point energy (ZPE) and thermal contributions (T = 298K and P = 1 bar) to the gas-phase free energy. Solvation free energies were then computed using a self-consistent reaction field model at the same level of theory as for the other steps. The Continuum Polarizable Conductor Model (*79*, *80*) was used with Bondi radii (*81*). These calculations were carried out with Gaussian 03 (*82*), Gaussian 09 (*83*) and NWChem (*84*, *85*).

Assessment of Quantum Mechanical Theories

We carried out an extensive assessment of the best level of theory in terms of accuracy and computational speed (*49*). The energetics (not the free energy) from various DFT GGA (*e.g.* PBE, BLYP, BP86) and hybrid functionals (*e.g.*, B3P86, B3LYP) were compared to post-Hartree-Fock calculations, such as MP2 and CCSD[T] methods. Benchmark calculations on the model complex $[Ni(P^{Me}{}_2N^{Me}{}_2)_2]^{2+}$ demonstrated that PBE (*86*, *87*) and B3P86 (*74*, *75*) results are in qualitative accord with CCSD(T) calculations, with B3P86 providing a generally better agreement. In contrast, the celebrated B3LYP (*75*, *88*, *89*) functional (widely used for studying organometallic chemistry) predicts the formation of the **e/e** isomer upon H_2 addition to be slightly endothermic, whereas the more accurate methods show the reaction to be strongly exothermic. An important consideration regards the ionic character of the bond breaking process, which suggests that the self-interaction error often associated with unpaired electrons and often seen in the description of bond breaking is small and consequently hybrid functionals, which include a fraction of the Hartree-Fock (HF) exchange, do not offer substantial accuracy advantages.

MP2 theory and DFT are often believed to offer a comparable level of accuracy, even though exceptions have been reported (*90*), notably when involving 3*d* transition metals. The systems of interest here offered a catastrophic breakdown of this 'rule' as MP2 was found to be strikingly incorrect. The HF level of theory yields the doubly protonated intermediate **e/e** considerably higher (+60 kcal/mol) in energy than the dihydrogen adduct **A**. In contrast MP2 gives a highly exothermic process (-110 kcal/mol). This is in contrast with CCSD(T), which yields a small (-7.2 kcal/mol) exothermicity for the overall reaction. The catastrophic behavior of MP2 is seen for the dihydride Ni(IV) species and the di-proton Ni(0) species, both of these states are electron rich at the Ni site. The latter state is formally a d^{10} configuration of the Ni atom, which is poorly described by the reference closed-shell HF single determinant.

In Applications of Molecular Modeling to Challenges in Clean Energy; Fitzgerald, G., et al.;
ACS Symposium Series; American Chemical Society: Washington, DC, 2013.

References

1. Le Goff, A.; Artero, V.; Jousselme, B.; Tran, P. D.; Guillet, N.; Métayé, R.; Fihri, A.; Palacin, S. *Fontecave Sci.* **2009**, *326*, 1384.
2. *Catalysis without Precious Metals*; Bullock, R. M., Ed.; Wiley-VCH: Weinheim, 2010.
3. Yang, J. Y.; Bullock, R. M.; Rakowski DuBois, M.; DuBois, D. L. *MRS Bull.* **2011**, *36*, 39.
4. Helm, M. L.; Stewart, M. P.; Bullock, R. M.; DuBois, M. R.; DuBois, D. L. *Science* **2011**, *333*, 863.
5. Appel, A. M.; Pool, D. H.; O'Hagan, M.; Shaw, W. J.; Yang, J. Y.; Rakowski DuBois, M.; DuBois, D. L.; Bullock, R. M. *ACS Catal.* **2011**, *1*, 777.
6. Yang, J. Y.; Bullock, R. M.; Dougherty, W. G.; Kassel, W. S.; Twamley, B.; DuBois, D. L.; Rakowski DuBois, M. *Dalton Trans.* **2010**, *39*, 3001.
7. Wilson, A. D.; Fraze, K.; Twamley, B.; Miller, S. M.; DuBois, D. L.; Rakowski DuBois, M. *J. Am. Chem. Soc.* **2008**, *130*, 1061.
8. Wilson, A. D.; Shoemaker, R. K.; Miedaner, A.; Muckerman, J. T.; DuBois, D. L.; Rakowski DuBois, M. *Proc. Natl. Acad. Sci. U.S.A.* **2007**, *104*, 6951.
9. Fraze, K.; Wilson, A. D.; Appel, A. M.; Rakowski DuBois, M.; DuBois, D. L. *Organometallics* **2007**, *26*, 3918.
10. Wilson, A. D.; Newell, R. H.; McNevin, M. J.; Muckerman, J. T.; Rakowski DuBois, M.; DuBois, D. L. *J. Am. Chem. Soc.* **2006**, *128*, 358.
11. Wiese, S.; Kilgore, U. J.; DuBois, D. L.; Bullock, R. M. *ACS Catal.* **2012**, *2*, 720.
12. Kilgore, U.; Roberts, J.; Pool, D. H.; Appel, A.; Stewart, M.; Rakowski DuBois, M.; Dougherty, W. G.; Kassel, W. S.; Bullock, R. M.; DuBois, D. L. *J. Am. Chem. Soc.* **2011**, *133*, 5861.
13. Kilgore, U. J.; Stewart, M. P.; Helm, M. L.; Dougherty, W. G.; Kassel, W. S.; DuBois, M. R.; DuBois, D. L.; Bullock, R. M. *Inorg. Chem.* **2011**.
14. Smith, S. E.; Yang, J. Y.; DuBois, D. L.; Bullock, R. M. *Angew. Chem., Int. Ed.* **2012**, *51*, 3152.
15. Jacques, P.-A.; Artero, V.; Pécaut, J.; Fontecave, M. *Proc. Natl. Acad. Sci. U.S.A.* **2009**, *106*, 20627.
16. Berben, L. A.; Peters, J. C. *Chem. Commun.* **2010**, *46*, 398.
17. Wiedner, E. S.; Yang, J. Y.; Dougherty, W. G.; Kassel, W. S.; Bullock, R. M.; Rakowski DuBois, M.; DuBois, D. L. *Organometallics* **2010**, *29*, 5390.
18. Jacobsen, G. M.; Yang, J. Y.; Twamley, B.; Wilson, A. D.; Bullock, R. M.; Rakowski DuBois, M.; DuBois, D. L. *Energy Environ. Sci.* **2008**, *1*, 167.
19. Chen, J.; Vannucci, A. K.; Mebi, C. A.; Okumura, N.; Borowski, S. C.; Swenson, M.; Lockett, L. T.; Evans, D. H.; Glass, R. S.; Lichtenberger, D. L. *Organometallics* **2010**, *29*, 5330.
20. Tard, C.; Pickett, C. J. *Chem. Rev.* **2009**, *109*, 2245.
21. Ott, S.; Kritikos, M.; Åkermark, B.; Sun, L.; Lomoth, R. *Angew. Chem., Int. Ed.* **2004**, *43*, 1006.
22. Chong, D.; Georgakaki, I. P.; Mejia-Rodriguez, R.; Sanabria-Chinchilla, J.; Soriaga, M. P.; Darensbourg, M. Y. *Dalton Trans.* **2003**, 4158.

23. Mejia-Rodriguez, R.; Chong, D.; Reibenspies, J. H.; Soriaga, M. P.; Darensbourg, M. Y. *J. Am. Chem. Soc.* **2004**, *126*, 12004.
24. Nicolet, Y.; Lemon, B. J.; Fontecilla-Camps, J. C.; Peters, J. W. *Trends Biochem. Sci* **2000**, *25*, 138.
25. Nicolet, Y.; Piras, C.; Legrand, P.; Hatchikian, C. E.; Fontecilla-Camps, J. C. *Structure* **1999**, *7*, 13.
26. Peters, J. W.; Lanzilotta, W. N.; Lemon, B. J.; Seefeldt, L. C. *Science* **1998**, *282*, 1853.
27. Fraze, K.; Wilson, A. D.; Appel, A. M.; Rakowski DuBois, M.; DuBois, D. L. *Organometallics* **2007**, *26*, 3918.
28. Jacobsen, G. M.; Shoemaker, R. K.; McNevin, M. J.; Rakowski DuBois, M.; DuBois, D. L. *Organometallics* **2007**, *26*, 5003.
29. Jacobsen, G. M.; Yang, J. Y.; Twamley, B.; Wilson, Aaron D.; Bullock, Morris; DuBois, M. R.; DuBois, D. L. *Energy Environ. Sci.* **2008**, *1*, 167.
30. Wilson, A. D.; Fraze, K.; Twamley, B.; Miller, S. M.; DuBois, D. L.; Rakowski DuBois, M. *J. Am. Chem. Soc.* **2008**, *130*, 1061.
31. Wilson, A. D.; Newell, R. H.; McNevin, M. J.; Muckerman, J. T.; Rakowski DuBois, M.; DuBois, D. L. *J. Am. Chem. Soc.* **2006**, *128*, 358.
32. Wilson, A. D.; Shoemaker, R. K.; Miedaner, A.; Muckerman, J. T.; DuBois, D. L.; DuBois, M. R. *Proc. Natl. Acad. Sci. USA* **2007**, *104*, 6951.
33. Yang, J. Y.; Bullock, R. M.; Shaw, W. J.; Twamley, B.; Fraze, K.; DuBois, M. R.; DuBois, D. L. *J. Am. Chem. Soc.* **2009**, *131*, 5935.
34. Rakowski DuBois, M.; DuBois, D. L. *Acc. Chem. Res.* **2009**, *42*, 1974.
35. Rakowski DuBois, M.; DuBois, D. L. *Chem. Soc. Rev.* **2009**, *38*, 62.
36. DuBois, D. L.; Bullock, R. M. *Eur. J. Inorg. Chem.* **2011**, *17*, 1017.
37. Kilgore, U.; Roberts, J.; Pool, D. H.; Appel, A.; Stewart, M.; Rakowski DuBois, M.; Dougherty, W. G.; Kassel, W. S.; Bullock, R. M.; DuBois, D. L. *J. Am. Chem. Soc.* **2011**, *133*, 5861.
38. Frey, M. *ChemBioChem* **2002**, *3*, 153.
39. Rakowski DuBois, M.; DuBois, D. L. In *Catalysis without Precious Metals*; Bullock, R. M., Ed.; Wiley-VCH: Weinheim, 2010.
40. Raugei, S.; Chen, S.; Ho, M.-H.; Ginovska-Pangovska, B.; Rousseau, R. J.; Dupuis, M.; DuBois, D. L.; Bullock, R. M. *Chem.−Eur. J.* **2012**, *18*, 6493.
41. Lense, S.; Ho, M. H.; Chen, S. T.; Jain, A.; Raugei, S.; Linehan, J. C.; Roberts, J. A. S.; Appel, A. M.; Shaw, W. *Organometallics* **2012**, *31*, 6719.
42. O'Hagan, M.; Ho, M.-H.; Yang, J. Y.; Appel, A. M.; DuBois, M. R.; Raugei, S.; Shaw, W. J.; DuBois, D. L.; Bullock, R. M. *J. Am. Chem. Soc.* **2012**, *134*, 17.
43. Dupuis, M.; Chen, S.; Raugei, S.; DuBois, D. L.; Bullock, R. M. *J. Phys. Chem. A* **2011**, *115*, 4861.
44. O'Hagan, M.; Shaw, W. J.; Raugei, S.; Chen, S.; Yang, J. Y.; Kilgore, U. J.; DuBois, D. L.; Bullock, R. M. *J. Am. Chem. Soc.* **2011**, *133*, 14301.
45. Jain, A.; Lense, S.; Linehan, J. C.; Raugei, S.; Cho, H.; DuBois, D. L.; Shaw, W. J. *Inorg. Chem.* **2011**, *50*, 4073.
46. Chen, S.; Rousseau, R.; Raugei, S.; Dupuis, M.; DuBois, D. L.; Bullock, R. M. *Organometallics* **2011**, *30*, 6108.

47. Wiedner, E. S.; Yang, J. Y.; Chen, S.; Raugei, S.; Dougherty, W. G.; Kassel, W. S.; Helm, M. L.; Bullock, R. M.; Rakowski DuBois, M.; DuBois, D. L. *Organometallics* **2011**, *31*, 144.
48. Yang, J. Y.; Chen, S.; Dougherty, W. G.; Kassel, W. S.; Bullock, R. M.; DuBois, D. L.; Raugei, S.; Rousseau, R.; Dupuis, M.; Rakowski DuBois, M. *Chem. Commun.* **2010**, *46*, 8618.
49. Chen, S.; Raugei, S.; Rousseau, R.; Dupuis, M.; Bullock, R. M. *J. Phys. Chem. A* **2010**, *114*, 12716.
50. Reback, M. L.; Ginovska-Pangovska, B.; Ho, M.-H.; Jain, A.; Squier, T. C.; Raugei, S.; Roberts, J. A. S.; Shaw, W. J. *Chem. Eur. J.* **2013**, *19*, 1928.
51. Horvath, S.; Fernandez, L. E.; Soudackov, A. V.; Hammes-Schiffer, S. *Proc. Natl. Acad. Sci. U.S.A.* **2012**, *109*, 15663.
52. Fernandez, L. E.; Horvath, S.; Hammes-Schiffer, S. *J. Phys. Chem. C* **2012**, *116*, 3171.
53. Horvath, S.; Fernandez, L. E.; Soudackov, A. V.; Hammes-Schiffer, S. *Abstr. Pap., Am. Chem. Soc.* **2011**, *242*.
54. Laino, T.; Mohamed, F.; Laio, A.; Parrinello, M. *J. Chem. Theory Comput.* **2006**, *2*, 1370.
55. Laio, A.; Gervasio, F. L. *Rep. Prog. Phys.* **2008**, *71*, 126601.
56. Stephan, D. W.; Erker, G. *Angew. Chem., Int. Ed.* **2010**, *49*, 46.
57. Stephan, D. W. In *Catalysis without Precious Metals*; Bullock, R. M., Ed.; Wiley-VCH: Weinheim, 2010.
58. Stephan, D. W. *Org. Biomol. Chem.* **2008**, *6*, 1535.
59. Kaljurand, I.; Kutt, A.; Soovali, L.; Rodima, T.; Maemets, V.; Leito, I.; Koppel, I. A. *J. Org. Chem.* **2005**, *70*, 1019.
60. Faviera, I.; Duñach, E. *Tetrahedron Lett.* **2004**, *45*, 3393.
61. Appel, A. M.; Pool, D. H.; O'Hagan, M.; Shaw, W. J.; Yang, J. Y.; Rakowski DuBois, M.; DuBois, D. L.; Bullock, R. M. *ACS Catal.* **2011**, *1*, 777.
62. Yang, J. Y.; Smith, S. E.; Liu, T.; Dougherty, W. G.; Hoffert, W. A.; Kassel, W. S.; Rakowski DuBois, M.; DuBois, D. L.; Bullock, R. M., submitted.
63. Kilgore, U. J.; Roberts, J. A. S.; Pool, D. H.; Appel, A. M.; Stewart, M. P.; DuBois, M. R.; Dougherty, W. G.; Kassel, W. S.; Bullock, R. M.; DuBois, D. L. *J. Am. Chem. Soc.* **2011**, *133*, 5861.
64. O'Hagan, M.; Shaw, W.; Raugei, S.; Chen, S.; Yang, J. Y.; Kilgore, U. J.; DuBois, D. L.; Bullock, R. M. *J. Am. Chem. Soc.* **2011**, *133*, 14301.
65. Helm, M. L.; Stewart, M. P.; Bullock, R. M.; DuBois, M. R.; DuBois, D. L. *Science* **2011**, *333*, 863.
66. Laio, A.; Gervasio, F. L. *Rep. Prog. Phys.* **2008**, *71*, 126601.
67. Laio, A.; Parrinello, M. *Proc. Natl. Acad. Sci. U.S.A.* **2002**, *99*, 12562.
68. Nikitin, A. M.; Lyubartsev, A. P. *J. Comput. Chem.* **2007**, *28*, 2020.
69. Perdew, J. P.; Burke, K.; Ernzerhof, M. *Phys. Rev. Lett.* **1997**, *78*, 1396.
70. Perdew, J. P.; Burke, K.; Ernzerhof, M. P. *Rev. Lett.* **1996**, *77*, 3865.
71. Grimme, S. *J Comp. Chem.* **2006**, *27*, 1787.
72. Raiteri, P.; Laio, A.; Gervasio, F. L.; Micheletti, C.; Parrinello, M. *J. Phys. Chem. B* **2005**, *110*, 3533.
73. VandeVondele, J.; Krack, M.; Mohamed, F.; Parrinello, M.; Chassaing, T.; Hutter, J. *Comp. Phys. Comm.* **2005**, *167*, 103.

74. Perdew, J. P. *Phys. Rev. B* **1986**, *33*, 8822.
75. Becke, A. D. *J. Chem. Phys.* **1993**, *98*, 5648.
76. Andrae, D.; Häußermann, U.; Dolg, M.; Stoll, H.; Preuß, H. *Theor. Chem. Acc.* **1990**, *77*, 123.
77. Rassolov, V. A.; Pople, J. A.; Ratner, M. A.; Windus, T. L. *J. Chem. Phys.* **1998**, *109*, 1223.
78. Chen, S.; Raugei, S.; Rousseau, R.; Dupuis, M.; Bullock, R. M. *J. Phys. Chem. A* **2010**, *114*, 12716.
79. Barone, V.; Cossi, M. *J. Phys. Chem. A* **1998**, *102*, 1995.
80. Cossi, M.; Rega, N.; Scalmani, G.; Barone, V. *J. Comput. Chem.* **2003**, *24*, 669.
81. Bondi, A. *J. Phys. Chem.* **1964**, *68*, 441.
82. Frisch, M. J.; Trucks, G. W.; Schlegel, H. B.; Scuseria, G. E.; Robb, M. A.; Cheeseman, J. R.; Scalmani, G.; Barone, V.; Mennucci, B.; Petersson, G. A.; Nakatsuji, H.; Caricato, M.; Li, X.; Hratchian, H. P.; Izmaylov, A. F.; Bloino, J.; Zheng, G.; Sonnenberg, J. L.; Hada, M.; Ehara, M.; Toyota, K.; Fukuda, R.; Hasegawa, J.; Ishida, M.; Nakajima, T.; Honda, Y.; Kitao, O.; Nakai, H.; Vreven, T.; Montgomery, J. A., Jr.; Peralta, J. E.; Ogliaro, F.; Bearpark, M.; Heyd, J. J.; Brothers, E.; Kudin, K. N.; Staroverov, V. N.; Kobayashi, R.; Normand, J.; Raghavachari, K.; Rendell, A.; Burant, J. C.; Iyengar, S. S.; Tomasi, J.; Cossi, M.; Rega, N.; Millam, J. M.; Klene, M.; Knox, J. E.; Cross, J. B.; Bakken, V.; Adamo, C.; Jaramillo, J.; Gomperts, R.; Stratmann, R. E.; Yazyev, O.; Austin, A. J.; Cammi, R.; Pomelli, C.; Ochterski, J. W.; Martin, R. L.; Morokuma, K.; Zakrzewski, V. G.; Voth, G. A.; Salvador, P.; Dannenberg, J. J.; Dapprich, S.; Daniels, A. D.; Farkas, O.; Foresman, J. B.; Ortiz, J. V.; Cioslowski, J.; Fox, D. J.; Revision B.01 ed.; Gaussian, Inc.: Wallingford CT, 2009, Gaussian 09.
83. Frisch, M. J.; Trucks, G. W.; Schlegel, H. B.; Scuseria, G. E.; Robb, M. A.; Cheeseman, J. R.; Scalmani, G.; Barone, V.; Mennucci, B.; Petersson, G. A.; Nakatsuji, H.; Caricato, M.; Li, X.; Hratchian, H. P.; Izmaylov, A. F.; Bloino, J.; Zheng, G.; Sonnenberg, J. L.; Hada, M.; Ehara, M.; Toyota, K.; Fukuda, R.; Hasegawa, J. I.; shida, M.; Nakajima, T.; Honda, Y.; Kitao, O.; Nakai, H.; Vreven, T.; Montgomery, J. A., Jr.; ; Peralta, J. E.; Ogliaro, F.; Bearpark, M.; Heyd, J. J.; Brothers, E.; Kudin, K. N.; Staroverov, V. N.; Kobayashi, R.; Normand, J.; Raghavachari, K.; Rendell, A.; Burant, J. C.; Iyengar, S. S.; Tomasi, J.; Cossi, M.; Rega, N.; Millam, J. M.; Klene, M.; Knox, J. E.; Cross, J. B.; Bakken, V.; Adamo, C.; Jaramillo, J.; Gomperts, R.; Stratmann, R. E.; Yazyev, O.; Austin, A. J.; Cammi, R.; Pomelli, C.; Ochterski, J. W.; Martin, R. L.; Morokuma, K.; Zakrzewski, V. G.; Voth, G. A.; Salvador, P.; Dannenberg, J. J.; Dapprich, S.; Daniels, A. D.; Farkas; O.; Foresman; J. B.; Ortiz; J. V.; Cioslowski;, J.; Fox; D. J., 2009.
84. Kendall, R. A.; Aprà, E.; Bernholdt, D. E.; Bylaska, E. J.; Dupuis, M.; Fann, G. I.; Harrison, R. J.; Ju, J.; Nichols, J. A.; Nieplocha, J.; Straatsma, T. P.; Windus, T. L.; Wong, A. T. *Computer Phys. Comm.* **2000**, *128*, 260.
85. Straatsma, T. P.; Aprà, E.; Windus, T. L.; Bylaska, E. J.; Jong, W. d.; Hirata, S.; Valiev, M.; Hacklr, M.; Pollack, L.; Harrison, R.; Dupuis, M.; Smith, D. M. A.; Nieplocha, J.; Tipparaju, V.; Krishnan, M.; Auer, A. A.; Brown,

E.; Cisneros, G.; Fann, G.; Früchtl, H.; Garza, J.; Hirao, K.; Kendall, R.; Nichols, J.; Tsemekhman, K.; Wolinski, K.; Anchell, J.; Bernholdt, D.; Borowski, P.; Clark, T.; Clerc, D.; Dachsel, H.; Deegan, M.; Dyall, K.; Elwood, D.; Glendening, E.; Gutowski, M.; Hess, A.; Jaffe, J.; Johnson, B.; Ju, J.; Kobayashi, R.; Kutteh, R.; Lin, Z.; Littlefield, R.; Long, X.; Meng, B.; Nakajima, T.; Niu, S.; Rosing, M.; Sandrone, G.; Stave, M.; Taylor, H.; Thomas, G.; Lenthe, J. V.; Wong, A.; Zhang, Z. Pacific Northwest National Laboratory: Richland, Washington .

86. Perdew, J. P.; Burke, K.; Ernzerhof, M. *Phys. Rev. Lett.* **1996**, *77*, 3865.
87. Perdew, J. P.; Burke, K.; Ernzerhof, M. *Phys. Rev. Lett.* **1997**, *78*, 1396.
88. Lee, C.; Yang, W.; Parr, R. G. *Phys. Rev. B* **1988**, *37*, 785.
89. Miehlich, B.; Savin, A.; Stoll, H.; Preuss, H. *Chem. Phys. Lett.* **1989**, *157*, 200.
90. Niu, S.; Hall, M. B. *Chem. Rev.* **2000**, *100*, 353.

Chapter 7

Molecular Modeling Aspects of Exploring Silica Properties

Istvan Halasz*,[1] and Jian-Jie Liang[2]

[1]PQ Corporation, Research & Development Center, 280 Cedar Grove Road, Conshohocken, Pennsylvania, 19428, United States
[2]Accelrys, Inc., 10188 Telesis Ct., San Diego, California, 92121, United States
***E-mail: istvan.halasz@pqcorp.com**

Silica and silicates are important ingredients of many catalysts, adsorbents, nano and composite materials that aid the generation and conservation of sustainable green energy. To modify the properties of these materials in desirable ways, it is essential to understand their chemistry and structure at the molecular level. Here we show three examples how molecular modeling aided our efforts to solve problems associated with practical applications of crystalline and amorphous silicates. They include grand canonical Monte Carlo (GCMC) statistical mechanics, density functional (DFT), and combined quantum mechanical/molecular mechanical (QM/MM) calculations in strict correlation with experimental data.

1. Introduction

Clean energy and green chemistry became extremely popular research areas in the past few decades as promising ways to significantly improve the conditions of our environment, health, and climate. However, both disciplines have to overcome numerous challenges before they will see truly wide-spread practical implementations. As participants of the associated interdisciplinary efforts, chemists have developed many innovative, environment-friendly production techniques and materials utilizing among others new catalysts, adsorbents, nano particles, and organic/inorganic composite materials. Many of these materials contain silica or its derivatives (*1*). Silicates are the most abundant ingredients of the Earth's crust hence have been utilized in many ways for thousands of

In Applications of Molecular Modeling to Challenges in Clean Energy; Fitzgerald, G., et al.;
ACS Symposium Series; American Chemical Society: Washington, DC, 2013.

years. Despite such long and extensive use, the chemistry and structure of many silicates is still poorly understood. Therefore most artificial silicate manufacturing processes include substantial empirical knowledge. To gain better control over desirable catalytic, sorption, mechanical, adhesive, etc. properties, efforts for understanding the chemistry and structure of silicates at the molecular level have significantly increased in the course of the past twenty years or so, along with the revolution of personal computers that has improved both the experimental instruments and the model calculations at an unparalleled rate.

In this chapter we show in a few examples how molecular modeling could help in answering certain practical questions that emerged while studying the properties of novel commercial silica products for environment friendly applications. We look at these model calculations with the eyes of an experimental chemist who is not trained formally in theoretical chemistry but has a problem to solve, might have some speculative ideas about the possible answers from experimental data, and needs reliable theoretical confirmation for a viable clue. Occasionally the theoretical approach reveals unexpected explanations. We will show examples for both variations. With respect to the possible practical (financial) consequences of these deductions, we put special emphasis on the compatibility of experimental and theoretical data. Most of the presented silicates and experiments were made in the laboratories of PQ Corporation (www.pqcorp.com). Every computational work was carried out on common commercial personal computers equipped with 2 to 64 processors. Calculations were carried out exclusively with programs from the Material Studio package of Accelrys, Inc. (www.accelrys.com) and the CERIUS2 package of Accelrys' predecessor, MSI.

2. Discovery of PSE (Polarity Sieving Effect) on a Siliceous Y Zeolite

The first example is related to the unusual sorption behavior of an aluminum deficient Y zeolite which became therefore a promising candidate, for example, to fill low temperature sorption air conditioners in fuel cell driven vehicles, to remove volatile organic contaminants (VOC) and other hazardous materials from air and water, and other applications (*2–5*).

Zeolites are crystalline microporous silicates composed of tetrahedral $[SiO_4]^{4-}$ building blocks. A certain number of silicon atoms (< 50 %!) can be isomorphously substituted by other elements capable of tetrahedral coordination with oxygen atoms. This might substantially alter the electron distribution in the zeolite lattice, which in turn might affect its mechanical, catalytic, sorption, electronic, etc. properties. The most frequent substituent is Al. Since Al has only three electrons to share with four oxygens sitting on each corner of the $[AlO_4]^{5-}$ tetrahedra, charge balance requires the attachment of an external positive ion to the lattice. An illustration with proton as an external cation is shown in Figure 1 a) and b). These external positive ions are exchangeable with any other positive ion that fits into pores of the lattice. When the isomorph substituent has four electrons on its external shell, like for example the Ti^{4+} in Figure 1 c), external exchangeable ions are not needed. We will deal with some properties of

In Applications of Molecular Modeling to Challenges in Clean Energy; Fitzgerald, G., et al.;
ACS Symposium Series; American Chemical Society: Washington, DC, 2013.

a Ti-substituted ZSM-5 zeolite in section 4. There are many other aspects of the ion-exchange which have been reviewed for example in some recent books on zeolites (*6*, *7*).

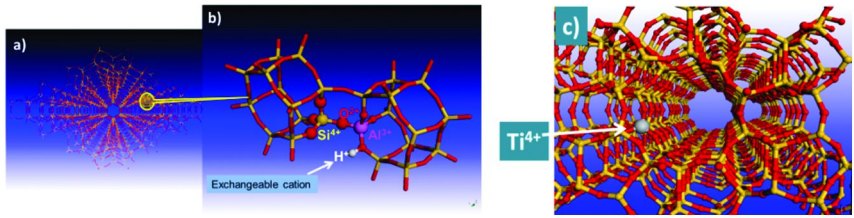

Figure 1. Examples for isomorphous substitution of Si^{4+} in zeolite lattices. In zeolite ***a)*** *the substituent is Al^{3+} cation which requires the presence of an external, exchangeable positive ion to maintain charge neutrality; its magnified lattice part* ***b)*** *shows proton as exchangeable cation sitting near one of four geometrically distinct oxygen ions of the [AlO_4] tetrahedron (note that depending on the zeolite structure less than four distinct positions are also possible);* ***c)*** *illustrates that external ions are not present when tetravalent ion is the isomorphous substituent, in this case Ti^{4+}. Color codes: Si = yellow; O = red; Al = pink; H = white; Ti = silver. (see color insert)*

The Y zeolites have cubic crystal structures and their microporous channels are equally accessible from three dimensions. Their average d ~ 7.5 Å diameter pores are formed by 12 [TO_4] tetrahedral units (T = Si or Al). Figure 2 a) illustrates these main channels from the 111 direction. The lattice constant and pore size slightly varies with the Al content. Most Y zeolites, including for example those used for the fluid catalytic cracking (FCC) of oil, one of the largest volume industrial technologies, have approximately Si/Al ~ 2.6 ratio. For this and other applications high hydrothermal stability is desirable. It has long been known, that one way to increase the hydrothermal stability of zeolites is the reduction of their Al-content. It is also well known that increasing Si/Al ratio increases the hydrophobic character of zeolites, which can be desirable when sorption of water is undesirable. Some zeolites, like ZSM-5, the pore structure of which is illustrated in Figure 3 a) and c), can be synthesized purely from SiO_2, without any Al content (*8*). This has not been successful until now with the Y zeolite. Its Si/Al ratio can be increased however by removing its Al-content by a variety of methods. However, this process easily leads to lattice defect formation. Too many defects can cause the collapse of the crystal lattice. Thus, rarely have been produced well crystallized, stable commercial Y zeolites with Si/Al ratios higher than ~ 40. Moreover, the reduced aluminum content usually does not increase, or only slightly increases, the hydrophobicity, partly because of the remaining Bronsted acidic Al-associated, so called bridging, hydroxyls (similar to that shown in Figure 1 b). The oxygens of [SiO_4] tetrahedra, around the vacancy of removed Al, form internal Si-OH silanol groups. It is a general view that the presence of hydroxyl groups makes surfaces hydrophilic.

In Applications of Molecular Modeling to Challenges in Clean Energy; Fitzgerald, G., et al.;
ACS Symposium Series; American Chemical Society: Washington, DC, 2013.

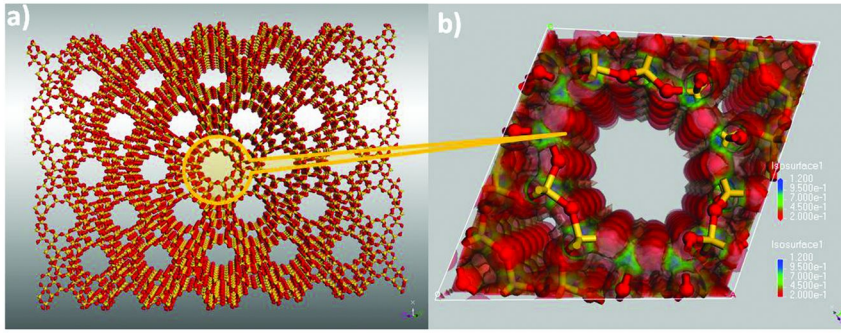

Figure 2. The channels of Y zeolite are accessible from three directions and equal from each direction. ***a)*** *View of the main channels of an Al-free Y-zeolite particle. Color code is the same as in Figure 1;* ***b)*** *Electrostatic potential map on the highest electron density isosurface; the overlapping negative fields homogeneously fill the zeolite channels (9–12); color strength is proportional with the strength of potential field; red is negative, green and blue are increasingly positive fields. (see color insert)*

With this general background, it was a big surprise that a Si/Al ~ 40 ratio Y zeolite, produced by Zeolyst International and commercially named CBV 901, proved to be highly hydrophobic (*9*, *13*, *14*). Figure 4 a) indicates that it adsorbs even less water than a Si/Al ~ 149 ratio ZSM5 although both are quite hydrophobic. As shown in Figure 4) by their FTIR spectra, it is even more puzzling that, in addition to the external silanol groups on the particle surfaces (~3740 cm^{-1}), both zeolites contain substantial amounts of internal hydroxyls (3400-3700 cm^{-1}).

It was an even bigger surprise that methanol showed a Type V adsorption isotherm on CBV 901 (Figure 5 a). For microporous materials Type I adsorption isotherms are characteristic regardless of the nature of adsorbate (*17–19*). The reason is that, unlike in meso and macro pores, micro pore adsorption is not based on layer by layer adsorption on the surface but rather on adsorbate-adsorbate interactions of the sorbate molecules in the confined space (< 20 Å diameter) that is filled with the overlapping potential fields of elements composing the pore walls (*10–12*). The permanent or London dispersion forces induce dipole moments of sorbate molecules in close proximity, which causes their quick condensation and pore filling below about $p/p_0 \sim 0.02$, which in turn generates the typical Langmuir isotherm shape of Type I isotherms. For illustration, Figure 5 a) shows the Type I isotherm of water adsorbing on a commercial Na-exchanged, Si/Al ~ 2.6 Y zeolite, CBV 100. By IUPAC's definition "The type V adsorption isotherm is uncommon" in any adsorbent-adsorbate pair (*18*). On microporous materials, only in the water adsorption on AlPO-5 has been observed an as yet unexplained Type V upswing in the isotherm at around $p/p_0 \sim 0.2$ (*20–22*).

In Applications of Molecular Modeling to Challenges in Clean Energy; Fitzgerald, G., et al.;
ACS Symposium Series; American Chemical Society: Washington, DC, 2013.

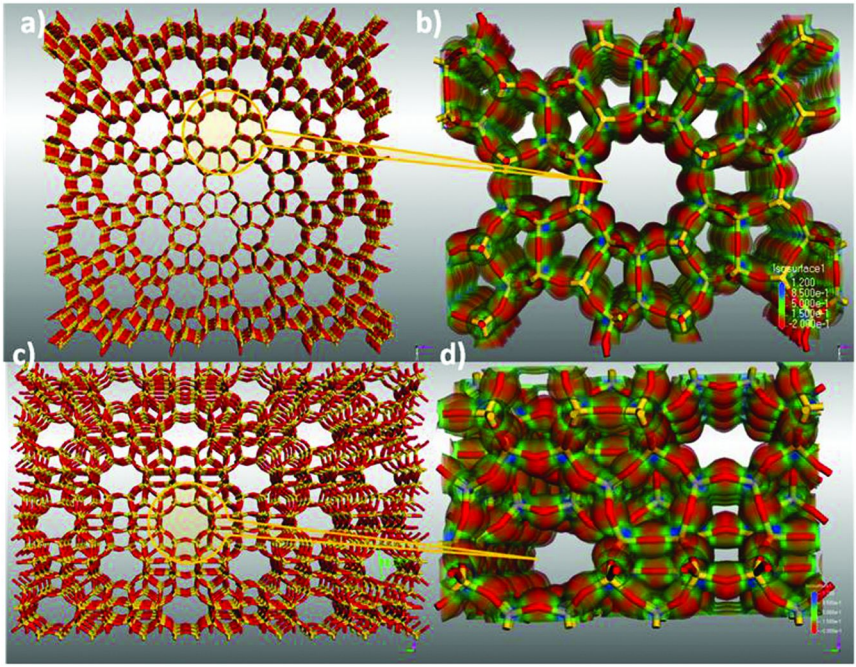

Figure 3. The channels of ZSM5 are accessible only from two directions and even these are not equivalent with each other. ***a)*** *View of the straight channels of siliceous ZSM5 (silicalite) from 101 direction;* ***b)*** *These channels are homogeneously filled with negative electrostatic potential similarly to the Y-zeolite channels in Figure 2 b);* ***c)*** *View of the "zigzag" channels of silicalite from 011 direction;* ***d)*** *These channels are asymmetric, with easier access for sorbate molecules to positive electrostatic potentials (9, 13). Colors mean the same as those in Figure 2. (see color insert)*

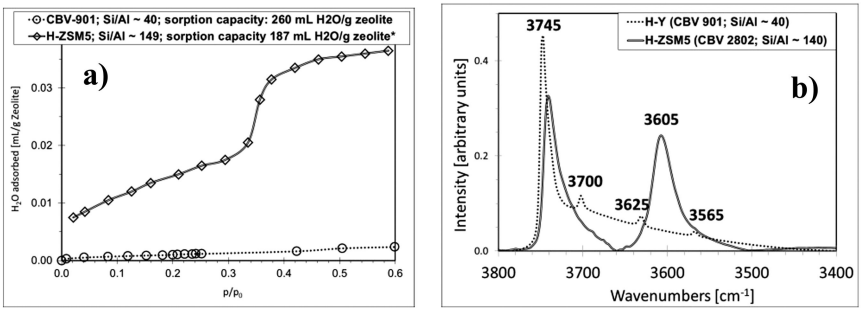

Figure 4. ***a)*** *The Si/Al ~ 40 ratio, proton exchanged Y zeolite (CBV 901) is more hydrophobic than a Si/Al ~ 149 ratio, proton exchanged ZSM5; data are from references (14, 15);* ***b)*** *Transmission FTIR spectra indicate that both zeolites have substantial internal hydroxyl contents (3400-3700 cm^{-1} range); spectra appeared in reference (16).*

In Applications of Molecular Modeling to Challenges in Clean Energy; Fitzgerald, G., et al.;
ACS Symposium Series; American Chemical Society: Washington, DC, 2013.

Since the "pressure swing" capability of this Met-OH isotherm made CBV 901 the best candidate among all materials tested for sorption based air conditioning on fuel cell driven vehicles on which very little heat is generated for higher boiling adsorbates (*2*, *3*), it generated an intense speculation about its possible origin. The role of hydrophobicity could be excluded based on the fact, that silicalite gave Type I isotherm also with Met-OH (*13*). Other speculations mostly included some sort of mesoporosity or defect effect on CBV 901. To see if these ideas have any merit, we turned to molecular modeling, using the Sorption module of the CERIUS2 package for methanol and many other sorbate molecules on both a siliceous ZSM5 and a Y zeolite at the same conditions as the experimental measurements were made (*9*, *13*). This statistical mechanics program is based on Monte Carlo algorithms with Metropolis selection method in canonical (NVT) and grand canonical (μVT) ensembles. Parameter assignment was made with the Buchart1.01- Dreiding2.21 force field as outlined by Mayo et al. (*23*) except that the charges were calculated with the electronegativity equalization method (*24*). Moreover the TIPS2 model was selected for the H_2O molecule (*25*) and the carbon atom in methanol was changed to C_33 with 12 g/mol mass. To assure energy equilibrium for each data point within ±2% accuracy at least 10^6 iterations were performed and in the inflection zone of the Met-OH isotherm this number was increased to 10^7. A number of other calculation parameters are described in details in references (*9*, *13*).

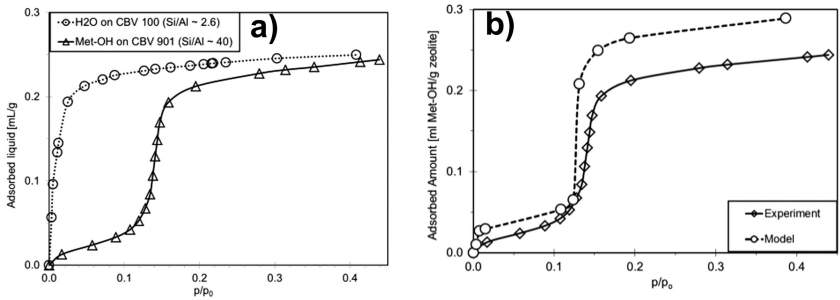

Figure 5. ***a)*** *Type I adsorption isotherms of H_2O on the Na-Y zeolite CBV 100 and Type V isotherm of Met-OH on the H-Y zeolite CBV 901;* ***b)*** *Model adsorption isotherm with methanol on an Al-free Y zeolite fits well the experimental isotherm on CBV 901. Data have been published in (9, 13, 14).*

All models gave reliably similar isotherms to the experimental ones including the Type V isotherm for Met-OH on the siliceous Y zeolite (Figure 5 b) and Type I isotherm for this adsorbate on silicalite. Yet they left four questions still unanswered: i) Why are CBV 901 and CBV 2802 highly hydrophobic despite their hydroxyl contents (Figure 4)?; ii) Why is it that the polar H_2O molecule cannot adsorb on these zeolites even though the also polar Met-OH can?; iii) Why are the Met-OH isotherms different on these two hydrophobic zeolites?; and iv) Why does Met-OH not give a Type I isotherm on the microporous CBV 901?

In Applications of Molecular Modeling to Challenges in Clean Energy; Fitzgerald, G., et al.;
ACS Symposium Series; American Chemical Society: Washington, DC, 2013.

In case of the siliceous ZSM5 material that has approximately d ~ 5.5 Å diameter pores, Carrot at al. (*18*, *24*, *26*) argued that its hydrophobicity is due to the inability of water molecules to form 3D hydrogen bonded 6-member rings (Figure 6 c), with approximately d ~ 6 Å diameter, which is the normal structure of the condensed water (*18*, *23*). Thus, the little water that adsorbs on the not fully aluminum-free structures might be due to interaction with the few remaining hydroxyls without forming a fully condensed phase. For the larger, d ~ 7.5 Å diameter Y zeolite pores this explanation is not acceptable. Indeed model experiments showed the ring-like arrangement of H_2O for example in a CBV 100 type hydrophilic zeolite (*13*). The only reasonable explanation seemed to be that the homogeneous negative potential field in a defect free siliceous Y structure (*9*) (Figure 2 b) repels the strongly polar (Figure 6a and Table in Figure 7) water molecules having a large negatively charged oxygen "head". We also showed (*9*, *13*, *14*) that lattice defects that cause inhomogeneity in the potential field allow water penetration even into Si/Al ~ 90 Y zeolite following water adsorptions as described above for the ZSM5 structure, which inherently has an inhomogeneous potential field in its channels (Figure 3 b and d) (*9*, *13*). Methanol, which is less polar than H_2O (Table in Figure 7) and has a relatively large positive potential field (Figure 6 b), can penetrate the repelling homogeneous negative potential field of Y zeolite when the pressure is increased beyond a critical, $p/p_0 \sim 0.15$ value and once in, its molecules condense (Figure 5 a). The equilibrated sorption models also showed that the condensed Met-OH molecules condense in a ring like arrangement in an Al-free Y structure while they can also condense in a chain-like arrangement in a ZSM5 silicalite structure (*13*). With this we have found answers to all four of the above questions. The only dubious point remained that some of these modeling explanations were based on results with Al-free Y zeolite and CBV 901 still has a substantial number of Al atoms that, along with the attached exchangeable protons, must disturb the homogeneity of its potential field. However, very recently we found experimental evidence that the elemental crystallites of this material have an Al-free outside "shell" and only the internal part of particles contain hydroxyls (*27*). Thus, the modified view is that every argument described above is totally valid for this external shell and the $p/p_0 \sim 0.15$ minimum relative pressure is needed presumably for the Met-OH molecules to break through this resistive, homogeneously negative potential shell. We also observed extremely slow water diffusion through this shell. For example, all internal hydroxyls were hydrogen bonded to H_2O molecules in an approximately 10 years old sample kept at ambient conditions (in a closed jar). The resistive power of this potential shell also worked against the diffusion of water from inside to outside: 96 hours needed to remove this small amount of water at 500 °C at 10^{-8} torr. Adsorbed water escapes from most zeolites within less than two hours at similar conditions.

As summarized in Figure 7, we have found that the aluminum deficient CBV 901 Y zeolite exerts a previously unknown polarity sieving effect, PSE. With the help of combined experimental and molecular modeling research we managed to explain this odd phenomenon. There is hope that this understanding will help to develop other materials with such desirable properties.

In Applications of Molecular Modeling to Challenges in Clean Energy; Fitzgerald, G., et al.;
ACS Symposium Series; American Chemical Society: Washington, DC, 2013.

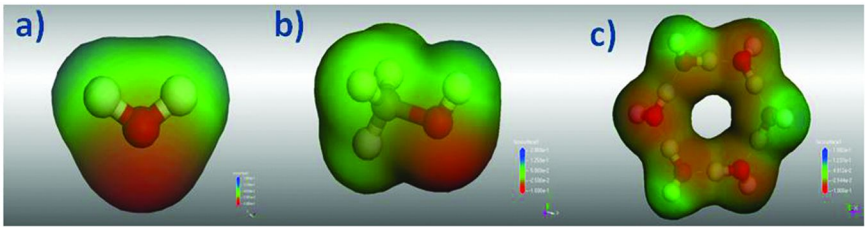

Figure 6. Electrostatic potential field around ***a)*** *H_2O and* ***b)*** *Met-OH molecules;* ***c)*** *6R hydrogen bonded water ring; Color codes are the same as in Figures 1 and 2. (see color insert)*

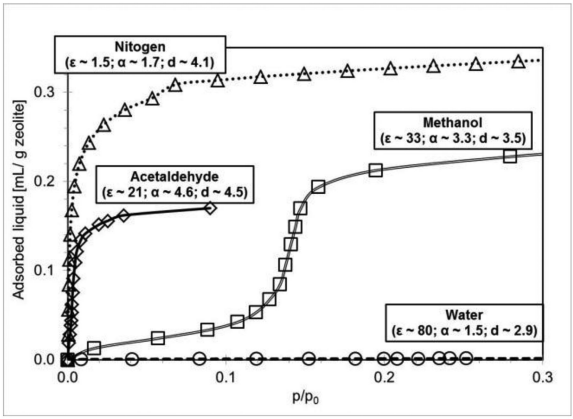

Figure 7. Adsorption isotherms of sorbate molecules with different polarity values (ε) illustrate that CBV 901 exerts a polarity sieving effect: the less polar is a molecule the easier it adsorbs. The α polarizability values [x 10^{-24} cm^{-1}] and d kinetic diameters [Å] of molecules do not correlate with the sorption data (14).

3. Raman Spectroscopy for Distinguishing Amorphous Porous Silica Structures

Silica gels are widely used adsorbents, catalyst supports, coating materials, and additives in numerous environment-friendly applications, including for example biofuel production, selective polyethylene synthesis, insulator additives, durable car tire manufacturing, and many more (*1*, *28*, *29*). In contrast to crystalline silicates, for which X-ray diffraction is a dedicated tool to explore their ordered bulk structure, little is known about the molecular constitution of amorphous silicates. It has been empirically observed that properties such as porosity, tackiness, elasticity, surface area, etc. vary depending on the preparation conditions, but lacking a clear understanding of how the starting dissolved siloxane molecules polymerize into a gel with desirable physical properties, the possibility of distinct molecular structures of different gels has been rarely questioned even at speculative level (*30*, *31*).

In Applications of Molecular Modeling to Challenges in Clean Energy; Fitzgerald, G., et al.;
ACS Symposium Series; American Chemical Society: Washington, DC, 2013.

A few years ago we noticed that the Raman spectra of differently made silica gels show sometimes distinct differences, especially when they are made at acidic or basic pH values (*32–34*). While these experiments started from aqueous alkaline silicate solutions, other research groups detected molecular differences between gels made from non-aqueous tetraethyl (TEOS) and tetra methyl (TMOS) orthosilicates using Raman as well as ^{29}Si NMR techniques (*35*, *36*). Parallel with these studies we also found distinct differences between the Raman and ^{29}Si NMR spectra of acid and base set silica gels made from TEOS (*37–39*). We observed, however, that the two methods lead to contradictory structural assignments. To resolve this issue, we used molecular modeling as described below.

One way to control the porosity of gels is to deposit them onto a porous organic substrate and then carefully burning out the organic material, which leaves its pores unchanged within the silica particles while hardening them to a near-glassy state. Using Amberlite for this process, we deposited silica gel from TEOS at acidic and basic conditions, naming these products SiHP-A and SiHP-B, respectively (*37–39*). Their calcined forms are Si-A and Si-B, respectively. The microscopic pictures in Figure 8 show that the acid set gel forms a very smooth surface while that of the base set gel is strongly fragmented. The physical appearance of these materials has virtually not changed after burning out the organic content. The porosity data in Figures 8 b) and c) do not show substantial differences between the freshly made SiHP-A and SiHP-B gels and both resemble those of the Amberlite support (*39*). However the pore structures of their calcined products, Si-A and Si-B, differ tremendously.

In Figure 9 the Raman and ^{29}Si NMR spectra of these materials provide the first experimental support for the decades old theoretical predictions (*30*, *31*) that the different physical properties of acid and base set gels might be associated with their molecular constitutions. According to Figure 9 a), a striking difference between the freshly prepared SiHP-A and SiHP-B samples is that the former one contains mainly Q^3 connected silicon atoms, which suggests a more flexible molecular constitution than the rigid Q^4 connections that characterize the base set material. The associated brittleness is in line with the fragmented appearance of the air dried SiHP-B, while the more elastic SiHP-A structure maintains a smooth surface (Figure 8 a). Figure 9 b) indicates that Q^4 connectivity becomes predominant in both calcined samples, which are mechanically harder than most other silica gels. We use here the widely accepted Qn nomenclature, coined by Engelhard et al. (*40*), to describe the average number of Si-O-Si connections of each [SiO_4] tetrahedron in a material; n can be 0, 1, 2, 3, or 4.

The Raman spectra in Figure 9 c) indicate that during the calcination process new rings are formed in both materials, presumably via the interacting Q^3 connections where the structure must be "capped" with silanol groups, which are prone to give up a H_2O molecule when they are close enough to each other. Indeed, one can identify the various siloxane rings on the high resolution transmission electron microscopic (TEM) pictures Figure 10. What is more, these pictures also show the typical mesopores as predicted in Figure 8 c). Some characteristic places are circled in red to facilitate the visualization. It is also clear that the structure of Si-B is more compact than the structure of Si-A, which is in line with the mainly macroporous character of the base set gel (Figure 8 b). All these

In Applications of Molecular Modeling to Challenges in Clean Energy; Fitzgerald, G., et al.;
ACS Symposium Series; American Chemical Society: Washington, DC, 2013.

experimental results are in good accordance with the conclusion that the physical properties of silica gels are based on their molecular structures and the molecular structure of the initial gel predetermines the shape of the final structures.

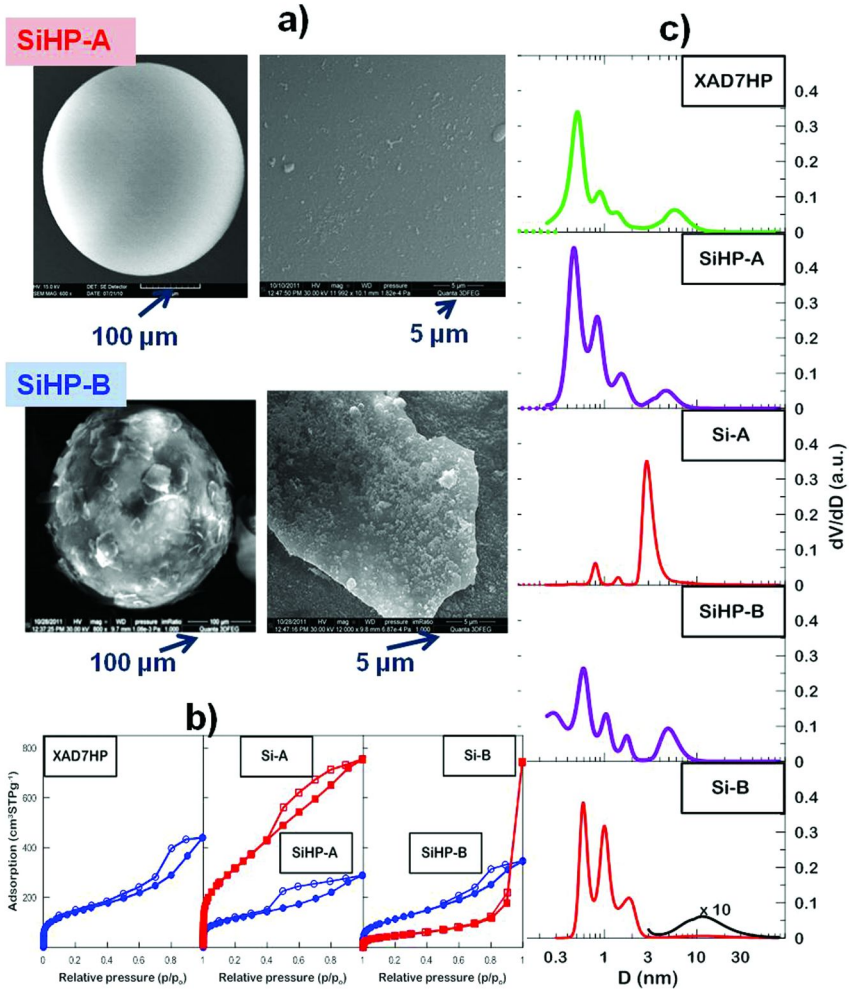

Figure 8. ***a)*** *The physical appearance of acid set SiHP-A and base set SiHP-B silica gels on Amberlite support differ.* ***b)*** *The corresponding N_2 sorption isotherms are similar to each other and that of the Amberlite (XAD7HP); the isotherms of calcined Si-A and Si-B suggest meso and macroporous characters, respectively.* ***c)*** *The pore size distributions, measured by PALS (positron annihilation lifetime spectroscopy), fit the N_2 sorption based deductions (39).*

In Applications of Molecular Modeling to Challenges in Clean Energy; Fitzgerald, G., et al.;
ACS Symposium Series; American Chemical Society: Washington, DC, 2013.

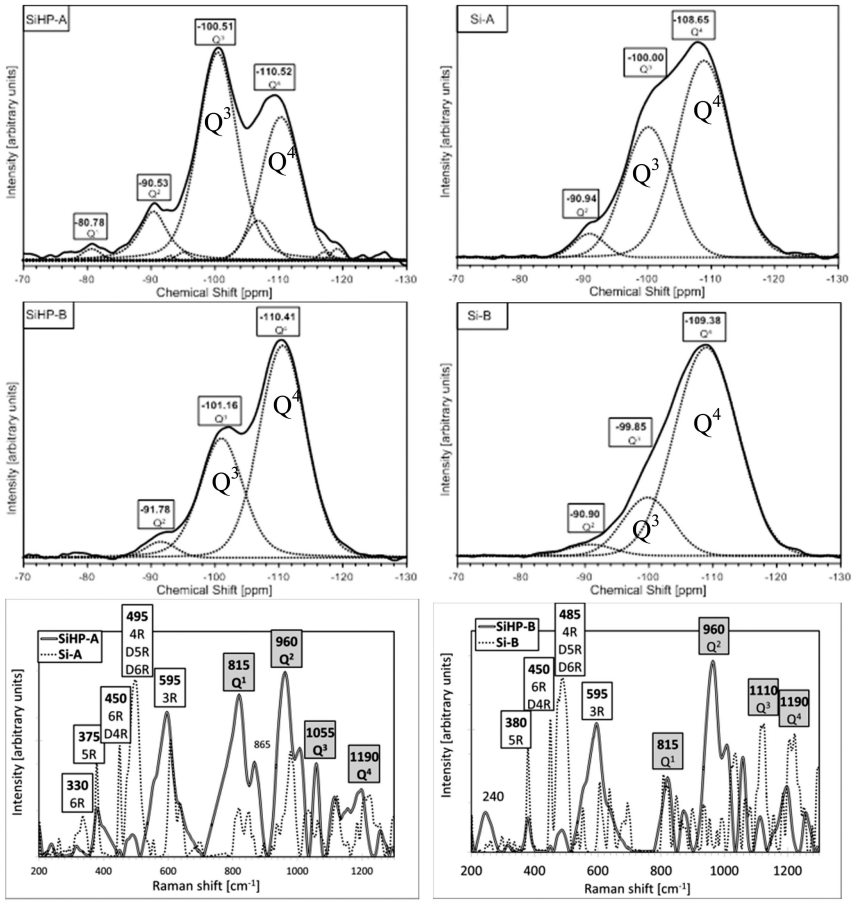

Figure 9. ***a)*** *The Q^3/Q^4 ratio of SiHP-A is much higher than that of SiHP-B.* ***b)*** *Both calcined products (Si-A and Si-B) contain mainly Q^4 connected $[SiO_4]$ tetrahedra.* ***c)*** *The substantially different Raman spectra of the fresh and calcined samples indicate structural changes during the calcination process. Spectra are taken from references (37, 38).*

The structure assignment of Raman bands in silicates is less firmly established than that of the ^{29}Si NMR bands. Yet due to its numerous advantages like easy mobility, speed, etc., Raman has been extensively applied for structure identification in zeolite and glass research and industry. Most researchers largely agree that the symmetric and asymmetric Si-O vibrations roughly in the 650-1250 cm^{-1} range can be assigned to the Qn connectivities in silicates while the Si-O-Si bending vibrations in 150-650 cm^{-1} range mostly depend on the ring structure of silicates (*41*). Using the most established assignments for the Raman spectra in

In Applications of Molecular Modeling to Challenges in Clean Energy; Fitzgerald, G., et al.;
ACS Symposium Series; American Chemical Society: Washington, DC, 2013.

Figure 9 c), we noticed with surprise that the Q^n connectivities with Raman do not reflect the same distribution as measured with ^{29}Si NMR. For better visualization Figure 11 a) repeats the SiHP-A and SiHP-B Raman spectra. The most puzzling is the large Q^1 and Q^2 bands that are extremely low in the dcorresponding NMR spectra (Figure 9).

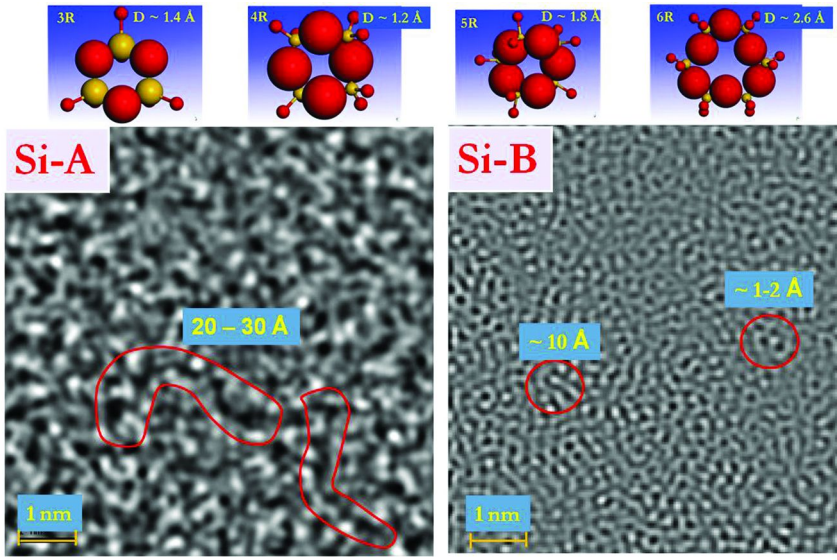

Figure 10. Atomic resolution TEM pictures of Si-A and Si-B show characteristic differences in their molecular constitutions that also affects their porosity and physical appearance. The attached models show the approximate diameters of various siloxane rings, also recognizable on the TEM snapshots. (see color insert)

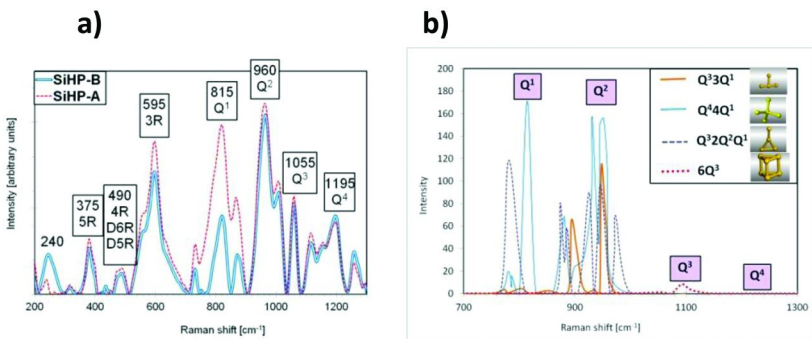

*Figure 11. **a)** Experimental Raman spectra of SiHP-B and SiHP-A samples and their most probable band assignments based on literature data (41). **b)** Computed Raman spectra of molecules from Figure 12, with various Q^n connectivities.*

In Applications of Molecular Modeling to Challenges in Clean Energy; Fitzgerald, G., et al.;
ACS Symposium Series; American Chemical Society: Washington, DC, 2013.

Since the NMR data are firmly established by theory, we decided to use molecular modeling to see if indeed the differential Raman cross section, for structure identification in the zeolite and glass research and industry. Most researchers largely agree that the symmetric and asymmetric Si-O vibrations roughly in the 650-1250 cm^{-1} range can be assigned to the Qn connectivities in silicates while the Si-O-Si bending vibrations in 150-650 cm^{-1} range mostly depend on the ring structure of silicates (*41*). Using the most established assignments for example for the Raman spectra in Figure 9 c), we noticed with surprise that the Q^n connectivities with Raman do not reflect the same distribution as measured with the ^{29}Si NMR. For better visualization Figure 11 a) repeats the SiHP-A and SiHP-B Raman spectra. The most puzzling is the large Q^1 and Q^2 bands that are extremely low in the NMR spectra (Figure 9).

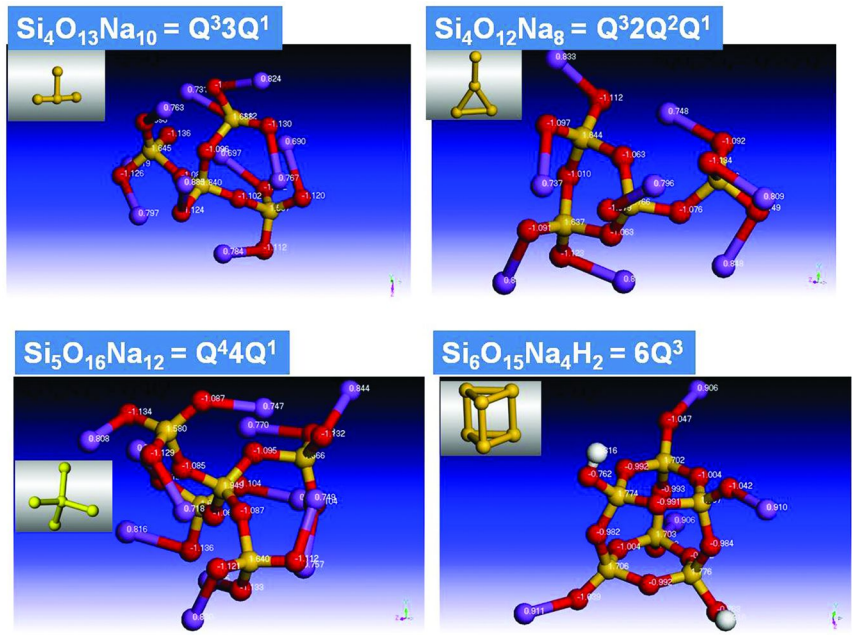

Figure 12. Minimized molecule structures created for model DFT calculation of Raman intensities for various Q^n [SiO_4] connectivities. Colors: Si = yellow; O = red; Na = purple; H = white. Inserts show the silicone backbone of molecules. (see color insert)

Since the NMR data are firmly established by theory, we decided to use molecular modeling to see if indeed the differential Raman cross section, $\delta\sigma_i/\delta\Omega$, where σ_i is the cross section and Ω is the angle of of signal collection, could be responsible for the different scattering activities of differently connected Si-O bonds (*38*, *42*, *43*). For this we created a few simple models with various Q^n connectivities, shown in Figure 12. DFT based Raman models with 532 nm incident light wavelength (equals to the experimental setup) were computed using the DMOL^3 (*44*, *45*) module of the Materials Studio package from

Accelrys. Gradient corrected PBE (*46*) functional was applied with all electron approximation in the double numeric basis set, DNP, and geometry optimization was performed until energy change remained below 10^{-5} Hartree. Raman shifts and activities were computed for this energy minimized structure with the DMOL^3 implementation of polarizability tensor calculation (*43*, *47*). As Figure 11 b) clearly demonstrates, the Q^1 and Q^2 intensities of computed Raman spectra are about one order of magnitude bigger than the intensity of Q^3 and almost two orders of magnitude bigger than that of Q^4 that approaches zero on this intensity scale. This unexpected molecular modeling result became the basis of a more extended novel reference to the relative intensities of ^{29}Si NMR and Raman spectra (*38*).

4. Identification of $Ti(OH)_4$ Nanoparticles in Highly Active and Selective Microporous Titanium Silicate Catalyst

The third example for utilizing molecular modeling in favor of clean energy gain is related to the properties of an MFI structured titanium silicate catalyst. Saving energy is a preferred way of making energy consumption more environment-friendly. Chemists and chemical engineers can contribute to this effort by improving the efficiency of technologies. It is estimated that 90 % of all chemical products are affected by catalytic processes (*48*). Thus, improving catalyst activity and selectivity, hence reducing reaction temperatures, pressures, and waste, has tremendous impact on the overall energy saving and environment improvement worldwide.

The discovery of TS-1, an MFI structured zeolite catalyst containing isomorphously substituted Ti^{4+} in its lattice (*49*), started for example a technological revolution in selective catalytic oxidation (*50*, *51*). Direct oxidation of propylene to propylene oxide, selective phenol hydroxylation to catechol, and salt-free production of cyclohexanone oxime via ammoximation are the first large scale commercial examples for the use of TS-1 (*51*), but many other catalysts and processes are also under development.

TS-1 is able to selectively oxidize for example paraffins by H_2O_2 into alcohols or aldehydes at near ambient conditions, which had been the unique province of enzymes before (*51–55*). Its unique catalytic activity and selectivity is generally associated with the presence of isolated, tetrahedral Ti^{4+} ions isomorphously inserted into the micro channel walls of the ZSM5 lattice as modeled in Figure 1 c). Such ions, embedded into their siliceous environment, are thought to be able to form temporarily peroxo ions with the most frequently effective H_2O_2 oxidizing agent and these titanium connected peroxo ions would transfer oxygen into the reactant molecules (*51*). A well prepared defect-free TS-1 is highly hydrophobic (*50*, *51*, *56*, *57*), presumably for the same reasons as the silicalite, discussed in the first part of this chapter. Any deviation from this strict structure is considered to deteriorate catalyst activity, selectivity, and or decompose H_2O_2 without utilizing its oxidation power. Therefore the oxidation state and coordination of titanium ions in the final catalysts are keenly analyzed.

In Applications of Molecular Modeling to Challenges in Clean Energy; Fitzgerald, G., et al.;
ACS Symposium Series; American Chemical Society: Washington, DC, 2013.

A sharp UV band in the 204-213 nm (47,000 – 49,000 cm^{-1}) range is a fingerprint for isolated, tetrahedral Ti^{4+} ions surrounded with four [SiO_4] tetrahedra. Therefore, UV spectroscopy is used most frequently to test if this peak is indeed present in the TS-1 product without any further adsorption at >235 nm (<42,500 cm^{-1}), which would mark the presence of higher coordinated, lower than 4+ oxidation state, non-isolated, and/or extra lattice titanium ions (*50*, *58*, *59*). During our UV tests of literally hundreds of differently fabricated samples (*60*, *61*), we noticed that some samples give an absorption maximum at around 225 nm (44,500 nm), a region for which none of the known oxidation or coordination states of titanium had been assigned. Some typical DR-FTUV spectra for the variously prepared TS-1 samples are illustrated in Figure 13 a).

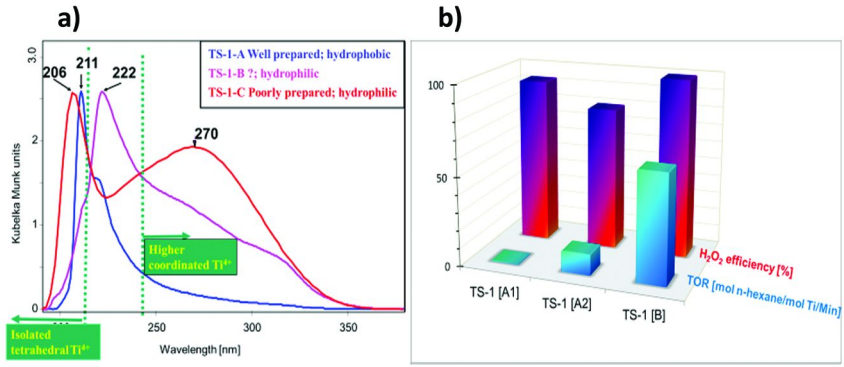

Figure 13. ***a)*** *Typical DR-FTUV (diffuse reflectance Fourier transform ultraviolet) spectra of a well prepared TS-1 catalyst (A) with isolated tetrahedral Ti^{4+} ions isomorphously inserted into a ZSM5 lattice; a poorly prepared TS-1 catalyst (C) that has plenty of higher coordinated titanium atoms and extra lattice $Ti_xO_y(OH)_z$ particles; and an active and selective TS-1 catalyst (B) in which the condition of Ti^{4+} ion is unknown (16, 53, 54, 63).* ***b)*** *The turnover rates and efficient use of H_2O_2 in the selective oxidation of n-hexane are higher over the best TS-1-B type catalyst (53, 54, 63) than over the best "regular" TS-1 catalysts (A1 and A2) (69, 70). (see color insert)*

Catalytic tests with these TS-1-B type samples indicated that they are highly active and selective oxidation catalysts with aqueous H_2O_2 despite of their hydrophilic character (*62*). In fact, it was observed that their activity for the selective oxidation of saturated hydrocarbons as well as their efficiency for H_2O_2 usage exceeds the levels of any other known TS-1 catalysts (*53*, *54*, *63*) even without the use of any co-solvent, which is usually considered to be necessary for such reactions (*51*, *55*, *57*, *64–68*). Figure 13 b) shows that the catalytic activity and H_2O_2 utilization over our best TS-1-B type catalyst is better than those over the best "regular" TS-1 catalysts published for this reaction.

These unusual catalytic properties of the TS-1-B type catalysts have generated various speculations about the possible molecular structure of these catalysts, which is reflected in the unusual position of their main UV absorption

In Applications of Molecular Modeling to Challenges in Clean Energy; Fitzgerald, G., et al.;
ACS Symposium Series; American Chemical Society: Washington, DC, 2013.

band. Assumptions ranged from isolated tetrahedral Ti^{4+} atoms with greater than tetrahedral coordination (*71*), to highly dispersed extra lattice TiO_2 particles (*61*), edge connections between $[TiO_4]$ and $[SiO_4]$ tetrahedra instead of the usual corner connections (*72*), tetrahedral Ti^{4+} ions being attached to the lattice at isomorphous position but with one to three broken Ti-O-Si connections (*53*, *63*, *73*), and other ideas, but none of them has been confirmed. Therefore, we decided to perform molecular modeling calculations to see, which one of the proposed or not proposed structures would give back the characteristic UV absorption of TS-1-B.

First we considered a variety of possible extra-lattice particles that might form in the zeolite channels causing the odd ~225 nm UV absorption. We learned more than one thing from these modeling attempts: i) The TiO_2 stoichiometry is valid only for a virtually infinite crystal lattice. Without double bonds between the Ti and O atoms such stoichiometry cannot be approached and such double bonds have never been observed in real life. Consequently assumptions in the literature about the presence of tiny TiO_2 fragments in poorly prepared samples can only mean crystallites composed of at least several ten atoms, hence these must be outside of the TS-1 crystals.; ii) From small, extra lattice $Ti_xO_y(OH)_z$ molecules only those can fit into the zeolite channels that do not contain more than two titanium atoms, as an example in Figure 14 b) illustrates. One could hardly imagine how could we gain superior catalytic activity even in this case, when the pores are literally blocked for diffusion.; iii) Edge connected tetra- or octahedral units fall apart into corner connected ones upon energy minimization, i.e., two neighboring units cannot share more than one oxygen, which has long been known in silica chemistry (*74*). An example for such decomposition is shown in Figure 14; iv) Every small octahedral $Ti_xO_y(OH)_z$ molecule that we tested decomposed into tetrahedral molecules upon energy minimization, as one example shows in Figure 14. Many more examples are discussed in reference (*75*). DFT calculations were used for these energy minimizations using the previously mentioned DMOL^3 (*44*, *45*) program. DND basis set (double-numerical atomic orbitals supplemented with d-orbitals) and BLYP (*76*) exchange-correlation functional were employed and geometry optimizations were converged until residual forces were less than 0.002 Hartree/Bohr (*75*).

Next we tested if the idea of broken Si-O-Ti bonds with tetrahedral Ti^{4+} still attached to the isomorphous position could generate the unusual UV absorption maxima. Since the TS-1 unit cell has 296 atoms, a DFT calculation for the entire zeolite was beyond our computing capabilities within a reasonable time. Therefore, we elected to use an embedded QM/MM (quantum mechanical/molecular mechanical) approach using the program QMERA (*77*). Within this program we selected a chemically significant area around the Ti^{4+} atom and treated it with DFT using the DMOL^3 (*44*, *45*) as described above. This QM region was mechanically embedded into a large periodic zeolite lattice, which was treated with molecular mechanics using the GULP program (*78*). For the MM approach Dreiding force field (*23*) was applied with partial charges on the atoms computed by electronegativity equalization (*24*). The UV spectra were calculated with TD-DFT (time dependent DFT) from DMOl3 (*79*) for the QM atoms within the minimized structure. Further details of these QM/MM calculations are described in reference (*75*).

In Applications of Molecular Modeling to Challenges in Clean Energy; Fitzgerald, G., et al.;
ACS Symposium Series; American Chemical Society: Washington, DC, 2013.

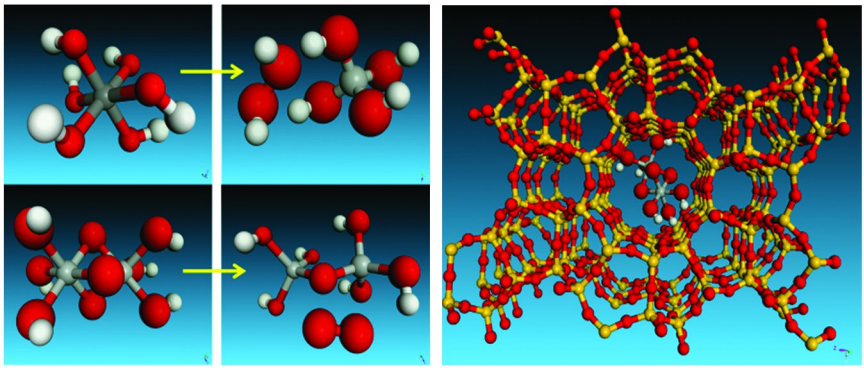

Figure 14. Hypothetical small octahedral molecules [$Ti(OH)_6$ and $Ti_2O_3(OH)_6$] fall apart to their tetrahedral forms upon energy minimizing their structures. Bigger molecules than the latter one cannot fit even into the straight zeolite channel, i.e., extralattice TiO_2 fragments can only reside outside the crystallites (75). Colors: Si = yellow; O = red; Ti = grey; H = white. (see color insert)

First we established the accuracy of these calculations by modeling the UV spectrum of the well described, defect free TS-1 material. As Figure 15 demonstrates, the experimental and computed results are in outstanding fit. Next we tested a TS-1 structure in which three Si-O-Ti bonds around the Ti^{4+} atom are broken. As the minimized structure in Figure 16 indicates, the titanium moves in this case from its original isomorphous position in the pore wall into a more confined space in the neighboring five-member ring, presumably to gain higher coordination with more oxygen atoms in its proximity as the matching model UV spectrum indicates. Thus, this theory is not the proper explanation for the 225 nm UV maximum. However, Figure 17 illustrates that we got an excellent match by assuming that a $Ti(OH)_4$ molecule is confined into the zeolite channel. This molecule was one of the very few small molecules that proved to be energetically stable after the above described energy minimizing tests. Thus modifying the "highly dispersed" expression to "molecularly dispersed" in one of the above mentioned speculations (*61*), it appears that this can indeed explain the odd 225 nm UV absorption maximum of our superior but hydrophilic titanium silicate catalyst. Such molecules might also be present in many other TS-1 catalysts in which the presence of this UV band has been overlooked (*75*).

In Applications of Molecular Modeling to Challenges in Clean Energy; Fitzgerald, G., et al.;
ACS Symposium Series; American Chemical Society: Washington, DC, 2013.

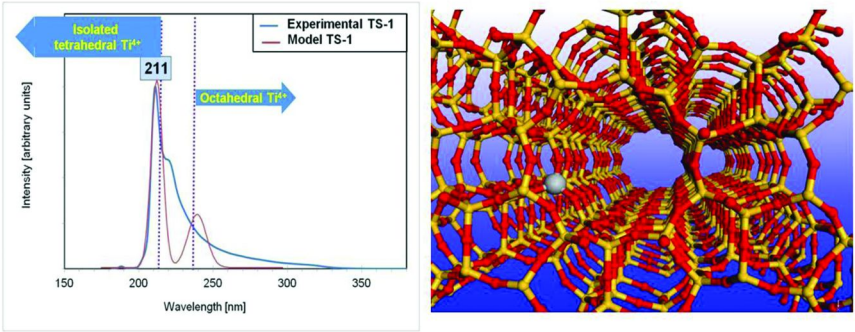

Figure 15. The TD-DFT computed UV spectrum of the QM/MM minimized TS-1 structure is in good agreement with the experimental UV spectrum of a well prepared TS-1 material (75). Color codes are the same as in Figure 14. (see color insert)

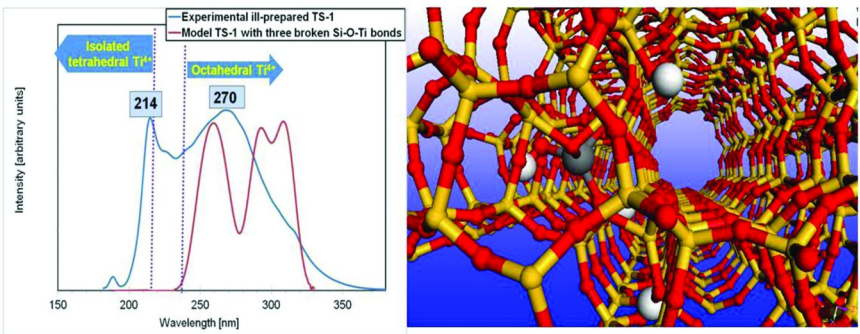

Figure 16. The QM/MM minimized structure of a TS-1 catalyst with three broken Si-O-Ti bonds indicates that the Ti atom moves from its original position on the surface of the main channel (compare with Figure 15) toward the more confined environment of five member rings. The matching TD-DFT computed UV spectrum could only fit to the higher coordinated titanium part of the experimental UV spectrum of an "ill-prepared" TS-1 catalyst. Color codes are the same as in Figure 14. (see color insert)

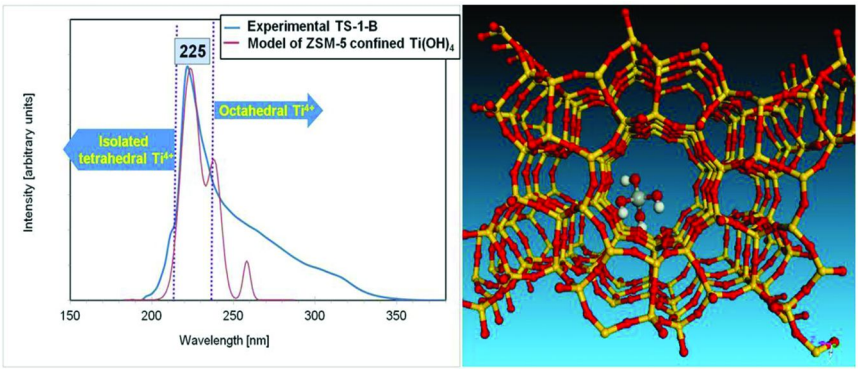

Figure 17. The TD-DFT computed UV spectrum of the QM/MM minimized $Ti(OH)_4$ molecule confined in a ZSM5 channel is in excellent agreement with the experimental UV spectrum of the hydrophilic TS-1-like material with superior catalytic activity for paraffin oxidation (53, 54, 63, 75). Color codes are the same as in Figure 14. (see color insert)

References

1. *Silica and Silicates in Modern Catalysis*; Halasz, I., Ed.; Transworld Research Network: Kerala, India, 2010.
2. Tchernev, D. A. *Waste Heat Driven Automotive Air Conditioning System*, International Sorption Heat Pump Conference, Munich, Germany, 1999.
3. Restuccia, G.; Freni, A.; Russo, F.; Vasta, S. *Appl. Therm. Eng.* **2005**, *25*, 1419.
4. Ellison, E. H.; Moodley, D.; Hime, J. *J. Phys. Chem. B* **2006**, *110*, 4772.
5. Navalon, S.; Alvaro, M.; Garcia, H. *J. Hazard. Mater.* **2009**, *166*, 553.
6. Xu, R., Pang, W., Yu, J., Huo, Q., Chen, J., *Chemistry of Zeolites and Related Porous Materials: Synthesis and Structure*; John Wiley & Sons: Singapore, 2007.
7. *Zeolites and Catalysis*; Cejka, J., Corma, A., Zones, S., Eds.; Wiley-WCH Verlag GmbH & Co.: Weinheim, Germany, 2010.
8. Flanigen, E. M.; Bennett, J. M.; Grose, R. W.; Cohen, J. P.; Patton, R. L.; Kirchner, R. M.; Smith, J. V. *Nature* **1978**, *271*, 512.
9. Halasz, I.; Kim, S.; Marcus, B. *J. Phys. Chem. B* **2001**, *105*, 10788.
10. Polanyi, M. *Trans. Faraday Soc.* **1932**, *28*, 316.
11. Gregg, s. J., Sing, K. S. W., *Adsorption, Surface Area and Porosity*; Academy Press: London, 1982.
12. Nguyen, C.; Do, D. D. *J. Phys. Chem.* **1999**, *103*, 6900.
13. Halasz, I.; Kim, S.; Marcus, B. *Mol. Phys.* **2002**, *100*, 3123.
14. Halasz, I.; Agarwal, M.; Marcus, B.; Cormier, W. E. *Microporous Mesoporous Mater.* **2005**, *84*, 318.
15. Olson, D. H.; Haag, W. O.; Borghard, W. S. *Microporous Mesoporous Mater.* **2000**, *35-36*, 435.

In Applications of Molecular Modeling to Challenges in Clean Energy; Fitzgerald, G., et al.;
ACS Symposium Series; American Chemical Society: Washington, DC, 2013.

16. Halasz, I.; Agarwal, M.; Senderov, E.; Marcus, B.; Cormier, W. E. *Stud. Surf. Sci. Catal.* **2005**, *158*, 647.
17. Brunauer, S.; Deming, L. S.; Deming, W. E.; Teller, E. *J. Am. Chem. Soc.* **1940**, *62*, 1723.
18. Sing, K. S.; Everett, D. H.; Haul, R. A. W.; Moscou, L.; Pierotti, R. A.; Rouquerol, J.; Siemieniewska, T. *Pure Appl. Chem.* **1985**, *57*, 603.
19. Webb, P. A., Orr, C. *Analytical Methods in Fine Particle Technology*; Micromeritics Instrument Co.: Norcross, GA, 1997.
20. Carrot, P. J. M.; Sing, K. S. W. *Stud. Surf. Sci. Catal.* **1991**, *62*, 685.
21. Theocaris, C. R.; Gelsthorpe, M. R. *Stud. Surf. Sci. Catal.* **1988**, *39*, 541.
22. Kornatowski, J.; Rosdanowski, M. *Proceedings of the 12th International Zeolite Conference*, Baltimore, MD, 1998, Treacy, M. M. J., Marcus, B. K., Bisher, M. E., Higgins, J. B., Eds.; Materials Research Society: Warrendale, Pennsylvania, 1999, 285.
23. Mayo, S. L.; Olafson, B. D.; Goddard, W. A., III *J. Phys. Chem.* **1990**, *94*, 8897.
24. Rappe, A. K.; Goddard, W. A., III *J. Phys. Chem.* **1991**, *95*, 3358.
25. Jorgensen, W. L.; Chandrasekhar, J.; Madura, J. D.; Impey, R. W.; Klein, M. L. *J. Chem. Phys.* **1983**, *79*, 926.
26. Karasawa, N.; Goddard, W. A., III *J. Phys. Chem.* **1989**, *93*, 7320.
27. Halasz, I., Moden, B., Petushkov, A., Agarwal, M., Liang, J-J., to be published.
28. Pullukat, T. J.; Patterson, R. E. Porous Silica in Transition Metal Polymerization Catalysis. In *Handbook of Transition Metal Polymerization Catalysis*; Hoff, R., Mathers, R. T. Eds.; John Wiley & Sons: Hoboken, NJ, 2010, p 29.
29. *Colloidal Silica, Surfactant Science Series*; Bergna, H. E., Roberts, W. O., Eds.; CRC Press Taylor & Francis Group: Boca Raton, FL, 2006; Vol. 131.
30. Iler, R. K. *The Chemistry of Silica*; John Wiley & Sons: New York, 1979.
31. Livage, J. *Stud. Surf. Sci. Catal.* **1994**, *85*, 1.
32. Halasz, I.; Li, R.; Agarwal, M.; Miller, N. *20th Congress of the North American Catalysis Society*, Houston, TX, 2007, O-S2-04.
33. Halasz, I.; Agarwal, M.; Li, R.; Miller, N. In *Characterization of Porous Solids VIII*; Kaskel, S., Llewellyn, P., Rodrigez-Reinoso, F., Seaton, N. A., Eds.; RSC Publishing: Cambridge, U.K., 2009; Vol 318, pp 416.
34. Halasz, I.; Agarwal, M.; Patterson, R. E. *Stud. Surf. Sci. Catal.* **2010**, *175*, 209.
35. Depla, A.; Lesthaeghe, D.; van Erp, T. S.; Aerts, A.; Houthoofd, K.; Fan, F.; Li, C.; van Speybroeck, V.; Waroquier, M. M.; Kirschhock, C. E.; Martens, J. A. *J. Phys. Chem. C* **2011**, *115*, 3562.
36. Depla, A.; Verheyen, E.; Veyfeyken, A.; van Houteghem, M.; Houthoofd, K.; van Speybroeck, V.; Waroquier, M.; Kirschhock, C. E.; Martens, J. A. *J. Phys. Chem. C* **2011**, *115*, 11077.
37. Halasz, I., Kierys, A., Goworek, J., Liu, H., Patterson, R. E. *22nd Congress of the North American Catalysis Society*, Detroit, MI, 2011.
38. Halasz, I.; Kierys, A.; Goworek, J.; Liu, H.; Patterson, R. E. *J. Phys. Chem. C* **2011**, *115*, 24788.

39. Zaleski, R.; Kierys, A.; Dziadosz, M.; Goworek, J.; Halasz, I. *RSC Adv.* **2012**, *2*, 3729.
40. Engelhard, G.; Jancke, H.; Hoebbel, D.; Wieker, D. *Z. Chem.* **1974**, *14*, 109.
41. Halasz, I.; Agarwal, M.; Li, R.; Miller, N. *Microporous Mesoporous Mater.* **2010**, *135*, 74.
42. McCreery, R. L. *Raman Spectroscopy for Chemical Analysis*; Wiley Interscience: New York, 2000.
43. Porezag, D.; Pederson, M. R. *Phys. Rev. B* **1996**, *54*, 7830.
44. Delley, B. J. *J. Chem. Phys.* **1990**, *92*, 508.
45. Delley, B. J. *J. Chem. Phys.* **2000**, *113*, 7756.
46. Perdew, J. P.; Burke, K.; Ernzerhof, M. *Phys. Rev. Lett.* **1996**, *77*, 3865.
47. Morisato, J., unpublished results.
48. Breakthrough Catalysts, Editorial. *R&D Magazine*, September 2005, p 20.
49. Taramasso, M.; Perego, G.; Notari, B. U.S. Patent 4,410,501, 1983.
50. Notari, B. *Adv. Catal.* **1996**, *41*, 253.
51. Clerichi, M. G. In *Metal Oxide Catalysis*; Jacson, S., Hargreaves, J., Eds.; Wiley-WCH: Wenheim, Germany, 2010, p 713.
52. Huybrechts, E. R. C.; Vaesen, I.; Li, H. X.; Jacobs, P. A. *Catal. Lett.* **1991**, *8*, 237.
53. Halasz, I.; Agarwal, M.; Senderov, E.; Marcus, B. *Stud. Surf. Sci. Catal.* **2003**, *145*, 435.
54. Halasz, I.; Agarwal, M.; Senderov, E.; Marcus, B. *Catal. Today* **2003**, *81*, 227.
55. Shul'pin, G. B.; Kirillova, M. V.; Sooknoi, T.; Pombeiro, A. J. L. *Catal. Lett.* **2008**, *123*, 135.
56. Ratnasamy, P.; Srinivas, D.; Knozinger, H. *Adv. Catal.* **2004**, *48*, 1.
57. Tatsumi, T. In *Zeolites and Catalysis*; Cejka, J., Corma, A., Zones, S., Eds.; Wiley-WCH Verlag GmbH & Co.: Weinheim, Germany, 2010.
58. Boccuti, M.; Rao, K.; Zecchina, A.; Leofanti, G.; Pertini, G. *Stud. Surf. Sci. Catal.* **1989**, *48*, 133.
59. Klein, S.; Weckhuysen, B.; Martens, J.; Maier, W.; Jacobs, P. *J. Catal.* **1996**, *163*, 489.
60. Senderov, E.; Hinchey, R.; Halasz, I.; Marcus, A.; Agarwal, M.; Connolly, P. *13th International Congress on Catalysis*, Paris, France, 2004, P-258.
61. Senderov, E.; Hinchey, R.; Marcus, A.; Agarwal, M.; Halasz, I.; Connolly, P.; Marcus, B. *Stud. Surf. Sci. Catal.* **2005**, *158*, 717.
62. Chammingkwan; Hoelderich, W. F.; Mongkhonshi, T.; Kanchanawanichakul, P. *Appl. Catal., A* **2009**, *352*, 1.
63. Halasz, I.; Agarwal, M.; Senderov, E.; Marcus, B. *Appl. Catal., A* **2003**, *241*, 167.
64. Bianchi, D.; Balducci, L.; Bortolo, R.; D'Aloisio, R.; Ricci, M.; Spano, G.; Tassinari, R.; Tonini, C.; Ungarelli, R. *Adv. Synth. Catal.* **2007**, *349*, 979.
65. Zhang, Z.; Kang, J.; Wang, Y. *React. Kinet. Catal. Lett.* **2007**, *92*, 49.
66. Shul'pin, G. B.; Sooknoi, T.; Shul'pina, L. S. *Pet. Chem.* **2008**, *48*, 36.
67. Fan, W.; Wu, P.; Tatsumi, T. *J. Catal.* **2008**, *256*, 62.
68. Ramachandran, C. E.; Du, H.; Kim, Y. J.; Kung, M. C.; Snurr, R. Q.; Broadbelt, L. J. *J. Catal.* **2008**, *253*, 148.

69. Clerici, M. G., Anfossi, B., Bellussi, G. U.S. Patent 5,126,491, 1992.
70. Huybrechts, D. R. C.; Buskens, P. L.; Jacobs, P. A. *J. Mol. Catal.* **1992**, *71*, 129.
71. Klaas, J.; Schulz-Ekloff, G.; Jaeger, N. I. *J. Phys. Chem. B* **1997**, *101*, 1305.
72. Tuel, A; Ben Taarit, Y. *Appl. Catal., A* **1994**, *110*, 137.
73. Yang, G.; Lan, X.; Zhuang, J.; Ma, D.; Zhou, L.; Liu, X.; Han, X.; Bao, X. *Appl. Catal., A* **2008**, *337*, 58.
74. Liebau, F. *Structural Chemistry of Silicates*; Springer-Verlag: Heidelberg, Germany, 1985.
75. Halasz, I.; Liang, J-J.; Fitzgerald, G. *Catal. Lett.* **2011**, *141*, 948.
76. Lee, C.; Yang, W; Parr, R. G. *Phys. Rev. B* **1988**, *37*, 786.
77. Sherwood, P.; De Vries, A. H.; Guest, F. M.; Schrenkenbach, G.; Catlow, C. R. A.; French, S. A.; Sokol, A. A.; Bomley, S. T.; Thiel, W.; Turner, A. J.; Billeter, S.; Terstegen, F.; Thiel, S.; Kendrick, J.; Rogers, S. C.; Casci, J.; Watson, M.; King, F.; Karlsen, E.; Sjovoll, M.; Schafer, A.; Lennartz, C. *J. Mol. Struct.: THEOCHEM* **2003**, *632*, 1.
78. Gale, J. D.; Rohl, A. L. *Mol. Simul.* **2003**, *29*, 291.
79. Delley, B. *J. Phys.: Condens. Matter* **2010**, *22*, 384208.

Chapter 8

Understanding Electrocatalytic Activity Enhancement of Bimetallic Particles to Ethanol Electro-Oxidation: Ethanol Adsorption and Decomposition on Pt_nM (n=6 and 9; M=Pt, Ru, and Sn)

Zhenfeng Xu and Yixuan Wang*

Computational Chemistry Laboratory, Department of Natural Sciences, Albany State University, Albany, Georgia 31705
***E-mail: yixuan.wang@asurams.edu**

The adsorption and dehydrogenation of ethanol through both hydroxyl and CH_2 groups over bimetallic clusters Pt_nM (n=6 and 9; M=Pt, Sn, and Ru) have been investigated with the density functional theory and statistical rate theory. One-layer Pt_6M (M=Pt, Sn, and Ru) and two-layer $(Pt_6M)Pt_3$ clusters are used to model the catalyst surfaces of bimetallic nanoparticles. The reaction potential energy profiles show that on pure Pt a favorable dehydrogenation channel is the decomposition of CH adsorption complex, while oppositely on the Sn site of the PtSn the hydroxyl adsorption is more favorable with respect to kinetics and thermodynamics. However, on the Pt-Ru alloy both adsorption reaction paths show low energy barriers. In addition, by including the energetics of the adsorption steps the overall rate constants of these three systems are approximately calculated in 200-500K by classical transition state theory. It is concluded that, k_{Pt2Sn1} is 2-12 times higher than k_{Pt2Ru1} and 1.0×10^4–8.8×10^4 times higher than k_{Pt}. The rate constants are all positive temperature dependent, and over the bimetallic catalysts Pt-Sn and Pt-Ru the hydroxyl adsorption dehydrogenation reaction is predicted to be more favorable.

In Applications of Molecular Modeling to Challenges in Clean Energy; Fitzgerald, G., et al.;
ACS Symposium Series; American Chemical Society: Washington, DC, 2013.

Introduction

A direct ethanol proton exchange membrane fuel cell (PEMFC) offers a promising alternative power source because of its superiority to the most studied H_2-O_2 PEMFC in a few aspects. Direct ethanol fuel cells provide attractive mass energy density (8.1kW·h/kg for ethanol vs. 0.42kW·h/kg for H_2 1.5wt% storage and 6.1kW·h/kg for methanol) (*1*). As a liquid fuel, it also avoids storage issue associated with H_2 gas fuel cell. In addition, ethanol is a renewable fuel since it can be produced in a great quantity from biomass and it is much less toxic than methanol as well. However, on the other hand, the complete oxidation of ethanol to H_2O and CO_2 is much more difficult than those of H_2 as well as methanol because of C-C bond in ethanol. Much effort has already been put into searching for efficient electrocatalysts for ethanol electro-oxidation reaction (EER) and considerable progress has also been made (*1–6*). For instance, PtSn/C has recently been demonstrated the ability to enhance the electrocatalytic activity of Pt towards the EER with respect to increasing current density as well as to lowering the onset potential of ethanol oxidation by approximately 0.2V compared to Pt alone (*1*, *3*, *7*, *8*). However, the experimental result shows that ethanol is still far from complete oxidation even at the PtSn/C anode, and the oxidation products are measured to be acetaldehyde (22.8%), acetic acid (74.7%), and CO_2 (2.5%) (*9*).

The mechanism of ethanol electro-oxidation on PtSn was widely interpreted with a bifunctional mechanism and ligand effect (*10*, *11*), where dissociative adsorption of ethanol occurs on platinum sites and tin primarily promotes adsorption and dissociation of water to form OH oxidizing intermediates from ethanol (*4*). Other researchers suggested rather similar mechanisms for the EER (*2*, *3*, *8*, *12*). Although some interesting assumptions have been made, several essential issues still remain uncertain. For example, although Sn and Ru have similar activity, and Re even shows more active than Sn to water dissociative adsorption (*13*). PtRu is not as active as PtSn to the EER. Thus, Sn must have another effect besides ligand effect and enhancing H_2O dissociation because otherwise Ru should display almost the same activity as Sn for the EER (*4*).

To well understand electrocatalytic enhancement of PtSn for the EER and eventually design more efficient catalysts for the EER, it is essential to investigate adsorption and dissociation of both water and ethanol over Pt-based bimetallic particles at an atomic level. Recently, the authors extensively investigated the adsorption and decomposition of water on Pt-based bimetallic clusters with the density functional theory (DFT) (*13*), and together with other pioneering work concluded that from both kinetic and thermodynamic viewpoints Sn is more active to water decomposition than pure Pt and the PtRu alloy, which well supports the assumption of the bi-functional mechanism that Sn site primarily accelerates the dissociation of H_2O. Regarding the electro-oxidation of ethanol on Pt, much theoretical effort has already been devoted to understanding its reaction mechanism, mainly with plane-wave based DFT-slab calculations (*14–16*). However, few theoretical studies have been reported on the EER over the Pt-based bimetallic surface (*15*, *17*). Alcala et. al discussed the electro-catalytic mechanism of ethanol on Pt/SiO_2 and Pt_3Sn/SiO_2 with periodic, self-consistent DFT with Perdew-Wang 1991 generalized gradient approximation

In Applications of Molecular Modeling to Challenges in Clean Energy; Fitzgerald, G., et al.;
ACS Symposium Series; American Chemical Society: Washington, DC, 2013.

(*15*), indicating that the lowest energy pathway for acetaldehyde formation is via the ethoxy species (CH_3CH_2O, reaction a) on Pt_3Sn while via the 1-hydroxyethyl species (CH_3CHOH, reaction b; * stands for the adsorption site.) on Pt. Both the α-hydrogen and hydroxyl adsorptions on Pt, as well as on the alloyed transition metal M sites of Pt_3M, were considered as initial reaction steps (*17*).

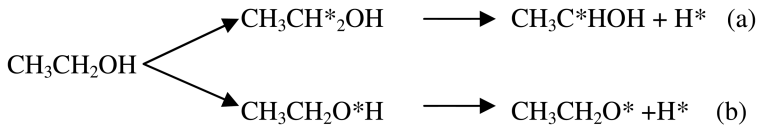

In the present work we will focus on the adsorption and decomposition mechanisms of ethanol on Pt_nM (n=6, 9; M=Pt, Ru, Sn). To clarify the initial steps of the ethanol electro-oxidation reaction on Pt_nM (n=6, 9; M=Pt, Ru, Sn), the reaction pathways for each alloy catalyst are compared with respect to thermodynamics and kinetics, and the overall reaction rate.

Methodology and Bimetallic Models

One-layer extended cluster model Pt_6M (M=Pt, Ru, and Sn) as well as two-layer model $(Pt_6M)Pt_3$ have been applied to study the adsorption and decomposition of CH_3CH_2OH over the nano-particles that usually have a well-defined face-centered cubic (fcc) lattice. The geometric and electronic structures of Pt_nM (n=6 and 9; M=Pt, Ru, Sn) in Figure 1 were studied in detail in our previous paper (*13*). In this work the geometric parameters of the ethanol adsorption complexes have been partially optimized with the fixed bimetallic cluster by the B3PW91 density functional theory (*18*, *19*) as implemented in Gaussian 03 (*20*). The LANL2DZ type of effective core potential (ECP) and the corresponding double-ξ basis set were employed for all of the involved metal atoms (*21*), while the basis sets for H, C and O are 6-311++G(d, p) (*22*). In the LANL2DZ ECP scheme, the valence electron shells for the ground state of Pt, Sn, and Ru, are $5s^25p^65d^96s^1$, $5s^25p^2$, and $4s^24p^64d^65s^2$, respectively. The transition states (TS) for dissociations of the adsorbed ethanol were directly searched for by either the transit guided quasi-Newton (STQN) method (*23*) or the eigenvector following with the Berny algorithm (*24*). A frequency analysis for Pt_6M-ethanol system was done at the same level as optimization for all stationary points to characterize the stationary points and make the zero point energy (ZPE) corrections. The dissociation transition state (TS) structures of adsorbed ethanol can be assigned by the imaginary vibration mode with an unique significant imaginary frequency. There are usually a few small imaginary frequencies in frequency analysis due to the fixed bimetallic cluster structure. Ethanol adsorption energy (E_{ads}) was defined as the energy difference between the adsorption complex and the summation of the cluster at ground state and ethanol, $E_{ads} = E(CH_3CH_2OH\text{-}Pt_nM \text{ in ground state}) - [E(CH_3CH_2OH) + E(Pt_nM \text{ in ground state})]$. The more negative E_{ads} is, the stronger the adsorption between ethanol and the cluster is. The energy barrier (E_a) and the dissociation energy (E_{diss}) refer

In Applications of Molecular Modeling to Challenges in Clean Energy; Fitzgerald, G., et al.;
ACS Symposium Series; American Chemical Society: Washington, DC, 2013.

to the energies of transition state and the dehydrogenation product relative to the adsorption complex, respectively.

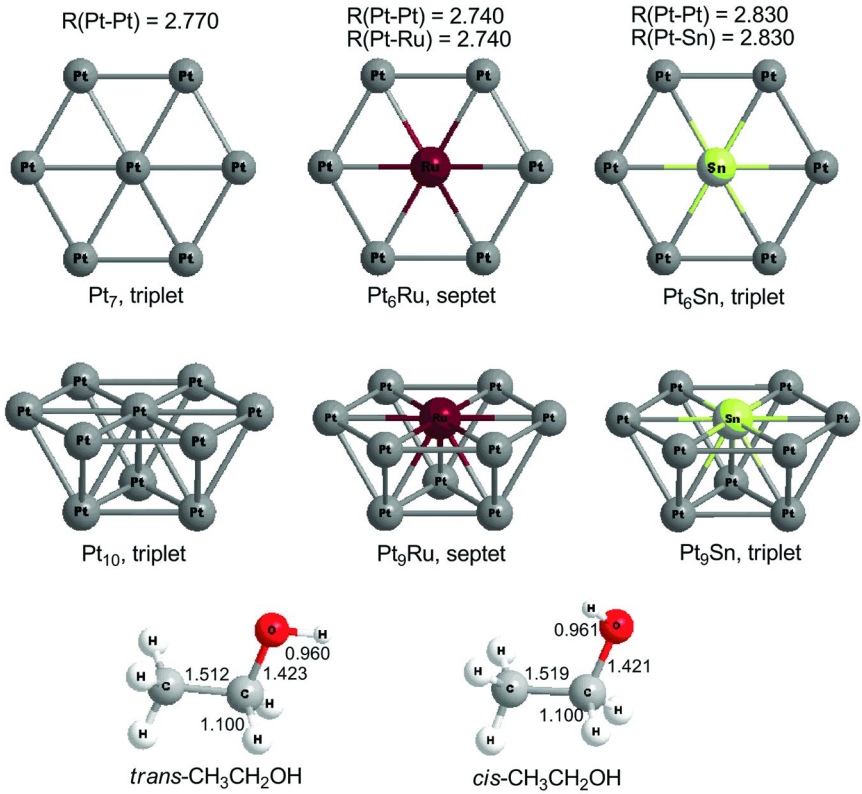

Figure 1. Structures of ethanol and Pt_nM (n=6 and 9; M=Pt, Ru, Sn) models with some bond length parameters in Å.

Results and Discussion

CH_3CH_2OH Adsorption and Decomposition over Pt_6M Clusters (M=Pt, Ru, and Sn)

As shown in Figure 1, Pt_7 is a one-layer model consisting of a hexagon of six Pt atoms surrounding a central Pt atom, while in the Pt_6M bimetallic alloy the central atom is replaced by the alloyed atom Sn or Ru. *Trans*-C_2H_5OH has slightly lower energy by 0.0003eV than the *cis*-C_2H_5OH. The geometric parameters of both structures are almost the same except for the dihedral angle of ÐHOCC, 180.0 and 59.9° for *trans*- and *cis*-C_2H_5OH, respectively. They can isomerize readily each other because of a low energy barrier 0.046 eV at the B3PW91/6-311++G(d, p) level. The optimized geometries of ethanol adsorbed on Pt_7, Pt_6Ru, and Pt_6Sn are shown in Figures 2, 3, and 4, respectively, while their relative energy profiles are illustrated in Figure 5.

In Applications of Molecular Modeling to Challenges in Clean Energy; Fitzgerald, G., et al.;
ACS Symposium Series; American Chemical Society: Washington, DC, 2013.

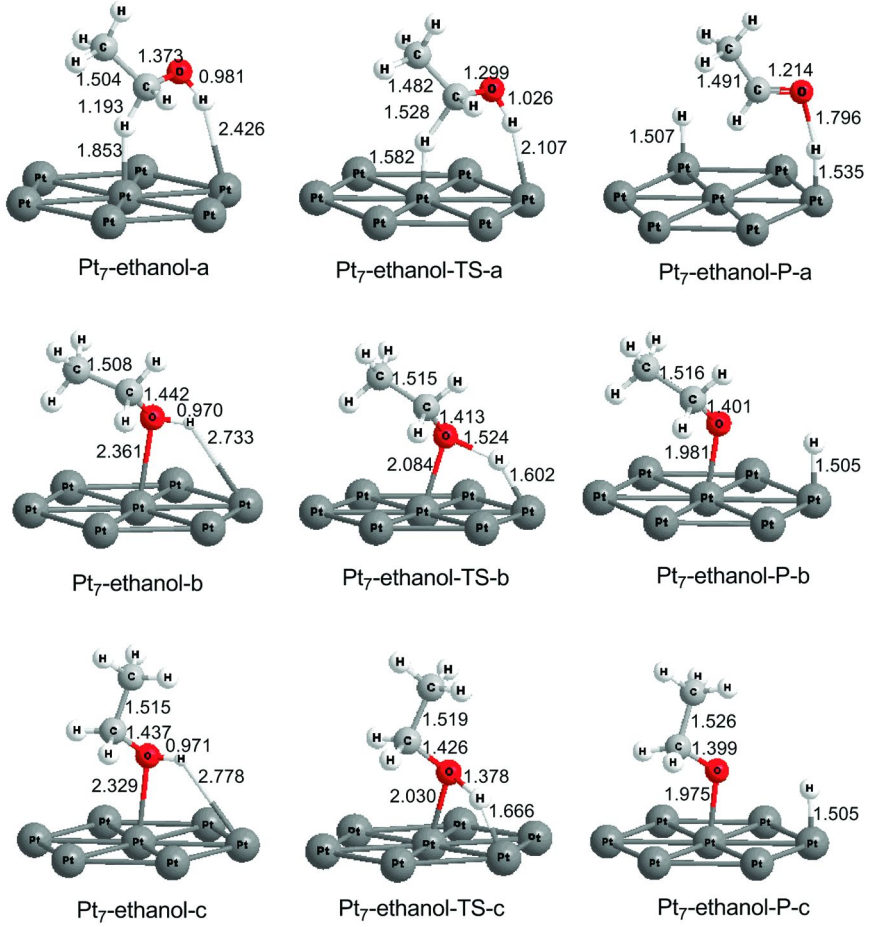

Figure 2. Structures of stationary points of Pt_7 + CH_3CH_2OH with some critical bond length parameters in Å.

In Applications of Molecular Modeling to Challenges in Clean Energy; Fitzgerald, G., et al.;
ACS Symposium Series; American Chemical Society: Washington, DC, 2013.

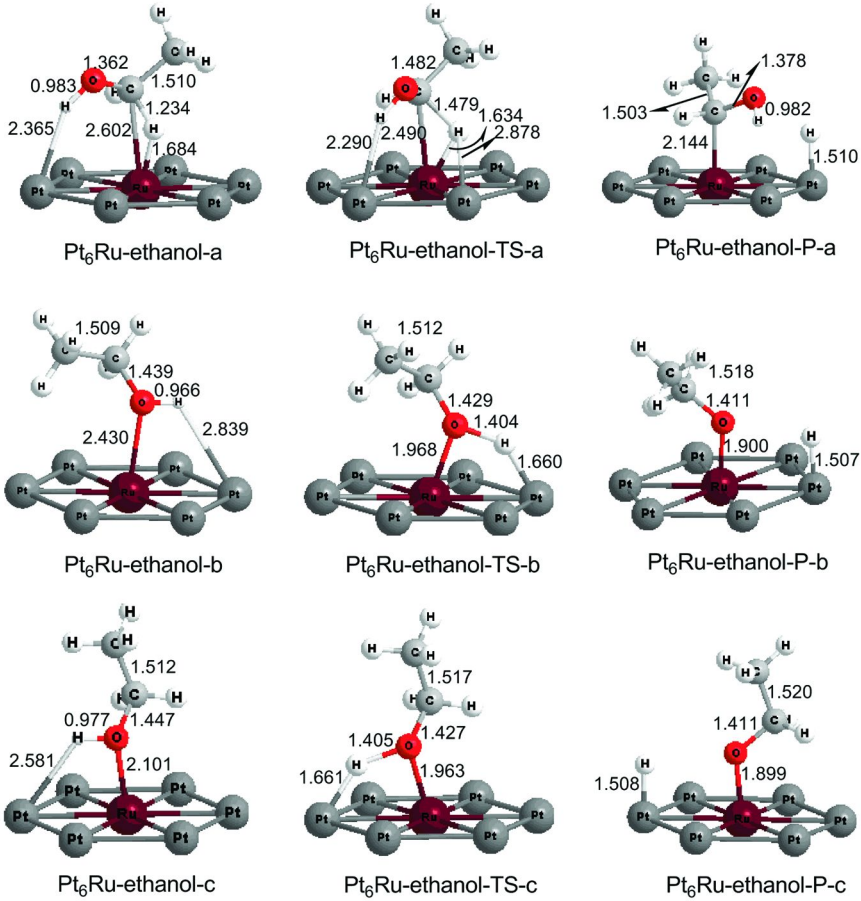

Figure 3. Structures of stationary points of Pt_6Ru + CH_3CH_2OH with some critical bond length parameters in Å.

In Applications of Molecular Modeling to Challenges in Clean Energy; Fitzgerald, G., et al.;
ACS Symposium Series; American Chemical Society: Washington, DC, 2013.

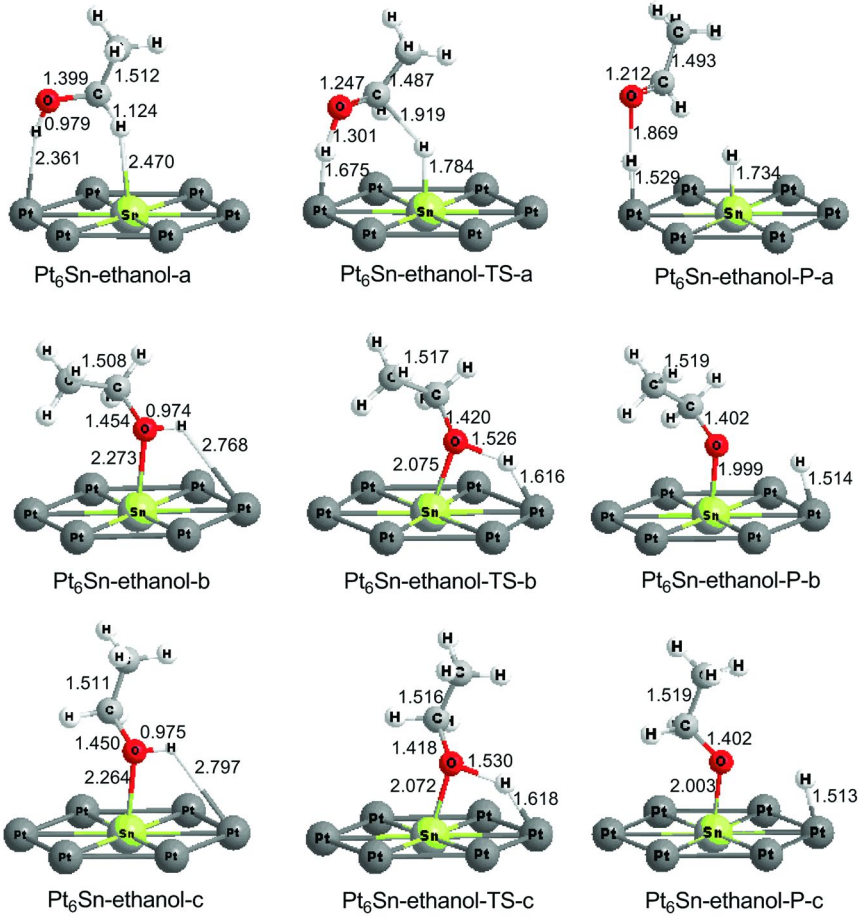

Figure 4. Structures of stationary points of Pt_6Sn + CH_3CH_2OH with some critical bond length parameters in Å.

In Applications of Molecular Modeling to Challenges in Clean Energy; Fitzgerald, G., et al.;
ACS Symposium Series; American Chemical Society: Washington, DC, 2013.

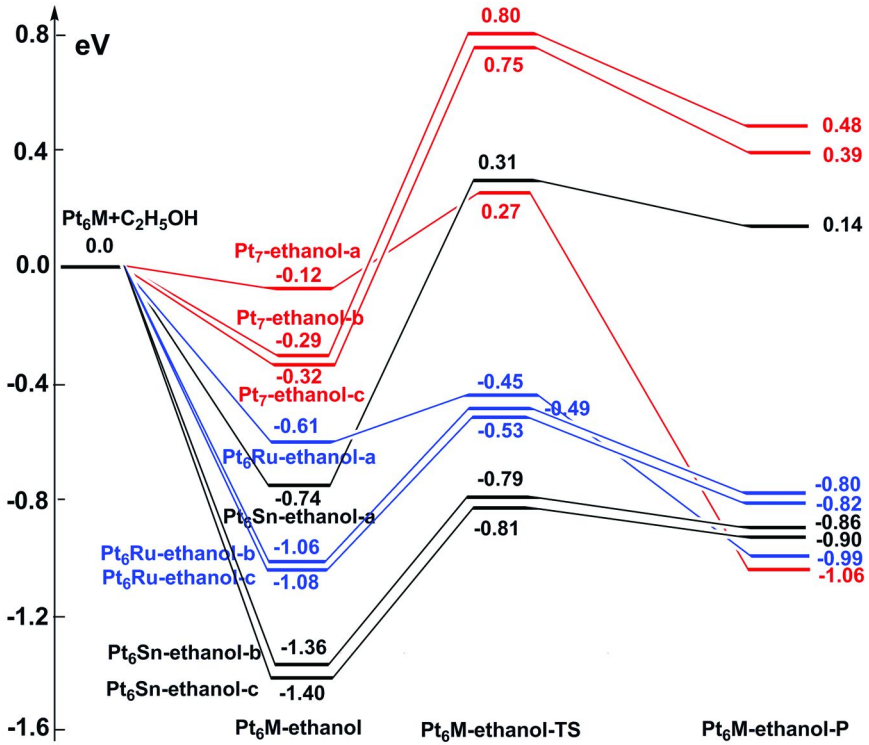

Figure 5. Reaction potential energy profiles of adsorption and dehydrogenation of CH_3CH_2OH on Pt_6M (M=Pt, Ru, Sn).

Pt_7 +CH_3CH_2OH

Three kinds of adsorption of ethanol on Pt_7 are considered through both hydroxyl and methylene groups. On the first one (Pt_7-ethanol-a) the -CH_2 (noted as -$C_\alpha H_\alpha$ hereafter) of *trans*-CH_3CH_2OH is directly adsorbed via the H_α on the central Pt, accompanied by a weak adsorption of hydroxyl hydrogen on one edge Pt. The distances of H_α-Pt and hydroxyl H-Pt are 1.853 and 2.426 Å, respectively. The bond lengths of C_α-H_α and H-O are elongated by 0.093 and 0.021 Å, respectively, compared to those of *trans*-CH_3CH_2OH. The adsorption energy is predicted to be -0.12 eV as shown in Figure 5. The adsorbed complex (Pt_7-ethanol-a) decomposes to the adsorbed product (Pt_7-ethanol-P-a) via the transition state (Pt_7-ethanol-TS-a, imaginary frequency 1914 cm^{-1}). On the TS the C_α-H_α significantly and O-H slightly elongate to 1.528 and 1.026 Å, while the C-O shortens to 1.299 Å; the H_α and hydroxyl H get closer to Pt atoms by approximately 0.3Å. It is interesting to note that the major eigenvectors correspond to the stretching of C_α-H_α and O-H bonds, which indicates the simultaneous cleavage of the two bonds; a visualization clearly shows that the TS (Pt_7-ethanol-TS-a) connects the adsorbed complex Pt_7-ethanol-a and the dehydrogenation product Pt_7-ethanol-P-a. The concerted dehydrogenation

In Applications of Molecular Modeling to Challenges in Clean Energy; Fitzgerald, G., et al.;
ACS Symposium Series; American Chemical Society: Washington, DC, 2013.

pathway agrees well with Wang's report (*16*); however, it was attributed to the adsorption complex via the hydroxyl instead of C_α-H_α adsorption. On the product Pt_7-ethanol-P-a, the H_α atom migrates from the central Pt to an edge Pt forming a H-Pt bond of 1.507 Å, and the broken O-H forms a hydrogen bond with H-O distance of 1.796 Å and H-Pt distance of 1.535 Å. Acetaldehyde, CH_3CHO, is generated through the concerted path. According to Figure 5, the energy barrier E_a and dissociation energy E_{diss} with respect to the adsorbed ethanol (Pt_7-ethanol-a) are 0.39 and -0.94 eV, respectively.

The second adsorption occurs with *trans*-CH_3CH_2OH on Pt_7 to form complex (Pt_7-ethanol-b) via the hydroxyl group. The O binds to the central Pt through lone electron pairs and its H atom connects to one edge Pt. On Pt_7-ethanol-b the O-Pt and H-Pt distances are 2.361 and 2.733 Å, respectively. The adsorption of Pt_7-ethanol-b (E_{ads}=-0.29 eV) is much stronger than that of Pt_7-ethanol-a (E_{ads}=-0.12 eV) which may be due to electrostatic attraction between the negatively charged O atom (-0.280e) and the positive central Pt atom (+0.387e). In the dehydrogenation process from Pt_7-ethanol-b passing over the transition state (Pt_7-ethanol-TS-b, imaginary frequency 714 cm^{-1}) to the product (Pt_7-ethanol-P-b), the O-H bond elongates from 0.970 Å to 1.524 Å and finally breaks; meanwhile, the H-Pt distance decrease from 2.733 Å to 1.602 Å on the TS and to 1.505 Å on the product, and the O-Pt distance changes from 2.361 Å to 2.084 Å and finally to 1.981Å. The dehydrogenation process has much higher energy barrier than the previous concerted pathway initiated by C_α-H_α adsorption (E_a: 1.09 vs. 0.39eV), and thermodynamically the dissociation energy is also less favorable (E_{diss}: 0.77 vs. -0.94eV).

The adsorption and subsequent dissociation of *cis*-CH_3CH_2OH on Pt_7 via the hydroxyl group are also investigated. As shown in Figure 2, the adsorbed complex (Pt_7-ethanol-c) adopts a titled atop adsorption geometry via oxygen with OH almost parallel to the surface, which is similar to the widely reported conformation for methanol as well as ethanol adsorptions over transition metal clusters or surfaces (*14*, *25–27*). The distances of O-Pt and H-Pt at the adsorption complex (Pt_7-ethanol-c) are 2.329 and 2.778 Å, respectively. The former is slightly shorter than that of Pt_7-ethanol-b and the latter is slightly longer than that of Pt_7-ethanol-b. Although the *trans*-CH_3CH_2OH has slightly lower energy than the *cis*-CH_3CH_2OH, the adsorbed *cis*-CH_3CH_2OH (Pt_7-ethanol-c) is more stable than the corresponding complex from the former (Pt_7-ethanol-b). Thus, among the three adsorption conformations over Pt surface, the Pt_7-ethanol-c is the most stable one with a binding energy of -0.32 eV, stronger than Pt-ethanol-b (E_{ads}=-0.29eV) and Pt-ethanol-a (E_{ads}=-0.12 eV) by 0.04 and 0.20eV, respectively. Alcala et al. found that *cis*-ethanol binds through oxygen at a top site on Pt(111) (*14*), in good agreement with the current result. Their calculated O-Pt bond length (2.59 Å) is much longer than the present one (2.33 Å), but the adsorption energy (-0.29 eV) is only slightly less than the current one of -0.32 eV. The present O-Pt distance and adsorption energy are rather similar to the reported values of methanol on Pt(111) (2.43 Å, -0.33eV) by Mavrikakis et al (*25*). On the dehydrogenation transition state (Pt_7-ethanol-TS-c), the O-Pt and H-Pt distances shorten to 2.030 Å and 1.666 Å, respectively, while the O-H bond elongates to 1.378 Å, also shorter by 0.146 Å than that of Pt_7-ethanol-TS-b.Accordingly,

In Applications of Molecular Modeling to Challenges in Clean Energy; Fitzgerald, G., et al.;
ACS Symposium Series; American Chemical Society: Washington, DC, 2013.

the imaginary frequency (*i*1157 cm^{-1}) of Pt_7-ethanol-TS-c is larger than that of Pt_7-ethanol-TS-b (*i*714 cm^{-1}). Similar to Pt-ethanol-b, its decomposition energy barrier (E_a=1.07eV) is much higher than that of Pt-ethanol-a (E_a=0.39eV), and thermodynamic dissociation energy is also less favorable than that of Pt-ethanol-a (E_{diss}=0.71eV). Above all, over Pt_7 surface the most favorable dehydrogenation path is the C_α-H_α cleavage in terms of kinetic as well as thermodynamic aspects. It was also reported by Alcala et al (*28*) that on Pt(111) the energy barrier for the first dehydrogenation of ethanol via hydroxyl cleavage to form CH_3CH_2O is higher than that via C_α-H_α to form CH_3C^*HOH (relative to gas phase ethanol, 0.53 vs. 0.46eV). For the dehydrogenation of methanol, C-H cleavage was also demonstrated to be more kinetic favorable than the O-H (E_a:0.67 vs. 0.81eV) (*25*). Our results basically supports the speculation that the first dehydrogenation of ethanol may proceed through the cleavage of C_α-H_α (*29*), rather than OH (*30*).

Pt_6Ru + CH_3CH_2OH

On Pt_6Ru ruthenium atom replaces the central Pt of Pt_7. Because of more unoccupied *d* orbitals on Ru, the bimetallic cluster Pt_6Ru might have different ligand effect on ethanol than Pt_7. The adsorption energy for Pt_6Ru-CH_3CH_2OH through the α-hydrogen is predicted to be -0.61 eV, more exothermic than Pt_7-CH_3CH_2OH by 0.49 eV. As shown in Figure 3, the distances of H_α-Ru and C_α-Ru in the complex, Pt_6Ru-ethanol-a, are 1.684 Å and 2.602 Å, respectively, much shorter than those on Pt_7-ethanol-a complex. This strong adsorption considerably weakens the C_α-H_α bond to 1.234Å. The energy of the transition state (Pt_6Ru-ethanol-TS-a from Pt_6Ru-ethanol-a to the product complex Pt_6Ru-ethanol-P-a) is predicted to be -0.45eV, only higher than Pt_6Ru-ethanol-a by 0.16 eV with an imaginary frequency 600 cm^{-1}. The C_α-H_α bond on Pt_6Ru-ethanol-TS-a is extended to 1.479 Å, and then is completely broken and α-H shifts to the neighbor Pt with C_α-Ru and H_α-Pt bond lengths of 2.144 and 1.510 Å, respectively. The C_α-H_α cleavage over Ru has a rather low energy barrier of 0.15eV. However, Pt_6Ru-ethanol-P-a shows that only the α-H atom is removed from CH_3CH_2OH in this dehydrogenation reaction, rather than a concert C_α-H_α and O-H cleavage as in the case of Pt_7-ethanol.

Similar hydroxyl adsorptions and dehydrogenation paths were also located over Pt_6Ru for both *trans*- and *cis*-CH_3CH_2OH with the adsorption energies of -1.06 and -1.08 eV, respectively. The O-Ru and H-Pt distances on the *trans*-CH_3CH_2OH adsorption complex (Pt_6Ru-ethanol-b) are 2.430 and 2.839 Å, respectively, while those are 2.101 and 2.581 Å, respectively, on the *cis*-CH_3CH_2OH adsorption complex (Pt_6Ru-ethanol-c). In the dehydrogenation processes, the energy barriers of the OH cleavage via the transition states Pt_6Ru-ethanol-TS-b (*i*900 cm^{-1}) and Pt_6Ru-ethanol-TS-c (*i*875 cm^{-1}) are 0.57 and 0.55 eV, respectively, which are lower than those over Pt_7 (1.09 and 1.07eV). The two TSs have very rather similar dominant reaction coordinates, such as O-H distance of approximately 1.40 Å and O-Ru distance of 1.96Å. The dissociation energy are the same, 0.260 eV.

Therefore, the adsorptions of CH_3CH_2OH via C–H as well as O-H over the Ru site of Pt_6Ru are stronger than those over Pt_7, and the subsequent dehydrogenation

In Applications of Molecular Modeling to Challenges in Clean Energy; Fitzgerald, G., et al.;
ACS Symposium Series; American Chemical Society: Washington, DC, 2013.

reactions also show less energy barrier and more exothermic due to the addition of ruthenium. Similar to Pt_7, among the three dehydrogenation paths C-H cleavage is the most favorable one. In addition, because the dehydrogenation transition states of CH_3CH_2OH on Pt_6Ru are all predicted to have much lower energy than the separated CH_3CH_2OH and the cluster, the adsorption and dehydrogenation reaction may spontaneously happen via either α-hydrogen adsorption or hydroxyl adsorption.

Pt_6Sn+CH_3CH_2OH

On account of the valence electronic configuration of Sn atoms different from those of platinum and ruthenium, the adsorption and dehydrogenation of CH_3CH_2OH on Sn site of the Pt_6Sn catalyst are somewhat different from those on the Pt_6Ru and Pt_7 clusters. Figure 4 shows that the H_α-Sn and H-Pt distances for the α-hydrogen absorption complex (Pt_6Sn-ethanol-a) are 2.470 and 2.361Å, respectively; and the C_α atom is far from the Sn atom. The adsorption energy is -0.74eV, stronger than Pt_7-ethanol-a and Pt_6Ru-ethanol-a as shown in Figure 5. Similar to the corresponding adsorption on Pt_7, the complex Pt_6Sn-ethanol-a also leads to a concerted O-H and C_α-H_α cleavage. However, its dehydrogenation transition state (Pt_6Sn-ethanol-TS-a) is of a very high energy, 0.31eV relative to Pt_6Sn + CH_3CH_2OH, with a rather high energy barrier of 1.05eV. The product (Pt_6Sn-ethanol-P-a) has only lower energy than that of the transition state by 0.17eV. Consequently, this reaction channel is an endothermic and may be a non-spontaneous process.

The adsorption and dehydrogenation of CH_3CH_2OH through the hydroxyl adsorption type is more feasible. The adsorption energies of *trans*- and *cis*-CH_3CH_2OH on Pt_6Sn through the hydroxyl are predicted to be -1.36 and -1.40 eV, respectively, which are the most strong adsorptions of the investigated cases in Figure 4. The O-Sn (H-Pt) distances are approximately 2.27(2.77) Å and 2.26(2.80)Å, respectively, on the adsorption complexes of *trans*-CH_3CH_2OH (Pt_6Sn-ethanol-b) and *cis*-CH_3CH_2OH (Pt_6Sn-ethanol-c). The strong adsorptions imply that, although these critical geometric parameters are similar to the ones of other adsorption complexes (Pt_7-ethanol-b and c, Pt_6Ru-ethanol-b and c), the interaction of the lone electron pairs of O with the vacant valence *p* orbitals of Sn seems stronger than with the vacant valence *d* orbitals of Pt and Ru. Following Pt_6Sn-ethanol-b, the dehydrogenation takes place with the H atom migrating to the neighbor Pt atom via the transition state structure (Pt_6Sn-ethanol-TS-b, *i*349 cm^{-1}) with an energy barrier of 0.57eV that is considerably lower than that of C_α-H_α cleavage by 0. 48eV. As for another dehydrogenation process deriving from Pt_6Sn-ethanol-c, its transition state (Pt_6Sn-ethanol-TS-c) and the product complex (Pt_6Sn-ethanol-P-c) are very similar to the case of Pt_6Sn-ethanol-b dehydrogenation, like an energy barrier of 0.59eV and dissociation energy of 0.50eV. Thus, as ethanol is adsorbed on Sn site of Pt_6Sn the favorable dehydrogenation path is through the O-H cleavage instead of C_α-H_α cleavage. This result qualitatively follows the trend reported by Alcala et al. (*15*), in which

In Applications of Molecular Modeling to Challenges in Clean Energy; Fitzgerald, G., et al.;
ACS Symposium Series; American Chemical Society: Washington, DC, 2013.

the transition state energy to form CH_3CH_2O* is lower by 0.12 eV than that to form CH_3CH*OH on Pt_3Sn

As discussed above, over Pt_7 and Pt_6Ru the favorable path for the first dehydrogenation reaction of ethanol is the C_α-H_α cleavage to form adsorbed CH_3CHOH (the respective E_a=0.39 and 0.15eV; E_{diss}=-0.94 and -0.38eV). However, over Pt_6Sn the cleavage of hydroxyl has much lower energy barrier and dissociation energy than the C_α-H_α breaking (E_a: 0.57 vs. 1.05eV; E_{diss}: 0.55 vs. 0.88eV). These results indicate that whether the ethanol decomposition can proceed initially via the O-H or C_α-H_α bond cleavage depends on the alloyed metal in Pt-based bimetallic catalyst. In addition, one can see that, for the favorable reaction path of Pt_6Sn+CH_3CH_2OH, the hydrogen atom is preferably in contact with platinum atom, while the oxygen atom would rather contact with tin atom. This agrees with the theoretical result of the water decomposition on Pt_6Sn (*13*). According to our calculated result shown in Figure 5, not only are the adsorption energies of Pt_7-ethanol-a, -b, and -c much smaller than that of Pt_6Sn-ethanol-a, -b and -c, but also Pt_7-ethanol-TS-a, the lowest energy transition state among the reaction of ethanol on Pt_7, is above reactants by 0.27 eV, whereas Pt_6Sn-ethanol-TS-b and –c are below the reactants by 0.79-0.81 eV. Thus, the adsorption and dehydrogenation reaction of ethanol on Sn site of Pt_6Sn is overwhelming. The electro-oxidation reaction of ethanol solution on the Pt-Sn catalyst would require certain atomic ratio of Sn to Pt in the metallic alloy so as to adsorb more ethanol and water molecules. Recently, some experimental data show that the reactivity of ethanol electro-oxidation increases with the Sn atomic concentration of the Pt-Sn alloy increasing and the best ratio (Pt:Sn) is in the range of 2:1-1:1 (*31–33*).

CH_3CH_2OH Adsorption and Decomposition over Pt_9M Clusters (M=Pt, Sn, Ru)

To discuss the layer effect, the second layer (Pt_3) was added to the relevant stationary points in Figure 5, forming Pt_9M. The potential energy profiles in Figure 6 were obtained with single-point energies for Pt_9M+ethanol. For the Pt_{10} + CH_3CH_2OH reaction, the relative energies of the C-H_α adsorption complex (Pt_{10}-ethanol-a) and the transition state (Pt_{10}-ethanol-TS-a) are almost the same as those of Pt_7-ethanol-a and Pt_7-ethanol-TS-a, respectively. However, the dehydrogenation product (Pt_{10}-ethanol-P-a) is dramatically above Pt_7-ethanol-P-a by 0.83 eV. The relative energies of two hydroxyl adsorption reaction channels of this reaction system show difference from the one layer model, e.g., the adsorption through the hydroxyl of *cis*-ethanol is relatively more stable.

For the Pt_9Ru+CH_3CH_2OH reaction, the adsorption energies of Pt_9Ru-ethanol-a, -b, and -c are more stable than those of Pt_6Ru-ethanol-a, -b, and -c by 0.12, 0.26, and 0.44 eV, respectively. The dehydrogenation products (Pt_9Ru-ethanol-P-a, -b, and -c) also have a small decrease in energy, and the energies of the dehydrogenation transition states have a small increase with a magnitude of less than 0.09 eV. Apparently, these changes are directly related to the fixed geometric parameters taken from the the Pt_6Ru + CH_3CH_2OH system.

In Applications of Molecular Modeling to Challenges in Clean Energy; Fitzgerald, G., et al.;
ACS Symposium Series; American Chemical Society: Washington, DC, 2013.

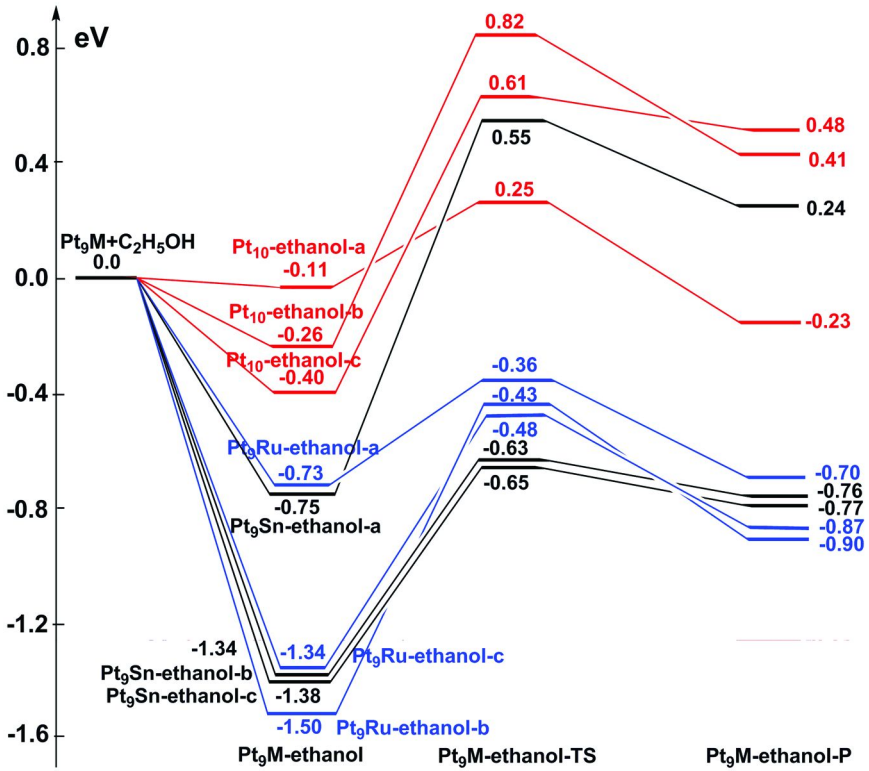

Figure 6. Reaction potential energy profiles of adsorption and dehydrogenation of CH_3CH_2OH on Pt_9M (M=Pt, Ru, Sn).

For the energy prediction of the $Pt_9Sn + CH_3CH_2OH$ reaction, there is a good agreement with the $Pt_6Sn + CH_3CH_2OH$ reaction. The relative energies of the adsorption complexes (Pt_9Sn-ethanol-a, -b, and -c) are only 0.02 eV different from those in the $Pt_6Sn + CH_3CH_2OH$ reaction. The energies of the dehydrogenation transition states of the α-hydrogen and hydroxyl adsorption types are 0.24 and 0.16 eV, respectively, higher than those of the corresponding transition states in the $Pt_6Sn + CH_3CH_2OH$ reaction. The energy increase of the dehydrogenation products is also less than 0.13 eV compared to the products of $Pt_6Sn + CH_3CH_2OH$.

It is apparent that the two layer Pt-based cluster model for the ethanol decomposition may not be accurate yet, but the results have the same trend as those of the one layer Pt-based cluster model, especially for the dominant reaction channels. Therefore, this consistency can make us believe that the calculated result, based on the one-layer model, may be reliable to clarify the electro oxidation mechanism of ethanol.

Kinetics of Adsorption and Decomposition of CH_3CH_2OH

The above adsorption and dehydrogenation mechanisms of ethanol on the surface of Pt-based alloy can be represented by the reaction scheme:

In Applications of Molecular Modeling to Challenges in Clean Energy; Fitzgerald, G., et al.;
ACS Symposium Series; American Chemical Society: Washington, DC, 2013.

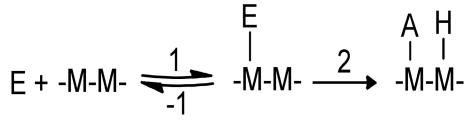

E is ethanol and –M- is the surface of the alloy, while A- and H- are the decomposition products of ethanol. Based on the steady state approximation, the overall rate constant can be expressed as

$$k = \frac{k_2 k_1}{k_{-1} + k_2} = \frac{K k_2}{1 + k_2 / k_{-1}} \quad (1)$$

where k_1 and k_{-1} are the adsorption and desorption reaction rate constants, and k_2 is the reaction rate constant for the decomposition; K (= k_1/k_{-1}) is the adsorption equilibrium constant. According to the transition state rate theory, the decomposition reaction rate constant is formulated as

$$k_2 = L \frac{\kappa T}{h} \frac{f^{\neq}}{f_M} \exp\left(-\frac{\Delta E}{RT}\right) \quad (2)$$

and the adsorption equilibrium constant is

$$K = \frac{f_{ME}}{f_E f_M} \exp\left(-\frac{\Delta H}{RT}\right) \quad (3)$$

In equations (2) and (3), κ is Boltzman constant and h is Plank constant; ΔE is the potential barrier of dehydrogenation reaction; ΔH is the adsorption energy of adsorption process; $f^{\neq}$ is the partition function of transition state; f_E, f_M, and f_{ME} are the partition functions of ethanol, metal, and metal-ethanol adsorption complex, respectively; L is the number of adsorption sites per area unit. For the pure Pt metallic surface, L is evaluated to be 5.79×10^{14} cm^{-2}, while the adsorption sites at the atomic ratio of 2:1 for Pt:Ru and Pt:Sn are evaluated to be 1.71×10^{14} and 1.60×10^{14} cm^{-2}, respectively. The partition function of ethanol is approximated as the sum of the translation, rotation, vibration, and electron contributions, while the partition functions of the Pt-based cluster and their adsorption complexes as well as transition states only involve both electronic and vibrational contributions because of their solid property.

In the light of the above discussion on the adsorption and dehydrogenation reaction mechanisms, the rate constants are calculated only for the most favorable reaction channels, such as α-hydrogen adsorption for Pt_7+CH_3CH_2OH, hydroxyl adsorption for Pt_6Sn+CH_3CH_2OH, and both α-hydrogen adsorption and hydroxyl adsorption for Pt_6Ru+CH_3CH_2OH. Figure 7 shows the predicted rate constants of three reaction systems in the temperature range from 200 K to 500 K. The rate constants of the Pt_7+CH_3CH_2OH, Pt_6Ru+CH_3CH_2OH, and Pt_6Sn+CH_3CH_2OH systems are denoted by k_{Pt}, k_{Pt2Ru1}, and k_{Pt2Sn1}, respectively. It can be seen that all of the reaction rate constants of ethanol with the metallic catalysts appear positive temperature dependent, which implies that their reactivity increases

In Applications of Molecular Modeling to Challenges in Clean Energy; Fitzgerald, G., et al.;
ACS Symposium Series; American Chemical Society: Washington, DC, 2013.

with the temperature increasing in spite of the weak temperature dependence of k_{Pt2Ru1}. Apparently, k_{Pt2Sn1} is the highest while k_{Pt} is the lowest; however, k_{Pt2Ru1} is less than the former but much higher than the latter. For example, at 300 K k_{Pt2Sn1} is 4.3 and 2.9×10^4 times greater than k_{Pt2Ru1} and k_{Pt}, respectively. Moreover, at 400 K k_{Pt2Sn1} is 7.7 and 1.7×10^4 times higher than k_{Pt2Ru1} and k_{Pt}, respectively. In addition, one can see that for k_{Pt2Ru1} the rate constant line of the hydroxyl adsorption type reaction is slightly greater than that of the α-hydrogen one. For example, k^{O}_{Pt2Ru1} is over k^{H}_{Pt2Ru1} by 1.3 and 1.4 times at 300 and 400 K, respectively. This shows in kinetics that the adsorption and dehydrogenation reaction of ethanol on Ru site of Pt-Ru and Sn site of Pt-Sn occurs favorably through the hydroxyl adsorption. For practical application, these predicted rate constants in units of $cm\cdot s^{-1}$ are fitted by three parameters Arrhenius expressions as follows in the temperature range from 200 K to 500 K.

$$k_{Pt} = 1.38 \times 10^{-18}\, T^{4.99} \exp(-299/T)$$
$$k^{H}_{Pt2Ru1} = 1.61 \times 10^{-6}\, T^{1.39} \exp(-53/T)$$
$$k^{O}_{Pt2Ru1} = 1.95 \times 10^{-7}\, T^{1.76} \exp(-15/T)$$
$$k_{Pt2Sn1} = 2.22 \times 10^{-13}\, T^{4.39} \exp(224/T)$$

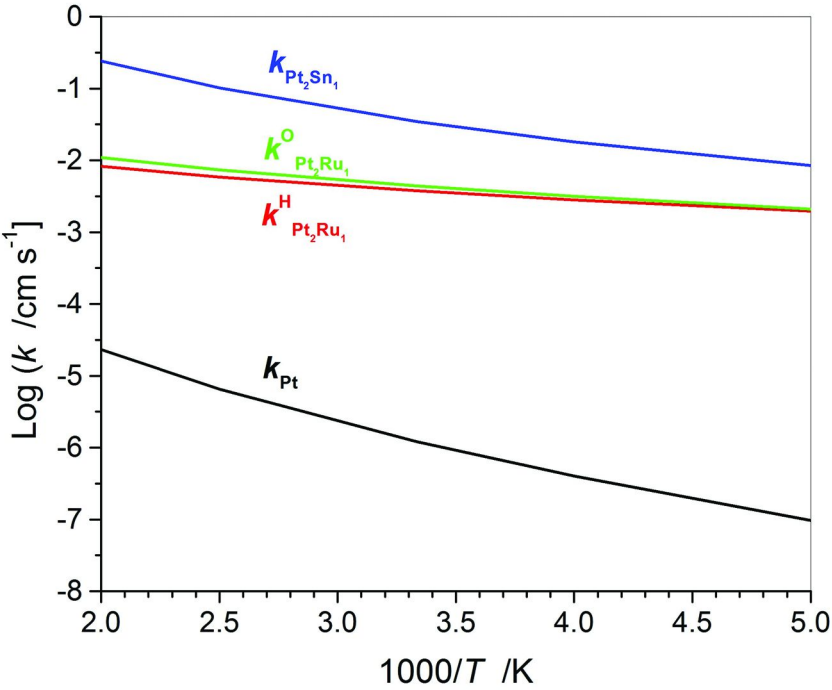

Figure 7. Predicted rate constants of adsorption and dehydrogenation of CH_3CH_2OH on Pt-M catalysts (M= Pt, Ru, Sn) versus reciprocal temperature.

In Applications of Molecular Modeling to Challenges in Clean Energy; Fitzgerald, G., et al.;
ACS Symposium Series; American Chemical Society: Washington, DC, 2013.

Conclusion

Two types of ethanol adsorption and decomposition on the Pt_nM(n=6 and 9, M=Pt, Ru, and Sn) clusters were investigated with the B3PW91 density functional theory. One is α-hydrogen adsorption and another one is hydroxyl adsorption. For the reaction of ethanol on pure platinum, the α-hydrogen adsorption type is predicted to be favorable, while for the Pt-Sn bimetallic catalysts the hydroxyl adsorption reaction of ethanol is more favorable with respect to kinetics and thermodynamics for the dehydrogenation step. However, for the Pt-Ru alloy the dehydrogenation transition states of the two adsorption complexes are rather comparable. The overall rate constants of these three reaction systems are calculated by the transition state theory in temperature range of 200-500 K for the pure platinum and the bimetallic alloys with the 2: 1 atomic ratio of Pt to Ru or Sn. The result shows that the rate constants depend on temperature positively and k_{Pt2Sn1} is greater than k_{Pt2Ru1} and even much greater than k_{Pt}. It means that the addition of Sn or Ru to Pt catalyst could greatly enhance the adsorption and decomposition reaction of ethanol. This conclusion is in good agreement with the experimental observation.

Acknowledgments

This research is supported by the American Chemical Society Petroleum Research Fund (47286-GB5). L. S. Zhang did calculation for a few systems in the paper.

References

1. Vigier, F. C. C.; Perrard, A.; Belgsir, E. M.; Lamy, C. *J. Appl. Electrochem.* **2004**, *34*, 439.
2. Song, S.; Tsiakaras, P. *Appl. Catal., B* **2006**, *63*, 187.
3. Jiang, L.; Sun, G.; Sun, S.; Liu, J.; Tang, S.; Li, H.; Zhou, B.; Xin, Q. *Electrochim. Acta* **2005**, *50*, 5384.
4. Vigier, F.; Coutanceau, C.; Hahn, F.; Belgsir, E. M.; Lamy, C. *J. Electroanal. Chem.* **2004**, *563*, 81.
5. Mann, J.; Yao, N.; Bocarsly, A. B. *Langmuir* **2006**, *22*, 10432.
6. Rousseau, S.; Coutanceau, C.; Lamy, C.; Leger, J.-M. *J. Power Sources* **2006**, *158*, 18.
7. Lamy, C.; Rousseau, S.; Belgsir, E. M.; Coutanceau, C.; Leger, J.-M. *Electrochim. Acta* **2004**, *49*, 3901.
8. Song, S. Q.; Zhou, W. J.; Zhou, Z. H.; Jiang, L. H.; Sun, G. Q.; Xin, Q.; Leontidis, V.; Kontou, S.; Tsiakaras, P. *Int. J. Hydrogen Energy* **2005**, *30*, 995.
9. Zhu, M.; Sun, G.; Xin, Q. *Electrochim. Acta* **2009**, *54*, 1511.
10. Watanabe, M.; Motoo, S. *J. Electroanal. Chem.* **1975**, *60*, 275.
11. Iwasita, T.; Pastor, E. *Electrochim. Acta* **1994**, *39*, 531.
12. Lux, K. W. C.; Elton, J. *J. Electrochem. Soc.* **2006**, *153*, A1139.
13. Wang, Y.; Mi, Y.; Redmon, N.; Holiday, J. *J. Phys. Chem. C* **2010**, *114*, 317.

14. Alcala, R.; Mavrikakis, M.; Dumesic, J. A. *J. Catal.* **2003**, *218*, 178.
15. Alcala, R.; Shabaker, J. W.; Huber, G. W.; Sanchez-Castillo, M. A.; Dumesic, J. A. *J. Phys. Chem. B* **2005**, *109*, 2074.
16. Wang, H.-F.; Liu, Z.-P. *J. Phys. Chem. C* **2007**, *111*, 12157.
17. Xu, Z.-F.; Wang, Y. *J. Phys. Chem. C* **2011**, *115*, 20565.
18. Perdew, J. P.; Burke, K.; Wang, Y. *Phys. Rev. B* **1996**, *54*, 16533.
19. Burke, K.; Perdew, J. P.; Wang, Y. In *Electronic Density Functional Theory: Recent Progress and New Directions*; Dobson, J. F., Vignale, G., Das, M. P., Eds.; Plenum: New York, 1998.
20. Frisch, M. J.; Trucks, G. W.; Schlegel, H. B.; et al. *Gaussian 03, Rev. D2*; Gaussian, Inc.: Pittsburgh, PA, 2003.
21. Hay, P. J.; Wadt, W. R. *J. Chem. Phys.* **1985**, *82*, 299.
22. Raghavachari, K.; Binkley, J. S.; Seeger, R.; Pople, J. A. *J. Chem. Phys.* **1980**, *72*, 650.
23. Peng, C.; Schlegel, H. B. *Isr. J. Chem.* **1993**, *33*, 449.
24. Li, X.; Frisch, M. J. *J. Chem. Theory Comput.* **2006**, *2*, 835.
25. Greeley, J.; Mavrikakis, M. *J. Am. Chem. Soc.* **2004**, *126*, 3910.
26. Desai, S. K.; Neurock, M.; Kourtakis, K. *J. Phys. Chem. B* **2002**, *106*, 2559.
27. Yang, M.-M.; Bao, X.-H.; Li, W.-X. *J. Phys. Chem. C* **2007**, *111*, 7403.
28. Alcala, R.; Shabaker, J. W.; Huber, G. W.; Sanchez-Castillo, M. A.; Dumesic, J. A. *J. Phys. Chem. B* **2005**, *109*, 2074.
29. Vigier, F. R. S.; Coutanceau, C.; Leger, J.-M.; Lamy, C. *Top. Catal.* **2006**, *40*, 111.
30. Lee, A. F.; Gawthrope, D. E.; Hart, N. J.; Wilson, K. *Surf. Sci.* **2004**, *548*, 200.
31. Zhou, W. J.; Song, S. Q.; Li, W. Z.; Suna, G. Q.; Xin, Q.; Kontou, S.; Poulianitis, K.; Tsiakaras, P. *Solid State Ionics* **2004**, *175*, 797.
32. Zhou, W. J.; Song, S. Q.; Li, W. Z.; Zhou, Z. H.; Suna, G. Q.; Xin, Q.; Douvartzides, S.; Tsiakaras, P. *J. Power Sources* **2005**, *140*, 50.
33. Tsiakaras, P. E. *J. Power Sources* **2007**, *171*, 107.

Chapter 9

Combining Vibrational Spectroscopies with Quantum Chemical Calculations for Molecular-Level Understanding of Reaction Mechanisms on Catalytic Surfaces

Simon G. Podkolzin,*[,1] George B. Fitzgerald,[2] and Bruce E. Koel[3]

[1]Department of Chemical Engineering and Materials Science, Stevens Institute of Technology, Hoboken, New Jersey 07030, U.S.A.
[2]Accelrys, Inc., 10188 Telesis Court, San Diego, California 92121, U.S.A.
[3]Department of Chemical and Biological Engineering, Princeton University, Princeton, New Jersey 08544, U.S.A.
***E-mail: Simon.Podkolzin@Stevens.edu**

Heterogeneous catalysis is a critical component in the improvement of existing technologies and development of new solutions in the area of clean energy and sustainability. Combining vibrational spectroscopies with quantum chemical calculations can provide molecular-level information on the structure of catalytic surfaces and reaction pathways. As an initial step, comparison between experimental and computational vibrational spectra can be used for identification of adsorption modes for reactants and products and also for determination of the nature of stable surface species under reaction conditions. In subsequent steps, quantum chemical models calibrated based on stable reaction species on appropriately selected surfaces can be used for evaluation of multiple reaction pathways, identification of transient reaction intermediates, and development of reaction mechanisms for incorporation into kinetic models and description of observable reaction rates. This methodology is illustrated with two spectroscopic techniques: infrared and high resolution electron energy loss spectroscopies and two catalytic systems: Fischer-Tropsch synthesis over Co/TiO_2 catalysts and hydrocarbon reactivity on catalytic Pt-Sn alloys.

In Applications of Molecular Modeling to Challenges in Clean Energy; Fitzgerald, G., et al.;
ACS Symposium Series; American Chemical Society: Washington, DC, 2013.

Advantages of Combining Vibrational Spectroscopies with Quantum Chemical Calculations

Heterogeneous catalysis is a critical component in the improvement of existing technologies and development of new solutions in the area of clean energy and sustainability. This chapter illustrates challenges and advances in catalytic technologies with two examples: (1) Fischer-Tropsch synthesis for the production of synthetic fuels over Co/TiO_2 catalysts and (2) characterization of hydrocarbon adsorption and reactivity on Pt-Sn catalysts for upgrading biomass-derived feedstocks.

These examples highlight advantages of combining experimental vibrational spectroscopies and quantum chemical calculation using density functional theory (DFT) for molecular-level understanding of reaction mechanisms on catalytic surfaces. The advantages of such an integrated experimental-theoretical approach can be grouped into two main areas. The first area is related to assignment of experimental vibrational peaks. Vibrational spectra of surfaces and adsorbates are usually complex and difficult to interpret. Assignments of vibrational bands have previously relied almost exclusively on referencing to model surfaces or model adsorbates. For example, model organometallic cluster compounds have been used for the interpretation of vibrational bands for hydrocarbons adsorbed on metal and metal oxide surfaces. Similarly, adsorption of, for example, halogen-containing model hydrocarbons, which are expected to adsorb by splitting the halogen fragment, have been used for interpretation of vibrational spectra of different types of hydrocarbon surface species. Use of reference surfaces and adsorbates requires significant experimental efforts and often does not provide sufficient accuracy for unambiguous interpretation of vibrational spectra in catalysis research.

DFT calculations are particularly useful for the interpretation of experimental spectra of surfaces and adsorbates because they can be used to generate simulated vibrational modes for comparison with experimental measurements. Different hypotheses on the structure and geometry of surfaces and adsorbates can be tested computationally. Calculations can provide information not only on the positions of vibrational bands but also estimates of their intensities for infrared and Raman measurements. An additional advantage compared to experimental referencing is the information on the energetic stability of different evaluated surfaces and adsorbates, which can also be obtained with DFT calculations. The information on relative stability provides additional guidance for discrimination between different options for assignments of experimental vibrational peaks. The challenge of using calculated frequencies, however, is that they usually require an adjustment based on an empirically obtained scaling factor or correction. It is, therefore, important to augment vibrational spectroscopic results with additional experimental catalyst characterization for validation of DFT models, as illustrated by the examples in this chapter.

The second area where the combination of vibrational spectroscopy with DFT calculations is particularly useful is in identification of reaction intermediates and development of reaction mechanisms. In purely spectroscopic studies, an assumption is usually made that the surface species observed under reaction

In Applications of Molecular Modeling to Challenges in Clean Energy; Fitzgerald, G., et al.;
ACS Symposium Series; American Chemical Society: Washington, DC, 2013.

conditions are the actual reaction intermediates because no other information on the reaction mechanism is typically available. Such assumptions, however, are frequently incorrect since the surface species that are easiest to detect at reaction conditions are likely to be spectators, which are the most stable and unreactive and, therefore, represent a dead end in one of the reaction pathways. A classical example is ethylidyne C-CH_3 species that dominate vibrational spectra under reaction conditions in ethylene and acetylene hydrogenation, ethane hydrogenolysis, and other transformations of C_2 hydrocarbons on metal surfaces. When initially identified spectroscopically under reaction conditions, ethylidyne C-CH_3 was proposed to be a reactive intermediate, only later to be shown to be the most stable and, therefore, the least reactive C_2 hydrocarbon species (*1–7*).

The experimental information about detectable stable surface species is, nevertheless, extremely valuable for the development of DFT reaction models. This information is needed as a reference for the selection of model surfaces (size and chemical composition of a cluster or unit cell, type of the surface termination, total number of surface layers and number of relaxed layers, etc.) and computational parameters (choice of a functional and a basis set, integration grid, convergence criteria, etc.). Without such experimental calibration, computational models are usually highly speculative.

Spectroscopic studies, therefore, can provide critical information required for the development of realistic surface models by identifying adsorption modes for reactants and products and also by determining the nature of stable surface species under reaction conditions. In turn, computational models calibrated based on stable reaction species on appropriately selected surfaces can be used to evaluate multiple reaction pathways and identify transient reaction intermediates, which would be difficult to observe experimentally.

Examples in this chapter illustrate advantages of combining quantum chemical calculations with two vibrational spectroscopies: infrared (IR) spectroscopy and high resolution electron energy loss spectroscopy (HREELS). The IR spectroscopic study illustrates identification of the composition and structure of a catalytic surface based on modeling of vibrational spectra for an adsorbed reactant molecule. The HREELS study illustrates identification of hydrocarbon adsorption modes and catalytic activity of surface sites based on modeling of vibrational spectra that change due to temperature-dependent evolution of adsorbates.

Initial State of Cobalt Catalytic Nanoparticles Under Fischer-Tropsch Reaction Conditions

Significance and Challenges of Fischer-Tropsch Catalysis

Fischer-Tropsch (F-T) synthesis is a commercial process for converting synthesis gas (or syngas – a mixture of carbon monoxide and hydrogen) into a mixture of hydrocarbons, which can be used as liquid transportation fuels or feedstocks for the chemical industry:

$$CO + H_2 \rightarrow \text{Hydrocarbons} + H_2O \qquad (1)$$

In Applications of Molecular Modeling to Challenges in Clean Energy; Fitzgerald, G., et al.;
ACS Symposium Series; American Chemical Society: Washington, DC, 2013.

Syngas can be produced from multiple traditional sources, such as crude oil, coal, and natural gas, and also from alternative sources: for example, from renewable biomass or even municipal solid waste. There is currently renewed interest in F-T technology, and there are multiple ongoing research activities in F-T catalysis and process development due to efforts in diversifying the energy supply and switching to alternative and sustainable feedstocks.

Compared to direct upgrading of biomass into bio-fuels, the syngas option offers greater flexibility for types of products that can be produced: from light olefins as a feedstock for the chemical industry to a wide range of fuels: from liquefied petroleum gas to gasoline, jet fuel and diesel. The syngas processing route also avoids the need to remove oxygen for increasing the caloric value of bio-fuels and, in general, affords greater control over the properties of the final product, allowing, for example, to produce fuels in compliance with existing specifications.

A common challenge in integrating F-T catalysis into new biomass conversion technologies is that the processing needs to be performed at a relatively small scale at the location of biomass collection. Transportation of large volumes of biomass is usually prohibitively expensive. As a result, small-scale, preferably mobile, F-T catalysis units need to be developed. An additional challenge for biomass conversion is a variable H/C and, correspondingly, H_2/CO ratio of feedstocks due to natural variability in biomass properties.

These new challenges are compounded by the limitations of the traditional F-T catalysts, which are usually Co and Fe nanoparticles supported on metal oxides (*8*). Specific issues related to inefficiencies of current catalysts with respect to their activity, selectivity and stability are outlined below.

Since most F-T reactions are exothermic, it is preferable to operate the chemistry at lower temperatures in order to shift the thermodynamic equilibrium to reaction products and, thus, increase the yield. In addition, lower temperatures suppress formation of methane – an undesirable byproduct. The choice of moderate reactor temperatures of about 500-620 K, however, leads to reaction rates that are low compared to traditional hydrocarbon conversion processes: usually less than 0.5 g hydrocarbon/(g catalyst h) (*9*), and, as a result, development of new more active catalysts is desirable for improving process economics (*8–10*).

The product distribution of F-T synthesis is usually described with an Anderson-Schulz-Flory (ASF) distribution or, more accurately, with an overlap of two separate ASF distributions (*10*). The parameters of these distributions depend on the catalyst composition, with some catalyst formulations being more efficient in reducing the formation of undesirable methane and maximizing formation of targeted higher hydrocarbons (*9–11*). Typical selectivities for C_5-C_{12} (gasoline) and C_{13}-C_{18} (diesel) fractions are 20-40 and 5-15 wt%, respectively. Further improvements in catalyst selectivity are, certainly, desirable.

Catalyst deactivation with time on stream is usually attributed to coking, chemical poisoning, for example with sulfur, and changes in the active phase through oxidation or metal particle agglomeration (*8*, *9*, *12*). A typical catalyst lifetime is about 6 months. As the catalyst deactivates, the process temperature is usually increased, resulting in even lower selectivities. More stable formulations can, reportedly, be obtained, for example, by incorporating noble-metal promoters, Ru, Re or Pt, that can increase hydrogenation of coke precursors and improve

In Applications of Molecular Modeling to Challenges in Clean Energy; Fitzgerald, G., et al.;
ACS Symposium Series; American Chemical Society: Washington, DC, 2013.

reducibility of the active Co or Fe phases (*9*, *13–15*). The stability issue is especially significant for Fe-based catalysts (*8*).

Since most reactions in F-T synthesis are highly exothermic, engineering solutions for efficient management of heat and mass transfer limitations contribute to process improvements. For example, there are studies on new reactor configurations where a catalyst is deposited on the walls of a monolith, serving as a heat exchanger and allowing for better heat management (*16*). Advances in reactor design bring the overall process performance closer to intrinsic catalytic kinetics and make catalysis research even more significant. There is, thus, general agreement that catalyst development is crucial for improvements in F-T technology (*8*, *9*, *11*, *12*, *17–23*). F-T catalysis research, however, remains mostly a trial and error exercise because of insufficient understanding of the reaction mechanism and properties of catalytic surfaces.

There are currently three main reaction mechanism schemes: (1) Carbide mechanism where the chain growth proceeds through C or CH_x species (*24–26*), which is also referred to as "CH_2 insertion" based on the CH_x species most often cited as the likely intermediate; (2) CO insertion mechanism where the chain is propagated by CO addition with subsequent hydrogenation (*10*, *27–30*); and (3) propagation through oxygenated intermediates other than CO, for example, through formates (*17*, *19*, *21*, *31–33*).

The uncertainty of the reaction mechanism is compounded by a lack of understanding of dynamic changes of the catalytic surface under reaction conditions. Depending on the feed composition, reaction temperature and pressure, and time on stream, supported Co and Fe catalytic nanoparticles may change their surface composition from metallic to different oxide and carbide phases. Although most researchers acknowledge the importance of such dynamic catalytic surface changes under reaction conditions, none of the current reaction mechanisms incorporates this complexity. This omission is mostly due to the difficulty of catalyst surface characterization under reaction conditions and a disconnect between experimental and computational studies.

The study presented in this section closely integrates IR spectroscopic measurements with DFT calculations for identification of surface changes for Co/TiO_2 catalysts under F-T reaction conditions and for selection of appropriate catalytic surface models. The developed surface models can be incorporated into improved reaction mechanisms and kinetic models, which are essential for optimization of operating conditions and process control systems with existing catalysts and for development of new catalyst formulations.

Experimental and Computational Details

Two Co/TiO_2 samples were prepared using different preparation methods: one by incipient wetness impregnation with a Co loading of 14.6 wt% and another by homogeneous deposition precipitation with a Co loading of 9.9 wt%. The samples were prepared similarly to those reported previously in studies of $Co\text{-}Mn/TiO_2$ catalysts (*34*, *35*). The two samples were calcined at 673 K and then reduced at either 573 or 623 K for 2 h, generating a total of 4 samples differentiated by two preparation methods and two reduction temperatures. The size of supported Co

In Applications of Molecular Modeling to Challenges in Clean Energy; Fitzgerald, G., et al.;
ACS Symposium Series; American Chemical Society: Washington, DC, 2013.

nanoparticles was estimated at 2.5-3.2 nm using transmission electron microscopy (TEM).

The samples were tested under F-T reaction conditions in a flow reactor with simultaneous collection of vibrational spectra using Diffuse Reflectance Infrared Fourier Transform (DRIFT) spectroscopy. In addition, the samples were characterized with CO adsorption at room temperature using DRIFT spectra as a function of He purging time.

DFT calculations were performed using the DMol^3 code in Materials Studio 4.0 software by Accelrys Software, Inc (*36*). The calculations employed the generalized gradient approximation (GGA) using the Perdew-Wang (PW-91) functional. The basis set used a double-numerical basis with polarization (DNP) (*37*). Tightly bound core electrons were represented with semicore pseudopotentials (*38*). Reciprocal-space integration over the Brillouin zone was approximated through *k*-point sampling with a separation of 0.5 nm^{-1} using the Monkhorst-Pack grid: (3×3×1). Convergence with respect to the number of *k*-points was tested by increasing their number for representative structures. The density mixing fraction of 0.1 with Direct Inversion in the Iterative Subspace (DIIS) and orbital occupancy with smearing of 0.04 Ha were used. The DMol^3 code employs real space cutoffs of the basis set to reduce computational cost. These cutoff distances were set at 0.41 nm for all atoms.

All surfaces were modeled with periodic slabs with a separation of 3 nm in the *c* direction. Surfaces were generated from Co and CoO bulk structures using optimized lattice constants: $a=b=0.2640$ nm, $c=0.4295$ nm for Co (experimental 0.2507 and 0.4069 nm) and $a=b=c=0.4328$ nm for CoO (experimental 0.4267 nm). Metallic surfaces were constructed using 4 layers of either a 2×2 super cell with a total of 16 atoms or a 2×3 super cell with a total of 24 atoms. Oxide surfaces of CoO(100) and CoO(111) were modeled using 4 layers of 2×2 super cells with a total of 16 Co and 16 O atoms. All surface layers were optimized with CO during geometry optimizations, simulating surface relaxation upon adsorption. Adsorption energies were calculated at 0 K without zero-energy corrections using as a reference the sum of energies for the appropriate clean surface and CO calculated separately.

Vibrational frequencies for adsorbed CO were obtained from the mass-weighted Hessian (second derivative) matrix (*39*). Evaluation of the Hessian matrix was performed using two-point numerical differentiation of analytical gradients (*36*). A step size of 0.01 Bohr was used for the numerical differentiation using the finite difference method. For molecular systems, the size of the Hessian matrix is $3N\times3N$, where N is the number of atoms. For periodic systems, however, the computational cost is higher. In order to reduce the computational cost of frequency calculations, the so-called "partial Hessian" approach was used. This approach is particularly well suited for use with the finite difference method. The vibration of adsorbed CO is localized compared to low-frequency motions of surface Co atoms and, therefore, the frequency of the CO vibration depends mostly on the motions of the C and O atoms. Consequently, a good estimate can be obtained with the finite difference approach using only the atoms of the adsorbate. Studies of other adsorption systems have shown that the partial Hessian approximation yields vibrational frequencies within a few

In Applications of Molecular Modeling to Challenges in Clean Energy; Fitzgerald, G., et al.;
ACS Symposium Series; American Chemical Society: Washington, DC, 2013.

wavenumbers of the corresponding exact calculations (*40–42*). The reported calculated vibrational frequencies were uniformly scaled with a single empirical factor of 1.0756 based on referencing to the experimental frequency of 2020 cm^{-1} for CO adsorbed on metallic Co in static adsorption experiments at room temperature.

Results and Discussion

Catalyst samples prior to reaction testing were analyzed by temperature-programmed reduction (TPR) in H_2/Ar flow from room temperature to 873 K at a rate of 10 K/min. Two H_2 consumption peaks were detected. The first one at 533-553 K for the transition from Co_3O_4 to CoO and the second one at 698-733 K for the transition to metallic Co. These TPR results show that Co may not be fully reduced (may not be fully metallic due to presence of Co(II) oxide) after reduction at our chosen reduction temperatures of 573 and 623 K and during F-T reaction testing at 493 K. Previous studies with Co-Mn/TiO_2 showed that larger Co_2O_3 clusters redisperse and form smaller metallic Co nanoparticles on reduction (*34*, *35*).

The conclusion that Co nanoparticles on the fresh catalyst may not be fully reduced is supported by X-ray photoelectron spectroscopic (XPS) results. XPS measurements were performed after reduction and consequent passivation with CO_2 at 423 K. All XPS spectra exhibited Co $2p_{3/2}$ and Co $2p_{1/2}$ peaks at 781.1–781.2 eV and 796.5–796.8 eV, respectively, and an energy separation between the Co $2p_{3/2}$ and Co $2p_{1/2}$ peaks of around 15.5–15.8 eV, indicating the presence of a CoO-like phase.

The IR spectra for the Co/TiO_2 catalyst prepared by incipient wetness and pre-reduced at 623 K under F-T reactions conditions at 493 K as a function of time on stream are shown in Figure 1. The feed gas hourly space velocity (GHSV) was kept at 3010 h^{-1} with the CO/H_2 feed molar ratio of 0.5. Consumption of reactants and formation of products was monitored using a gas chromatograph. The initial strong rovibrational band for gas-phase CO centered at 2143 cm^{-1} at 22 min of time on stream significantly reduces as the reaction progresses, and CO adsorbed on the catalyst surface is observed at 98 min on stream. The band for atop-bonded (linear) CO is usually located at about 2010-2060 cm^{-1}.

Interestingly, *two distinct* atop CO peaks are observed in Figure 1: one peak at ~2056 and another at ~2010 cm^{-1}. The same two peaks for adsorbed CO were observed under reaction conditions for the three other evaluated Co/TiO_2 catalyst samples obtained with different preparation procedures. Furthermore, these two bands (at ~2050 and ~2020 cm^{-1}) were also observed in separate CO adsorption experiments without hydrogen at room temperature (additional IR spectra are not shown for brevity).

These two bands can be attributed to CO adsorbed on Co nanoparticles and not on the TiO_2 support because similar double-feature IR bands were previously reported for Co catalysts on different supports: for Co/SiO_2 (*22*, *43–45*) and Co/Al_2O_3 (*19*, *46*, *47*). In the study on the effects of water addition on the performance of Co/SiO_2 catalysts, the apparent intensity ratio of the bands at 2056 and 2010 cm^{-1} changes with the partial pressure of added water and corresponding changes in

In Applications of Molecular Modeling to Challenges in Clean Energy; Fitzgerald, G., et al.;
ACS Symposium Series; American Chemical Society: Washington, DC, 2013.

catalyst activity and selectivity, demonstrating the importance of dynamic catalyst surface changes (*44*). Although the two atop CO bands were reported in multiple previous studies, their assignments are conflicting and mostly speculative. For example, they were assigned to vertical and angled CO on metallic Co sites, CO adsorbed on a single metallic Co atom with and without co-adsorbed H on the same atom, CO adsorbed on metallic Co and partially charged $Co^{\delta+}$, or simply labeled as CO on Co Type 1 and Co Type 2 sites (*11*, *12*, *45–47*).

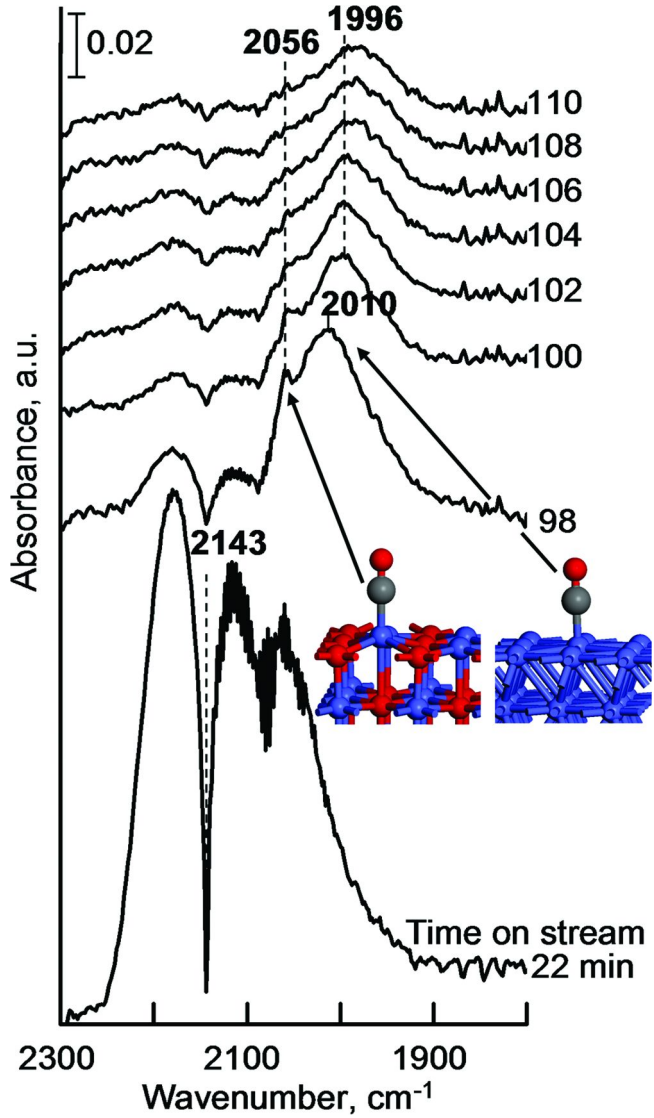

Figure 1. In-situ IR spectra of a Co/TiO_2 catalyst (pre-reduced at 623 K) under F-T reaction conditions as a function of time on stream. Feed GHSV 3010 h^{-1}, 1 atm, CO/H_2 mol feed ratio of 0.5, 493 K. (see color insert)

In Applications of Molecular Modeling to Challenges in Clean Energy; Fitzgerald, G., et al.;
ACS Symposium Series; American Chemical Society: Washington, DC, 2013.

In order to explain the origin of the two atop-bonded CO species observed in IR experiments, DFT calculations were used to develop catalyst surface models and test different assignments by evaluating CO adsorption energies and vibrational frequencies on different surface sites. First, the hypothesis that CO adsorbs on different Co metallic sites was evaluated. CO adsorption on a flat Co(001) surface (Figure 2a) (*48*) was compared to that on step sites of Co(102) (Figure 2b) (*24*, *48*) and on Co(001) with 2 top atom rows removed (Figure 2c) (*24*, *25*). The results in Table 1 for calculated adsorption energies and normal vibrational modes show that the estimated frequency for CO on step sites is within several wavenumbers from that for CO on the flat Co sites. In addition, higher adsorption energies for CO on step sites compared to that on the flat Co(001) are inconsistent with a more rapid decrease of the peak at 2056 cm^{-1} on He purging in CO adsorption experiments at room temperature. The DFT calculations, therefore, suggest that atop-bonded CO on different metallic Co sites (flat and step surfaces) have similar frequencies and, thus, the two atop-bonded CO peaks cannot be explained by the morphology of Co particles. In addition, if one of the experimentally observable bands was indeed associated with CO on steps or other coordinatively unsaturated sites (defects), then the intensity of such a band should correlate with a number of defects and exhibit a trend with the size of Co nanoparticles. The absence of such a trend in previous studies is consistent with our conclusion that the morphology of metallic Co particles cannot explain the two experimentally observed atop-bonded CO peaks.

Since the calculation results in Table 1 suggest that CO species adsorbed on different metallic Co sites are spectroscopically indistinguishable, the same conclusion applies to CO species adsorbed at different angles to the surface on Co metallic sites, for example on steps or defects. The computational results, therefore, also do not support the hypothesis that the two spectroscopic peaks can be explained by vertical and angled CO species. The hypothesis of hydrogen co-adsorption was not evaluated computationally because the same two atop-bonded CO peaks were observed in our CO adsorption experiments in the absence of hydrogen.

The second hypothesis, which was evaluated computationally, attributed the two different adsorption sites to metallic Co and metallic Co on top of Co oxide. An arrangement of a metallic Co layer on top of CoO would generate partially charged $Co^{\delta+}$ surface atoms. For this evaluation, the adsorption of CO on metallic Co was compared to that on surfaces with 2 layers (Figure 2d) and then with 1 layer of metallic Co on top of CoO(100) oxide surface (Figure 2e) as representations of materials with a metallic shell surface over an oxide core. The CO frequency results in Table 1 for these shell structures (entries d and e) indicate that even a single layer of metallic Co on top of an oxide structure would adsorb CO similarly to purely metallic Co: the CO frequency is predicted to be the same within 2 cm^{-1}. In addition, a shell metal model would not be able to explain the experimentally observed decrease in the concentration of three- fold and bridge-bonded CO associated with the dominance of the atop-bonded peak at 2056 cm^{-1} in our CO adsorption measurements at room temperature.

In Applications of Molecular Modeling to Challenges in Clean Energy; Fitzgerald, G., et al.;
ACS Symposium Series; American Chemical Society: Washington, DC, 2013.

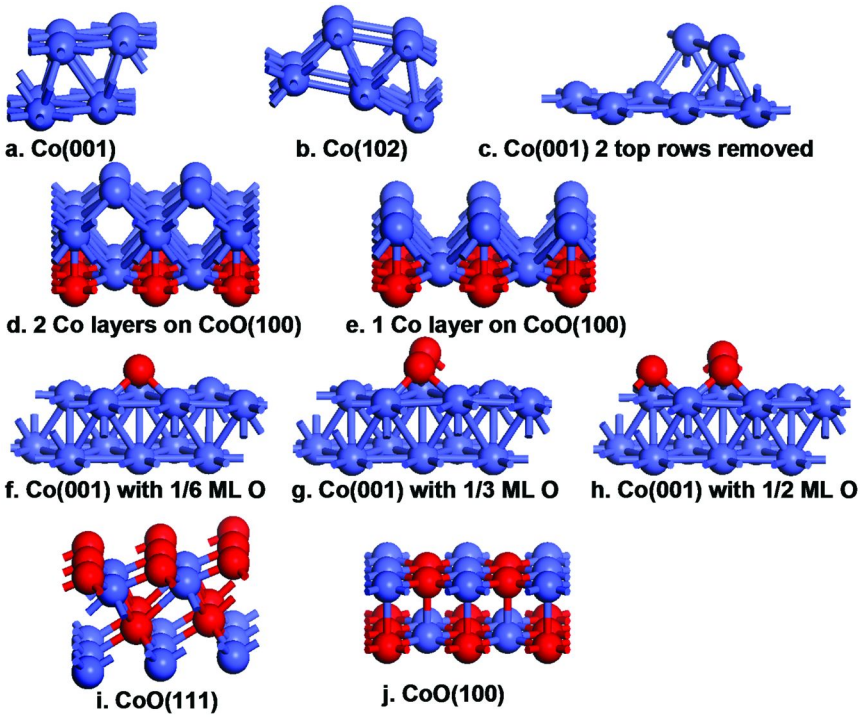

Figure 2. Models of metallic and Co oxide surfaces used in DFT calculations for interpretation of IR spectra for CO adsorption on Co/TiO_2 in Figure 1. Only two top layers are shown for each model for clarity. DFT results for CO adsorption are presented in Table 1. (see color insert)

The experimentally observed decrease in the coverage of three-fold and bridge-bonded CO could be explained if the atop-bonded CO at 2056 cm^{-1} were associated with Co atoms surrounded by oxygen atoms on the surface, eliminating Co three-fold sites and reducing the number of Co bridge sites. Accordingly, the third hypothesis assumed that the band at 2056 cm^{-1} may be associated with CO surrounded by adsorbed oxygen as neighboring surface species. Surface oxygen can be present due to, for example, bulk oxygen diffusion from a partially reduced core of Co particles. The hypothesis of surface oxygen was tested by evaluating CO adsorption on the metallic Co(001) surfaces with a variable concentration of adsorbed oxygen: 1/6, 1/3 and 1/2 of monolayer atomically adsorbed oxygen (Figures 2f-h). The results in Table 1 indicate that the calculated CO frequency is significantly affected by oxygen coverage. The band is shifted to higher values by 10, 19 and 58 cm^{-1} for, respectively, 1/6, 1/3, and 1/2 ML oxygen coverage. These results suggest that the CO peak in the presence of surface oxygen would be broad, and that its position would change significantly with oxygen coverage caused, for example, by different reduction temperatures. Since this is not observed experimentally and the positions of the two CO peaks are fairly constant, this suggests that oxygen on the surface is not simply adsorbed at a variable coverage but is a part of a well-defined Co phase.

In Applications of Molecular Modeling to Challenges in Clean Energy; Fitzgerald, G., et al.;
ACS Symposium Series; American Chemical Society: Washington, DC, 2013.

Table 1. DFT Calculation Results for Adsorption Energies and Vibrational Frequencies for Atop-Bonded CO on Different Metallic Cobalt and Cobalt Oxide Surfaces*

Model surface	*-ΔE ads, kJ/mol*	*Calculated frequency, cm-1*
a. Co(001) flat surface	143	2020
b. Co(102) step surface 1/6 ML coverage	160	2018
c. Co(001) step surface (2 rows removed) 1/6 ML coverage	167	2020
d. Two layers of Co on top of CoO(100) flat surface	161	2020
e. One layer of Co on top of CoO(100) flat surface	176	2018
f. Co(001) flat surface 1/6 ML coverage with 1/6 ML coverage by oxygen atoms	140	2030
g. Co(001) flat surface 1/6 ML coverage with 1/3 ML coverage by oxygen atoms	135	2039
h. Co(001) flat surface 1/6 ML coverage with 1/2 ML coverage by oxygen atoms	128	2078
i. CoO(111) flat surface	132	2040
j. CoO(100) flat surface	133	2043

* 1/4 ML CO coverage unless otherwise noted. Model surfaces with the same letter labels as the entries in Table 1 are shown in Figure 2.

The final hypothesis assumed that the two CO peaks can be attributed to adsorption on metallic Co and CoO oxide since TPR and XPS measurements suggest that both of these phases are present. Two CoO surfaces, CoO(111) and Co(100) shown in, correspondingly, Figures 2i and 2j, were evaluated and compared to metallic Co(001). The CoO(100) surface was found to be more energetically stable than CoO(111). The CO frequency on CoO(100) is calculated to be at 2043 cm^{-1} (Table 1), in good agreement with the experimental peak at 2056 cm^{-1}. This peak for CO on CoO is predicted to be at a higher wavenumber than that for CO on the flat metallic Co(001) at 2020 cm^{-1}, which is also in good agreement with the second experimental band at 2010 cm^{-1} in Figure 1. For comparison, a previous DFT study for CO adsorption on Co(001) reported a frequency of 2017 cm^{-1} (*49*). In addition, the calculated adsorption energy for CO on CoO is lower than that on metallic Co by about 10 kJ/mol (Table 1) and, therefore, the former can be expected to desorb preferentially on He purge, again in agreement with our experimental observations. Moreover, the adsorption of CO on CoO explains the decrease in intensity of CO adsorbed on three-fold and bridge Co sites when the 2056 cm^{-1} band dominates the spectra in CO adsorption experiments at room temperature. The CoO(100) surface (Figure 2g) has atop Co sites, a reduced number of bridge bonding sites and no three-fold Co sites due to neighboring lattice oxygen.

In Applications of Molecular Modeling to Challenges in Clean Energy; Fitzgerald, G., et al.;
ACS Symposium Series; American Chemical Society: Washington, DC, 2013.

Atop-bonded CO on Co^{+2} sites of CoO is sometimes assigned to an IR peak at ~2143 cm^{-1}, which was not observed in our studies. Such an assignment, however, is based on limited evidence because CO adsorption on Co oxides, compared to metallic Co, has not been well studied. For example, this assignment, as a tentative interpretation, was made based on an apparent correlation between the intensity of the IR peak at 2143 cm^{-1} and XRD measurements for Co/SiO_2 samples at different extents of Co oxidation (*50*). Since XRD measurements do not provide information about the surface composition, such a correlation is not reliable. In addition, in IR measurements of CO adsorption on Co sites in CoO-MgO samples (*51–53*), the dominant peaks were at ~2028 and ~2076 cm^{-1}, in agreement with the results in Figure 1. Furthermore, the same peaks were observed with CoO-MoO samples at 77 K and room temperature, indicating that CO adsorbs predominantly on metallic Co and CoO sites, and not on Co carbides, because CO decomposition and formation of Co carbide phases at 77 K can be expected to be minimal.

In summary, a combination of DFT calculations with IR spectroscopic results provided a molecular-level understanding of the initial surface structure of Co/TiO_2 catalysts. Evaluation of multiple possible Co surfaces (metallic Co with flat and step sites, metallic Co with surface oxygen at different coverage values, cobalt oxide, and metallic cobalt layers on top of cobalt oxide) with DFT calculations suggests that only metallic Co and a Co oxide surface similar to Co(II) oxide are consistent with the IR measurements and additional catalyst characterization with TPR and XPS measurements. The assignment of one of the IR bands to CO adsorbed on a Co oxide phase can be specifically tested in future experiments. If this assignment is confirmed, calibrations of IR peak intensities will make it possible to evaluate the ratio of the two Co phases (metallic and oxidized) under reaction conditions and analyze its effects on the catalyst activity, selectivity, and stability. Additional studies can also evaluate the effects of the formation of Co carbides on the catalyst surface due to decomposition of CO under reaction conditions. Understanding of such dynamic surface changes is critical for optimization of reaction conditions for current catalysts and development of improved catalyst formulations.

Adsorption and Reactivity of Acetylene on Platinum-Tin Surface Alloys

Platinum Bimetallic Nanoparticles as Catalysts of Choice for Upgrading Biomass-Derived Oils to Fuels and Chemicals

Biomass conversion to transportation fuels and chemical feedstocks remains an area of high profile and intensive research (*54–62*). Triglycerides from vegetable oils, animal fats or algae can be used directly as a component of diesel fuel or upgraded by esterification (*60*, *63–65*). Conversion technologies for other types of biomass (lignocellulosic feedstocks) can be classified into three main types: (1) gasification to produce synthesis gas for further processing using Fischer-Tropsch synthesis, (2) pyrolysis or liquefaction to produce bio-oil, and (3) hydrolysis for the production of aqueous sugars and lignin. These technologies have different efficiencies, depending on the nature of the biomass source (*e.g.*,

wood, corn stover, crop residues, sugar cane, grasses, or aquatic plants). The first two technologies, gasification and production of bio-oil, offer greater flexibility and robustness with respect to the type of biomass than the third route, hydrolysis (*59*). Although the first route offers the greatest flexibility (practically all biomass types can be gasified), gasification has a major disadvantage: all the existing carbon-hydrogen bonds in the biomass need to be broken in the production of synthesis gas in order to be reassembled later using a capital and energy-intensive Fischer-Tropsch synthesis. This breaking and reassembling of chemical bonds is inherently inefficient.

The inefficiency of breaking all carbon-hydrogen bonds is avoided in the second route: production of bio-oil. Since it is a potentially more efficient technology, bio-oil production and conversion to fuels and chemicals are actively studied as a sustainable and environmentally friendly technology for obtaining transportation fuels and feedstocks for the chemical industry. Bio-oils can be produced by two methods: pyrolysis and liquefaction. In pyrolysis, biomass is heated in the absence of air, forming a gaseous product, which then condenses as bio-oil with yields of up to 80 wt% (*55*, *56*, *61*). A number of pyrolysis technologies have been commercialized. In contrast to simple pyrolysis, liquefaction is usually performed at elevated pressures (50-200 atm) in a controlled atmosphere, for example, in the presence of hydrogen and a catalyst, and longer reactor residence times in order to obtain bio-oil with better properties, mostly with lower oxygen content (*55–58*).

Bio-oils produced by pyrolysis typically contain about 40-45 wt% oxygen and 25-30 wt% water. Bio-oils obtained by liquefaction typically have 15 wt% oxygen and 5 wt% water (*55–58*). Bio-oils are usually hydrophilic and cannot be used directly as a component of petroleum-based transportation fuels. As a result, all bio-oils, including the higher quality bio-oils obtained from liquefaction, have to be upgraded in order to reduce the concentration of oxygenates (oxygen-containing hydrocarbons) and water. A high oxygen concentration makes bio-oils (a) acidic and corrosive, (b) unstable with respect to polymerization and other reactions during storage, (c) too viscous for use as a fuel component, and (d) less energetically valuable per unit weight than petroleum-derived hydrocarbons. Although there are efficient processes for the production of bio-oils, there are significant challenges in the development of efficient bio-oil upgrading technologies.

Direct upgrading of bio-oils is currently dominated by technologies adapted from petroleum refining: (1) oxygen removal and hydrogenation with catalysts traditionally used for desulfurization of petroleum products and (2) cracking and oxygen removal with catalysts traditionally used for cracking of heavier petroleum fractions to produce gasoline and diesel fractions. Bio-oils can also be converted to hydrogen or synthesis gas using steam reforming for further conversion using Fischer-Tropsch synthesis (*66–69*).

Oxygen removal in the presence of hydrogen (hydrodeoxygenation) is usually performed at 573-873 K at a hydrogen pressure above 100 atm over sulfided Co-Mo or Ni-Mo supported catalysts (*56*, *59*, *70–72*). These catalysts have been developed for sulfur and nitrogen removal in the petroleum refining industry, and they are not optimized for bio-oil upgrading. Insufficient activities and low

In Applications of Molecular Modeling to Challenges in Clean Energy; Fitzgerald, G., et al.;
ACS Symposium Series; American Chemical Society: Washington, DC, 2013.

hydrogen efficiencies have prompted introduction of a two-stage process (*73*, *74*). The other major disadvantage of Co-Mo and Ni-Mo catalysts is that they are most active in the sulfided form, which needs to be maintained by a sulfur supply in the feed, such as H_2S addition. Utilization of sulfides presents a significant environmental hazard. Furthermore, process operation at high hydrogen pressures is expensive and requires a source of hydrogen, which for sustainability reasons should be obtained from renewable sources, and therefore, requires additional processing (*59*, *71*). Hydrogen efficiency and catalyst stability are also issues that require improvement (*70*). As a result, there are intensive research efforts aimed at replacing sulfided catalysts with supported metals such as Pt (*71*, *75*).

Bio-oil upgrading with zeolite catalysts is typically performed at atmospheric pressure and 623-773 K. The most common zeolite is ZSM-5, which is adapted from fluid catalytic cracking (FCC) in petroleum refining. Cracking over zeolites reduces oxygen content and improves thermal stability. The products include hydrocarbons (aromatic and aliphatic), water-soluble organics, water, oil-soluble organics, gases (CO_2, CO, light alkanes) and coke. Similarly to hydrodeoxygenation over Co-Mo and Ni-Mo sulfides, these catalysts are not tailored for bio-oil upgrading and, therefore, the amount of coke produced can be significant, up to 40 wt%, and the yield of the organic liquid fraction is small at 15-35 wt% (*55*, *56*). As an alternative to cracking over zeolites, hydrocracking over Pt/ZSM-5 catalysts has been recently evaluated (*76*).

Since upgrading of bio-oils over sulfided Co-Mo or Ni-Mo and over zeolites is not sufficiently effective, significant research efforts are directed at identifying more efficient new technologies. The following promising chemistries have been recently reported that utilize Pt and Pt bimetallic catalysts: (a) aqueous-phase reforming to CO_2 and high-purity H_2, (b) generation of high purity synthesis gas (mixture of CO and H_2), and (c) hydrogenolysis for simultaneous cracking and oxygen removal. In addition, glycerol has been evaluated for use in direct alcohol fuel cells by utilizing Pt catalysts (*77*).

Aqueous-phase reforming for production of high purity hydrogen was initially reported for a number of oxygenated hydrocarbons over Pt/Al_2O_3 catalysts in 2002 (*78–80*). A similar chemistry was later proposed for production of light alkanes from biomass-derived feedstocks over Pt/SiO_2-Al_2O_3 (*81*). Addition of Sn to Pt/Al_2O_3 has been found to improve catalyst performance (*82*). Catalyst and process development has relied primarily on kinetic studies and high-throughput (trial and error) screening (*83*, *84*). For example, more than 130 bimetallic Pt and Pd-based formulations were screened for aqueous-phase reforming (APR) of ethylene glycol, and Pt-Ni and Pt-Co bimetallics were identified as promising leads (*84*). The increased activity of the alloys was proposed to be linked to lower adsorption energies of the reaction products, CO and H_2. In contrast, surface science studies of oxygenates on Pt(111) and Ni/Pt(111) bimetallic surfaces were used to propose that the reforming activity was correlated with the *d*-band center of the surfaces (*62*, *85*).

Empirical studies on the effects of the Pt particle size, catalyst composition and supports demonstrate the potential for optimization of the catalyst formulation and process conditions (*86–89*). For example, larger Pt nanoparticles were linked to a selectivity change towards hydrodeoxygenation rather than formation of H_2

In Applications of Molecular Modeling to Challenges in Clean Energy; Fitzgerald, G., et al.;
ACS Symposium Series; American Chemical Society: Washington, DC, 2013.

and CO_2 based on kinetic studies (*90*). As another example, a Pt-Re catalytic system was reported to be more selective than pure Pt (*91*). Similarly to these examples, most of the recent studies on promising pure Pt and Pt bimetallic catalysts, such as Pt-Sn, rely on trial and error methodology for the selection of the catalyst and process variables (*92–94*). Development of molecular models for the adsorption and reactivity of hydrocarbons on platinum bimetallic nanoparticles will provide guidance for the identification of the most preferable technologies for bio-oil upgrading (*e.g.*, aqueous or gas-phase reforming, one or two-stage hydrodeoxygenation), efficient catalyst formulations for these preferable technologies and, moreover, optimized reaction conditions for the preferable catalysts.

The study in this section illustrates a synergistic combination of HREELS spectroscopic measurements and DFT calculations with vibrational analyses for the development of a molecular-level understanding of acetylene adsorption and reactivity on catalytic surfaces of Pt and Pt-Sn alloys. The developed methodology can be extended from acetylene to other hydrocarbons, particularly to model compounds that represent derivatives from the three main components of bio-oils: (1) hemicellulose (*e.g.*, formic and acetic acids, methanol and ethanol, acetone and formaldehyde), (2) cellulose (*e.g.*, glucose and fructose), and (3) lignin (*e.g.*, phenol, 2-methoxyphenol and isoeugenol). The methodology can, similarly, be extended to adsorption and reactivity studies on other bimetallic surfaces.

Experimental and Computational Details

Acetylene adsorption was studied with HREELS and temperature programmed desorption (TPD) in ultrahigh vacuum (UHV) at 90-1000 K on two ordered Pt surface alloys with different Sn concentrations: Pt_3Sn/Pt(111) and Pt_2Sn/Pt(111).

The (2×2) Sn/Pt(111) surface alloy (Pt_3Sn) was prepared by evaporating 0.7 ML Sn onto the Pt(111) surface and subsequently annealing to 1000 K for 10 s. The ($\sqrt{3}\times\sqrt{3}$)R30° Sn/Pt(111) surface (Pt_2Sn) was prepared by evaporating 1.0 ML Sn on the Pt(111) surface and annealing to 850 K for 10 s. The 2-D order of both surfaces was observed by low energy electron diffraction (LEED). The coverage of Sn in the topmost surface layer was θ_{Sn}=0.25 for the (2×2) Sn/Pt(111) alloy and θ_{Sn}=0.33 for the ($\sqrt{3}\times\sqrt{3}$)R30° Sn/Pt(111) alloy, corresponding to the (111) plane of Pt_3Sn and Pt_2Sn surface layers, respectively.

HREELS spectra were collected with the sample initially at 90 K with a typical resolution of 50 cm^{-1} and incident beam energy of 4.5 eV. All TPD measurements were made using the QMS ionizer in line-of-sight with the sample surface and a linear heating rate of 3 K/s. The crystal was positioned 1 mm away from the entrance aperture of the QMS shield to reduce contributions to the spectra from the crystal back and edges (*95*). Two highly transparent, fine, grounded screens were in place to eliminate possible damage to the adsorbed layer from low energy electrons emitted by the QMS ionizer region (*96*).

Gradient-corrected periodic DFT calculations were performed with the DMol^3 code in Materials Studio 4.0 software by Accelrys Software, Inc.

In Applications of Molecular Modeling to Challenges in Clean Energy; Fitzgerald, G., et al.;
ACS Symposium Series; American Chemical Society: Washington, DC, 2013.

The calculations used the DNP basis set and the GGA RPBE functional. Tightly bound core electrons were represented with semicore pseudopotentials. Reciprocal-space integration over the Brillouin zone was approximated through *k*-point sampling with a separation of 0.5 nm^{-1} using the Monkhorst-Pack grid: (2×2×1). Convergence with respect to the number of *k*-points was tested by increasing their number for representative structures. The density mixing fraction of 0.1 with DIIS and orbital occupancy with smearing of 0.005 Ha were used. The orbital cutoff distance was set at 0.41 nm for all atoms.

All surfaces were modeled using infinite slabs constructed with periodic unit cells, similarly to our previous studies for ethylene oxide and cyclohexanone adsorption (*97*, *98*). The optimized Pt lattice constant of 0.4028 nm was used to generate the surface from the bulk crystal with a vacuum spacing between the slabs in the *c* direction of 3 nm. An infinite slab with a 4×4×4 unit cell with a total of 64 Pt atoms (Figure 3a) was used to model the Pt(111) surface. The Pt_3Sn/Pt(111) surface was constructed using a 4×4×4 unit cell of Pt(111) and then substituting 4 out of 16 surface Pt atoms by Sn in the appropriate positions (Figure 3b). The Pt_2Sn/Pt(111) surface was constructed using a 3×3×4 unit cell of Pt(111) and then substituting 3 out of 9 surface Pt atoms by Sn in the appropriate positions (Figure 3c).

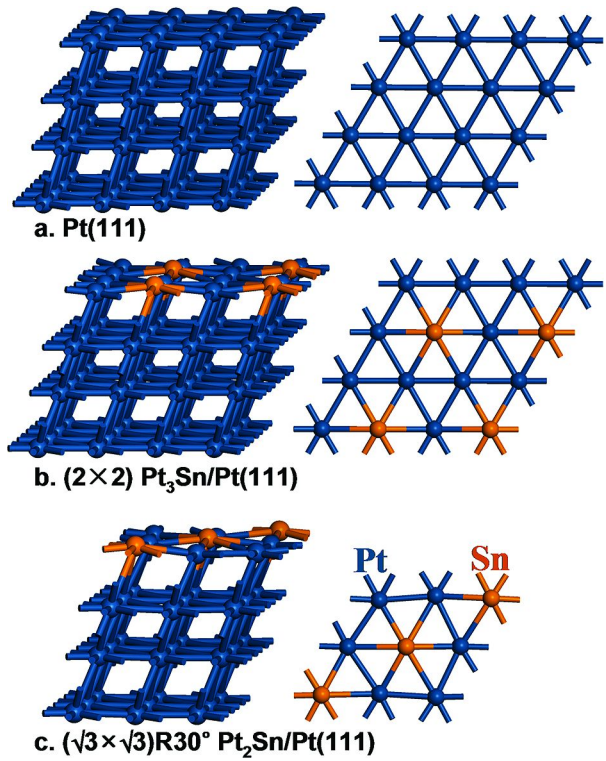

Figure 3. Unit cells of periodic infinite surface models for Pt and Pt-Sn: side view (left) and top view of the first layer (right). (see color insert)

In Applications of Molecular Modeling to Challenges in Clean Energy; Fitzgerald, G., et al.;
ACS Symposium Series; American Chemical Society: Washington, DC, 2013.

All surface layers were optimized with acetylene during geometry optimizations, simulating surface relaxation upon adsorption. Adsorption energies were calculated at 0 K without zero-energy corrections using as a reference the sum of energies for the appropriate clean surface and acetylene calculated separately. Frequency calculations were performed with a partial Hessian for the adsorbed hydrocarbon species. Calculated frequencies are reported without adjustments.

Results and Discussion

HREELS spectra for acetylene adsorption on the Pt_3Sn alloy at the dosing temperature of 90 K exhibit a single carbon-carbon bond stretching, ν_{CC}, peak at 1601 cm^{-1} (spectrum is not shown for brevity). This peak can be assigned to acetylene species π-bonded to a single Pt atom because acetylene is expected to adsorb initially without bond breaking at low temperatures. The corresponding peak at 1635 cm^{-1} for the Pt_2Sn alloy in the spectrum collected at 200 K in Figure 4 can also be assigned to π-bonded acetylene.

The calculated carbon-carbon bond stretching frequencies for different acetylene adsorption modes and $C\text{-}CH_2$ vinylidene species on Pt(111) and the two Pt-Sn alloys are summarized in Table 2. The calculated frequencies for π-bonded acetylene are significantly different from the experimentally observed values. The calculated frequencies at 1817-1830 cm^{-1} in Table 2 are close to that of gas-phase acetylene at 1974 cm^{-1} and overestimate the experimental values by about 200 cm^{-1}. In contrast, for strongly bound acetylene species, calculated and experimental frequencies are in good agreement without any adjustments or corrections. For example, the calculated ν_{CC} of 1351 cm^{-1} (Table 2) for the most stable acetylene configuration on Pt(111) in a di-σ/π-bonded mode (Figure 5a) is close to the reported experimental value of ~1310 cm^{-1} (*99*, *100*).

The value of ν_{CC} for di-σ/π-bonded acetylene on the Pt_3Sn surface is calculated to be at 1326 cm^{-1}, similar to that on Pt(111). Since there are no experimental peaks that are close to this value in Figure 4, we can conclude that di-σ/π-bonded acetylene does not form on this Pt-Sn alloy. DFT calculations suggest that this is due to relative destabilization of this adsorption mode compared to other configurations caused by the presence of surface Sn atoms. The di-σ/π-bonded acetylene is not observed on the Pt_2Sn alloy because there are no three-fold Pt sites due to the arrangement of Sn atoms on the surface (Figure 3c). In addition, DFT calculations suggest that adsorption on 2Pt-Sn sites or, more broadly, on any Sn sites for both alloys is less energetically favorable than adsorption on Pt-only sites.

On annealing from 90 to 200 K, π-bonded acetylene on the alloys transforms to a more stable di-σ-bonded configuration (ν_{CC} peak at 1495 cm^{-1} for the Pt_2Sn alloy in Figure 4). The calculated frequency of 1476 cm^{-1} in Table 2 is in good agreement with the experimental value. On the Pt_3Sn surface, the calculated frequency is similar at 1460 cm^{-1}. The experimental peak for Pt_3Sn in Figure 4, however, is observed at a significantly lower value of 1417 cm^{-1}, which indicates the presence of different hydrocarbon species. This peak can be assigned to vinylidene, $C\text{-}CH_2$,

In Applications of Molecular Modeling to Challenges in Clean Energy; Fitzgerald, G., et al.;
ACS Symposium Series; American Chemical Society: Washington, DC, 2013.

species that form upon acetylene isomerization (ν_{CC} calculated at 1445 cm^{-1} in Table 2).

DFT calculated reaction energies for acetylene isomerization to C-CH_2 are summarized in Figures 5d-f. These results suggest that it is energetically preferable for acetylene to transform into C-CH_2 on the Pt(111) and Pt_3Sn surfaces where C-CH_2 species can be di-σ/π-bonded to three-fold Pt sites in the μ_3-η^2 configuration (Figures 5d and e). In contrast, on the Pt_2Sn alloy in the absence of three-fold Pt sites, C-CH_2 species are predicted to be di-σ-bonded to a bridge Pt-Pt site (μ_2-η^1 configuration, Figure 5f) and, therefore, to be less stable. As a result, the isomerization of acetylene to C-CH_2 on Pt_2Sn is estimated to become endothermic at +13 kJ/mol and, therefore, less favorable. This energetic difference provides a preliminary explanation of why di-σ-bonded acetylene is observed on Pt_2Sn while C-CH_2 vinylidene is observed on Pt_3Sn. Additional DFT calculations can evaluate transition states and provide further insight on the geometric and energetic requirements for acetylene isomerization.

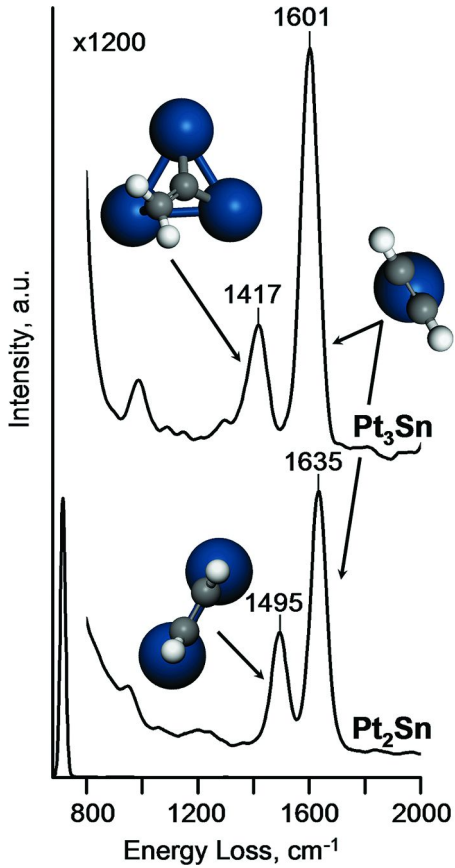

Figure 4. HREELS spectra for acetylene on Pt-Sn alloys at 200 K and DFT computational models of stable adsorbates with vibrational modes that match experimental frequencies. (see color insert)

In Applications of Molecular Modeling to Challenges in Clean Energy; Fitzgerald, G., et al.;
ACS Symposium Series; American Chemical Society: Washington, DC, 2013.

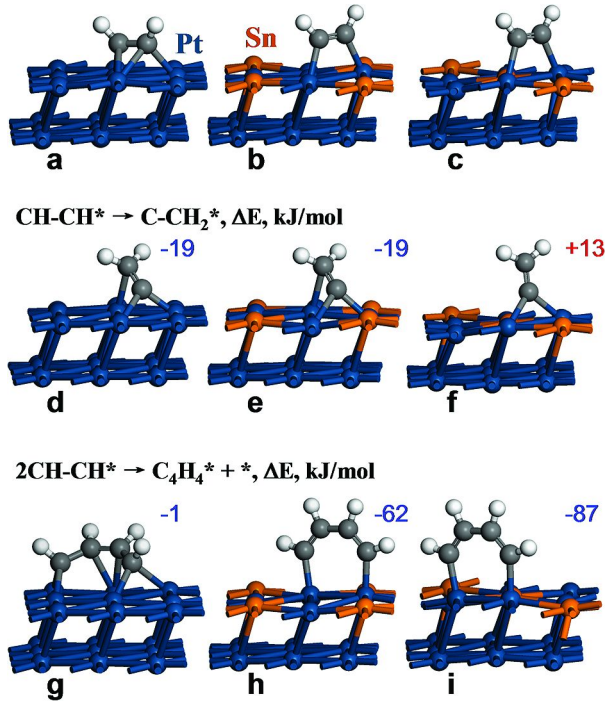

Figure 5. DFT computational models of acetylene CH-CH (a-c), vinylidene C-CH_2 (d-f) and acetylene dimer C_4H_4 (g-i) on Pt(111) (a, d, g), Pt_3Sn (b, e, h) and Pt_2Sn (c, f, i). Reaction energies are shown for the transformation of adsorbed acetylene to C-CH_2 and C_4H_4. (see color insert)

Table 2. DFT Calculation Results for the Carbon-Carbon Bond Stretching Vibrational Mode, ν_{CC}, of Acetylene and Vinylidene Species Adsorbed on Different surfaces, cm^{-1}

Surface species / Surface	*Pt(111)*	*Pt_3Sn/Pt(111)*	*Pt_2Sn/Pt(111)*
di-σ/π CH-CH	1351	1326	N/A
di-σ CH-CH	1426	1460	1476
π CH-CH	1830	1825	1817
C-CH_2	1460	1445	1535

In acetylene TPD spectra for the alloys, C_4 hydrocarbons and benzene are detected, indicating that in addition to isomerization and dehydrogenation, acetylene can produce dimers and trimers. The amount of produced C_4 and C_6 hydrocarbons is larger over the Pt_2Sn alloy with a higher Sn concentration. In contrast, no coupling products are observed in the absence of Sn on Pt(111) where adsorbed acetylene on annealing decomposes to carbon and hydrogen in line with our previously reported study (*101*). In another study in the presence of gas-phase hydrogen, the activity of the Pt_2Sn alloy for dimerization and trimerization was found to be 4-5 times higher than that over Pt(111) (*102*). The origin of this reactivity difference was evaluated by comparing the energetics of acetylene coupling to produce C_4H_4 surface-bound dimer species on Pt(111) and the two alloys (Figures 5g-i). The calculation results summarized in Figure 5 suggest that while the coupling reaction is estimated to be thermoneutral at -1 kJ/mol on Pt(111), it is predicted to become exothermic and, therefore, energetically favorable in the presence of Sn. Increasing the Sn concentration makes the reaction more favorable from -62 kJ/mol for Pt_3Sn to -87 kJ/mol for Pt_2Sn. The Sn content, however, has to be at an optimal level for activity enhancement since the reaction proceeds only on Pt sites, and Sn atoms only modify the energetics of Pt sites and their geometric arrangements.

In summary, this study identifies the adsorption modes of acetylene on Pt-Sn surface alloys. The results demonstrate that the presence of Sn changes preferential hydrocarbon adsorption sites, decreases stability of adsorbed species and favors associative reactions, thus, enabling formation of C_4 hydrocarbons and benzene. The developed experimental-theoretical approach can be applied to studying the adsorption and reactivity of other hydrocarbons, *e.g.*, biomass-derived hydrocarbons, on promising Pt and Pt bimetallic catalytic surfaces. The same methodology can be extended to other bimetallic materials.

Acknowledgments

Infrared spectra under Fischer-Tropsch reaction conditions were collected by Emiel de Smit under supervision of Prof. Bert Weckhuysen, Utrecht University, Netherlands. The research on Fischer-Tropsch catalysis in Prof. Bert Weckhuysen's group was partially funded by the Dutch government grant NRSC-C 2009-2013. The HREELS spectra for acetylene adsorption on Pt-Sn alloys were collected by Haibo Zhao and interpreted by Xiaofang Yang under supervision of Prof. Bruce Koel, Princeton University. The work on Pt-Sn alloys in Prof. Bruce Koel's group was partially supported by the National Science Foundation under grant CHE-1129417. DFT calculations were performed by Jie Gao under supervision of Prof. Simon Podkolzin, Stevens Institute of Technology. Prof. Simon Podkolzin's research was partially supported by the National Science Foundation under grant OISE-1157600. Additional funding for Prof. Simon Podkolzin's research was provided by Stevens Institute of Technology.

References

1. Cremer, P. S.; Su, X.; Shen, Y. R.; Somorjai, G. A. *J. Am. Chem. Soc.* **1996**, *118* (12), 2942–2949.
2. Cremer, P. S.; Su, X.; Ron Shen, Y.; Somorjai, G. A. *J. Phys. Chem. B* **1997**, *101* (33), 6474–6478.
3. Natal-Santiago, M. A.; Podkolzin, S. G.; Cortright, R. D.; Dumesic, J. A. *Catal. Lett.* **1997**, *45* (3,4), 155–163.
4. Podkolzin, S. G.; Alcala, R.; De Pablo, J. J.; Dumesic, J. A. *J. Phys. Chem. B* **2002**, *106* (37), 9604–9612.
5. Podkolzin, S. G.; Alcalá, R.; Dumesic, J. A. *J. Mol. Catal. A: Chem.* **2004**, *218* (2), 217–227.
6. Podkolzin, S. G.; Watwe, R. M.; Yan, Q.; de Pablo, J. J.; Dumesic, J. A. *J. Phys. Chem. B* **2001**, *105* (36), 8550–8562.
7. Shen, J.; Hill, J. M.; Watwe, R. M.; Podkolzin, S. G.; Dumesic, J. A. *Catal. Lett.* **1999**, *60* (1,2), 1–9.
8. de Smit, E.; Weckhuysen, B. M. *Chem. Soc. Rev.* **2008**, *37* (12), 2758–2781.
9. Diehl, F.; Khodakov, A. Y. *Oil Gas Sci. Technol.* **2009**, *64* (1), 11–24.
10. Gaube, J.; Klein, H. F. *J. Mol. Catal. A: Chem.* **2008**, *283* (1-2), 60–68.
11. Khodakov, A. Y. *Catal. Today* **2009**, *144* (3-4), 251–257.
12. Khodakov, A. Y.; Chu, W.; Fongarland, P. *Chem. Rev.* **2007**, *107* (5), 1692–1744.
13. Iglesia, E.; Soled, S. L.; Fiato, R. A.; Via, G. H. *J. Catal.* **1993**, *143* (2), 345–368.
14. Guczi, L.; Stefler, G.; Borkó, L.; Koppány, Z.; Mizukami, F.; Toba, M.; Niwa, S. *Appl. Catal., A* **2003**, *246* (1), 79–86.
15. Jacobs, G.; Ji, Y.; Davis, B. H.; Cronauer, D.; Kropf, A. J.; Marshall, C. L. *Appl. Catal., A* **2007**, *333* (2), 177–191.
16. Farrauto, R.; Hwang, S.; Shore, L.; Ruettinger, W.; Lampert, J.; Giroux, T.; Liu, Y.; Ilinich, O. *Annu. Rev. Mater. Res.* **2003**, *33*, 1–27.
17. Davis, B. H. *Catal. Today* **2009**, *141* (1-2), 25–33.
18. Lohitharn, N.; Goodwin, J. G., Jr *Catal. Commun.* **2009**, *10* (6), 758–762.
19. Sanchez-Escribano, V.; Larrubia Vargas, M. A.; Finocchio, E.; Busca, G. *Appl. Catal., A* **2007**, *316* (1), 68–74.
20. Iglesia, E.; Krishnamoorthy, S.; Tu, M.; Ojeda, M. P.; Pinna, D. *J. Catal.* **2002**, *211* (2), 422–433.
21. Davis, B. H. *Fuel Process. Technol.* **2001**, *71* (1-3), 157–166.
22. Sun, S.; Tsubaki, N.; Fujimoto, K. *Appl. Catal., A* **2000**, *202* (1), 121–131.
23. Geerlings, J. J. C.; Wilson, J. H.; Kramer, G. J.; E., K. H. P. C.; Hoek, A.; Huisman, H. M. *Appl. Catal., A* **1999**, *186*, 27–40.
24. Cheng, J.; Gong, X. Q.; Hu, P.; Lok, C. M.; Ellis, P.; French, S. *J. Catal.* **2008**, *254* (2), 285–295.
25. Cheng, J.; Hu, P.; Ellis, P.; French, S.; Kelly, G.; Lok, C. M. *J. Phys. Chem. C* **2008**, *112* (25), 9464–9473.
26. Cheng, J.; Hu, P.; Ellis, P.; French, S.; Kelly, G.; Lok, C. M. *J. Phys. Chem. C* **2008**, *112* (15), 6082–6086.

27. Kummer, J. T.; Browning, L. C.; Emmett, P. H. *J. Chem. Phys.* **1948**, *16* (7), 739–740.
28. Kummer, J. T.; DeWitt, T. W.; Emmett, P. H. *J. Am. Chem. Soc.* **1948**, *70* (11), 3632–3643.
29. Podgurski, H. H.; Kummer, J. T.; Dewitt, T. W.; Emmett, P. H. *J. Am. Chem. Soc.* **1950**, *72* (12), 5382–5388.
30. Zhuo, M.; Tan, K. F.; Borgna, A.; Saeys, M. *J. Phys. Chem. C* **2009**, *113* (19), 8357–8365.
31. Inderwildi, O. R.; Jenkins, S. J.; King, D. A. *J. Phys. Chem. C* **2008**, *112* (5), 1305–1307.
32. Huo, C. F.; Li, Y. W.; Wang, J.; Jiao, H. *J. Phys. Chem. C* **2008**, *112* (36), 14108–14116.
33. Huo, C. F.; Li, Y. W.; Wang, J.; Jiao, H. *J. Phys. Chem. C* **2008**, *112* (10), 3840–3848.
34. Morales, F.; Grandjean, D.; Mens, A.; De Groot, F. M. F.; Weckhuysen, B. M. *J. Phys. Chem. B* **2006**, *110* (17), 8626–8639.
35. Morales, F.; de Smit, E.; de Groot, F. M. F.; Visser, T.; Weckhuysen, B. M. *J. Catal.* **2007**, *246* (1), 91–99.
36. Delley, B. *J. Chem. Phys.* **2000**, *113* (18), 7756–7764.
37. Delley, B. *J. Chem. Phys.* **1990**, *92* (1), 508–517.
38. Delley, B. *Phys. Rev. B: Condens. Matter Mater. Phys.* **2002**, *66* (15), 1551251–1551259.
39. Wilson, E. B., Jr. ; Decius, J. C.; Cross, P. C. *Molecular Vibrations: The Theory of Infrared and Raman Vibrational Spectra*; Courier Dover Publications: New York, 1955.
40. Orita, H.; Uchida, K.; Itoh, N. *J. Mol. Catal. A: Chem.* **2003**, *193* (1-2), 197–205.
41. van Helden, P.; van Steen, E. *J. Phys. Chem. C* **2008**, *112* (42), 16505–16513.
42. Santana, J. A.; Ishikawa, Y. *Electrochim. Acta* **2010**, *56* (2), 945–952.
43. Heal, M. J.; Leisegang, E. C.; Torrington, R. G. *J. Catal.* **1978**, *51* (3), 314–325.
44. Krishnamoorthy, S.; Tu, M.; Ojeda, M. P.; Pinna, D.; Iglesia, E. *J. Catal.* **2002**, *211* (2), 422–433.
45. Song, D.; Li, J.; Cai, Q. *J. Phys. Chem. C* **2007**, *111* (51), 18970–18979.
46. Kadinov, G.; Bonev, C.; Todorova, S.; Palazov, A. *J. Chem. Soc., Faraday Trans.* **1998**, *94* (19), 3027–3031.
47. Couble, J.; Bianchi, D. *Appl. Catal., A* **2012**, *445-446*, 1–13.
48. Ge, Q.; Neurock, M. *J. Phys. Chem. B* **2006**, *110* (31), 15368–15380.
49. Pick, S. *Surf. Sci.* **2007**, *601* (23), 5571–5575.
50. Khodakov, A. Y.; Lynch, J.; Bazin, D.; Rebours, B.; Zanier, N.; Moisson, B.; Chaumette, P. *J. Catal.* **1997**, *168* (1), 16–25.
51. Zecchina, A.; Spoto, G.; Coluccia, S.; Guglielminotti, E. *J. Phys. Chem.* **1984**, *88* (12), 2575–2581.
52. Zecchina, A.; Spoto, G.; Borello, E.; Giamello, E. *J. Phys. Chem.* **1984**, *88* (12), 2582–2587.
53. Zecchina, A.; Spoto, G.; Garrone, E.; Bossi, A. *J. Phys. Chem.* **1984**, *88* (12), 2587–2591.

54. Savage, N. *Nature* **2011**, *474* (7352), S9–S11.
55. Corma, A.; Iborra, S.; Velty, A. *Chem. Rev.* **2007**, *107* (6), 2411–2502.
56. Huber, G. W.; Iborra, S.; Corma, A. *Chem. Rev.* **2006**, *106* (9), 4044–4098.
57. Luque, R.; Herrero-Davila, L.; Campelo, J. M.; Clark, J. H.; Hidalgo, J. M.; Luna, D.; Marinas, J. M.; Romero, A. A. *Energy Environ. Sci.* **2008**, *1* (5), 542–564.
58. Naik, S. N.; Goud, V. V.; Rout, P. K.; Dalai, A. K. *Renewable Sustainable Energy Rev.* **2010**, *14* (2), 578–597.
59. Bulushev, D. A.; Ross, J. R. H. *Catal. Today* **2011**, *171* (1), 1–13.
60. Barrón Cruz, A. E.; Melo Banda, J. A.; Mendoza, H.; Ramos-Galvan, C. E.; Meraz Melo, M. A.; Esquivel, D. *Catal. Today* **2011**, *166* (1), 111–115.
61. Brandner, A.; Lehnert, K.; Bienholz, A.; Lucas, M.; Claus, P. *Top. Catal.* **2009**, *52* (3), 278–287.
62. Skoplyak, O.; Menning, C. A.; Barteau, M. A.; Chen, J. G. *Top. Catal.* **2008**, *51* (1−4), 49–59.
63. Meher, L. C.; Vidya Sagar, D.; Naik, S. N. *Renewable Sustainable Energy Rev.* **2006**, *10* (3), 248–268.
64. Zabeti, M.; Wan Daud, W. M. A.; Aroua, M. K. *Fuel Process. Technol.* **2009**, *90* (6), 770–777.
65. Boey, P. L.; Maniam, G. P.; Hamid, S. A. *Chem. Eng. J.* **2011**, *168* (1), 15–22.
66. Czernik, S.; French, R.; Feik, C.; Chornet, E. *Ind. Eng. Chem. Res.* **2002**, *41* (17), 4209–4215.
67. Tomishige, K.; Miyazawa, T.; Asadullah, M.; Ito, S.; Kunimori, K. *J. Jpn. Pet. Inst.* **2003**, *46* (5), 322–327.
68. Dieuzeide, M. L.; Amadeo, N. *Chem. Eng. Technol.* **2010**, *33* (1), 89–96.
69. Li, C. S.; Hirabayashi, D.; Suzuki, K. *Fuel Process. Technol.* **2009**, *90* (6), 790–796.
70. Furimsky, E. *Appl. Catal., A* **2000**, *199* (2), 147–190.
71. Choudhary, T. V.; Phillips, C. B. *Appl. Catal., A* **2011**, *397* (1-2), 1–12.
72. Lin, Y. C.; Li, C. L.; Wan, H. P.; Lee, H. T.; Liu, C. F. *Energy Fuels* **2011**, *25* (3), 890–896.
73. Elliott, D. C.; Baker, E. G.; Piskorz, J.; Scott, D. S.; Solantausta, Y. *Energy Fuels* **1988**, *2* (2), 234–235.
74. Elliott, D. C.; Oasmaa, A. *Energy Fuels* **1991**, *5* (1), 102–109.
75. Zhu, X.; Lobban, L. L.; Mallinson, R. G.; Resasco, D. E. *J. Catal.* **2011**, *281* (1), 21–29.
76. Murata, K.; Liu, Y. Y.; Inaba, M.; Takahara, I. *Catal. Lett.* **2010**, *140* (1-2), 8–13.
77. Martins, C. A.; Giz, M. J.; Camara, G. A. *Electrochim. Acta* **2011**, *56* (12), 4549–4553.
78. Cortright, R. D.; Davda, R. R.; Dumesic, J. A. *Nature* **2002**, *418* (6901), 964–967.
79. Davda, R. R.; Dumesic, J. A. *Angew. Chem., Int. Ed.* **2003**, *42* (34), 4068–4071.
80. Shabaker, J. W.; Davda, R. R.; Huber, G. W.; Cortright, R. D.; Dumesic, J. A. *J. Catal.* **2003**, *215* (2), 344–352.

81. Huber, G. W.; Cortright, R. D.; Dumesic, J. A. *Angew. Chem., Int. Ed.* **2004**, *43* (12), 1549–1551.
82. Shabaker, J. W.; Dumesic, J. A. *Ind. Eng. Chem. Res.* **2004**, *43* (12), 3105–3112.
83. Davda, R. R.; Shabaker, J. W.; Huber, G. W.; Cortright, R. D.; Dumesic, J. A. *Appl. Catal., B* **2005**, *56* (1-2 SPEC. ISS.), 171–186.
84. Huber, G. W.; Shabaker, J. W.; Evans, S. T.; Dumesic, J. A. *Appl. Catal., B* **2006**, *62* (3-4), 226–235.
85. Skoplyak, O.; Barteau, M. A.; Chen, J. G. *J. Phys. Chem. B* **2006**, *110* (4), 1686–1694.
86. Lehnert, K.; Claus, P. *Catal. Commun.* **2008**, *9* (15), 2543–2546.
87. Luo, N.; Fu, X.; Cao, F.; Xiao, T.; Edwards, P. P. *Fuel* **2008**, *87* (17−18), 3483–3489.
88. Wen, G.; Xu, Y.; Ma, H.; Xu, Z.; Tian, Z. *Int. J. Hydrogen Energy* **2008**, *33* (22), 6657–6666.
89. Nichio, N. N.; Pompeo, F.; Santori, G. *Int. J. Hydrogen Energy* **2010**, *35* (17), 8912–8920.
90. Wawrzetz, A.; Peng, B.; Hrabar, A.; Jentys, A.; Lemonidou, A. A.; Lercher, J. A. *J. Catal.* **2010**, *269* (2), 411–420.
91. King, D. L.; Zhang, L.; Xia, G.; Karim, A. M.; Heldebrant, D. J.; Wang, X.; Peterson, T.; Wang, Y. *Appl. Catal., B* **2010**, *99* (1-2), 206–213.
92. Kim, T. W.; Kim, H. D.; Jeong, K. E.; Chae, H. J.; Jeong, S. Y.; Lee, C. H.; Kim, C. U. *Green Chem.* **2011**, *13* (7), 1718–1728.
93. Luo, N. J.; Wang, J. A.; Xiao, T. C.; Cao, F. H.; Fang, D. Y. *Catal. Today* **2011**, *166* (1), 123–128.
94. Menezes, A. O.; Rodrigues, M. T.; Zimmaro, A.; Borges, L. E. P.; Fraga, M. A. *Renewable Energy* **2011**, *36* (2), 595–599.
95. Peck, J. W.; Koel, B. E. *J. Am. Chem. Soc.* **1996**, *118* (11), 2708–2717.
96. Panja, C.; Saliba, N. A.; Koel, B. E. *J. Phys. Chem. B* **2001**, *105* (18), 3786–3796.
97. Kim, J.; Fu, J.; Podkolzin, S. G.; Koel, B. E. *J. Phys. Chem. C* **2010**, *114* (40), 17238–17247.
98. Kim, J.; Welch, L. A.; Olivas, A.; Podkolzin, S. G.; Koel, B. E. *Langmuir* **2010**, *26* (21), 16401–16411.
99. Ibach, H.; Lehwald, S. *J. Vac. Sci. Technol.* **1978**, *15* (2), 407–415.
100. Avery, N. R. *Langmuir* **1988**, *4* (2), 445–448.
101. Xu, C.; Peck, J. W.; Koel, B. E. *J. Am. Chem. Soc.* **1993**, *115* (2), 751–755.
102. Szanyi, J.; Paffett, M. T. *J. Am. Chem. Soc.* **1995**, *117* (3), 1034–1040.

Chapter 10

Challenges and Development of a Multi-Scale Computational Model for Photosystem I Decoupled Energy Conversion

Scott S. Pendley,[1] Amy K. Manocchi,[2] David R. Baker,[2] James J. Sumner,[2] Cynthia A. Lundgren,[2] and Margaret M. Hurley*,[1]

[1]Weapons and Materials Research Directorate, United States Army Research Laboratory, Aberdeen Proving Ground, Maryland 21005
[2]Sensors and Electron Devices Directorate, United States Army Research Laboratory, Adelphi, Maryland 20783
***E-mail: margaret.m.hurley12.civ@mail.mil**

The light-harvesting and charge-transfer abilities of Photosystem I (PSI) have generated interest in the development of this system for alternative energy production and energy conversion. We describe multi-scale computational approaches that were used to study electron transfer at the PSI-biological and inorganic interfaces and to model this large protein complex. Our work in the development of an all molecular dynamics model of the PSI monomer is shown and compared to the published experimental and ONIOM optimized models with differences noted in protein and ligand structure, electron branch characterization, and ionization and orbital potentials in the P700 chlorophylls. Differences between the docking of cytochrome c_6 and plastocyanin to PSI using established docking algorithms and molecular dynamics are described. Finally, dipole calculations, luminal surface hydropathicity and polarity characterization were used to predict improvements in surface-assembled monolayer design.

Keywords: Photosystem I; cytochrome c_6; computational chemistry; molecular modeling; docking; quantum mechanics; self-assembled monolayer; photoelectrochemistry; electron transfer

In Applications of Molecular Modeling to Challenges in Clean Energy; Fitzgerald, G., et al.; ACS Symposium Series; American Chemical Society: Washington, DC, 2013.

Introduction

Oxygenic photosynthesis provides the energy source, directly or indirectly, for all complex, multi-cellular organisms on Earth. This biological process couples the energy derived from photo-excitation to split water and reduce CO_2 in order to create complex carbohydrates in plants, algae, and cyanobacteria. Two large transmembrane protein complexes, photosystems (PS) I and II, are instrumental in the first steps involved in charge separation and the resulting translocation of electrons across the thylakoid membrane. The first step of the light-driven reactions in photosynthesis occurs in PSII, where light energy is harnessed by the chlorophylls within PSII, followed by the oxidation of water to produce protons, oxygen gas, and electrons. The electrons produced in this reaction are quickly transferred through a chain of cofactors and carriers (including plastoquinones, plastocyanin, and cytochromes) to the other light harvesting complex, PSI. Depending upon the organism, PSI receives the transferred electrons from either plastocyanin or cytochrome c_6 at the P700 chlorophylls on its luminal side and rapidly transports the electrons to the terminal iron-sulfur cluster, FB, at its stromal side. There the electrons are used to reduce NADP+ to NADPH in the ferrodoxin-NADP+ oxidoreductase complex. The transmembrane potential created from the electron transport through the two photosystems and the proton concentration gradient is further used to drive ATP synthesis and other cellular processes.

PSI has become popular in the solar energy conversion literature recently because of its light harvesting ability and charge transfer properties. Most importantly, PSI is able to transport electrons across the thylakoid membrane with an internal quantum efficiency near unity (*1*). Although the comparison of energy conversion efficiency among disparate processes is not not straightforward (*2*), the harnessing and enhancement of natural photosynthetic processes is of great interest, and the integration of PSI into chemical or electrical systems for the conversion of light energy to chemical energy has been pursued for several decades. These efforts were initially focused on the optimization of H_2 production in algae (*3–6*) through metabolic (*7–9*) and later genetic controls (*8*, *10*). More recent work has focused on decoupling photosynthesis by crosslinking PSI with hydrogenases (*11–16*) or metal complexes (*17*, *18*) in order to direct electron flow to drive hydrogen evolution. Despite this increased interest in PSI, the fundamental understanding of the dynamic docking of transfer proteins to PSI, as well interactions between PSI and non-native environments is lacking. This work focuses on elucidating the fundamental interactions between PSI and its surrounding non-native environment in order to improve the integration of PSI into energy generating devices.

Computational analysis of proteins and their interaction with surrounding environments is highly valuable in predicting the dynamic behavior of these complex biological systems. Interest in Photosystem I in particular has increased dramatically with the release of the 2.5 Å resolution cyanobacterial PSI structure in 2001 (*19*). The extremely large size of the protein complex, approximately one megadalton for the cyanobacterial trimer, makes computational characterization highly challenging. Much of the earlier work used the published structure to

In Applications of Molecular Modeling to Challenges in Clean Energy; Fitzgerald, G., et al.;
ACS Symposium Series; American Chemical Society: Washington, DC, 2013.

develop models of spectral properties and energy transfer kinetics (*20–22*). Ivashin et al. optimized select ligands (α-chlorophyll *a*, phylloqionones) and residues at the B3LYP/6-31G* level in combination with ZINDO/S level electronic coupling calculations to study differences between the A- and B-branches of the electron transfer chain in PSI (*23*). Much attention has also been paid to the advanced treatment of electrostatics in this system (*24–26*). The P700 site has been studied with TDDFT (*24*, *27*) and semiempirical methods (*28*). Lin and O'Malley used a two layer (B3LYP/6-31G(d):UFF) ONIOM methodology to optimize models of the phyllosemiqionone free radical in the A_{1A} and A_{1B} sites (*29*). Canfield et al. utilized the ONIOM methodology to systematically partition and optimize the entire protein in a sequential fashion (*30*). This optimized structure was then used for a variety of analyses (*31*). Attempts to dock PSI are less numerous in the literature. Myshkin et al. used a variety of standard docking algorithms to model the plastocyanin/PSI complex (*32*). Jollet et al. used a specialized algorithm to dock the PsaC subunit onto PsaA/PsaB (*33*).

The computational approaches in this study are focused on understanding the interactions between PSI and its charge carrier proteins or surrounding non-native environment in order to develop improved coupling (and electron transport) between biological components (cytochrome c_6/PSI and also between PSI and physical components of electrochemical devices). Simulations at multiple scales were used to address these challenges. Modeling approaches included docking, all-atom molecular dynamics (MD), and quantum mechanics (QM) using density functional theory (DFT). Development of coarse grained models when system size and sampling time scales exceed the current limits of all-atom MD are also underway and will be reported elsewhere. Here we detail initial findings for this ongoing project which is the first to report PSI dynamics and extend multiscale modeling of the PSI complex past the QM/MM level.

Modeling the PSI Complex

In cyanobacteria, photosystem I exists as a clover-shaped trimer embedded in the lipid bilayer of the thylakoid membrane. Each monomer is composed of 12 protein chains, 96 chlorophylls, 22 carotenoids (β-carotene), 2 phyloquinones, 3 iron-sulfur clusters, 4 unique lipid molecules, and a multimer-coordinating calcium ion (*19*). Nine of the protein subunits feature transmembrane domains while subunits PsaC, PsaD, and PsaE compose the stromal hump. The interface of the two largest subunits, PsaA and PsaB, creates a pseudo C_2 axis at the center of the PSI monomer complex with pigment and lipid cofactors arranged in two branches along the axis (*19*). β-carotene, the lipids (1,2-dipalmitoyl-phosphatidyl-glycerole and 1,2-distearoyl-monogalactosyl-diglyceride), and most of the axial chlorophylls make direct contact with PsaA and PsaB (*19*). Protein chains PsaJ, PsaK, PsaL, PsaM and PsaX coordinate antennae α-chlorophyll *a* molecules directly or through bridging solvent contacts (*19*). Stabilizing hydrophobic contacts with the carrotenoids are made by amino acid residues in chains PsaF, PsaI, PsaJ, PsaL, PsaM, and PsaK (*19*). PsaF has also been proposed to coordinate docking of

In Applications of Molecular Modeling to Challenges in Clean Energy; Fitzgerald, G., et al.;
ACS Symposium Series; American Chemical Society: Washington, DC, 2013.

plastocyanin and cytochrome c_6 to the P700 domain found at the center of the C_2 axis (*34*). In cyanobacteria, this protein chain is significantly truncated compared to its plant complement (*19*) and interaction may be limited due to its relatively distal location. A graphical representation of the PSI monomer from both the side and stromal views is shown in Figures 1a and 1b.

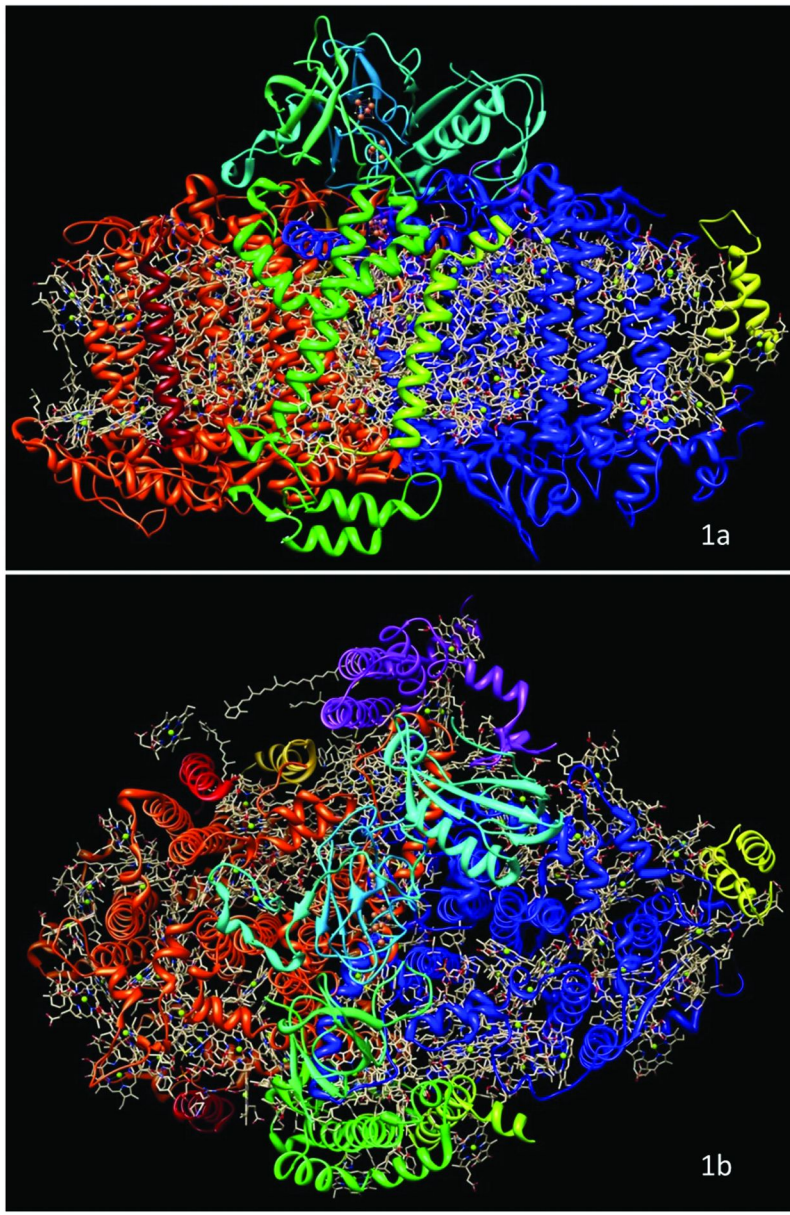

Figure 1. Ribbon representation of cyanobacterial PSI (PDB ID: 1JB0) from side (1a) and stromal views (1b). Coloring was chosen to differentiate the protein chains that compose the complex and emphasize the C_2 axis.

Initial PSI Molecular Dynamics (MD) Model

An all-atom molecular model of PSI was built using the high resolution crystal structure (2.5 Å resolution) of Photosystem I from cyanobacteria (*19*) (PDB ID: 1JB0) as the initial starting trajectory. Some modifications to the structure were necessary and included: splitting the PsaA chain between residues 262 and 266 due to missing residues, inserting an alanine residue into position 33 of the PsaK chain, splitting the PsaK chain between residues 43 and 55 due to missing residues, and removal of native waters and calcium ion from the model structure. Ligand parameters and atomic charges were determined using the R.E.D. vIII (*35*) and antechamber (*36*) programs. Parameterization of the iron-sulfur (4Fe4S) clusters assumed an oxidized state and atomic charges were calculated using a tetra-coordinated methyl sulfide capping groups whose group atomic charges were constrained to zero, similar to work performed by Torres et al. (*37*). RESP (restrained electrostatic potential) derived atomic charges (*38*) based on QM calculations were determined consistent with the AMBER ff99SBildn/GAFF (*39*) force fields using the HF-6/31G* basis set for all ligands with the exception of the iron-sulfur cluster. Due to the known limitations of the Hartree-Fock basis sets to model metal centers, the 4Fe4S structure was optimized and molecular electrostatic potential (MEP) calculated using the DFT BVP86/cc-pVDZ basis set. The all-atom molecular dynamics simulation was performed using the AMBER ff99SBildn force field (*40*) with adjustments to the phi and psi amino acids dihedrals consistent with the Robert Best parameter set (*41*). The protein complex was solvated using a surrounding octahedron shell of explicit TIP3P waters which extended at least 12 angstroms from the structure in all directions. Explicit salt ions using the Cheatham and Joung parameter set (*42*) were used to neutralize the system. Periodic boundary conditions were applied using the particle mesh Ewald method approach with a small (1 fs) time step to ensure stability in the large complex. Minimization was performed in two stages, allowing for initial solvent minimization in the presence of restrained solute molecules and later unrestrained system minimization. Equilibration, similiarly, used three stages with weak solute restraints during a slow heating stage to the final temperature of 300K followed by 500 ps of unrestrained equilibration to remove any hot spots in the simulation prior to production MD.

During the first 3 ns of all-atom MD of the PSI complex, the all-atom RMSD consistently increased from the starting trajectory (Figure 2). Comparing the final snapshot at 3 ns to published structure, significant loss of secondary structure can be seen originating in the PsaC domain (Figure 2). Using scanning RMSD (*43*) to measure local fluctuations on the time course of the simulation, the majority of large motions found in and near PsaC occurred proximal to the F_B iron-sulfur cluster. At this region many of the stabilizing salt bridges and hydrogen bonds between PsaC and nearby PsaD and PsaE chains are formed. The large atomic charges assigned to the iron-sulfur clusters create competitive electrostatic interactions at the protein tertiary domains which disrupt neighboring salt bridges and eventually lead to structure deformation. After the results from the QM atomic charge fitting were re-evaluated, it was determined that the molecular electrostatic potential for the iron-sulfur clusters was further distributed along

attached thiol ligands and that the charge constraints resulted in artificially large charges to the iron-sulfur molecules. Variance between ligand-complex fit and complex-alone fit atomic charges confirm the need to include 4Fe4S bound amino acids in the charge assignment protocol. While developing improved 4Fe4S parameters, a second model of the PSI complex lacking the stromal hump (PsaC, PsaD, PsaE protein chains and the iron-sulfur clusters) was constructed to complete simulations focused on dynamic structural fluctuations in the lower portion of the electron transfer chain and interactions of external moieties (e.g. transfer proteins and SAMs) with the luminal surface.

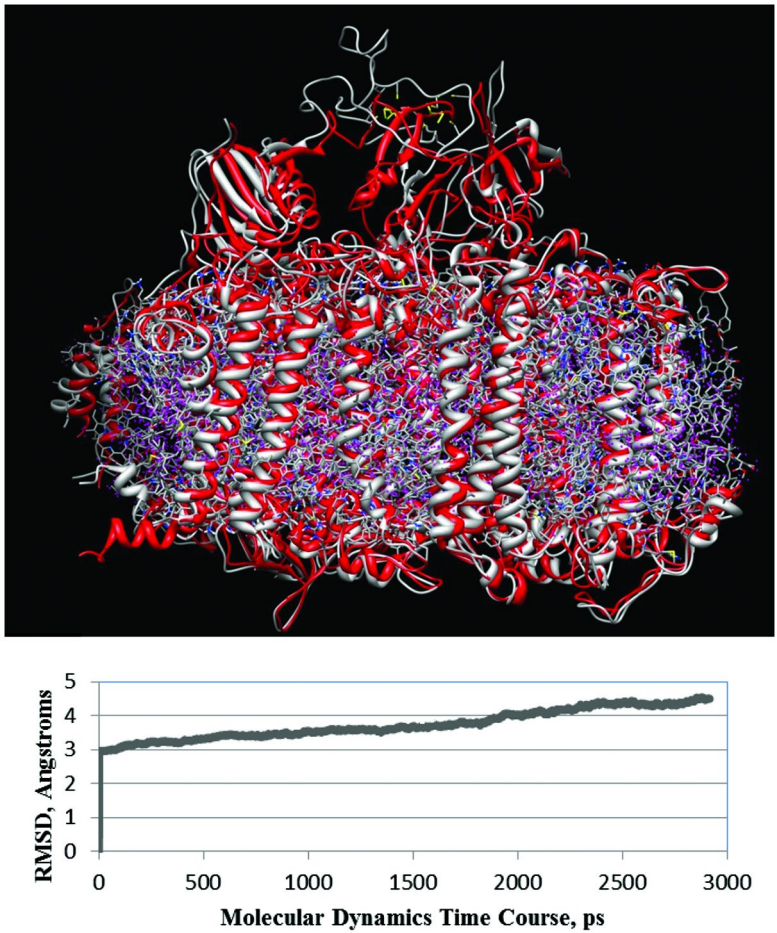

Figure 2. Variance of the initial MD model from the published structure shows deformation in the PsaC chain. In the ribbon diagram (top) the published structure is shown in red, while the MD model is shown in white. On the bottom, all-atom RMSD of initial MD model from PSI X-ray structure is shown over the simulation time course.

In Applications of Molecular Modeling to Challenges in Clean Energy; Fitzgerald, G., et al.;
ACS Symposium Series; American Chemical Society: Washington, DC, 2013.

PSI MD Model Lacking a Stromal Hump

The design of a PSI model lacking a stromal hump followed the approach described above. A one-dimension all-atom RMSD plot from the published structure through the 68 ns time course can be seen in Figure 3.

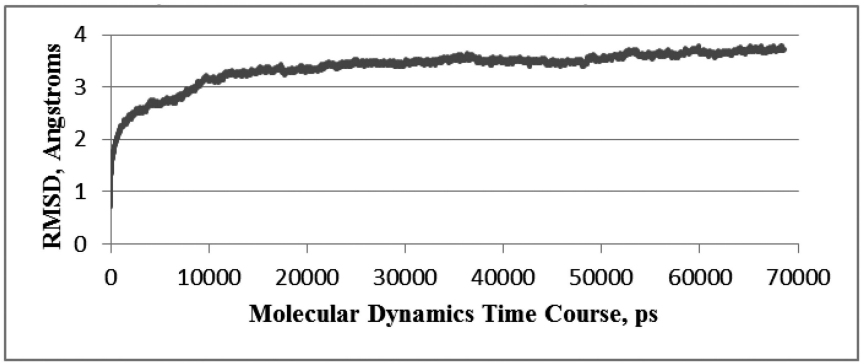

Figure 3. All-atom RMSD of MD model (lacking stromal hump) from PSI X-ray structure.

Several differences between the computational model and published structure are observed in the ligand interactions, the electron transport paths, and at the solvent interface. In general, the MD model is a more compressed system than the X-ray structure showing constriction of solvent-exposed hydrophobic surfaces in both protein and ligand molecules. Several of the most visible changes are found among the antennae α-chlorophyll *a* molecules. Of these, CL1 1601 (a chlorophyll in the M chain) shows the greatest movement among the chlorophylls at 13 Å from its initial, isolated position to close proximity with a neighboring chlorophyll, CL1 1201 (see Figure 4). Similar movements are seen with chlorophylls CL1 1217 and 1302. CL1 1217 moves 6 Å from a staggered position with CL1 1209 to bridge CL1 1209 and CL1 1218 (Figure 4). CL1 1302 moves 8.3 Å to improve contacts with neighboring pigments. The energetic driving forces for other chlorophyll movements are less clear: for example, CL1 1303 moves 7 Å without visible improvement in local interactions with antennae chlorophyll neighbors. The published structure of the PSI complex lacks many coordinates for atoms associated with the chlorophyll hydrocarbon tails and many of these positions were built at the time of model generation based on a fairly simplistic energy minimizer. It is plausible that the 80 ns time frame of this MD simulation may not be sufficient to allow for optimal packing or refolding of those regions and this may contribute to some of the differences seen.

In Applications of Molecular Modeling to Challenges in Clean Energy; Fitzgerald, G., et al.;
ACS Symposium Series; American Chemical Society: Washington, DC, 2013.

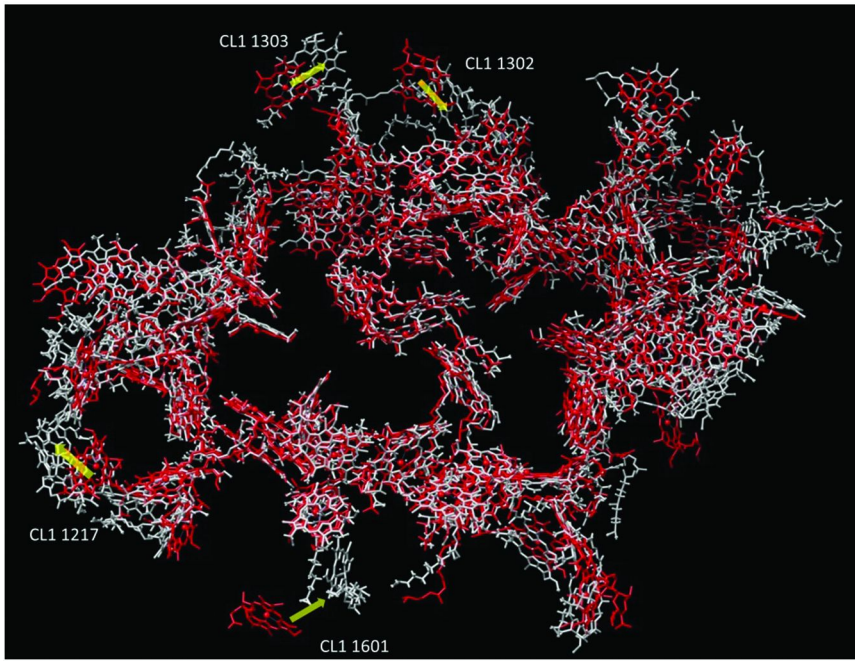

Figure 4. Localization of chlorophyll molecucles in X-ray (red) and molecular dynamics (white) structures.

In Figure 5, a side view ribbon representation of both crystal and MD models of PSI is shown. Differences in protein positions can be observed with the emphasis on the PsaL chain which is shown in dark grey. The movement of solvent-exposed helices from solution to the transmembrane region is fairly consistent with structural motions in the MD model. The crystallization of photosystem I was accomplished using β-dodecylmaltoside as a detergent for the lipoprotein complex. Detergents and surfactants can minimize hydrophobic forces in protein molecules which may account many of the differences seen at the solvent interface. Furthermore, some uncharacteristically fast motions in the solvent-exposed peptide transmembrane helices are seen in the MD model which suggests that future simulations which lack detergent (such as ours) should include additional bilayer lipid molecules beyond those defined in the X-ray structure to maintain ideal, native structure.

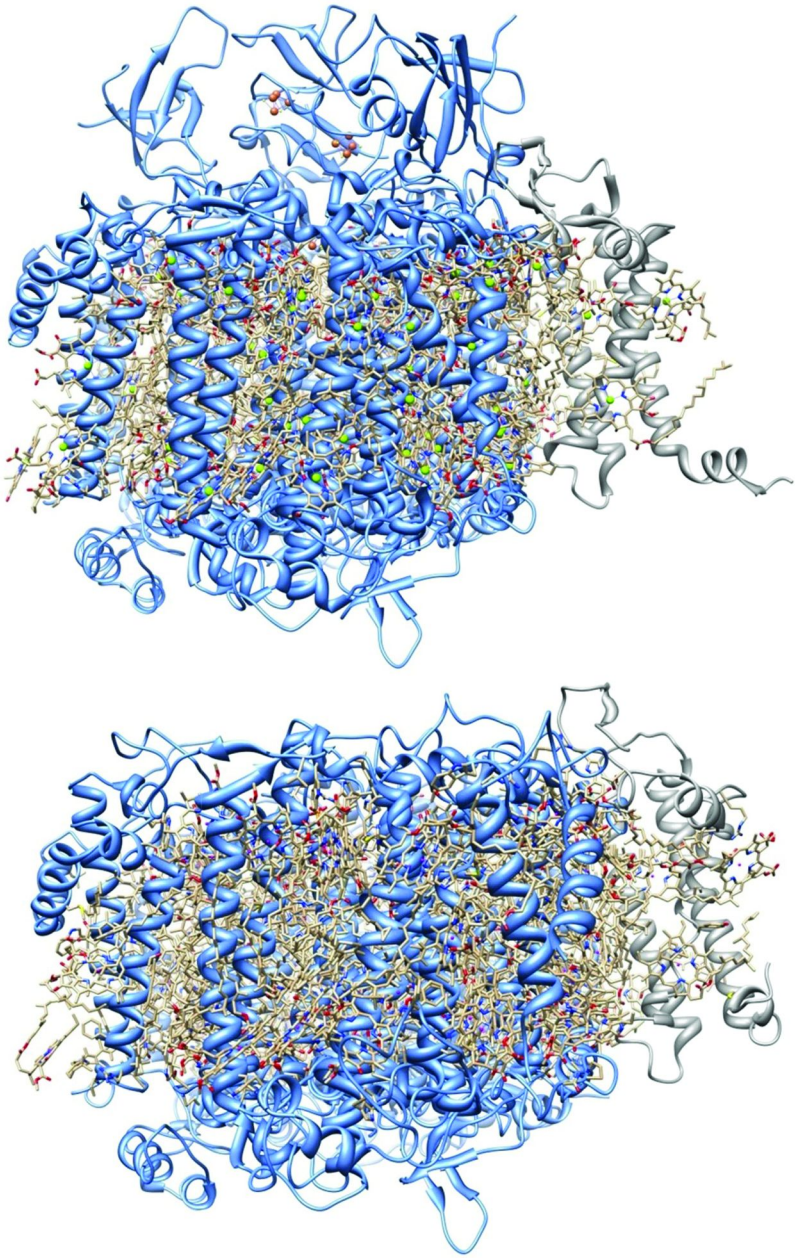

Figure 5. Structural differences between the PSI X-ray structure (top) and the MD model (bottom).

Electron transfer through the core of PSI takes places through one of two electron transfer pathways; branch A or branch B (*44*). These branches begin at the luminal pair of chlorophyll molecules that are designated the P700 site based on the absorbance maxima at 700 nm (*1*). From here, the branches diverge to separate chlorophyll molecules with decreasing redox potentials. Along the A branch, electron flow proceeds from the P700 chlorophylls to A_{-1A} (an α-chlorophyll *a* molecule), A_{0A} (another α-chlorophyll *a* molecule), A_{1A} (a phyloquinone molecule), to F_X, F_A, and F_B which are 4Fe4S iron-sulfur clusters (*23*). The B branch uses similar intermediates: A_{-1B} (an α-chlorophyll *a* molecule), A_{0B} (an α-chlorophyll *a* molecule), A_{1B} (a phyloquinone molecule), and convergence with the A branch on the use of F_X, F_A, and $F_{B(23)}$. Electron transfer rates through the respective branches are species specific and are often a function of distances between intermediates in the branch. In *Synechococcus elongatus*, a 10 fold increase in electron transfer rate (*44–46*) is seen in the B branch compared to the A branch. A variety of factors have been investigated to determine their role in this behavior, including the contribution of surrounding residues on the midpoint potential of phylloquinones A_{1A} and A_{1B} (*24*, *47*), as well as a B branch specific inclusion of a tryptophan residue (TRP B673) which may act as an electron acceptor between A_{1B} and the F_x iron-sulfur cluster (*19*, *23*). Some preliminary measurements of the chlorophyll and phylloquinone distances along the A and B branches were made to compare against the published structure (see Table I).

Table I. Measured Distances between Electron Carriers in the PSI X-ray and MD Structures

Measured Distance	*X-ray Structure*	*MD model*
P700 chlorophylls	6.34 Å	5.80 Å
$P700_A$ to A_{-1A}	11.72 Å	12.74 Å
A_{-1A} to A_{0A}	8.13 Å	8.74 Å
A_{0A} to A_{1A}	8.78 Å	9.89 Å
$P700_B$ to A_{-1B}	11.95 Å	12.62 Å
A_{-1B} to A_{0B}	8.22 Å	7.60 Å
A_{0B} to A_{1B}	8.78 Å	9.37 Å
$P700_B$ to A_{1A}	26.0 Å	26.2 Å

While the molecular coordinates in the interior of PSI complex are very similar between the MD model and X-ray structure, some changes are notable. In the computational model, an increase is seen in the distance between the P700 chlorophylls and the first set of chlorophyll intermediates, as well as the distance between the second pair of chlorophyll and the phylloquinone intermediates. The distances between the magnesium ions of the P700 chlorophyll pair has decreased

In Applications of Molecular Modeling to Challenges in Clean Energy; Fitzgerald, G., et al.;
ACS Symposium Series; American Chemical Society: Washington, DC, 2013.

by a half angstrom, although the chlorophyll ring distance itself is relatively unchanged (Figure 6 and next section). The distance between the B branch P700 chlorophyll and the A branch phylloquinone has increased slightly compared to the published structure and the experimental value of 25.4 Angstroms obtained from spin-echo modulation experiments (*48*). In the X-ray structure the distances between electron intermediates is smallest in the A branch while in the MD model, smaller distances are found in B branch which may contribute to the differences seen in the electron transfer rates.

Preliminary PSI Quantum Mechanical (QM) Model

Theoretical studies of α-chlorophyll *a* and similar porphyrins have been a topic of interest for decades due to their critical involvement in photosynthesis. Numerous TDDFT (time dependent density functional theory) studies of the single α-chlorophyll *a* (Chl a) molecule exist, which were able to reproduce experimental adsorption energies with varying success (*49*, *50*).

The P700 site in photosystem I is a dimer made of Chl a and Chl a′ (the C10 epimer of Chl a). Computational analysis of the P700 dimer has also been performed. It is interesting to note that a variety of P700 models have been studied. The molecular orbital analysis of Plato et al. (*28*), which was performed at the RHF-INDO level, started from the experimental X-ray crystal structure and expanded to a series of models of varying sophistication, although no complete geometry optimization of the P700 site was attempted. This work demonstrated the effect of the interactions of the chlorophyll with the protein environment, in particular Thr A743, His A860, and His B660, which they postulated to be implicitly involved in the development of spin and charge asymmetry within the P700 dimer. Sun et al. (*27*) utilized TDDFT on an optimized model of P700 obtained from the crystal structure and found its excitation to be "intrinsically asymmetric" without the inclusion of neighboring residues. Saito and Ishikita (*51*) used QM/MM to study the cationic state and spin distribution of the P700 site, keeping the coordinates of the MM region fixed to the crystal structure.

Gunner (*52*) noted the importance of accounting for the normal thermal motions of photosynthetic proteins and their subtle but far-reaching effects on redox potential and other important properties. Dreuw et al. (*53*) stressed the importance of quantum mechanical optimization from the experimental crystal structure when studying excited states of pigment-protein complexes. The most complete structural optimization of PSI was generated by Canfield et al. (*30*). However, this work utilized the ONIOM model and optimized sections of the complex in a sequential fashion. We are unaware of any studies of the P700 site, or indeed any portion of the PSI electron transfer chain, starting from a classically thermalized structure of the PSI complex.

The current work attempts to address this. What follows is a preliminary assessment of the physical and electronic structure of a model P700 dimer derived from a 2 ns averaged structure of the PSI MD model described in the previous section. Results are compared to similar data derived from the experimental X-ray crystal structure (1JB0), and to the optimized structure of Canfield et al. Quantum calculations are performed at the B3LYP/6-31G(d,p) level of both the neutral and

In Applications of Molecular Modeling to Challenges in Clean Energy; Fitzgerald, G., et al.;
ACS Symposium Series; American Chemical Society: Washington, DC, 2013.

charged (+1) P700 complex. For ease of computation in the single point quantum runs only, the phytyl ester of both Chl a and Chl a′ has been replaced with a methyl ester, as is common in the literature (*54*). Differences between the thermalized P700 structure and the original crystal structure are moderate and can be seen in Figure 6.

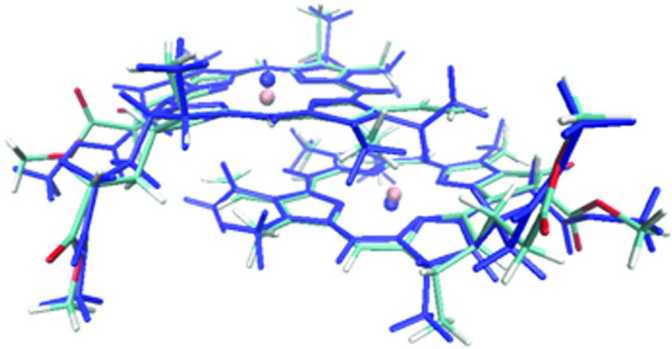

Figure 6. Overlay of thermalized P700 structure (standard coloring by element) and X-ray crystal structure (shown in blue).

The heavy-atom RMSD of our structure with respect to the X-ray structure is 0.61 angstroms. There is obvious fluctuation in sidechains, as expected, and some variation in twisting of the 5 membered moities of the chlorin ring. The most prominent difference is a marked movement in plane of the chlorin central magnesium atoms. The Canfield structure (not shown) has a heavy-atom RMSD of 0.29 angstroms with respect to the crystal structure, also due to sidechain fluctuation and some chlorin ring twisting. The central magnesiums atoms in this instance remain slightly out of plane. In all cases the average interplanar distance between the chlorin rings remains close to the published value of 3.6 angstroms (*19*).

Ionization potentials are calculated from the electronic energy in the neutral and cationic states. For all three models, the calculated IP is within the range for variations in the chlorophyll dimer P680 in photosystem II calculated at the B3LYP/6-31G(d) level by Takahashi et al. (*55*).

The role of His A680 and B660 has been discussed at length within the literature (*28*, *56*, *57*). Within the crystal structure 1JB0 it is apparent that these residues are ligands of the P700 Mg atoms, as shown by the short HisN-Mg distances given in Table II. Canfield et al. chose to honor this bonding pattern and protonate at the delta position (*30*), while in the current model these residues are protonated at the epsilon position. Loss of this explicit ligand may in part account for the relaxation of the magnesium ions back into the plane of the chlorin rings, as well as the larger HisN-Mg distance in the current model relative to the crystal structure and Canfield structure. This point is of great computational interest, as previous studies have argued that complexation of the chlorin with the central magnesium leads to the destabilization of the chlorophyll *a* HOMO and LUMO+1,

In Applications of Molecular Modeling to Challenges in Clean Energy; Fitzgerald, G., et al.;
ACS Symposium Series; American Chemical Society: Washington, DC, 2013.

with little effect on the HOMO-1 or LUMO, leading to a slight change in the HOMO/LUMO gap (*49*, *58*). While the frontier orbitals of the current model do differ from the 1JB0 and Canfield models, the stated HOMO/LUMO trend is not followed, and therefore the effect of Mg complexation, while undeniably important, has been lost in the other effects from thermalizing the protein complex. It must be pointed out, however, that the calculated HOMO-LUMO gaps of the three models are in very reasonable agreement both with each other and with previously published values. HOMO-1 and LUMO+1 values are not provided for the current model, but differ only slightly from the HOMO and LUMO values, as has frequently been noted within the literature for Chl a and similar systems (*59*).

Table II. Physical and Electronic Structure Properties of Three P700 Models at B3LYP/6-31G(d,p)

	Current Work	*1JB0*	*Canfield*
IP (eV)	6.01	5.78	5.78
Frontier Orbital energy HOMO (eV)	-5.11	-4.88	-4.89
Frontier Orbital Energy LUMO (eV)	-2.91	-2.57	-2.7
HOMO-LUMO eV	2.19	2.31	2.19
Mg-Mg distance (angstroms)	5.8	6.34	6.26
HisN-Mg distance (angstroms)	3.99/4.49	2.36/2.26	2.20/2.22
Heavy-Atom RMSD wrt 1JB0 (angstroms)	0.61	0	0.29

A variety of additional measurable properties are intimately related to the geometric and electronic structure of the cyanobacterial P700 moiety (in both its singlet and triplet form), as well as for additional sites within the electron transfer chain. Methods used have included FTIR (*60–62*), as well as EPR and ENDOR techniques (*28*, *63*, *64*), and some quantum chemical analysis has been performed. Work evaluating our thermalized model within the context of this data is underway.

Biological Interactions with PSI

In cyanobacteria, electron transfer to PSI occurs through the intermediate of charge carrier proteins, plastocyanin or cytochrome c_6. In order to efficiently couple the charge carrier protein, cytochrome c_6 in this case, to PSI outside of its natural environment, a detailed fundamental understanding of this dynamic protein-protein docking event is vital. Significant prior research focused on the binding of plastocyanin and cytochrome c_6 to PSI has been published and while

In Applications of Molecular Modeling to Challenges in Clean Energy; Fitzgerald, G., et al.;
ACS Symposium Series; American Chemical Society: Washington, DC, 2013.

the conformation and orientation of the plastocyanin-PSI complex has been well elucidated, the cytochrome c_6 docking structure is still unknown. Ford et al. were able to characterize the binding site of plastocyanin to PSI in vascular plants using Fourier difference analysis of arrays of PSI located on the chloroplast granula (*65*). They propose that plastocyanin binds close to the center of PSI complex between the PsaA and PsaB domains with a slight bias towards the PsaL subunit of the complex (*65*). In this binding pocket, two solvent-exposed, hydrophobic tryptophan residues may form an important feature of the ligand recognition site (*66*). While no structures of cytochrome c_6 bound to PSI have been resolved or published in the scientific literature, cytochrome c_6 has been proposed to bind to PSI in a similar manner as plastocyanin. Plastocyanin and cytochrome c_6 share many attributes which suggest a common docking orientation including similar hydrophobic faces that match the docking surface of PSI (*67*), similar response to docking site mutations (*68*), and similar increases in affinity when positive mutations are introduced to increase the electrostatic attraction between the proteins and PSI (*68*).

Initial efforts to determine the cytochrome c_6-PSI binding site followed the efforts of Myshkin et al. (*32*) by using established docking algorithms to compare the plastocyanin and cytochrome c_6 predicted docking complexes. Molecular structures used in docking (and later all-MD simulation) were taken from RCSB Protein Data Bank and include the crystal structure of Photosystem I from *Synechococcus elongatus* (PDB ID: 1JB0) (*19*), an NMR structure of reduced plastocyanin from *Synechocystic* sp. PCC 6803 (PDB ID: 1JXD) (*69*), and the NMR solution structure of cytochrome c_6 from *Synechococcus elongatus* (PDB ID: 1C6S) (*70*). Due to the limitations of the docking software, only protein components were used. Docked complex structures from the HADDOCK (*71*), CLUSPRO (*72*), GRAMM-X (*73*), and RosettaDOCK (*74*) servers emphasized a noncannonical, unlikely transmembrane localization of the electron carriers with respect to PSI. Refinement of both plastocyanin and cytochrome c_6 docking to the luminal surface of PSI followed using a Python based interface to the Rosetta docking program (*75*). These docking simulations implemented a 3 angstrom translation and 8 degree rotation angle of the ligand molecules, followed by a subsequent alignment of the molecules to explore the PSI surface. 4000 docking configurations were tested and the docking energy predicted by the Rosetta algorithm was calculated for each structure. This Rosetta energy term was plotted against the calculated distance of the ligand ion (copper in plastocyanin and a heme iron in cytochrome c_6) and the magnesium ions found in the P700 chlorophylls. Five representative structures were chosen that minimized both terms and the structures were compared as seen in Figures 7 and 8. In the models of plastocyanin docked to PSI, a common docking face and domain were seen in all five models which compared favorably with the predictions of Ford et al. (*65*). In the models using cytochrome c_6, at least two different docking motifs were seen which lacked a common docking face and orientation. Possible causes for this alignment failure may have resulted from several sources including: the exclusion of metal ions which may contribute to aligning electrostatic interactions during the protein-protein docking; the rigid docking preformed may not be able to capture structural changes that occur at the time of docking (*76*) to stabilize

the bound complex, in which case flexible docking should be pursued; or driving forces in the diffusion controlled (*77*) docking of cytochrome c_6 with PSI may be sufficiently small that Rosetta was unable to correctly estimate their value.

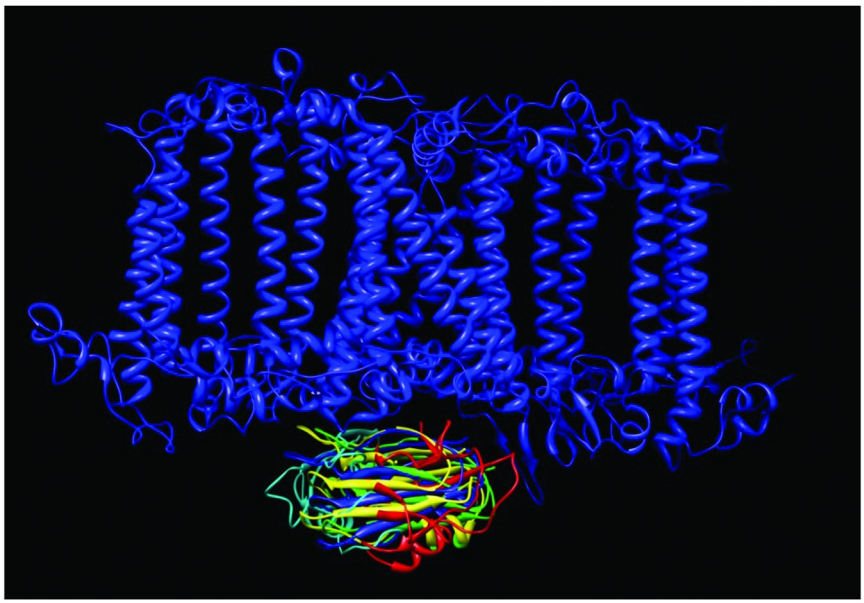

Figure 7. Combined structures showing docking convergence in the five most favorable docked PSI-plastocyanin Rosetta models.

To address the possible causes of failure in the rigid docking calculation of cytochrome c_6 to PSI, follow-up all-atom MD simulations of the docked complexes using the most favorable five Rosetta-docked structures as the initial starting trajectories were run. These MD simulations of the docked structures were completed using the AMBER modeling suite and Best phi and psi adjustment of the ff99SBildn force field as described earlier. Heme parameters were taken from the contributions of Bayly and Case which are distributed with the AMBER modeling suite (*36*). Copper bond, angle, and dihedral parameters were taken from Ross Walker's tutorial using poplar plastocyanin. After 80 ns of production MD, large differences were seen between the plastocyanin and cytochrome c_6 docking trajectories. MD simulations of the docked plastocyanin-PSI complex showed little structural fluctuations and varied minimally from the starting coordinates. Cytochrome c_6, on the other hand, was seen to traverse nearly the entire luminal surface of the PSI complex. While all the plastocyanin docking trajectories maintained the original PSI contacts, rotations in cytochrome c_6 molecules were evident with three of the five docking trajectories adopting a common docking orientation following the MD time course. Rotation of the

In Applications of Molecular Modeling to Challenges in Clean Energy; Fitzgerald, G., et al.;
ACS Symposium Series; American Chemical Society: Washington, DC, 2013.

cytochrome c_6 molecules to the common orientation was seen in two (of the three) instances to occur in proximity to the PsaF domain which may play a role in orienting cytochrome c_6 prior to docking and electron transfer. Further studies will be necessary to confirm this observation.

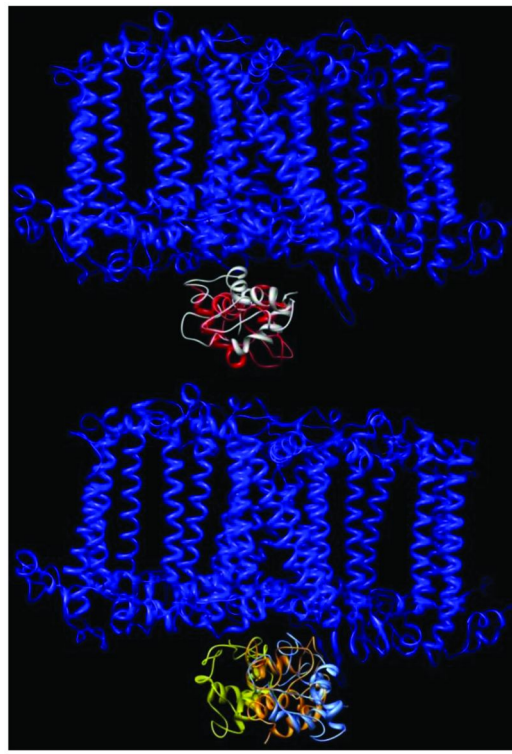

Figure 8. Rosetta docked models showing orientation and faces of the most favorable PSI-cytochrome c_6 structures. Clustering of the docked structures suggest at least two different motifs among the predicted complexes.

PSI Surface Interactions

Computational Approaches

Optimization of the interface between PSI and inorganic surfaces is necessary for the effective electron transfer between the surface and biomolecule. For instance, attachment of PSI to gold nanoparticles and unmodified gold electrodes has produced photosensitive and photoreactive systems (*78*, *79*); however this direct attachment to the gold surface can lead to protein denaturation and block access to active sites. The use of self-assembled monolayers (SAMs) to enhance binding and stability of PSI, as well as control its orientation on the electrode has been shown in the literature (*80*, *81*), however with limited fundamental understanding of the PSI/SAM interaction. Therefore, a comprehensive study of the surface assembly of PSI on various SAM modified electrodes was proposed

utilizing experimental and computational approaches to characterize the surface of PSI and to optimize SAM candidates. Computational surface characterization was focused on polarity, luminal surface electrostatic potential, and luminal surface hydropathicity.

Our previous analysis of the PSI complex structure showed a very strong dipole oriented at slight tilt from the complex central axis, which may possibly contribute to orientation of the complex stromal- or luminal-side down during deposition on a surface (*82*). The Kyte-Doolittle representation of the hydropathicity of the photosystem I monomer (1JB0) shows distinct segregation of hydrophobic residues (red) to the interior and external, bilayer-exposed sides of the complex (Figure 9). Hydrophilic residues (blue) congregate to both stromal and luminal faces consistent with aqueous exposure. Notably, distribution of the luminal hydrophobic residues (in red) is uniform across the plane.

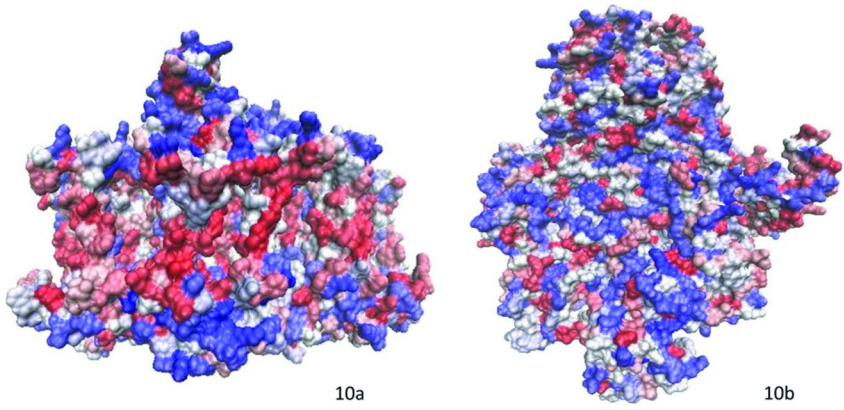

Figure 9. Hydropathicity analysis (Kyte-Doolittle algorithm) of side (10a) and luminal surfaces (10b) of photosystem I.

When the surfaces are remapped according to residue type, most of the hydrophilic luminal regions are shown to be composed of polar, non-charged residues (see Figure 10). The P700 docking site can be found near the center of luminal face, composed of a hydrophobic pocket surrounded by distinct positive and negative regions which is consistent with predicted long-range electrostatic steering of plastocyanin to the P700 binding site (*83*). Upon complex formation, short range hydrophobic and dipole-dipole interactions guide and ensure the optimal configuration of the mediator prior to electron transfer (*83*, *84*).

From these surface mapping studies, some characteristics for a luminal bound probe or SAM were made and later tested. The luminal surface of PSI is highly polar suggesting the favorability of a charged or polar probe. The calculated dipole traverses the stromal hump showing a vector moving away from the luminal face which indicates that a negative charge would be preferred over a positive SAM. The fairly homogenous distribution of hydrophobic and hydrophilic regions along the luminal surface may indicate the benefits of an amphiphilic molecule.

In Applications of Molecular Modeling to Challenges in Clean Energy; Fitzgerald, G., et al.;
ACS Symposium Series; American Chemical Society: Washington, DC, 2013.

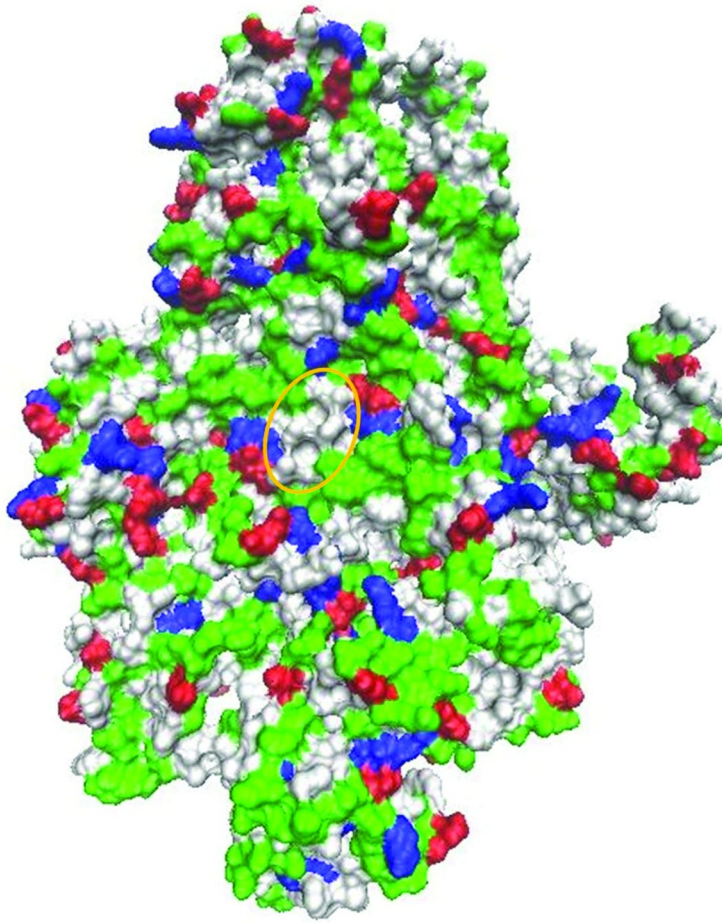

Figure 10. Luminal surface mapping of the PSI published structure (1JB0) by residue type. Acidic residues are shown in red, basic in blue, polar in green, and nonpolar in white. The P700 docking site is indicated by a yellow ellipsoid.

Experimental Results

In order to understand the dynamic effect of PSI surface functionalities in non-native environments, experimental surface assembly studies were performed on modified surfaces. Alkanethiol self assembled monolayers (SAMs) on gold substrates were chosen for the surface modifications in this work because of their facile fabrication, high reproducibility and easy of tailoring exposed functional groups. SAMs were composed of six-carbon length alkanethiol chains with varied terminal functional groups; amine (aminohexanethiol, AHT), methyl (hexanethiol, HT), alcohol (mercaptohexanol, MHO) and carboxylic acid (mercaptohexanoic acid, MHA).

Gold substrates were formed via E-beam evaporation of gold on Silicon wafers (3000Å with 300Å Ti binding layer), followed by gold island flattening by intermittent flaming. SAMs were formed on Au electrodes by three day assembly in 1mM thiol ethanolic solution. The SAMs were rinsed with ethanol, and dried with nitrogen gas. PSI assembly on the SAMs was conducted via 90 minute adsorption at 4°C in the dark. After adsorption, all samples were rinsed with deionized water, and dried with nitrogen gas.

Experimental analysis of PSI surface assembly via Atomic Force Microscopy (AFM) showed that PSI assembled in higher density to hydrophilic surfaces. The hydrophobic SAM, hexanethiol (HT), showed negligible PSI assembly, with some PSI adherence at the gold island edge sites (Figure 11a). In contrast, aminohexanethiol (AHT) showed high PSI binding with approximately 621 PSI/μm^2. Similarly, mercaptohexanol (MHO) and mercaptohexanoic acid (MHA), negatively charged hydrophilic surfaces, showed similar densities of PSI; 626 and 502 PSI/μm^2 respectively.

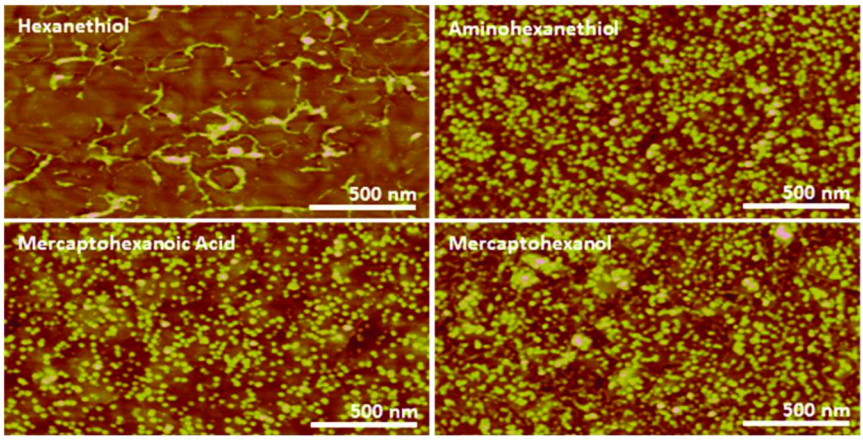

Figure 11. AFM images of PSI adsorption on (a) hexanethiol, (b) aminohexanethiol, (c) mercaptohexanoic acid, and (d) mercaptohexanol SAMs.

In agreement with the computational based predictions, hydrophilic SAMs were more effective than their hydrophobic complement, however the predictions of charge preference are more complex. Hydroxyl (MHO) and amine terminated (AHT) SAMs show similar PSI adherence rates with a slight improvement for the electronegative reactive groups (in agreement with predictions).

Mercaptohexananoic acid which is more electronegative than MHO showed a decrease in PSI binding suggesting that charged (or highly polar) probes may experience electrostatic repulsion from the PSI surface. Due to the limitations of available SAM head groups we were unable to test the effects of amphilicity on PSI adherence but intend to address those questions in future studies.

In Applications of Molecular Modeling to Challenges in Clean Energy; Fitzgerald, G., et al.;
ACS Symposium Series; American Chemical Society: Washington, DC, 2013.

Conclusions

Computational approaches are used to model the photosystem I complex and its interactions with biological electron carriers which can be used predict improvement with electrochemistry components. Long term all-atom simulations of PSI reveal contraction of solvent exposed protein domains and repacking of α-chorophyll antennae molecules. These changes were especially prevalent with the PsaL protein chain and chlorophylls CL1 1601, CL1 1217, CL1 1302, and CL1 1303. Many of these structural changes can be attributed to differences in simulation and crystallization solutions and suggest the need of lipid molecules or bilayer embedding for improved long-term simulation. Additionally, loss of secondary structure in our initial PSI molecular dynamics model, principally within the stromal hump, expose limitations in current iron-sulfur cluster parameterization approaches and demonstrate the need to include full amino acid ligands in the charge calculation. Structure and distance comparison of electron transfer branches show similarity to published structure with a decrease in B branch electron transfer distances. Early quantum analysis of ionization potential and orbital energies of the P700 chlorophylls from this model, the published X-ray structure and the Canfield ONIOM-optimized model show a consistent ionization potential and orbital energies with reasonable agreement.

Docking studies performed with established algorithms and subsequent all-atom MD simulations suggest a difference between plastocyanin and cytochrome c_6 docking and interaction with the PSI luminal surface. In particular cytochrome c_6 was found to traverse and sample much of the PSI luminal surface while plastocyanin forms a more static interaction at the P700 site. In addition, PsaF may play a role in orientation correction of cytochrome c_6 at the luminal surface in cyanobacteria.

Computational PSI luminal surface characterization and dipole calculations were used to improve design of surface-assembly molecules (SAM). It was shown that SAM probes that were hydrophilic and electronegative demonstrated best PSI attachment to gold-plated electrodes; however, experimental verification indicated that highly electronegative or ionic head groups may actually decrease PSI counts.

Acknowledgments

We gratefully acknowledge financial support from the U. S. Department of the Army and U.S. Army Materiel Command. Research was supported in part by a contractual appointment to the U.S. Army Research Laboratory Postdoctoral Fellowship Program administered by the Oak Ridge Associated Universities. We would also like to thank the Department of Defense High Performance Computing (DOD HPC) modernization program and CCAC for computer resources and support without which this work would not be possible.

References

1. Palsson, L. O.; Flemming, C.; Gobets, B.; van Grondelle, R.; Dekker, J. P.; Schlodder, E. Energy transfer and charge separation in photosystem I:

P700 oxidation upon selective excitation of the long-wavelength antenna chlorophylls of *Synechococcus elongatus*. *Biophys. J.* **1998**, *74* (5), 2611–2622.
2. Blankenship, R. E.; Tiede, D. M.; Barber, J.; Brudvig, G. W.; Fleming, G.; Ghirardi, M.; Gunner, M. R.; Junge, W.; Kramer, D. M.; Melis, A.; Moore, T. A.; Moser, C. C.; Nocera, D. G.; Nozik, A. J.; Ort, D. R.; Parson, W. W.; Prince, R. C.; Sayre, R. T. Comparing photosynthetic and photovoltaic efficiencies and recognizing the potential for improvement. *Science* **2011**, *332*, 805–809.
3. Ghirardi, M. L.; Zhang, L.; Lee, J. W.; Flynn, T.; Seibert, M.; Greenbaum, E.; Melis, A. Microalgae: A green source of renewable H_2. *Trends Biotechnol.* **2000**, *18* (12), 506–511.
4. Ghirardi, M. L.; Posewitz, M. C.; Maness, P. C.; Dubini, A.; Yu, J.; Seibert, M. Hydrogenases and hydrogen photoproduction in oxygenic photosynthetic organisms. *Annu. Rev. Plant Biol.* **2007**, *58*, 71–91.
5. Healey, F. Hydrogen evolution by several algae. *Planta* **1970**, *91* (3), 220–226.
6. Stuart, T. S.; Kaltwasser, H. Photoproduction of hydrogen by photosystem I of *Scenedesmus*. *Planta* **1970**, *91* (4), 302–313.
7. Winkler, M.; Hemschemeier, A.; Gotor, C.; Melis, A.; Happe, T. [Fe]-hydrogenases in green algae: Photo-fermentation and hydrogen evolution under sulfur deprivation. *Int. J. Hydrogen Energy* **2002**, *27* (11), 1431–1439.
8. Rupprecht, J. From systems biology to fuel: *Chlamydomonas reinhardtii* as a model for a systems biology approach to improve biohydrogen production. *J. Biotechnol.* **2009**, *142* (1), 10–20.
9. Hemschemeier, A.; Fouchard, S.; Cournac, L.; Peltier, G.; Happe, T. Hydrogen production by *Chlamydomonas reinhardtii*: An elaborate interplay of electron sources and sinks. *Planta* **2008**, *227* (2), 397–407.
10. Melis, A.; Zhang, L.; Forestier, M.; Ghirardi, M. L.; Seibert, M. Sustained photobiological hydrogen gas production upon reversible inactivation of oxygen evolution in the green alga *Chlamydomonas reinhardtii*. *Plant Physiol.* **2000**, *122* (1), 127–136.
11. Ihara, M.; Nakamoto, H.; Kamachi, T.; Okura, I.; Maedal, M. Photoinduced hydrogen production by direct electron transfer from photosystem I cross-linked with cytochrome c3 to [NiFe]-hydrogenase. *Photochem. Photobiol.* **2006**, *82* (6), 1677–1685.
12. Ihara, M.; Nishihara, H.; Yoon, K. S.; Lenz, O.; Friedrich, B.; Nakamoto, H.; Kojima, K.; Honma, D.; Kamachi, T.; Okura, I. Light-driven hydrogen production by a hybrid complex of a [NiFe]-hydrogenase and the cyanobacterial photosystem I. *Photochem. Photobiol.* **2007**, *82* (3), 676–682.
13. McTavish, H. Hydrogen evolution by direct electron transfer from photosystem I to hydrogenases. *J. Biochem.* **1998**, *123* (4), 644–649.
14. Lubner, C. E.; Knörzer, P.; Silva, P. J. N.; Vincent, K. A.; Happe, T.; Bryant, D. A.; Golbeck, J. H. Wiring an [FeFe]-hydrogenase with photosystem I for light-induced hydrogen production. *Biochemistry* **2010**, *49* (48), 10264–10266.

15. Schwarze, A.; Kopczak, M. J.; Rögner, M.; Lenz, O. Requirements for construction of a functional hybrid complex of photosystem I and [NiFe]-hydrogenase. *Appl. Environ. Microbiol.* **2010**, *76* (8), 2641–2651.
16. Qian, D. J.; Liu, A. R.; Nakamura, C.; Wenk, S. O.; Miyake, J. Photoinduced hydrogen evolution in an artificial system containing photosystem I, hydrogenase, methyl viologen and mercaptoacetic acid. *Chin. Chem. Lett.* **2008**, *19* (5), 607–610.
17. Millsaps, J. F.; Bruce, B. D.; Lee, J. W.; Greenbaum, E. Nanoscale photosynthesis: Photocatalytic production of hydrogen by platinized photosystem I reaction centers. *Photochem. Photobiol.* **2001**, *73* (6), 630–635.
18. Lubner, C. E.; Grimme, R.; Bryant, D. A.; Golbeck, J. H. Wiring photosystem I for direct solar hydrogen production. *Biochemistry* **2009**, *49* (3), 404–414.
19. Jordan, P.; Fromme, P.; Witt, H. T.; Klukas, O.; Saenger, W.; Kraub, N. Three-dimensional structure of cyanobacterial photosystem I at 2.5 A resolution. *Nature* **2001**, *411*, 909–917.
20. Byrdin, M.; Jordan, P.; Krauss, N.; Fromme, P.; Stehlik, D.; Schlodder, E. Light harvesting in photosystem I: Modeling based on the 2.5-Å structure of photosystem I from *Synechococcus elongatus*. *Biophys. J.* **2002**, *83* (1), 433–457.
21. Sener, M. K.; Lu, D.; Ritz, T.; Park, S.; Fromme, P.; Schulten, K. Robustness and optimality of light harvesting in cyanobacterial photosystem I. *J. Phys. Chem B* **2002**, *106* (32), 7948–7960.
22. Yang, M.; Damjanović, A.; Vaswani, H. M.; Fleming, G. R. Energy transfer in photosystem I of cyanobacteria *Synechococcus elongatus*: Model study with structure-based semi-empirical hamiltonian and experimental spectral density. *Biophys. J.* **2003**, *85* (1), 140–158.
23. Ivashin, N.; Larsson, S. Electron transfer pathways in photosystem I reaction centers. *Chem. Phys. Lett.* **2003**, *375* (3), 383–387.
24. Adolphs, J.; Müh, F.; Madjet, M. E. A.; Busch, M. S.; Renger, T. Structure-based calculations of optical spectra of photosystem I suggest an asymmetric light-harvesting process. *J. Am. Chem. Soc.* **2010**, *132* (10), 3331–3343.
25. Ishikita, H.; Knapp, E. W. Redox potential of quinones in both electron transfer branches of photosystem I. *J. Biol. Chem.* **2003**, *278* (52), 52002–52011.
26. Ptushenko, V. V.; Cherepanov, D. A.; Krishtalik, L. I.; Semenov, A. Y. Semi-continuum electrostatic calculations of redox potentials in photosystem I. *Photosynth. Res.* **2008**, *97* (1), 55–74.
27. Sun, Y.; Dai, Z.; Wang, W.; Sun, Y. A TDDFT study on the excitation of P700. *Chem. Phys. Lett.* **2007**, *434* (1), 111–115.
28. Plato, M.; Krauß, N.; Fromme, P.; Lubitz, W. Molecular orbital study of the primary electron donor P700 of photosystem I based on a recent X-ray single crystal structure analysis. *Chem. Phys.* **2003**, *294* (3), 483–499.
29. Lin, T. J.; O'Malley, P. J. Binding site influence on the electronic structure and electron paramagnetic resonance properties of the phyllosemiquinone free radical of photosystem I. *J. Phys. Chem. B* **2011**, *115* (29), 9311–9319.

30. Canfield, P.; Dahlbom, M. G.; Hush, N. S.; Reimers, J. R. Density-functional geometry optimization of the 150 000-atom photosystem-I trimer. *J. Chem. Phys.* **2006**, *124*, 024301.
31. Yin, S.; Dahlbom, M. G.; Canfield, P. J.; Hush, N. S.; Kobayashi, R.; Reimers, J. R. Assignment of the Q y absorption spectrum of photosystem-I from *Thermosynechococcus elongatus* based on CAM-B3LYP calculations at the PW91-optimized protein structure. *J. Phys. Chem. B* **2007**, *111* (33), 9923–9930.
32. Myshkin, E.; Leontis, N. B.; Bullerjahn, G. S. Computational simulation of the docking of *Prochlorothrix hollandica* plastocyanin to photosystem I: Modeling the electron transfer complex. *Biophys. J.* **2002**, *82* (6), 3305–3313.
33. Jolley, C. C.; Wells, S. A.; Hespenheide, B. M.; Thorpe, M. F.; Fromme, P. Docking of photosystem I subunit C using a constrained geometric simulation. *J. Am. Chem. Soc.* **2006**, *128* (27), 8803–8812.
34. Farah, J.; Rappaport, F.; Choquet, Y.; Joliot, P.; Rochaix, J. Isolation of a psaF-deficient mutant of Chlamydomonas reinhardtii: Efficient interaction of plastocyanin with the photosystem I reaction center is mediated by the PsaF subunit. *EMBO J.* **1995**, *14* (20), 4976.
35. Pigache, A.; Cieplak, P.; Dupradeau, F. In *Automatic and Highly Reproducible RESP and ESP Charge Derivation: Application to the Development of Programs RED and X RED*, 227th ACS National Meeting, Anaheim, CA, 2004.
36. Case, D. A.; Cheatham, T. E.; Darden, T.; Gohlke, H.; Luo, R.; Merz, K. M.; Onufriev, A.; Simmerling, C.; Wang, B.; Woods, R. J. The Amber biomolecular simulation programs. *J. Comput. Chem.* **2005**, *26* (16), 1668–1688.
37. Torres, R. A.; Lovell, T.; Noodleman, L.; David, A. Density functional and reduction potential calculations of Fe4S4 clusters. *J. Am. Chem. Soc.* **2003**, *125* (7), 1923–1936.
38. Bayly, C. I.; Cieplak, P.; Cornell, W. D.; Kollman, P. A. A well-behaved electrostatic potential based method using charge restraints for deriving atomic charges: The RESP model. *J. Phys. Chem.* **1993**, *97*, 10269–10280.
39. Wang, J.; Wolf, R. M.; Caldwell, J. W.; Kollman, P. A.; Case, D. A. Development and testing of a general amber force field. *J. Comput. Chem.* **2004**, *25* (9), 1157–1174.
40. Lindorff-Larsen, K.; Piana, S.; Palmo, K.; Maragakis, P.; Klepeis, J. L.; Dror, R. O.; Shaw, D. E. Improved side-chain torsion potentials for the Amber ff99SB protein force field. *Proteins: Struct., Funct., Bioinf.* **2010**, *78* (8), 1950–1958.
41. Best, R. B.; Hummer, G. Optimized molecular dynamics force fields applied to the helix−coil transition of polypeptides. *The J. Phys. Chem. B* **2009**, *113* (26), 9004–9015.
42. Joung, I. S.; Cheatham, T. E., III Determination of alkali and halide monovalent ion parameters for use in explicitly solvated biomolecular simulations. *The J. Phys. Chem. B* **2008**, *112* (30), 9020–9041.

43. Pendley, S. S.; Yu, Y. B.; Cheatham, T. E. Molecular dynamics guided study of salt bridge length dependence in both fluorinated and non-fluorinated parallel dimeric coiled-coils. *Proteins: Struct., Funct., Bioinf.* **2008**, *74* (3), 612–629.
44. Guergova-Kuras, M.; Boudreaux, B.; Joliot, A.; Joliot, P.; Redding, K. Evidence for two active branches for electron transfer in photosystem I. *Pro. Natl. Acad. Sci.* **2001**, *98* (8), 4437–4442.
45. Joliot, P.; Joliot, A. In vivo analysis of the electron transfer within Photosystem I: Are the two phylloquinones involved? *Biochemistry* **1999**, *38* (34), 11130–11136.
46. Xu, W.; Chitnis, P.; Valieva, A.; van der Est, A.; Brettel, K.; Guergova-Kuras, M.; Pushkar, J.; Zech, S. G.; Stehlik, D.; Shen, G. Electron transfer in cyanobacterial photosystem I. II. Determination of forward electron transfer rates of site-directed mutants in a putative electron transfer pathway from A0 through A1 to FX. *J. Biol. Chem.* **2003**, *270* (30), 27876–27887.
47. Karyagina, I.; Pushkar, Y.; Stehlik, D.; van der Est, A.; Ishikita, H.; Knapp, E.-W.; Jagannathan, B.; Agalarov, R.; Golbeck, J. H. Contributions of the protein environment to the midpoint potentials of the A1 phylloquinones and the Fx iron-sulfur cluster in photosystem I. *Biochemistry* **2007**, *46*, 10804–10816.
48. Bittl, R.; Zech, S. G.; Fromme, P.; Witt, H. T.; Lubitz, W. Pulsed EPR structure analysis of photosystem I single crystals: Localization of the phylloquinone acceptor. *Biochemistry* **1997**, *36*, 12001–12004.
49. Parusel, A. B. J.; Grimme, S. A theoretical study of the excited states of chlorophyll a and pheophytin a. *J. Phys. Chem. B* **2000**, *104* (22), 5395–5398.
50. Suendo, V.; Viridi, S. Ab initio calculation of UV-Vis absorption spectra of a single molecule chlorophyll a: Comparison study between RHF/CIS, TDDFT, and semi-empirical methods. *ITB J. Sci.* **2012**, *44A* (2), 93–112.
51. Saito, K.; Ishikita, H. Cationic state distribution over the P700 chlorophyll pair in photosystem I. *Biophys. J.* **2011**, *101* (8), 2018–2025.
52. Gunner, M. Computational analysis of photosynthetic systems. *Photosynth. Res.* **2008**, *97* (1), 1–3.
53. Dreuw, A.; Harbach, P. H. P.; Mewes, J. M.; Wormit, M. Quantum chemical excited state calculations on pigment–protein complexes require thorough geometry re-optimization of experimental crystal structures. *Theor. Chem. Acc.* **2010**, *125* (3), 419–426.
54. Sinnecker, S.; Koch, W.; Lubitz, W. Chlorophyll a radical ions: A density functional study. *J. Phys. Chem. B* **2002**, *106* (20), 5281–5288.
55. Takahashi, R.; Hasegawa, K.; Noguchi, T. Effect of charge distribution over a chlorophyll dimer on the redox potential of P680 in photosystem II as studied by density functional theory calculations. *Biochemistry* **2008**, *47* (24), 6289–6291.
56. Ishikita, H.; Saenger, W.; Biesiadka, J.; Loll, B.; Knapp, E. W. How photosynthetic reaction centers control oxidation power in chlorophyll pairs P680, P700, and P870. *Proc. Natl. Acad. Sci.* **2006**, *103* (26), 9855–9860.

57. Webber, A. N.; Lubitz, W. P700: The primary electron donor of photosystem I. *Biochim. Biophys. Acta, Bioenerg.* **2001**, *1507* (1), 61–79.
58. Hasegawa, J.; Ozeki, Y.; Ohkawa, K.; Hada, M.; Nakatsuji, H. Theoretical study of the excited states of chlorin, bacteriochlorin, pheophytin a, and chlorophyll a by the SAC/SAC-CI method. *J. Phys. Chem. B* **1998**, *102* (7), 1320–1326.
59. Vokáčová, Z.; Burda, J. V. Computational study on spectral properties of the selected pigments from various photosystems: Structure−transition energy relationship. *J. Phys. Chem. A* **2007**, *111* (26), 5864–5878.
60. Kim, S.; Sackstedert, C. A.; Bixby, K. A.; Barry, B. A. A reaction-induced FTIR study of cyanobacterial photosystem I. *Biochemistry* **2001**, *40*, 15384–15395.
61. Breton, J.; Nabedryk, E.; Leibl, W. FTIR study of the primary electron Donor of photosystem I (P700) revealing delocalization of the charge in P700+ and localization of the triplet character in 3P700. *Biochemistry* **1999**, *38*, 11587–11593.
62. Bender, S. L.; Keough, J. M.; Boesch, S. E.; Wheeler, R. A.; Barry, B. A. The vibrational spectrum of the secondary electron acceptor, A1, in photosystem I. *J. Phys. Chem. B* **2008**, *112*, 3844–3852.
63. Niklas, J.; Epel, B.; Antonkine, M. L.; Sinnecker, S.; Pandelia, M.-E.; Lubitz, W. Electronic structure of the quinone radical anion $A_1^{\bullet-}$ of photosystem I investigated by advanced pulse EPR and ENDOR techniques. *J. Phys. Chem. B* **2009**, *113*, 10367–10379.
64. Lubitz, W. EPR Studies of the Primary Electron Donor P700 in Photosystem I. In *Photosystem I. The Light-Driven Plastocyanin: Ferredoxin Oxidoreductase*; Goldbeck, J. H., Ed.; Springer: Dortrecht, 2006; Vol. 24, pp 245−269.
65. Ruffle, S. V.; Mustafa, A. O.; Kitmitto, A.; Holzenburg, A.; Ford, R. C. The location of plastocyanin in vascular plant photosystem I. *J. Biol. Chem.* **2002**, *277* (28), 25692.
66. Sommer, F.; Drepper, F.; Hippler, M. The luminal helix of PsaB is essential for recognition of plastocyanin or cytochrome c6 and fast electron transfer to photosystem I in Chlamydomonas reinhardtii. *J. Biol. Chem.* **2002**, *227* (8), 6573–6581.
67. Frazao, C.; Soares, C.; Carrondo, M.; Pohl, E.; Dauter, Z.; Wilson, K.; Herves, M.; Navarro, J.; De la Rosa, M.; Sheldrick, G. Ab initio determination of the crystal structure of cytochrome c6 and comparison with plastocyanin. *Structure* **1995**, *3* (11), 1159–1169.
68. Molina-Heredia, F. P.; Diaz-Quintana, A.; Hervas, M.; Navarro, J. A.; De la Rosa, M. A. Site-directed mutagenesis of cytochrome c6 from Anabaena species PCC 7119. Identification of surface residues of the heme protein involved in photosystem I reduction. *J. Biol. Chem.* **1999**, *274* (47), 33565–33570.
69. Bertini, I.; Bryant, D. A.; Ciurli, S.; Dikiy, A.; Fernández, C. O.; Luchinat, C.; Safarov, N.; Vila, A. J.; Zhao, J. Backbone dynamics of plastocyanin in both oxidation states: Solution structure of the reduced form and comparison with the oxidized state. *J. Biol. Chem.* **2001**, *276* (50), 47217–47226.

70. Beißinger, M.; Sticht, H.; Sutter, M.; Ejchart, A.; Haehnel, W.; Rösch, P. Solution structure of cytochrome c6 from the thermophilic cyanobacterium *Synechococcus elongatus*. *The EMBO J.* **1998**, *17* (1), 27–36.
71. De Vries, S. J.; Van Dijk, M.; Bonvin, A. M. J. J. The HADDOCK web server for data-driven biomolecular docking. *Nat. Protoc.* **2010**, *5* (5), 883–897.
72. Comeau, S. R.; Gatchell, D. W.; Vajda, S.; Camacho, C. J. ClusPro: An automated docking and discrimination method for the prediction of protein complexes. *Bioinformatics* **2004**, *20* (1), 45–50.
73. Tovchigrechko, A.; Vakser, I. A. GRAMM-X public web server for protein–protein docking. *Nucleic Acids Res.* **2006**, *34* (suppl 2), W310–W314.
74. Lyskov, S.; Gray, J. J. The RosettaDock server for local protein–protein docking. *Nucleic Acids Res.* **2008**, *36* (suppl 2), W233–W238.
75. Chaudhury, S.; Lyskov, S.; Gray, J. J. PyRosetta: A script-based interface for implementing molecular modeling algorithms using Rosetta. *Bioinformatics* **2010**, *26* (5), 689.
76. Diaz-Moreno, I.; Diaz-Quintana, A.; Molina-Heredia, F. P.; Nieto, P. M.; Hansson, O.; De la Rosa, M. A.; Karlsson, B. G. NMR analysis of the transient complex between membrane photosystem I and soluble cytochrome c6. *J. Biol. Chem.* **2005**, *280* (9), 7925.
77. Fromme, P.; Melkozernov, A.; Jordan, P.; Krauss, N. Structure and function of photosystem I: Interaction with its soluble electron carriers and external antenna systems. *FEBS Lett.* **2003**, *555* (1), 40–44.
78. Lee, I.; Lee, J. W.; Stubna, A.; Greenbaum, E. Measurement of electrostatic potentials above oriented single photosynthetic reaction centers. *J. Phys. Chem. B* **2000**, *104* (11), 2439–2443.
79. Ciesielski, P. N.; Scott, A. M.; Faulkner, C. J.; Berron, B. J.; Cliffel, D. E.; Jennings, G. K. Functionalized nanoporous gold leaf electrode films for the immobilization of photosystem I. *ACS Nano* **2008**, *2* (12), 2465–2472.
80. Faulkner, C. J.; Lees, S.; Ciesielski, P. N.; Cliffel, D. E.; Jennings, G. K. Rapid assembly of photosystem I monolayers on gold electrodes. *Langmuir* **2008**, *24* (16), 8409–8412.
81. Yan, X.; Faulkner, C.; Jennings, G. K.; Cliffel, D. E. Photosystem I in Langmuir−Blodgett and Langmuir−Schaefer monolayers. *Langmuir* **2012**, *28* (42), 15080–15086.
82. Manocchi, A. K.; Baker, D. R.; Pendley, S. S.; Hurley, M. M.; Bruce, B. D.; Sumner, J. J.; Lundgren, C. A. Photocurrent generation from surface assembled photosystem I on alkanethiol modified electrodes. *Langmuir* **2012**, *29* (7), 2412–2419.
83. Hope, A. Electron transfers amongst cytochrome *f*, plastocyanin and photosystem I: Kinetics and mechanisms. *Biochim. Biophys. Acta, Bioenerg.* **2000**, *1456* (1), 5–26.
84. Hippler, M.; Reichert, J.; Sutter, M.; Zak, E.; Altschmied, L.; Schröer, U.; Herrmann, R.; Haehnel, W. The plastocyanin binding domain of photosystem I. *EMBO J.* **1996**, *15* (23), 6374.

Chapter 11

Computational Studies of the Oxygen-Evolving Complex of Photosystem II and Biomimetic Oxomanganese Complexes for Renewable Energy Applications

Ivan Rivalta,[*,1,2] Gary W. Brudvig,[1] and Victor S. Batista[1]

[1]Department of Chemistry, Yale University, New Haven, Connecticut 06520-8107, United States
[2]Dipartimento di Chimica "G. Ciamician", Università di Bologna, V. F. Selmi 2, 40126 Bologna, Italy
[*]E-mail: ivan.rivalta@yale.edu

Solar-driven water-to-fuel conversion, analogous to natural photosynthesis, is an attractive energy conversion technology since it could provide an alternative to the current combustion of fossil fuels. Further understanding of catalysis in natural photosynthetics could benefit such technological developments. Photosynthetic organisms convert solar energy into NADPH and ATP (the biological fuels) through a process that is initiated at the oxygen evolving complex (OEC) of photosystem II (PSII). Such a catalytic site oxidizes water to generate the reducing equivalents for NADPH production and a pH gradient necessary for ATP biosynthesis. Water oxidation is a challenging four-electron reaction [$2H_2O \rightarrow O_2 + 4e^- + 4H^+$] that is difficult to carry out efficiently in artificial photosynthetic systems. In this chapter, we review our recent studies of the OEC of PSII based on the recent X-ray diffraction model resolved at 1.9 Å resolution. We characterize the dark-adapted S_1 state of the OEC and address the potential functional role of chloride during O_2 evolution in PSII. These results are discussed in light of recent comparative studies on biomimetic oxomanganese complexes, revealing how Lewis base centers (such as carboxylate groups from the buffer solution, or surrounding environment) can play an important role as

In Applications of Molecular Modeling to Challenges in Clean Energy; Fitzgerald, G., et al.;
ACS Symposium Series; American Chemical Society: Washington, DC, 2013.

acid/base and redox cofactors in photosynthtetic water splitting. These findings have direct implications to catalytic water oxidation in photosystem II and provide useful information for the design of Mn-based biomimetic catalysts for artificial photosynthesis.

Introduction

Photocatalytic solar cells can mimic photosynthetic organisms by using sunlight to make chemical fuels. These artificial photosynthetic devices use solar light to extract reducing equivalents from water (electrons and protons) and then use them to make renewable fuels, such as hydrogen (or methanol) by reduction of protons (or CO_2). The key reaction is water oxidation that splits water into molecular oxygen, protons and electrons, as follows:

$$2H_2O \rightarrow O_2 + 4e^- + 4H^+$$

In natural photosynthesis, water splitting is catalyzed by the oxygen-evolving complex (OEC) of photosystem II (PSII), an oxomanganese complex embedded in the D1 protein subunit of PSII in the thylakoid membrane of green plant chloroplasts and internal membranes of cyanobacteria. Recent breakthroughs in X-ray crystallography have resolved the structure of PSII crystals from *Thermosynechococcus vulcanus* at 1.9 Å resolution (*1*), revealing the detailed structure of the OEC (Figure 1). The X-ray diffraction (XRD) data provided for the first time direct evidence of terminal water ligands bound to a cuboidal oxomanganese cluster, with metal centers ligated by carboxylate groups of surrounding amino acid residues and linked by μ-oxo bridges (Figure 1). These advances in the field have stimulated several studies aiming to elucidate the structural rearrangements of the OEC during the multistep photocatalytic cycle (i.e., the 'Kok-cycle' proposed by Joliot and Kok (*2*, *3*)) and the functional role of cofactors during water oxidation (*4–8*).

Insights into fundamental aspects of the water-splitting reaction mechanism have emerged from comparative studies of biomimetic oxomanganese complexes, including the Mn–terpyridine dimer $[H_2O(terpy)Mn(\mu\text{-}O)_2Mn(terpy)OH_2]^{3+}$ (**1**, terpy=2,2′:6′,2"-terpyridine) (Figure 1) (*8–14*). In this chapter, we review these recent advances including studies of the OEC and biomimetic oxomanganese complexes, with emphasis on the functional roles of carboxylate moieties as redox and acid/base cofactors during the accumulation of multiple oxidizing equivalents in the OEC.

In photosystem II, the harvested solar energy is initially used to form the radical species $P680^{+\bullet}$ by oxidation of the chlorophyll a species P680. The $P680^{+\bullet}$ radical is a strong oxidizing species that oxidizes tyrosine Y_Z, an amino acid residue located in close proximity to the OEC. The oxidized Y_Z in turn oxidizes the OEC, storing an oxidizing equivalent in the Mn cluster. This light-driven electron-transfer process is repeated multiple times, while evolving the Mn cluster through five oxidation state intermediates (S_0-S_4) along the catalytic cycle

In Applications of Molecular Modeling to Challenges in Clean Energy; Fitzgerald, G., et al.;
ACS Symposium Series; American Chemical Society: Washington, DC, 2013.

(*i.e.*, the Kok cycle) proposed by Joliot and Kok (*2*, *3*). After four oxidizing equivalents are accumulated in the OEC, molecular oxygen evolves producing protons that are released to the lumen, and electrons that reduce the oxidized the Mn cluster, regenerating it for the next turn of the cycle. Remarkably, while the overall catalytic mechanism was proposed more than 40 years ago (*2*, *3*), several fundamental aspects remain to be established including the underlying structural changes of the OEC along the catalytic cycle, and the nature of acid/base redox cofactors responsible for redox leveling the four oxidation state transitions of the OEC at about ~1 Volt.

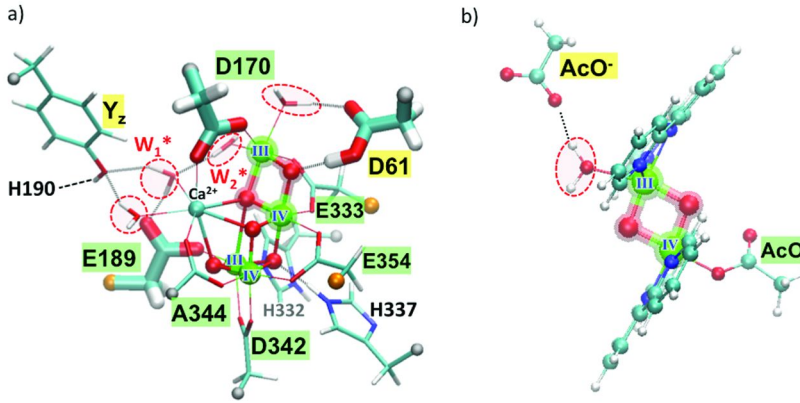

Figure 1. (a) DFT-QM/MM model of the OEC in the S_1 state, based on the X-ray structure at 1.9 Å resolution. (b) DFT structural model of the biomimetic oxomanganese complex ***1-OAc****. Carboxylate groups are highlighted, including those bound to Mn centers (green), or unbound proton acceptors (yellow). Terminal water ligands are circled in red. Note that amino acid residue Alanine344 (A344) is a C-terminal residue with a terminal carboxyl group.*

Structure of OEC

X-ray absorption spectroscopy has been extensively applied to characterize the structural changes in the OEC along the S_0–S_4 transitions (*15*–*17*). However, the molecular nature of the catalytic intermediates has remained elusive for many years. Recent progress has been focused on the structure of the dark-stable state of the OEC (S_1 state). The first X-ray model of the OEC ligated by the surrounding protein environment was proposed almost a decade ago (*18*), from the analysis of the X-ray diffraction (XRD) data at 3.5 Å resolution. The proposed XRD model included a cuboidal core $MnCaMn_3$ with a 'dangling' Mn, as previously suggested by electron paramagnetic resonance (EPR) studies (*19*). The Mn centers were shown to be bound by carboxylate ligands and proposed to be linked by μ-oxo bridges. Subsequently, X-ray data at 3.0 Å resolution suggested a different proteinaceous ligation scheme, with bidentate carboxylate groups bridging the metal centers of the OEC (*20*). However, the precise positions of the metal centers, water, proteinaceous ligands, and μ-oxo bridges remained

In Applications of Molecular Modeling to Challenges in Clean Energy; Fitzgerald, G., et al.;
ACS Symposium Series; American Chemical Society: Washington, DC, 2013.

undetermined until recently when the resolution of the electron density map was improved to 1.9 Å (*1*). The resulting high-resolution X-ray model confirmed structural features common to previous XRD and computational models (*21–26*), and also introduced new features (i.e., features not previously proposed by earlier empirical, or computational models). In particular, the model confirmed a cuboidal structure of the OEC, bound carboxylate groups bridging the metal centers, and the presence of chloride in close proximity to the OEC. In addition, the XRD model showed for the first time the coordination of terminal water molecules bound to Ca and the dangling Mn, an additional μ-oxo bridge linking the dangling Mn to the cuboidal $CaMn_3$ cluster, and the coordination of the side chain of D170 bridging Ca and the dangling Mn. These breakthroughs have stimulated a series of studies that aimed to establish the molecular nature of the catalytic intermediates, including the protonation pattern and the oxidation state of the Mn centers for the various S-states along the Kok cycle (*4*, *27*).

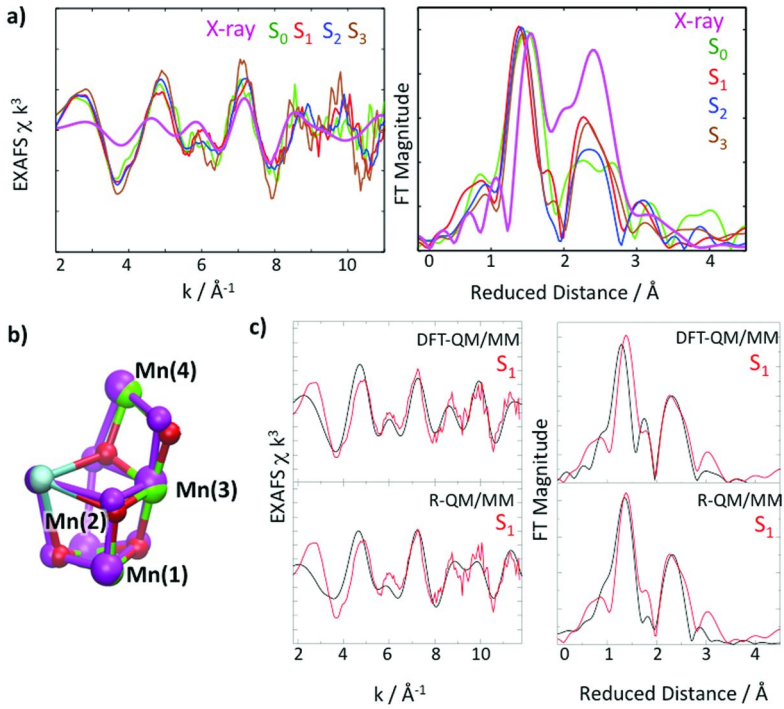

Figure 2. (a) Comparison between the simulated isotropic EXAFS spectrum in k-space (left) and Fourier transform (right), based on the XRD model at 1.9 Å resolution (magenta) and the experimental spectra of S-state intermediates S_0-S_3. (b) Superposition of the OEC core from the XRD model at 1.9 Å and the DFT-QM/MM S_1 state model. (c) Comparison between experimental (red) and calculated (black) isotropic EXAFS spectra for the OEC of PSII in the S1 state calculated with the DFT-QM/MM and refined R-QM/MM model. Adapted with permission from reference (4). Copyright 2011 American Chemical Society.

In a recent study, the XRD model of the OEC at 1.9 Å has been analyzed in terms of calculations of its extended X-ray absorption fine structure (EXAFS) spectrum and direct comparisons to the experimental EXAFS spectra of the S_0–S_3 states (Figure 2) (*15*–*17*). It was found that the spectrum of the XRD model did not match the spectra of any S-state intermediates (or a mixture of them) (*4*), as observed along the catalytic cycle (*16*, *17*). Since radiation damage of PSII samples is a common problem during the process of X-ray data collection (*16*, *28*, *29*), it was proposed that the XRD structure correspond to a mixture of states containing highly reduced forms (such as S_{-1}, S_{-2}, etc.) (*4*), a proposal later supported by density functional theory (DFT) calculations (*26*).

Direct comparisons between experimental and simulated EXAFS spectra based on the XRD model have, therefore, ruled out the XRD model at 1.9 Å as a possible structure of the system in the S_1 state (*4*). However, a similar structure obtained by structural refinement of the XRD model by using DFT-quantum mechanics/molecular mechanics (QM/MM) method has been found to be consistent with both the ligation scheme suggested by the new XRD model and with high-resolution EXAFS data (Figure 1) (*4*). Further refinement based on EXAFS structural refinement of the DFT-QM/MM model (*25*), provided quantitative agreement with experimental EXAFS data (including polarized EXAFS spectra (*4*), not shown in Figure 2). The overlay of the Mn_4O_5Ca core in the DFT-QM/MM model in the S_1 Mn_4(IV,III,IV,III) oxidation state and the XRD model at 1.9 Å is shown in Figure 2. Longer Mn-Mn distances (e.g., Mn(3)-Mn(4)) consistent with Mn reduction are observed in the XRD model when compared to the DFT QM/MM structure, explaining the differences in the EXAFS spectra.

Role of Chloride Cofactor

In a chloroplast, the chloride concentration is regulated very effectively under a variety of conditions (*30*, *31*) and it is known that chloride depletion from PSII suppresses O_2 evolution (*32*–*34*) by hindering the oxidation of the OEC beyond the S_2 state (*35*, *36*). While this has been known for quite some time, the characterization of the chloride binding sites in PSII and the specific functional/structural roles of chloride ions have remained elusive until very recently (*1*, *37*, *38*). In the absence of crystallographic information on the chloride position, a series of proposals on its binding mode were suggested, including ligation to manganese (*32*, *33*, *39*–*43*) and association with amino-acid residues in the Mn coordination shell (*44*, *45*). In addition, several proposals for the functional roles of chloride were proposed, including regulation of the redox potentials of the Mn cluster (*46*), participation in hydrogen-bond networks (*21*, *47*–*49*), and activation of the substrate water (*47*). Significant progress was reported in 2008, with the X-ray crystallographic studies of bromide-substituted and iodine-substituted PSII revealing two binding sites for halide anions in the proximity of the OEC (*37*). Those binding sites initially observed for bromide have been recently confirmed for chloride binding in the X-ray structure at 1.9 Å resolution (*1*).

Figure 3 shows the two chloride binding site (BS1 and BS2) as revealed by the latest X-ray crystal structures (*1*). In contrast to binding at the BS1 site, where chloride is stabilized by interaction with the protein backbone, binding of chloride at the BS2 site involves ion-pair interaction with the positively charged amino-acid residue D2-Lys317 and hydrogen-bonding interactions with water molecules bridging between D2-Lys317 and D1-Asp61. The BS2 binding site is particularly interesting since it involves titratable amino-acid residues D2-Lys317 and D1-Asp61 and is located along one of the postulated proton exit channels from the OEC to the lumen (*18*).

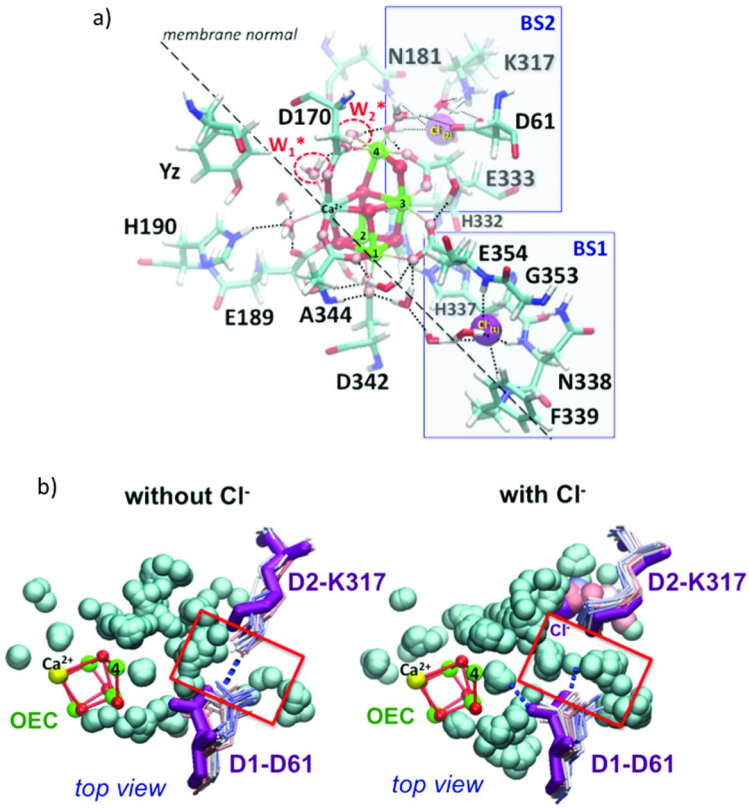

Figure 3. Chloride binding sites (BS1 and BS2) as proposed by the X-ray structure at 1.9 Å resolution. Superposition of instantaneous configurations along MD simulations (waters represented as spheres and D61, K317 side chains colored from red to blue for 0–24 ns) of the OEC with (right) or without (left) Cl^- at the BS2 site. A salt bridge between K317 and D61 forms upon Cl^- depletion, and is interrupted by water in the presence of Cl_. The X-ray configuration is shown in magenta. Adapted with permission from reference (5). Copyright 2011 American Chemical Society.

In Applications of Molecular Modeling to Challenges in Clean Energy; Fitzgerald, G., et al.;
ACS Symposium Series; American Chemical Society: Washington, DC, 2013.

Molecular Dynamics (MD) and Monte Carlo (MC) Multi-Conformer Continuum Electrostatics (MCCE) simulations based on the DFT-QM/MM S_1 model have explored the effect of chloride binding on specific hydrogen-bonding interactions and protonation states of amino-acid residues at the BS2 binding site (*5*). The titratable side chain of the amino acid residue D1-Asp61 is located between the Mn cluster of the OEC and the (D2-Lys317)-NH_3^+/Cl^- ion-pair. MD simulations show relatively high flexibility of the D1-Asp61 carboxylate group, which could form H-bonds with a water ligand of the 'dangling' Mn, a μ-oxo bridge linking Mn(3) and Mn(4), and solvent water molecules surrounding the (D2-Lys317)-NH_3^+/Cl^- ion-pair. However, upon chloride ion depletion, the negatively charged side chain of D1-Asp61 is stabilized by formation of a salt-bridge with the positively charged side chain of D2-Lys317 (Figure 3). Formation of a stable salt bridge locks the protonation state and limits side chain conformations of D1-Asp61, taking it away from the OEC and the surrounding water molecules, effectively reducing the functionality of D1-Asp61 as a proton acceptor. Therefore, while the nature of the base responsible for proton abstraction from the OEC has yet to be established, MD simulations suggest that D1-Asp61 should be further investigated. Chloride at the BS2 binding site allows D1-Asp61 to form hydrogen bonds with the OEC. The involvement of D1-Asp61 as a key residue affecting the efficiency of oxygen evolution has been nicely confirmed by site-directed mutagenesis experiments targeting this residue (*50*). In particular, mutation of Asp with Asn induces a dramatic deceleration of the S_3 to S_0 transition and the accompanying oxygen release, providing direct evidence of the central role of D1-Asp61 in the catalytic mechanism.

Acid/Base and Redox Cofactors

Nature has designed the OEC and its proteinaceous environment to efficiently transfer electrons to oxidized $P680^{+\bullet}$ and to rapidly transfer protons to the lumenal surface of the protein. Proton-coupled electron transfer (PCET) has been proposed as the mechanism responsible for activation of OEC at low overpotentials. Fundamental understanding of PCET during the oxidation of oxomanganese complexes has been achieved by studies of biomimetic synthetic complexes (*13*, *14*), including the homogeneous catalyst $[H_2O(terpy)Mn^{III}(\mu\text{-}O)_2Mn^{IV}(terpy)OH_2]^{3+}$ (**1**, terpy=2,2′:6′,2"-terpyridine) (*9*, *11*, *12*, *51*). Here, we review recent theoretical work on complex **1** (*i.e.*, the Mn-terpy dimer) as a biomimetic model of oxygen evolution. Compound **1** catalyzes water splitting when activated by a primary oxidant in either homogeneous solutions (*51*, *52*), deposited on TiO_2 thin-films (*53*), or immobilized in clays (*54*, *55*). In addition to its catalytic functionality, **1** shares common structural features with the OEC, including high-valent Mn centers linked by μ-oxo bridges, terminal water ligands and carboxylate ligands when dissolved in acetate buffer solutions. Therefore, the reviewed studies have significant implications on the water-oxidation mechanism in PSII and provide fundamental insights that are valuable for the design of catalysts based on earth-abundant metals for artificial photosynthesis.

In Applications of Molecular Modeling to Challenges in Clean Energy; Fitzgerald, G., et al.;
ACS Symposium Series; American Chemical Society: Washington, DC, 2013.

Quantum mechanical (QM) calculations (*11*, *12*), pH dependent cyclic voltammetry (CV) experiments (*9*), and EPR studies (*56*) suggest that one terminal water ligand of complex **1** exchanges with acetate in buffered solutions. In particular, DFT calculations indicate that the acetate ligand has higher affinity for Mn(IV) than Mn(III). Binding of a second acetate molecule to a Mn(III) center is, instead, an endergonic reaction, in agreement with pH-dependent cyclic voltammetry experiments (*9*) showing that only one of the terminal waters of **1** is displaced by acetate (complex **1-OAc**) in 50 mM acetate buffer.

Comparison between computations at the DFT/B3LYP level and experimental CV data provide fundamental information on the PCET mechanism and redox potentials in complexes **1** and **1-OAc**. Table I shows that both DFT/B3LYP and experimental CV results indicate that acetate binding stabilizes the oxidized form of the Mn(III)-Mn(IV) complex throughout the whole pH range, decreasing the reduction potential of the IV→III transition by as much as 90-220 mV.

Table I. Standard Reduction Potentials (vs NHE, in Volts) for 1 and 1-OAc Complexes

	DFT/B3LYP[11] $E_{1/2}$ *(pH < 3)*	*exp[9]* $E_{1/2}$ *(pH < 3)*	*DFT/B3LYP[11]* $E_{1/2}$ *(pH=5)*	*exp[9]* $E_{1/2}$ *(pH=5)*
1	1.40	1.34	1.20	1.16
1-OAc	1.18	-	1.04	1.07

In fact, acetate binding to Mn(IV) decreases the reduction potential from 1.40 to 1.18 V at low pH (<3), when a water molecule is bound to the Mn(III) center. At high pH (>13), the terminal water molecule is deprotonated and acetate binding to Mn(IV) decreases the potential for oxidation of Mn(III) from 0.65 V in complex **1** to 0.56 V in complex **1-OAc**. Moreover, DFT calculations indicate that acetate binding affects the pK_a of the terminal water, reducing the pH range for PCET from pH 1.2-13.9 in the absence of acetate to pH 2.9-13.3 with acetate. These results show that carboxylate ligands bound to Mn facilitate oxidation of the oxomanganese complex and modulate the pH range for PCET. Similar redox effects due to coordination of carboxylate groups might be expected in the OEC of PSII, where the Mn centers are bound to several proteinaceous carboxylate moieties, including Asp170, Glu189, Glu333, Glu354, (C-terminal)Ala344 and Asp342. Therefore, these carboxylate groups are expected to affect the redox potentials of the OEC during the S-state transitions.

DFT/B3LYP calculations of redox potentials and pK_a's of complexes **1** and **1-OAc** (*11*) show good agreement with experimental data from CV measurements (*9*), demonstrating the capabilities of current DFT techniques as applied to modeling PCET in oxomanganese complexes.

In Applications of Molecular Modeling to Challenges in Clean Energy; Fitzgerald, G., et al.;
ACS Symposium Series; American Chemical Society: Washington, DC, 2013.

Carboxylate Groups as Acid/Base Cofactors

Several studies of the water oxidation catalyzed by PSII (*18*, *23*, *24*, *41*, *42*, *57*, *58*) and biomimetic oxomanganese complexes (*59–61*) have suggested that an oxyl radical Mn(IV)-O• is formed upon deprotonation and partial oxidation of a terminal water ligand. The O-O bond formation is thought to involve nucleophilic attack of the oxyl radical by a substrate water. However, DFT studies have disfavored that mechanism for water oxidation in PSII due to the large energy barriers associated with O-O bond formation, as obtained by calculations that did not include any surrounding proton-acceptor center other than μ-oxo bridges linking the high-valent Mn centers (*59*, *60*, *62*). More recent computational studies of the O-O bond formation catalyzed by complex **1** in acetate buffer solution (**1-OAc**) suggested that surrounding proton-acceptor centers (such as carboxylate groups of acetate buffer molecules) can lower the activation-energy barriers during the water nucleophilic attack (*63*).

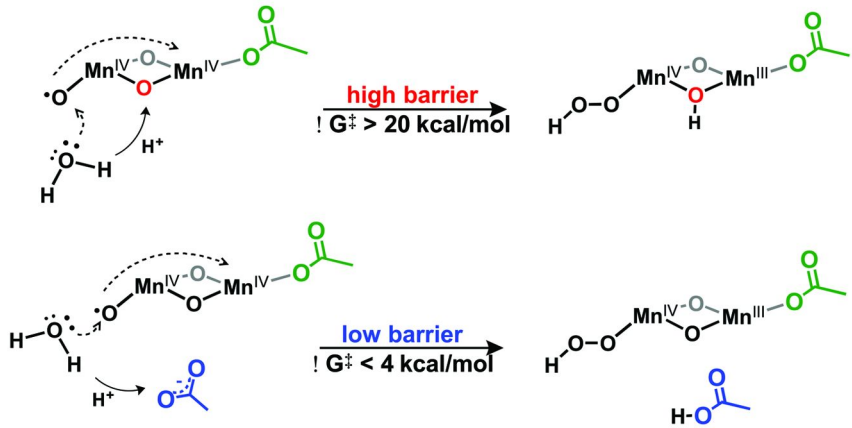

*Figure 4. Schematic representation of O-O bond formation during O_2 evolution as catalyzed by **1-OAc** in the absence (top panel) and presence (bottom panel) of an acetate buffer moiety functioning as a sacrificial proton acceptor.*

Figure 4 shows the O-O bond-formation mechanism suggested by DFT/B3LYP calculations, modeling the catalytic cycle of complex **1-OAc** (*63*). This computational study as well as a previous theoretical analysis of a reduced model of complex **1** (*60*), indicate that, if the μ-oxo bridge is the only possible proton acceptor, the free activation energy for O-O bond formation is higher than 20 kcal mol^{-1}, in disagreement with the experiments. Kinetic measurements indicate that oxidation of the complex (leading in the proposed mechanism to formation of the Mn(IV)-O• oxyl radical species) is the rate-determining step, with an activation barrier of ~18 kcal mol^{-1} as predicted by transition state theory consistent with a turnover number of ~0.67 s^{-1} (*51*, *60*). Therefore, the activation barrier for O-O bond formation must be lower than 18 kcal mol^{-1}. It has recently been found that the resulting free energy barrier drops dramatically (<4 kcal mol^{-1}) in the presence a buffer acetate molecule that uptakes the proton released during O-O bond formation (*63*). In addition, the calculated pK_a of the μ-hydroxo bridge

in the Mn(IV)-Mn(IV)-O$^{\bullet}$ species (pK_a<0) is much lower than that of acetic acid (pK_a=4.75). Therefore, the μ-oxo bridge linking Mn(IV) centers is not favored to function as a proton acceptor in the presence of acetate. Such a dependency of the activation-energy barrier with the basicity of the proton-acceptor center is expected to be common to other systems where O-O bond formation involves a nucleophilic attack activated by deprotonation of the nucleophile water, as observed in other systems, such as the Ru single-site water-oxidation catalysis (*64*) and for base-assisted proton–electron transfer reactions in tyrosine oxidation (*65*).

The reviewed studies of biomimetic oxomanganese complexes are expected to be particularly relevant to catalytic water oxidation in PSII, where the OEC cluster is ligated and surrounded by carboxylate groups of titratable amino-acid side chains, including Asp170, Glu189, Glu333, Glu354, (C-terminal)Ala344, Asp342 and Asp61 (Figures 1 and 3). In particular, carboxylate groups bound to Mn centers are expected to play a role to modulate the redox potential during the activation (oxidation) of the OEC while carboxylate in the proximity of the OEC might function as acid/base cofactors transferring protons to the lumen. In particular, D1-Asp61 has been shown to interact directly with the OEC through various H-bond interactions and could function as a proton acceptor in the presence of chloride (*5*). Several factors could favor the deprotonated form of D1-Asp61, increasing its pK_a, including the presence of vicinal positive charges such as that on D2-K317 or on the Mn cluster, the hydrogen-bonding network and the flexibility of the sidechain in the chloride-binding site. MCCE calculations, accounting exclusively for electrostatic interactions, indicated that the pK_a of the D1-Asp61 side chain is higher (by at least 1 pH unit) than the pK_a of aspartate side chain (pK_a=3.86) (*5*). Further computational and experimental studies should provide accurate measurements of the D1-Asp61's pK_a, addressing the role of this carboxylate group in the proton-coupled electron-transfer mechanism of PSII.

Conclusions

Computational studies based on quantum mechanics/molecular mechanics (QM/MM), Molecular Dynamics (MD) and Monte Carlo (MC) Multi-Conformer Continuum Electrostatics (MCCE), as well as simulations of extended X-ray absorption fine structure (EXAFS) have provided fundamental understanding of water oxidation in the OEC when based on the most recent X-ray structure of PSII at 1.9 Å resolution. It has been shown that the XRD structure does not correspond to any of the S-state intermediates along the catalytic cycle, presumably due to reduction of the complex during the process of X-ray data collection. However, a DFT-QM/MM model of the dark-stable S1 state of the OEC has been shown to be consistent with both the ligation scheme suggested by the new XRD model and with high-resolution EXAFS data. Based on this DFT-QM/MM model, MD and MC studies have explored the functional role of the chloride cofactor in PSII, finding that chloride depletion induces formation of a salt bridge between D2-K317 and D1-D61 amino acid residues along a postulated proton-exit channel. Therefore, it has been concluded that chloride

In Applications of Molecular Modeling to Challenges in Clean Energy; Fitzgerald, G., et al.;
ACS Symposium Series; American Chemical Society: Washington, DC, 2013.

might work as an allosteric regulator of PSII by favoring a flexible conformation of the proton acceptor (D1-D61), thus assisting proton abstraction from the OEC.

Comparative studies of biomimetic oxomanganese complexes have been performed to explore the functional role of cofactors that influence the underlying proton-coupled electron-transfer (PCET) mechanism. DFT calculations on biomimetic oxomanganese complexes suggest that buffer acetate moieties participate not only as redox potential regulators, upon exchanging with terminal water ligands and binding to high-valent Mn centers, but also as proton acceptors that facilitate the reaction of the nucleophilic water molecules during O-O bond formation. The reported computational studies, thus, provide fundamental insights into Mn-based water-oxidation catalysis that are particularly relevant for the understanding of natural photosynthetic processes and the development of artificial photosynthetic devices based on biomimetic oxomanganese catalysts.

Acknowledgments

This work was supported by U.S. Department of Energy Grants DE-FG02-07ER15909 and DE-FG02-05ER15646 (G.W.B., biochemical studies of PSII and model complexes). Computer resources were provided by NERSC supercomputer center and the High Performance Computing facilities at Yale University.

References

1. Umena, Y.; Kawakami, K.; Shen, J.-R.; Kamiya, N. *Nature* **2011**, *473*, 55.
2. Joliot, P.; Barbieri, G.; Chabaud, R. *Photochem. Photobiol.* **1969**, *10*, 309.
3. Kok, B.; Forbush, B.; McGloin, M. *Photochem. Photobiol.* **1970**, *11*, 457.
4. Luber, S.; Rivalta, I.; Umena, Y.; Kawakami, K.; Shen, J.-R.; Kamiya, N.; Brudvig, G. W.; Batista, V. S. *Biochemstry* **2011**, *50*, 6308.
5. Rivalta, I.; Amin, M.; Luber, S.; Vassiliev, S.; Pokhrel, R.; Umena, Y.; Kawakami, K.; Shen, J.-R.; Kamiya, N.; Bruce, D.; Brudvig, G. W.; Gunner, M. R.; Batista, V. S. *Biochemistry* **2011**, *50*, 6312.
6. Ames, W.; Pantazis, D. A.; Krewald, V.; Cox, N.; Messinger, J.; Lubitz, W.; Neese, F. *J. Am. Chem. Soc.* **2011**, *133*, 19743.
7. Yamanaka, S.; Isobe, H.; Kanda, K.; Saito, T.; Umena, Y.; Kawakami, K.; Shen, J. R.; Kamiya, N.; Okumura, M.; Nakamura, H.; Yamaguchi, K. *Chem. Phys. Lett.* **2011**, *511*, 138.
8. Rivalta, I.; Brudvig, G. W.; Batista, V. S. *Curr. Opin. Chem. Biol.* **2012**, *16*, 11.
9. Cady, C. W.; Shinopoulos, K. E.; Crabtree, R. H.; Brudvig, G. W. *Dalton T.* **2010**, *39*, 3985.
10. Tagore, R.; Chen, H. Y.; Crabtree, R. H.; Brudvig, G. W. *J. Am. Chem. Soc.* **2006**, *128*, 9457.
11. Wang, T.; Brudvig, G.; Batista, V. S. *J. Chem. Theory Comput.* **2010**, *6*, 755.
12. Wang, T.; Brudvig, G. W.; Batista, V. S. *J. Chem. Theory Comput.* **2010**, *6*, 2395.

13. Luo, S.; Rivalta, I.; Batista, V.; Truhlar, D. G. *J. Phys. Chem. Lett.* **2011**, *2*, 2629.
14. Cady, C. W.; Crabtree, R. H.; Brudvig, G. W. *Coord. Chem. Rev.* **2008**, *252*, 444.
15. Sauer, K.; Yano, J.; Yachandra, V. K. *Coord. Chem. Rev.* **2008**, *252*, 318.
16. Dau, H.; Liebisch, P.; Haumann, M. *Phys. Chem. Chem. Phys.* **2004**, *6*, 4781.
17. Haumann, M.; Muller, C.; Liebisch, P.; Iuzzolino, L.; Dittmer, J.; Grabolle, M.; Neisius, T.; Meyer-Klaucke, W.; Dau, H. *Biochemistry* **2005**, *44*, 1894.
18. Ferreira, K. N.; Iverson, T. M.; Maghlaoui, K.; Barber, J.; Iwata, S. *Science* **2004**, *303*, 1831.
19. Britt, R.; Campbell, K.; Peloquin, J.; Gilchrist, M.; Aznar, C.; Dicus, M.; Robblee, J.; Messinger, J. *Biochim. Biophys. Acta, Bioenerg.* **2004**, *1655*, 158.
20. Loll, B.; Kern, J.; Saenger, W.; Zouni, A.; Biesiadka, J. *Nature* **2005**, *438*, 1040.
21. Sproviero, E. M.; Gascon, J. A.; McEvoy, J. P.; Brudvig, G. W.; Batista, V. S. *J. Chem. Theory Comput.* **2006**, *2*, 1119.
22. Sproviero, E. M.; Gascon, J. A.; McEvoy, J. P.; Brudvig, G. W.; Batista, V. S. *Curr. Opin. Struct. Biol.* **2007**, *17*, 173.
23. Sproviero, E. M.; Gascon, J. A.; McEvoy, J. P.; Brudvig, G. W.; Batista, V. S. *J. Am. Chem. Soc.* **2008**, *2*, 3428.
24. Sproviero, E. M.; Gascon, J. A.; McEvoy, J. P.; Brudvig, G. W.; Batista, V. S. *Coord. Chem. Rev.* **2008**, *252*, 395.
25. Sproviero, E. M.; Gascon, J. A.; McEvoy, J. P.; Brudvig, G. W.; Batista, V. S. *J. Am. Chem. Soc.* **2008**, *130*, 6728.
26. Sproviero, E. M.; Shinopoulos, K.; Gascon, J. A.; McEvoy, J. P.; Brudvig, G. W.; Batista, V. S. *Philos. Trans. R. Soc., Bs* **2008**, *363*, 1149.
27. Galstyan, A.; Robertazzi, A.; Knapp, E. W. *J. Am. Chem. Soc.* **2012**, *134*, 7442.
28. Yano, J.; Kern, J.; Irrgang, K.; Latimer, M.; Bergmann, U.; Glatzel, P.; Pushkar, Y.; Biesiadka, J.; Loll, B.; Sauer, K.; Messinger, J.; Zouni, A.; Yachandra, V. *Proc. Natl. Acad. Sci. U.S.A.* **2005**, *102*, 12047.
29. Grabolle, M.; Haumann, M.; Muller, C.; Liebisch, P.; Dau, H. *J. Biol. Chem.* **2006**, *281*, 4580.
30. Demmig, B.; Winter, K. *Planta* **1983**, *159*, 66.
31. Critchley, C. *Biochim. Biophys. Acta* **1985**, *811*, 33.
32. Sandusky, P. O.; Yocum, C. F. *Biochim. Biophys. Acta* **1984**, *766*, 603.
33. Brudvig, G. W.; Beck, W. F.; de Paula, J. C. *Annu. Rev. Biophys. Biophys. Chem.* **1989**, *18*, 25.
34. Popelkova, H.; Yocum, C. F. *Photosynth. Res.* **2007**, *93*, 111.
35. Kühne, H.; Szalai, V. A.; Brudvig, G. W. *Biochemistry* **1999**, *38*, 6604.
36. Wincencjusz, H.; van Gorkom, H. J.; Yocum, C. F. *Biochemistry* **1997**, *36*, 3663.
37. Murray, J. W.; Maghlaoui, K.; Kargul, J.; Ishida, N.; Lai, T. L.; Rutherford, A. W.; Sugiura, M.; Boussac, A.; Barber, J. *Energy Environ. Sci.* **2008**, *1*, 161.

38. Guskov, A.; Kern, J.; Gabdulkhakov, A.; Broser, M.; Zouni, A.; Saenger, W. *Nat. Struct. Mol. Biol.* **2009**, *16*, 334.
39. Hureau, C.; Blondin, G.; Charlot, M. F.; Philouze, C.; Nierlich, M.; Cesario, M.; Anxolabehere-Mallart, E. *Inorg. Chem.* **2005**, *44*, 3669.
40. Yachandra, V. K.; Sauer, K.; Klein, M. P. *Chem. Rev.* **1996**, *96*, 2927.
41. Pecoraro, V. L.; Baldwin, M. J.; Caudle, M. T.; Hsieh, W. Y.; Law, N. A. *Pure Appl. Chem.* **1998**, *70*, 925.
42. Vrettos, J. S.; Limburg, J.; Brudvig, G. W. *Biochim. Biophys. Acta, Bioenerg.* **2001**, *1503*, 229.
43. Britt, R. D.; Campbell, K. A.; Peloquin, J. M.; Gilchrist, M. L.; Aznar, C. P.; Dicus, M. M.; Robblee, J.; Messinger, J. *Biochim. Biophys. Acta, Bioenerg.* **2004**, 1655–158.
44. Haumann, M.; Barra, M.; Loja, P.; Loscher, S.; Krivanek, R.; Grundmeier, A.; Andreasson, L. E.; Dau, H. *Biochemistry* **2006**, *45*, 13101.
45. Hasegawa, K.; Kimura, Y.; Ono, T. A. *Biochemistry* **2002**, *41*, 13839.
46. Boussac, A.; Rutherford, A. W. *J. Biol. Chem.* **1994**, *269*, 12462.
47. McEvoy, J. P.; Brudvig, G. W. *Phys. Chem. Chem. Phys.* **2004**, *6*, 4754.
48. Olesen, K.; Andreasson, L. E. *Biochemistry* **2003**, *42*, 2025.
49. Pokhrel, R.; McConnel, I.; Brudvig, G. W. *Biochemistry* **2011**, *50*, 2725.
50. Dilbeck, P. L.; Hwang, H. J.; Zaharieva, I.; Gerencser, L.; Dau, H.; Burnap, R. L. *Biochemistry* **2012**, *51*, 1079.
51. Limburg, J.; Vrettos, J. S.; Chen, H. Y.; de Paula, J. C.; Crabtree, R. H.; Brudvig, G. W. *J. Am. Chem. Soc.* **2001**, *123*, 423.
52. Limburg, J.; Vrettos, J. S.; Liable-Sands, L. M.; Rheingold, A. L.; Crabtree, R. H.; Brudvig, G. W. *Science* **1999**, *283*, 1524.
53. Li, G.; Sproviero, E. M.; Snoeberger, R. C., III; Iguchi, N.; Blakemore, J. D.; Crabtree, R. H.; Brudvig, G. W.; Batista, V. S. *Energy Environ. Sci.* **2009**, *2*, 230.
54. Narita, K.; Kuwabara, T.; Sone, K.; Shimizu, K.-i.; Yagi, M. *J. Phys. Chem. B* **2006**, *110*, 23107.
55. Yagi, M.; Narita, K. *J. Am. Chem. Soc.* **2004**, *126*, 8084.
56. Milikisiyants, S.; Chatterjee, R.; Lakshmi, K. V. *J. Phys. Chem. B* **2011**, *115*, 12220.
57. Limburg, J.; Szalai, V. A.; Brudvig, G. W. *J. Chem. Soc., Dalton Trans.* **1999**, 1353.
58. Hillier, W.; Messinger, J.; Wydrzynski, T. *Biochemistry* **1998**, *37*, 16908.
59. Lundberg, M.; Siegbahn, P. E. M. *Chem. Phys. Lett.* **2005**, *401*, 347.
60. Lundberg, M.; Blomberg, M. R. A.; Siegbahn, P. E. M. *Inorg. Chem.* **2004**, *43*, 264.
61. Sameera, W. M. C.; McKenzie, C. J.; McGrady, J. E. *Dalton Trans.* **2011**, *40*, 3859.
62. Siegbahn, E. M. *Chem.−Eur. J.* **2008**, *14*, 8290.
63. Rivalta, I.; Brudvig, G. W.; Batista, V. S. Unpublished (in preparation).
64. Chen, Z.; Concepcion, J. J.; Hu, X.; Yang, W.; Hoertz, P. G.; Meyer, T. J. *Proc. Natl. Acad. Sci. U.S.A.* **2010**, *107*, 7225.
65. Fecenko, C. J.; Thorp, H. H.; Meyer, T. J. *J. Am. Chem. Soc.* **2007**, *129*, 15098.

In Applications of Molecular Modeling to Challenges in Clean Energy; Fitzgerald, G., et al.;
ACS Symposium Series; American Chemical Society: Washington, DC, 2013.

Chapter 12

Atomic-Level Modeling of Organic Electrolytes in Lithium-Ion Batteries

Glen Ferguson[*,1] and Larry A. Curtiss[1,2]

[1]Materials Science Division, Argonne National Laboratory, 9700 South Cass Avenue, Argonne, Illinois 60439, U.S.A.
[2]Center for Nanoscale Materials, Argonne National Laboratory, 9700 South Cass Avenue, Argonne, Illinois 60439, U.S.A.
[*]E-mail: gferguson@anl.gov

Lithium-ion (Li-ion) batteries are a widely used and important technology. Recent expansion of Li-ion batteries into automotive applications has resulted in intense scientific interest. In Li-ion batteries the multitude of reactions occurring under harsh conditions along with difficulties in characterization have made calculations and simulations an important part of this research. Application of atomic level methods has expanded the knowledge concerning the basic chemistry of the Li-ion battery, especially as applied to electrolytes and their relationship to the solid electrolyte interphase (SEI), a key component of many Li-ion batteries. In this chapter we review methods for atomic-level computations and simulations of Li-ion battery electrolytes with a focus on the chemistry of the organic solvents of the electrolyte. Each section includes a short overview of computational methodology and some applications, followed by a highlight of recent work. The first section describes how quantum chemical methods can be used to interrogate problems in Li-ion batteries. The highlighted work in this section is a study of the reactions of organic solvent on model systems to form an oligomeric SEI layer. In the next section the use of classical and ab initio molecular dynamics to simulate reactions in the SEI layer is reviewed and two studies are highlighted. The final method is the use of data from ab initio calculations to screen electrolytes for improved reactivity.

In Applications of Molecular Modeling to Challenges in Clean Energy; Fitzgerald, G., et al.;
ACS Symposium Series; American Chemical Society: Washington, DC, 2013.

The chapter closes with a section on the future outlook of atomic-level modeling of Li-ion electrolytes.

1. Introduction

Lithium-ion (Li-ion) batteries are a prominent and important energy storage technology. Batteries based on Li-ion technology have high energy density and excellent charge retention when not in use. This technology also lacks the memory effect that is present in nickel-cadmium batteries. These qualities have made Li-ion batteries crucial to the expansion of the consumer electronics industry (*1–4*). Li-ion technology has recently expanded into automotive applications. The desire for all-electric and hybrid vehicles is expected to be a significant driver for future growth of Li-ion technology (*5*, *6*). Due to their expanding role and large number of scientific challenges, interest in Li-ion batteries has been strong (*1*, *2*, *4–21*). A great deal of this research has been in the form of experimental characterization of current materials used in batteries and the development of novel materials that address one or more the scientific problems necessary to improve the technology. The complex nature of battery materials and difficulty of *in situ* experimental measurements have increased the role of modeling and simulation in solving scientific problems to understand and improve Li-ion technology. In this chapter we examine several aspects of atomic level computational research on Li-ion battery materials. First-principles and molecular dynamics studies provide important information for understanding the operation of Li-ion batteries. In many cases information from computations and simulations can be used to predict novel materials (directly or indirectly) either alone, or along with experiential data.

The battery constituents targeted for improvement are central to battery operation. While the construction of Li-ion batteries involves many components, all of which are necessary for proper battery operation, the primary component is the Li-ion electrochemical cell. The cell contains two electrodes and an electrolyte using a lithium charge carrier. The electrodes are typically a metal oxide and carbon with an electrolyte composed of lithium salts in an organic solvent. While variations are used, e.g. metal phosphides for one electrode, the basic electrochemistry of battery operation are the same. During the discharge the lithium ions (Li^+) migrate from the carbon electrode to the metal oxide. During charging the Li^+ return to the carbon electrode. Computational studies on improving the electrodes using materials design are one example of successfully using atomic-level simulations for understanding and improving cell operation by improving the cathode material (*22–26*).

Other important components of the cell are the electrolyte and the electrode/electrolyte interface. The electrolyte must conduct Li^+ ions between the electrodes. To accomplish this lithium salts are dissolved in organic solvents such as ethylene carbonate (EC). Aqueous solvents lack a large enough electrochemical window, and water vigorously reacts with lithium, prohibiting their use. Other additives are used to improve performance such as redox shuttles to protect against cell damage from overcharge. While under standard conditions the electrolyte

In Applications of Molecular Modeling to Challenges in Clean Energy; Fitzgerald, G., et al.;
ACS Symposium Series; American Chemical Society: Washington, DC, 2013.

is unlikely to react with the electrodes; under electrochemical conditions the probability for reactivity is increased. At lower voltages electrolyte reduction at the anode is common. At higher voltages oxidation at the cathode is possible. The product of the electrolyte reacting with or at the electrode surface forms a layer at the surface called the solid electrolyte interphase (SEI) and its formation has significant implications for operation of the electrochemical cell. The SEI layer forms spontaneously on the electrode surface during the first discharge of the cell. The reactions driving its formation have been previously described. The overall performance of the battery is significantly affected by the existence and nature of the SEI (*8*, *10–12*, *14*, *17*, *19*, *20*, *27–37*). The existence of the SEI prevents further electrolyte breakdown and improves cell safety. Continued battery operation requires that the SEI must still allow rapid Li^+ diffusion. The critical function of the SEI has made it the subject of intense interest along with the electrolyte itself. Therefore, there are two distinct aspects for modeling the electrolyte as shown in Figure 1. The first is in modeling the chemistry of the electrolyte itself and the second is modeling the electrode/electrolyte interface.

Atom-level modeling of the electrolyte and SEI layer has been accomplished using a variety of methods. Ab initio modeling using density functional theory has provided many insights into electrolyte stability and reactivity (*7*, *10–12*, *14*, *15*, *17–19*, *21*, *27*, *30*, *32–63*). Density functional theory has proven to be a very accurate and robust method for calculating properties of molecules and crystals. Some of the shortcomings of ab initio modeling are the lack of time-dependent information and the limited number of electrons and, therefore, atoms that can be included in a calculation. Molecular dynamics (MD) calculations using empirical potentials allows for the calculation of time-dependent properties and simulations of many atoms (millions for very simple potentials to thousands for more complex potentials). The empirical potentials used are often fit to data from ab initio calculations but can be fit to experimental data as well (*64*, *65*). MD studies have allowed for the determination of a number of interesting properties (*8*, *9*, *13–16*, *31*, *43*, *66–72*). While many MD simulations do not effectively model the bonds breaking and bond formation, newer MD methods are being developed to overcome this limitation (*8*, *66*). However, these MD methods have not been extensively used for electrolytes. Ab initio molecular dynamics (AIMD) is a method of performing time-dependent simulations using potentials generated from first-principles (*28*, *29*, *42*, *73*, *74*). The method is significantly more expensive, but has an accuracy equal to or approaching DFT and allows for calculations when empirical parameters are unavailable. Finally, high-throughput screening based on quantum chemical calculations has been used to find candidates for new electrolytes with improved properties (*10*, *20*, *75*, *76*). The use of electrolyte screening is likely to be of increasing interest in the improvement of Li-ion batteries.

The use of atomic-level modeling to understand the chemical processes occurring in batteries and to propose solutions to improve their operation is extensive. If the range of work is restrained only to organic electrolytes, the amount of work remains large. What follows are examples of how atomic-level modeling and simulations have been used to study organic electrolytes used in Li-ion batteries and are meant to be illustrative rather than exhaustive. The

In Applications of Molecular Modeling to Challenges in Clean Energy; Fitzgerald, G., et al.;
ACS Symposium Series; American Chemical Society: Washington, DC, 2013.

remainder of the chapter is organized as follows. In section 2 we discuss the use of quantum chemical calculations for modeling the battery electrolytes and highlight one study on understanding the mechanism reaction of the electrolyte resulting in formation of an oligomeric SEI on gold anodes. In section 3 the use of MD and AIMD simulations is discussed and the two studies leading to SEI formation includs one using the forces from ReaxFF force feilds and another using AIMD simulations to understand the mechanism of the two-electron reduction of EC. In section 5 screening based on quantum chemical calculations is discussed along with its use to find more suitable electrolytes. Section 6 contains the future outlook for modeling electrolytes in Li-ion batteries.

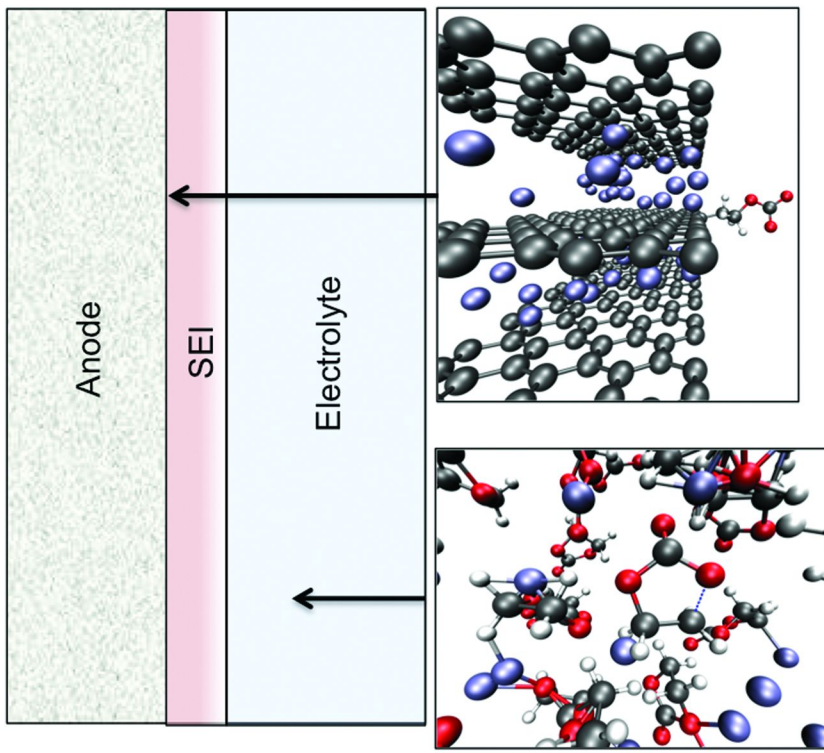

Figure 1. The organic solvent molecules of the electrolyte can react in two chemically distinct regions as pictured above. The top region illustrates the organic solvent reacting at the interface of the graphite (or other) anode. The bottom region illustrates when the reaction of the electrolyte occurs in the solvent after becoming activated. The color code is carbon=grey, oxygen=red, lithium=blue-violet and hydrogen=white. (see color insert)

2. Quantum Chemical Modeling

Quantum chemical calculations based on density functional theory (DFT) are currently the most popular method used in ab initio electronic structure theory. While wavefunction–based methods are used in electrolyte solvent modeling (*38*, *46*, *47*, *49*, *58*, *62*, *77*, *78*), DF methods strike a balance between cost and accuracy that have made them the *de facto* method in first principles calculations. DF methods calculate the energy as a functional (function of a function) of the electronic density. Many properties can also be calculated using this method either directly as derivatives of the energy (e.g., the vibrational frequencies of a molecule can be calculated as the second partial derivative of the energy w.r.t. atomic displacements) or as derived quantities from directly calculated values (e.g., atomic charges are calculated by partitioning the density using a predefined scheme). Due to the outstanding quality of the information provided and wide spread availability of DF codes available, many studies of Li-ion battery electrolyte solvents have used DFT. Several areas of DFT to study Li-ion electrolytes concentrating on the solvents are explored along with highlights of several recent studies.

Areas of study for quantum chemical methods have included polymer electrolytes, lithium salts in the electrolyte, redox shuttles to protect against overcharge, additives for SEI formation, interactions of Li^+ with other battery components, organic solvent oxidation, and SEI formation (*79*). The reduction of organic solvent molecules is generally discussed in SEI formation on the battery anode. Due to the complexity and size of the SEI, methods such as the effective fragment potential have been used to speed up calculations of the electrolyte chemistry (*62*). Calculation of polymer electrolytes is extensive. Some work in this area includes the interaction of Li^+ with polymers (*46*, *47*) and the development of new classes of polymer electrolytes (*45*, *77*, *78*, *80–82*). The chemistry of the lithium salt interactions with solvent molecules has been studied using DFT (*40*, *46*, *47*). Another area of study is the chemistry of redox shuttles. These additives are used to protect against oxidation of the organic solvent at the cathode due to overcharge (*18*, *63*). Another area of study is the interactions of Li^+ with other battery components. This area has had extensive publication including the interaction of Li^+ with graphite, the interaction of Li^+ with organic solvent molecules, and the diffusion or conduction of Li^+ thought the electrolyte. Some studies of the interaction of lithium with the graphite anode include the intercalation of the Li- ion between the graphite layers with and without the solvent molecules (*71*) and the transfer to the lithium from the graphite into the solvent (*37*, *49*, *61*, *71*). A study of the diffusion of Li^+ through graphite has also been reported (*61*). The effect of lithium binding to the organic solvent has been studied in the context of solvent decomposition (*39*, *40*) as well as binding to the organic solvents (*10*, *40*). An especially fertile area has been the diffusion of Li^+ through the electrolyte. The studies include diffusion of the Li^+ through the liquid electrolyte without additives (*41*) and with salts present (*43*). The diffusion of lithium through solid electrolytes has also been studied (*12*, *41*, *44*, *50*).

The final area to be discussed is SEI formation at the anode. This area has been one of intense interest. Many studies in this area are concerned with the

In Applications of Molecular Modeling to Challenges in Clean Energy; Fitzgerald, G., et al.;
ACS Symposium Series; American Chemical Society: Washington, DC, 2013.

decomposition of electrolytes and subsequent reaction of the decomposition products. These seminal studies showed that the decomposition of EC was responsible for the formation of some components of the SEI (*19*, *33*, *54–56*, *79*). This early work also indicated the importance of vinyl carbonate as an additive in Li-ion electrolytes. Later work (*14*, *18*, *20*, *43*, *52*, *53*, *71*) extensively studied the reduction of solvent molecules and the other organic solvents or additives. One recent study that shows the formation of an oligomer SEI layer at model gold anode surface is described in the remainder of this section (*17*).

An oligomer SEI layer that forms spontaneously *in situ* is one possible route to a stable SEI layer. This method is significantly less costly than *ex situ* synthesis of nanoscale thin-film polymers on the anode surface. The oligomers in this process were formed spontaneously *in situ* from EC and propylene carbonate (PC) solvents on Au anodes. In this study the Au coated glass electrodes were emersed in EC or PC/dimethyl carbonate solutions and cycled five times. An electrochemical quartz microbalance detected a layer forming on the surface of the electrode and subsequent matrix-assisted laser desorption/ionization-time of flight (MALDI-TOF) mass spectrometry indicated an oligomer forming on the surface of the electrode. While the formation of the oligomeric layer was also detected on Sn anodes these were not stable and degraded. The monomer weight of the EC was 176 g/mol while PC was lower at 166 g/mol. DFT calculations of the possible solvent reactions leading to these products were performed to determine the mechanism of oligomer formation.

The calculations used the B3LYP/cc-pVDZ model chemistry and included solvation as an additive correction to the geometry calculated in the gas-phase. It is worth noting that the solvation can be included in a variety of ways. The simplest, as performed in this study is to calculate the additive correction to the energy. This method fails to take into account changes in geometry due to solvation, which may be important in some systems. The electrochemical environment is known to create EC or PC radicals during SEI formation immediately suggesting a radical chain-type polymerization mechanism. The pathway calculated for this reaction begins from the generally accepted method of solvent reduction where the EC is reduced at the electrode and undergoes ring opening to form a radical. This radical anion molecule can then (a) react with a solvent molecule, (b) become reduced a second time, (c) react with another reduced solvent molecule or (d) react with the surface. In this study the radical reaction was proposed to be with another neutral solvent molecule (a). This reaction creates a radical that can act as a polymerization initiator by reacting with another neutral solvent molecule to propagate the chain reaction. This mechanism is similar to a general polymerization mechanism that was previously proposed (*83*). In the present study the ceiling temperature and the mechanism of termination were beyond the scope of the study. The present study explored all possible reaction sites of the radical site with a neutral solvent to form the initiator and all possible reactions of these initiators with every site on another neutral solvent molecule. The results of these calculations are shown in Figure 2 a,b for the creation of the radical polymerization initiators and in Figure 2 c,d for the proposed monomers (repeat units). The initial reaction site is the ethyl carbon of EC that creates a carbon-carbon bond and radical delocalized over the carboxyl

In Applications of Molecular Modeling to Challenges in Clean Energy; Fitzgerald, G., et al.;
ACS Symposium Series; American Chemical Society: Washington, DC, 2013.

group. The carboxyl radical then reacts at the ethyl carbon of a second neutral EC with ring opening to form a subsequent carboxyl radical. This propagation step is repeated until a terminating reaction or the entropic cost of propagation is higher than the stabilization from reacting further. Following this mechanism for EC the proposed mechanism would lead to a monomer with a molecular weight of 176 g/mol in agreement with the experimental results. The monomer from the PC would have a molecular weight of 200 g/mol that is much higher than experimentally observed. However, the terminal carboxyl group can undergo decarboxylation, which is slightly exothermic w.r.t the reactants indicating that some number of the PC molecules will undergo decarboxylation. If the number undergoing decarboxylation were about half then the molecular weight would be 160 g/mol, which is very close to the experimentally observed value of 166 g/mol. The difference could be due to associated lithium atoms. The reason for the lack of decarboxylation of the EC oligomer is that that the reaction is less favorable and creates a radical that is less likely to polymerize.

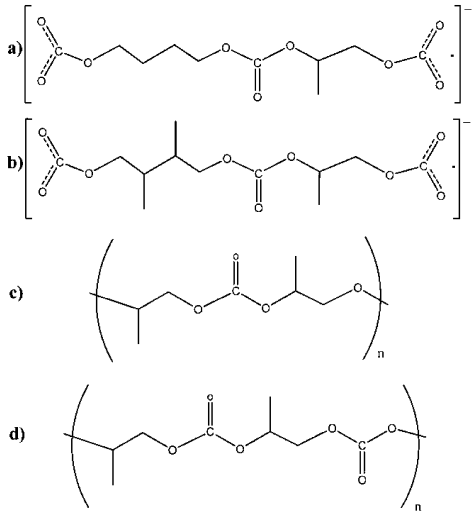

Figure 2. The predicted products of oligomerization reaction for the radical oligomerization of ethylene carbonate (EC) on Au electrodes showing the products of the first propagation steps starting from EC a) and propylene carbonate (PC) b). The monomers for the predicted oligomers are shown for EC c) and PC d). Reproduced with permission from reference (17). Copyright 2012 The Electrochemical Society.

3. Classical and Ab Initio Molecular Dynamics Simulations

One of the major failings of DFT is the lack of time-dependent information. Solutions to the time-dependent Schrödinger equation are too computationally costly for all but the simplest systems. To find properties that are not possible with time-independent calculations MD simulations are used. MD numerically

solves Newton's equations of motion by calculating the forces acting on the atoms starting from a particular trajectory. These trajectories can be randomly generated or directed. The methods are designed to calculate the quantity of interest from an appropriate statistical ensemble e.g., an isothermal-isobaric ensemble (NPT) to calculate Gibbs free energy. The energy and forces are generated by either fitting parameters (classical MD) using either experimental data or by directly calculating values using ab initio calculations. Parameterizing predefined functions of the intra- and intermolecular interactions using ab initio computations is often the method used to generate fitting parameters. These sets functions are called force fields and are, in general, non-transferable to other systems unless very closely related. If the forces are directly computed using an ab initio method such as DFT then the method is termed ab initio molecular dynamics (AIMD). The later form is much more accurate, but limited in time scale due to the much higher computational cost. AIMD that calculates the ab initio forces by recomputing the quantum mechanical energy at every step are termed Born-Oppenheimer molecular dynamics. To speed up the number of time steps other methods that compute the quantum mechanical energy once and then propagating the forces using fictitious dynamics has been developed. Methods using plane-wave basis sets and a fictitious mass scalar are called Car-Parrinello dynamics after the original developers while some methods that use localized Gaussian orbitals and fictitious mass tensor are called atom-centered density matrix propagation (ADMP). Since both of these methods use the quantum mechanical potential energy surfaces they are usually just as good at calculating bond breaking and bond forming as the quantum mechanical method used. While other methods are possible in almost all cases AIMD utilizes DFT.

Classical MD has not seen as extensive use in solving problems related to Li-ion batteries as quantum chemical methods due to the lack of accurate and available parameter set for classical MD. As parameter sets become available this method will likely become more prominent. An early study using classical MD simulations of Li-ion batteries was on the intercalation of lithium into metal oxides (*68*). Several studies on the association of salts with lithium and organic solvents have been carried out (*70*, *71*). The decomposition of the organic solvent or salt and the lithium solvation studies have been completed along with a study of the dynamics of the electrolyte under potential. The last study is notable for including the entire electrolyte composition in the study.

AIMD methods have also not seen as widespread use as quantum chemical methods. The cause is twofold. AIMD calculations have a significant computational cost and expertise in this method is much less prevalent than quantum chemical methods. As the usage of AIMD in the modeling community increases and computational cost of AIMD decreases this method will gain traction for Li-ion applications. Several current studies of Li-ion batteries using AIMD include the diffusion of Li^+ and its solvation shell (*41*, *42*) along with a series on the formation of the SEI (*8*, *66*).

In a study by Bedrov *et al.* (*66*) the reactivity of a singly reduced EC reacting to form the products of the outer SEI was studied using the ReaxFF force field. This force field uses a bond-order method with a polarizable charge calculation (*8*, *66*). The method was fit for systems containing Li/C/H/O and constrained to

In Applications of Molecular Modeling to Challenges in Clean Energy; Fitzgerald, G., et al.;
ACS Symposium Series; American Chemical Society: Washington, DC, 2013.

reproduce the DFT value for the EC ring-opening reaction barrier. The reactions simulated included gas-phase pathways using a bias potential to enforce the desired reaction path in addition to constrained and unconstrained solution phase calculations. The simulations indicated the most likely pathway for the reaction of two EC molecules that have undergone ring opening is of butyl dicarbonate $(CH_2CH_2OCO_2Li)_2$. The most likely path for one ring-opened EC and one closed EC is an ester carbonate compound, Figure 3. The simulation showed that at high ring-opened EC radical concentrations diradicals could form and undergo chain reaction. The concentrations required for this latter reaction are too high to be realistic. Interestingly the study did not predict the presence of the ethylene dicarbonate that is believed to be the experimentally observed product (*84*). In this instance the theoretical results are in disagreement with the experimental results indicating that, if correct, the proposed mechanism for the formation of the outer SEI layer is incomplete.

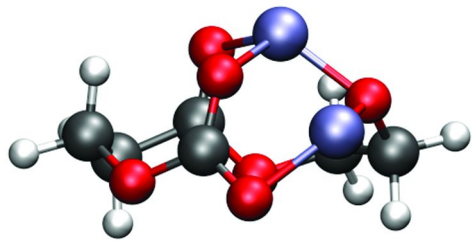

Figure 3. The ester-carbonate compound is predicted to be a possible minimum by MD simulations using the ReaxFF force field in reference (66). The color used above code is carbon=grey, oxygen=red, lithium=blue-violet and hydrogen=white. (see color insert)

While the use of AIMD in modeling Li-ion electrolytes is not wide spread there are several very interesting studies. One particularly interesting study based on the AIMD is on the two-electron reduction mechanism of EC. While much of the study in which this reaction is included is concerned with using atomic layer deposition to reduce electrolyte decomposition, the AIMD results and its subsequent analysis are significant on their own. In AIMD the reaction mechanism is not predefined, therefore reactions that have not been previously considered can emerge from the simulation. In the case of this simulation eleven EC molecules were placed proximate to a Li(100) surface. During a simulation of 15 picoseconds all of the EC molecules become reduced and decompose. The accepted mechanism of EC decomposition is two-electron reduction close to the electrode to form ethylene along with a carbonate that combines with two Li^+ to form lithium carbonate. The one-electron reduction of EC is transfer of an electron followed by ring opening. The mechanism seen in this study is the two-electron

In Applications of Molecular Modeling to Challenges in Clean Energy; Fitzgerald, G., et al.;
ACS Symposium Series; American Chemical Society: Washington, DC, 2013.

reduction of EC to form $OCH_2CH_2O^{2-}$ and CO. This intermediate has not been previously proposed but has significant implications if subsequently verified. It was postulated that the $OCH_2CH_2O^{2-}$ could react with two CO_2 molecules to form ethylene dicarbonate, which is proposed to be the major constituent of the SEI layer (*84*). This mechanism challenges the typically assumed one-electron and two-electron reduction mechanisms and highlights the likely importance of the two-electron mechanism.

4. Ab Initio Screening

Many problems in chemistry suffer from a dearth of fundamental understanding. In these problems there are too many degrees of freedom to be effectively understood using small datasets. One area in which this is a significant problem is in computational drug design. The number of possible drug candidates and protein targets is very large and the data on proteins, drugs candidates, and their interaction is insufficient to arrive at general rules for drug design. This problem is also found in materials design where there is a similar problem of a vast number of materials compositions and structures whose connection to materials properties is either poorly understood or unknown. A method for overcoming this problem has been developed for drug discovery and in catalyst design. This method is to reduce the information needed to only that required to solve the problem of interest. This information can then be experimentally measured or calculated for a large library of molecules. Automation of data collection and analysis is used due to the large number of molecules necessary to include in the library. This method is called high-throughput screening, or if the data is provided from computations, virtual high-throughput screening. In lead discovery in drug design virtual high-throughput screening is *de rigueur,* but in materials science several challenges have prevented the widespread adoption of this method outside of catalyst design and some new efforts in materials design. These challenges include a lack of computational methods to accurately and efficiently calculate or measure properties and a lack of knowledge about how the properties are related to calculable or observable quantities. One important direction in virtual high-throughput screening of materials has used data from first principles calculations along with outstanding insights to design catalysts and other materials (*10*, *20*, *22–26*, *75*, *76*, *85–91*). These high-throughput methods for catalyst design rely upon descriptors of catalytic activity that can be calculated at a reasonable computational cost. While other descriptors may exist, current methods use the binding energy of elements to the catalytic active site (*22–26*, *85–92*).

The use of virtual high-throughput screening of electrolytes is a new area with few studies. The literature describing the theory of how descriptors relate to electrolyte properties is sparse. However, some excellent studies relating the values of electrolytes to quantities necessary for designing descriptors do exist. These include the fast evaluation of the reduction potential using semiempirical data and a review of electrolyte additive effects. The translation of these quantities into descriptors for the suitability of electrolytes that were then used for high-

In Applications of Molecular Modeling to Challenges in Clean Energy; Fitzgerald, G., et al.;
ACS Symposium Series; American Chemical Society: Washington, DC, 2013.

throughput screening has, to our knowledge, only been the subject of a small number of studies (*10*, *20*, *75*) one of which will be highlighted below.

In this study the effect of alkylated and fluorinated functional groups on EC was examined using high-throughput screening techniques. The basis of the screening was inspired from previous studies. A chemical motif was chosen, relevant quantities were decided upon, a virtual library was generated, and the library was screened for molecules with properties in the range of interest. The chemical motif used EC functionalized with alkyl groups of less three or less carbon atoms. These groups were then functionalized with some number of fluorine atoms replacing hydrogen. All possible variations of the motif were generated and used to form the virtual library.

The choice of descriptors is important for determining the usefulness of the data. In this work a set of values were generated for rapid estimation of the stability and reactivity of the electrolyte candidates, specifically, the formation of the SEI layer on the anode. The quantities chosen are the highest occupied molecular orbital (HOMO), lowest unoccupied molecular orbital (LUMO), vertical ionization potential, vertical electron affinity, dipole moment, polarizability, and chemical hardness. The values used in screening were calculated as the difference between the candidate molecule value and the EC value as computed using the PM3 model chemistry. The semiempirical values for the molecular LUMO were previously correlated to the electron affinity as might be expected from Koopman's theorem (*76*). The value of the vertical electron affinity is directly calculated as well. The quantities give an indication of the reduction potential of the candidate molecule relative to the EC reference. The reduction potential is directly related to the electron affinity of the molecule and reduced EC is implicated in formation of the SEI. This descriptor would indicate which candidates are more likely to become reduced than the EC and form an SEI. The dipole moment and polarizability give some measure of the ability of the electrolyte solvent molecule to interact with lithium cations in the electrolyte. The chemical hardness defined as ½ the difference of the vertical ionization potential and the electron affinity is a measure of the reactivity of the candidate. If a candidate is very unreactive then it is a poor choice because it will not react to form the SEI layer. The structures determined to be optimal were those with a high dipole moment and vertical electron affinity while having a small value for chemical hardness. Since changing the vertical electron affinity also affects the chemical hardness there is a tradeoff. Therefore, the best candidates will be Pareto-optimal.

The results of the study showed that most of the fluorinated structures had significantly higher vertical electron affinities than EC making them better candidates to undergo reduction and subsequent SEI formation. This trend was also observed for chemical hardness with fluorinated EC derivatives being more reactive. The candidate molecule that best maximized the vertical electron affinity and dipole moment, but minimized the chemical hardness (lower hardness is higher reactivity) is shown in Figure 4. A subsequent study also showed the importance of these descriptors and proposed low Li^+ binding affinity as another important descriptor (*10*).

In Applications of Molecular Modeling to Challenges in Clean Energy; Fitzgerald, G., et al.;
ACS Symposium Series; American Chemical Society: Washington, DC, 2013.

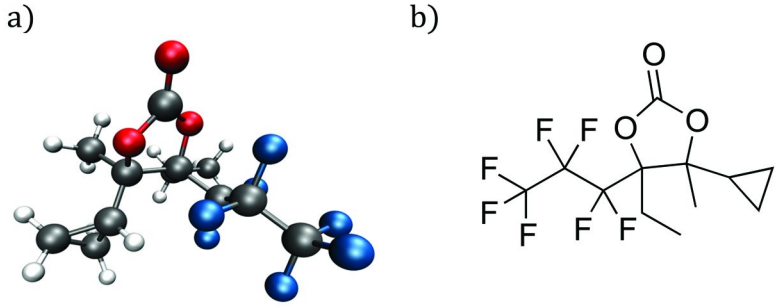

Figure 4. The 4-cyclopropyl-5-ethyl-4-methyl-5-(perfluoropropyl)-1,3-dioxolan-2-one molecule that was determined to be the best organic solvent molecule for SEI formation as predicted by ab initio screening calculations, Ref (75). The color used above code is carbon=grey, oxygen=red, fluorine=blue and hydrogen=white. (see color insert)

5. Future Directions

While Li-ion batteries are extensively used, improvements in battery technology are necessary to further expand their use. Continued scientific development that addresses the battery shortcomings includes increased capacity, elimination of voltage fade, improved safety, and decreased cost among many others. The use of atomic-level simulations to study organic solvents and other components of the electrolytes has generated information concerning the basic chemistry of Li-ion batteries and the formation of the critically important SEI layer. As the power and detail provided by atomic-level simulations increases so will their potential to solve ever more challenging problems in Li-ion technology. While some questions can only be answered by mesoscale or continuum calculations the information provided by atomic-level simulations can play an important role in driving forward this important technology. The most used method to date is quantum chemical calculations. In addition to providing more data about the detailed chemistry of Li-ion battery electrolytes, DFT and wavefunction methods will likely be used as benchmarks for more approximate, but less computationally intensive methods such as MD. In Li-ion batteries one of the failings is that all reactions that are reasonably possible must be sampled to determine the reaction pathway. In the complex environment of the electrochemical cell, the time and effort to accomplish this goal can be prohibitive. Methods that do not assume the reaction path prior to the calculation using MD are rarely used. The simple reason is that the requirements of forming and breaking bonds negated the use of many force fields. Reactive force fields, like those highlighted in Section 3 require accurate fitting. Once the fitting sets for these reactive force fields are well established and distributed then it

In Applications of Molecular Modeling to Challenges in Clean Energy; Fitzgerald, G., et al.;
ACS Symposium Series; American Chemical Society: Washington, DC, 2013.

is likely these methods will become more important to the battery community. Some simulations will require the accuracy of DFT methods realized in AIMD. The challenge for this method is the exceptional computational cost and lack of widespread expertise in the battery community. Both of these can reasonably be expected to change in the future augmenting simulations to understand Li-ion batteries. The final area involves screening that could reasonably be expected to increase in the near-term since these methods are currently available. The component that is missing from this work is the use of databases and informatics. The chemistry community has not traditionally used these methods. Recent trends in materials design indicate a growing acceptance as the amount of data produced by quantum calculations exceeds the amount that can be analyzed using straightforward means. With this advent, screening is likely to be an important tool in materials design of Li-ion batteries.

Outside of already explored areas it is possible to consider the use of techniques that utilize atomic-level information to predict or model the structure or properties of electrolytes and electrolyte/electrode interfaces. Determination of the structure of the SEI layer could be accelerated by adapting other optimization techniques such as kinetic Monte Carlo and particle swarm optimization (*93–97*). Kinetic Monte Carlo uses the rates, determined from atomic-level calculations, to model surface growth as well as applications. If a sufficient amount of data were available it would be possible to use kinetic Monte Carlo to predict the SEI structure. Particle swarm optimization has been previously used to determine the structure of gas phase clusters (*94–97*). These techniques utilize methods inspired by natural systems to find the global minimum for clusters and could likely be adapted to structure determination accelerating the process of understanding SEI growth.

Another interesting possibility that has not yet been attempted is the use of genetic algorithms and machine learning to optimize the electrolytes for SEI growth in a manner similar to screening. Like particle swarm optimization, genetic algorithms is a method inspired by natural processes to evolve a better material by selecting and recombining molecules or species that best optimize a parameter or set of parameters (*98–106*). The process has been successfully used for atomic cluster geometry optimization. The method might be an improvement from electrolyte screening. Screening requires that the electrolyte's properties must be calculated before it can be tested. In evolving better electrolytes with a genetic algorithm the input of the researcher is less important since the algorithm itself optimizes the electrolyte by forming new molecules. While the synthesis of these molecules might be difficult or impossible the method would inform the construction of novel electrolytes. This may also be true for machine learning. The idea of machine learning encompasses many algorithms with the goal of training a system to learn from data. Machine learning has been at demonstrated for in chemistry for applications including kernel ridge regression to solve for the energy of small organic molecules with reasonable accuracy (*107*). These methods could be implemented in a similar manner to solve problems in from organic electrolytes and electrolyte/electrode interfaces in Li-ion batteries.

In Applications of Molecular Modeling to Challenges in Clean Energy; Fitzgerald, G., et al.;
ACS Symposium Series; American Chemical Society: Washington, DC, 2013.

Acknowledgments

Office of Vehicle Technologies of the U.S. Department of Energy under the Batteries for Advanced Transportation Technologies Program, U.S. Department of Energy, under contract under Contract No. DE-AC02-06CH11357.

References

1. Etacheri, V.; Marom, R.; Elazari, R.; Salitra, G.; Aurbach, D. *Energy Environ. Sci.* **2011**, *4*, 3243.
2. Oh, Y.; Nam, S.; Wi, S.; Hong, S.; Park, B. *Electron. Mater. Lett.* **2012**, *8*, 91.
3. Wu, D.-h.; Zhou, Z. *Front. Phys.* **2011**, *6*, 197.
4. Zhao, Y.-J.; Feng, H.-L.; Zhao, C.-S.; Sun, Z.-Q. *J. Inorg. Mater.* **2011**, *26*, 673.
5. Aditya, J. P.; Ferdowsi, M. *2008 IEEE Vehicle Power and Propulsion Conference (VPPC)*, Hei Longjiang, China, September 3−5, 2008.
6. Fang, W.; Kwon, O. J.; Wang, C.-Y. *Int. J. Energy Res.* **2010**, *34*, 107.
7. Han, Y.-K.; Jung, J.; Yu, S.; Lee, H. *J. Power Sources* **2009**, *187*, 581.
8. Kim, S.-P.; van Duin, A. C. T.; Shenoy, V. B. *J. Power Sources* **2011**, *196*, 8590.
9. Li, H.; Wang, Z.; Chen, L.; Huang, X. *Adv. Mater.* **2009**, *21*, 4593.
10. Park, M. H.; Lee, Y. S.; Lee, H.; Han, Y.-K. *J. Power Sources* **2011**, *196*, 5109.
11. Shang, S.-L.; Hector, L. G., Jr.; Shi, S.; Qi, Y.; Wang, Y.; Liu, Z.-K. *Acta Mater.* **2012**, *60*, 5204.
12. Shi, S.; Lu, P.; Liu, Z.; Qi, Y.; Hector, L. G., Jr.; Li, H.; Harris, S. J. *J. Am. Chem. Soc.* **2012**, *134*, 15476.
13. Tasaki, K. *J. Electrochem. Soc.* **2002**, *149*, A418.
14. Tasaki, K. *J. Phys. Chem. B* **2005**, *109*, 2920.
15. Tasaki, K.; Kanda, K.; Nakamura, S.; Ue, M. *J. Electrochem. Soc.* **2003**, *150*, A1628.
16. Tasaki, K.; Nakamura, S. *J. Electrochem. Soc.* **2001**, *148*, A984.
17. Tavassol, H.; Buthker, J. W.; Ferguson, G. A.; Curtiss, L. A.; Gewirth, A. A. *J. Electrochem. Soc.* **2012**, *159*, A730.
18. Wang, R. L.; Buhrmester, C.; Dahn, J. R. *J. Electrochem. Soc.* **2006**, *153*, A445.
19. Wang, Y. X.; Balbuena, P. B. *J. Phys. Chem. A* **2002**, *106*, 9582.
20. Zhang, S. S. *J. Power Sources* **2006**, *162*, 1379.
21. Zhang, X. R.; Kostecki, R.; Richardson, T. J.; Pugh, J. K.; Ross, P. N. *J. Electrochem. Soc.* **2001**, *148*, A1341.
22. Ceder, G.; Hautier, G.; Jain, A.; Ong, S. P. *MRS Bull.* **2011**, *36*, 185.
23. Hautier, G.; Fischer, C.; Ehrlacher, V.; Jain, A.; Ceder, G. *Inorg. Chem.* **2011**, *50*, 656.
24. Hautier, G.; Jain, A.; Chen, H.; Moore, C.; Ong, S. P.; Ceder, G. *J. Mater. Chem.* **2011**, *21*, 17147.

25. Hautier, G.; Jain, A.; Ong, S. P.; Kang, B.; Moore, C.; Doe, R.; Ceder, G. *Chem. Mater.* **2011**, *23*, 3495.
26. Jain, A.; Hautier, G.; Moore, C. J.; Ong, S. P.; Fischer, C. C.; Mueller, T.; Persson, K. A.; Ceder, G. *Comput. Mater. Sci.* **2011**, *50*, 2295.
27. Leggesse, E. G.; Jiang, J.-C. *RSC Adv.* **2012**, *2*, 5439.
28. Leung, K. *Chem. Phys. Lett.* **2012**.
29. Leung, K.; Budzien, J. L. *Phys. Chem. Chem. Phys.* **2010**, *12*, 6583.
30. Mengqing, X.; Liu, Z.; Liansheng, H.; Lidan, X.; Weishan, L.; Lucht, B. L. *J. Power Sources* **2011**, *196*, 6794.
31. Tasaki, K.; Harris, S. J. *J. Phys. Chem. C* **2010**, *114*, 8076.
32. Wang, B.; Qu, Q. T.; Xia, Q.; Wu, Y. P.; Li, X.; Gan, C. L.; van Ree, T. *Electrochim. Acta* **2008**, *54*, 816.
33. Wang, Y. X.; Balbuena, P. B. *J. Phys. Chem. B* **2002**, *106*, 4486.
34. Xing, L. D.; Wang, C. Y.; Xu, M. Q.; Li, W. S.; Cai, Z. P. *J. Power Sources* **2009**, *189*, 689.
35. Xu, M.; Zhou, L.; Hao, L.; Xing, L.; Li, W.; Lucht, B. L. *J. Power Sources* **2011**, *196*, 6794.
36. Xu, M.; Zhou, L.; Xing, L.; Li, W.; Lucht, B. L. *Electrochim. Acta* **2010**, *55*, 6743.
37. Yamada, Y.; Iriyama, Y.; Abe, T.; Ogumi, Z. *Langmuir* **2009**, *25*, 12766.
38. Abe, T.; Kawabata, N.; Mizutani, Y.; Inaba, M.; Ogumi, Z. *J. Electrochem. Soc.* **2003**, *150*, A257.
39. Bhatt, M. D.; Cho, M.; Cho, K. *Appl. Surf. Sci.* **2010**, *257*, 1463.
40. Bhatt, M. D.; Cho, M.; Cho, K. *Can. J. Chem.* **2011**, *89*, 1525.
41. Bhatt, M. D.; Cho, M.; Cho, K. *J. Solid State Electrochem.* **2012**, *16*, 435.
42. Bhatt, M. D.; Maenghyo, C.; Kyeongjae, C. *Modell. Simul. Mater. Sci. Eng.* **2012**, *20*, 065004.
43. Borodin, O.; Smith, G. D. *J. Phys. Chem. B* **2009**, *113*, 1763.
44. Chen, Y. C.; Ouyang, C. Y.; Song, L. J.; Sun, Z. L. *J. Phys. Chem. C* **2011**, *115*, 7044.
45. Golodnitsky, D.; Livshits, E.; Kovarsky, R.; Peled, E.; Chung, S. H.; Suarez, S.; Greenbaum, S. G. *Electrochem. Solid-State Lett.* **2004**, *7*, A412.
46. Johansson, P. *Polymer* **2001**, *42*, 4367.
47. Johansson, P. *Phys. Chem. Chem. Phys.* **2007**, *9*, 1493.
48. Lidan, X.; Weishan, L.; Mengqing, X.; Tiantian, L.; Liu, Z. *J. Power Sources* **2011**, *196*, 7044.
49. Marquez, A.; Vargas, A.; Balbuena, P. B. *J. Electrochem. Soc.* **1998**, *145*, 3328.
50. Nakayama, M.; Kotobuki, M.; Munakata, H.; Nogami, M.; Kanamura, K. *Phys. Chem. Chem. Phys.* **2012**, *14*, 10008.
51. Shevlin, S. A.; Cazorla, C.; Guo, Z. X. *J. Phys. Chem. C* **2012**, *116*, 13488.
52. Tasaki, K.; Kanda, K.; Kobayashi, T.; Nakamura, S.; Ue, M. *J. Electrochem. Soc.* **2006**, *153*, A2192.
53. Vollmer, J. M.; Curtiss, L. A.; Vissers, D. R.; Amine, K. *J. Electrochem. Soc.* **2004**, *151*, A178.
54. Wang, Y. X.; Balbuena, P. B. *Int. J. Quantum Chem.* **2005**, *102*, 724.

55. Wang, Y. X.; Nakamura, S.; Tasaki, K.; Balbuena, P. B. *J. Am. Chem. Soc.* **2002**, *124*, 4408.
56. Wang, Y. X.; Nakamura, S.; Ue, M.; Balbuena, P. B. *J. Am. Chem. Soc.* **2001**, *123*, 11708.
57. Xing, L.; Borodin, O. *Phys. Chem. Chem. Phys.* **2012**, *14*, 12838.
58. Xing, L.; Borodin, O.; Smith, G. D.; Li, W. *J. Phys. Chem. A* **2011**, *115*, 13896.
59. Xing, L.; Li, W.; Wang, C.; Gu, F.; Xu, M.; Tan, C.; Yi, J. *J. Phys. Chem. B* **2009**, *113*, 16596.
60. Xing, L.; Wang, C.; Li, W.; Xu, M.; Meng, X.; Zhao, S. *J. Phys. Chem. B* **2009**, *113*, 5181.
61. Yao, F.; Guenes, F.; Huy Quang, T.; Lee, S. M.; Chae, S. J.; Sheem, K. Y.; Cojocaru, C. S.; Xie, S. S.; Lee, Y. H. *J. Am. Chem. Soc.* **2012**, *134*, 8646.
62. Yoshikawa, A.; Morales, J. A. *J. Mol. Struct.: THEOCHEM* **2004**, *681*, 27.
63. Zhang, Z.; Zhang, L.; Schlueter, J. A.; Redfern, P. C.; Curtiss, L.; Amine, K. *J. Power Sources* **2010**, *195*, 4957.
64. Albe, K.; Nordlund, K.; Averback, R. S. *Phys. Rev. B* **2002**, *65*, 195124.
65. Erhart, P.; Albe, K. *Phys. Rev. B* **2005**, *71*, 035211.
66. Bedrov, D.; Smith, G. D.; van Duin, A. C. T. *J. Phys. Chem. A* **2012**, *116*, 2978.
67. Kalcher, I.; Dzubiella, J. *J. Chem. Phys.* **2009**, *130*.
68. Kulp, D. T.; Garofalini, S. H. *J. Electrochem. Soc.* **1996**, *143*, 2211.
69. Seo, D. M.; Borodin, O.; Han, S.-D.; Ly, Q.; Boyle, P. D.; Henderson, W. A. *J. Electrochem. Soc.* **2012**, *159*, A553.
70. Takeuchi, M.; Matubayasi, N.; Kameda, Y.; Minofar, B.; Ishiguro, S.-i.; Umebayashi, Y. *J. Phys. Chem. B* **2012**, *116*, 6476.
71. Tasaki, K.; Goldberg, A.; Winter, M. *Electrochim. Acta* **2011**, *56*, 10424.
72. Vatamanu, J.; Borodin, O.; Smith, G. D. *J. Phys. Chem. C* **2012**, *116*, 1114.
73. Leung, K. *J. Phys. Chem. C* **2012**, *116*, 9852.
74. Leung, K.; Qi, Y.; Zavadil, K. R.; Jung, Y. S.; Dillon, A. C.; Cavanagh, A. S.; Lee, S.-H.; George, S. M. *J. Am. Chem. Soc.* **2011**, *133*, 14741.
75. Halls, M. D.; Tasaki, K. *J. Power Sources* **2010**, *195*, 1472.
76. Heaton, C. A.; Miller, A. K.; Powell, R. L. *J. Fluorine Chem.* **2001**, *107*, 1.
77. Redfern, P. C.; Curtiss, L. A. *J. Power Sources* **2002**, *110*, 401.
78. Sutjianto, A.; Curtiss, L. A. *J. Phys. Chem. A* **1998**, *102*, 968.
79. Balbuena, P. B.; Wang, Y. *Lithium-Ion Batteries*; World Scientific: Hackensack, NJ, 2004.
80. Borodin, O.; Smith, G. D.; Bandyopadhyaya, R.; Redfern, P.; Curtiss, L. A. *Modell. Simul. Mater. Sci. Eng.* **2004**, *12*, S73.
81. Kerr, J. B.; Liu, G.; Curtiss, L. A.; Redfern, P. C. *Electrochim. Acta* **2003**, *48*, 2305.
82. Mao, G.; Baboul, A. G.; Curtiss, L. A.; Price, D. L.; Saboungi, M. L.; Armand, M. B.; Howells, W. S.; Fischer, H. E. Structure and Dynamics of Lithium Polymer Electrolytes. Proceedings of the International Symposium on Molten Salts XII, Electrochemical Society, Pennington, NJ, 2000, Vol. 99.
83. Lee, J. C.; Litt, M. H. *Macromolecules* **2000**, *33*, 1618.
84. Xu, K. *Chem. Rev.* **2004**, *104*, 4303.

In Applications of Molecular Modeling to Challenges in Clean Energy; Fitzgerald, G., et al.;
ACS Symposium Series; American Chemical Society: Washington, DC, 2013.

85. Andersson, M. P.; Bligaard, T.; Kustov, A.; Larsen, K. E.; Greeley, J.; Johannessen, T.; Christensen, C. H.; Norskov, J. K. *J. Catal.* **2006**, *239*, 501.
86. Christensen, C. H.; Norskov, J. K. *J. Chem. Phys.* **2008**, *128*.
87. Hummelshoj, J. S.; et al. *J. Chem. Phys.* **2009**, *131*.
88. Hummelshoj, J. S.; et al. *J. Chem. Phys.* **2009**, *131*, 014101.
89. Norskov, J. K.; Abild-Pedersen, F. *Nature* **2009**, *461*, 1223.
90. Norskov, J. K.; Abild-Pedersen, F.; Studt, F.; Bligaard, T. *Proc. Natl. Acad. Sci. U.S.A.* **2011**, *108*, 937.
91. Norskov, J. K.; Bligaard, T.; Rossmeisl, J.; Christensen, C. H. *Nat. Chem.* **2009**, *1*, 37.
92. Munter, T. R.; Landis, D. D.; Abild-Pedersen, F.; Jones, G.; Wang, S.; Bligaard, T. *Comput. Sci. Discovery* **2009**, *2*, 015006(27 pp.).
93. Battaile, C. C.; Srolovitz, D. J. *Ann. Rev. Mater. Res.* **2002**, *32*, 297.
94. Call, S. T.; Zubarev, D. Y.; Boldyrev, A. I. *J. Comput. Chem.* **2007**, *28*, 1177.
95. Fournier, R.; Bulusu, S.; Chen, S.; Tung, J. *J. Chem. Phys.* **2011**, *135*.
96. Ivanov, A. S.; Boldyrev, A. I. *Phys. Chem. Chem. Phys.* **2012**, *14*, 15943.
97. Lv, J.; Wang, Y.; Zhu, L.; Ma, Y. *J. Chem. Phys.* **2012**, *137*.
98. Herbers, C. R.; Johnston, K.; van der Vegt, N. F. A. *Phys. Chem. Chem. Phys.* **2011**, *13*, 10577.
99. Johnston, R. L. *Dalton Trans.* **2003**, 4193.
100. Johnston, R. L.; Mortimer-Jones, T. V.; Roberts, C.; Darby, S.; Manby, F. R. In *Proceedings of Applications of Evolutionary Computing*; Cagnoni, S., Gottieb, J., Hart, E., Middendorf, M., Raidl, G. R., Eds;. 2002; Vol. 2279, p 92.
101. Lloyd, L. D.; Johnston, R. L.; Roberts, C.; Mortimer-Jones, T. V. *ChemPhysChem* **2002**, *3*, 408.
102. Lloyd, L. D.; Johnston, R. L.; Salhi, S. In *Proceedings on Genetic and Evolutionary Computation Gecco 2004, Part 2*; Deb, K., Poli, R., Banzhaf, W., Beyer, H. G., Burke, E., Darwen, P., Dasgupta, D., Floreano, D., Foster, O., Harman, M., Holland, O., Lanzi, P. L., Spector, L., Tettamanzi, A., Thierens, D., Tyrrell, A., Eds.; 2004; Vol. 3103, p 1316.
103. Logsdail, A. J.; Li, Z. Y.; Johnston, R. L. *J. Comput. Chem.* **2012**, *33*, 391.
104. Luo, X.; Yang, J.; Liu, H.; Wu, X.; Wang, Y.; Ma, Y.; Wei, S.-H.; Gong, X.; Xiang, H. *J. Am. Chem. Soc.* **2011**, *133*, 16285.
105. McLeod, A. S.; Johnston, M. E.; Gladden, L. F. *J. Catal.* **1997**, *167*, 279.
106. Mueller, C. L.; Sbalzarini, I. F. *Evol. Comput.* **2012**, *20*, 543.
107. Rupp, M.; Tkatchenko, A.; Mueller, K.-R.; von Lilienfeld, O. A. *Phys. Rev. Lett.* **2012**, *108*.

Editors' Biographies

George Fitzgerald

George Fitzgerald received his B.S. in Chemistry from Case Western Reserve University in 1980 and his Ph.D. from the University of California, Berkeley in 1984, where he worked on the development of *ab initio* modeling methods. Currently, he is an Advisory Scientist at Accelrys, Inc., where he helps scientists in the chemical, electronic, energy, and materials sectors address some of their most challenging research problems using molecular modeling and informatics. His personal research interests include nanotechnology, alternative energy, and evolutionary computing method

Niranjan (Niri) Govind

Niranjan (Niri) Govind (Ph.D.) is a senior scientist in the Environmental Molecular Sciences Laboratory (EMSL) at the Pacific Northwest National Laboratory (PNNL) in Richland, Washington. He is a current member of the NWChem development team, and his research interests include the development of methods and algorithms in density functional theory (DFT), linear response and real-time time-dependent density functional theory (TDDFT), orbital-free DFT, solid-state embedding methods for materials, excited state properties of molecules and materials, solid-state NMR and EPR, geometry, and transition-state optimization algorithms. He has authored or co-authored over 80 peer-reviewed publications in these areas. Before joining PNNL in 2007, he was a lead scientist at Accelrys, Inc. in San Diego, California, where he made significant contributions to the widely used commercial DFT programs, DMol3 and CASTEP.

In Applications of Molecular Modeling to Challenges in Clean Energy; Fitzgerald, G., et al.;
ACS Symposium Series; American Chemical Society: Washington, DC, 2013.

Subject Index

In Applications of Molecular Modeling to Challenges in Clean Energy; Fitzgerald, G., et al.; ACS Symposium Series; American Chemical Society: Washington, DC, 2013.

E

F

H

In Applications of Molecular Modeling to Challenges in Clean Energy; Fitzgerald, G., et al.;
ACS Symposium Series; American Chemical Society: Washington, DC, 2013.

I

L

M

O

P

In Applications of Molecular Modeling to Challenges in Clean Energy; Fitzgerald, G., et al.; ACS Symposium Series; American Chemical Society: Washington, DC, 2013.

Q

R

In Applications of Molecular Modeling to Challenges in Clean Energy; Fitzgerald, G., et al.; ACS Symposium Series; American Chemical Society: Washington, DC, 2013.

S

W

In Applications of Molecular Modeling to Challenges in Clean Energy; Fitzgerald, G., et al.;
ACS Symposium Series; American Chemical Society: Washington, DC, 2013.